Development and characterization of the balloon borne instrument TELIS (TErahertz and submillimeter LImb Sounder): 1.8 THz receiver

Vom Fachbereich für Physik und Elektrotechnik
der Universität Bremen

zur Erlangung des akademischen Grades eines
Doktor der Naturwissenschaften (Dr. rer. nat.)
genehmigte Dissertation

von
M.Sc. Nopporn Suttiwong
aus Bangkok, Thailand

1. Gutachter:	Prof. Dr. Justus Notholt
2. Gutachter:	Prof. Dr. Klaus Künzi
1. Prüfer:	Prof. Dr. Stefan Bornholdt
2. Prüfer:	Prof. Dr. Thomas Trautmann

Eingereicht am:	01.06.2010
Tag des Promotionskolloquiums:	25.10.2010

Promotionsort : Universität Bremen (2010)

This research described in this thesis was carried out at the Remote Sensing Technology Institute, German Aerospace Center (DLR, Oberpfaffenhofen).

„Misunderstanding leads to disaster”

For my mother, Yenta Chaodee

Abstract

Research on ozone has increased since the mid-1970s at which the ozone depletion was discovered. Both observational data and laboratory studies are demanded in order to improve the understanding of the global climate change which yield better numerical models for predictions. Nevertheless, there is still lack of observational data for enhancing the understanding of the related atmospheric and chemical processes of stratospheric ozone. Over the years, many remote sensing instruments have been developed and used for observing the atmospheric trace gas distributions associated with e.g. ozone destruction in various latitudes.

Since 2001, a balloon-borne instrument called "TELIS (TErahertz and submillimeter LImb Sounder)" is under development at the German Aerospace Center (DLR), and this instrument has already successfully been used for measuring atmospheric constituents within the lower stratosphere.

The work of this thesis is dedicated to the development and characterization of a cryogenic heterodyne receiver of the TELIS instrument used for measuring the OH emission at a frequency of 1.8 THz. In the framework of this thesis, all major components of the 1.8 THz channel were individually characterized before they were installed together. The methods and results for developing and characterizing the 1.8 THz channel are described in this thesis. In addition, radiometric characterization of the receiver was done by gas cell measurements of methanol gas.

The present work also includes the integration of the 1.8 THz receiver into the TELIS flight module cryostat, and putting the instrument into operation in scientific flight campaigns. The integration was successfully done since the end of 2006. The characterization after the integration was fully done during 2007/2008 which yields the sensitivity improvement of the 1.8 THz heterodyne receiver of about 70% with respect to the prototype developed in 2005.

After a first test flight in Teresina, Brazil, in May 2008, the 1.8 THz receiver was improved and operated well during a second flight campaign in Kiruna, Sweden, in March 2009. Various important atmospheric constituents within the lower stratosphere, such as the profiles of OH, HO_2, O_3, H_2O+isotopologues and CO were measured by the 1.8 THz receiver. The performance of the 1.8 THz receiver and some DSB (quick-look) calibrated spectra from the Kiruna campaign (2009) are presented in this thesis.

Kurzfassung

Die Ozon-Forschung hat seit Mitte der 70er-Jahre, in denen das sogenannte „Ozonloch“ entdeckt wurde, stark zugenommen. Weitere Beobachtungsdaten und Labor-Studien sind notwendig, um das Verständnis des globalen Klimawandels zu verbessern. Dennoch gibt es auch heute noch nicht hinreichend Messdaten um die mit dem Klimawandel verbundenen atmosphärischen und chemischen Prozesse des stratosphärischen Ozons zufriedenstellend erklären zu können. Im Laufe der Jahre sind viele Fernerkundungs-Instrumente entwickelt worden, um mit dem Ozon-Abbau in verschiedenen Breiten der Erde verbundene Änderungen der Spurgas-Verteilung bestimmen zu können.

Seit 2001 wird ein ballongetragenes Instrument namens "TELIS (Terahertz-und Submillimeter-Limb Sounder)" vom Deutschen Zentrums für Luft- und Raumfahrt (DLR) entwickelt und für die Messung atmosphärischer Bestandteile innerhalb der unteren Stratosphäre verwendet.

Die vorliegende Arbeit ist der Entwicklung und Charakterisierung eines kryogenen Heterodynempfängers von TELIS zur Messung der OH-Emission bei einer Frequenz von 1,8 THz gewidmet. Im Rahmen dieser Arbeit wurden alle Komponenten des 1,8 THz-Empfängers (Hot Electron Bolometer, lokaler Oszillator, Diplexer, digitales Autokorrelator Spektrometer) einschließlich der Zwischenfrequenz-Kette zunächst individuell charakterisiert, bevor sie auch im Zusammenspiel getestet wurden. Die Verfahren und Ergebnisse für die Entwicklung und Charakterisierung des 1,8 THz-Kanals werden in dieser Arbeit dargestellt. Darüber hinaus wurde die radiometrische Charakterisierung des gesamten Kanals mittels Gaszellenmessungen mit Methanol durchgeführt.

Die vorliegende Arbeit behandelt auch die Integration des 1,8 THz-Empfängers in den TELIS Flug-Kryostaten und die Inbetriebnahme des Instruments während der ersten wissenschaftlichen Flug-Kampagnen. Die Integration wurde erfolgreich seit Ende 2006 umgesetzt. Während der Jahre 2007/2008 wurde die Charakterisierung des Systems durchgeführt, wobei gegenüber dem Prototypen eine um 70% verbesserte Empfindlichkeit des 1,8 THz Heterodyn-Empfängers nachgewiesen werden konnte.

Nach einem ersten Testflug in Teresina, Brasilien, Mai 2008, wurde der 1,8 THz-Empfänger erneut getestet, verbessert und anschließend während einer Mess-Kampagne in Kiruna, Schweden, März 2009 erfolgreich betrieben. Verschiedene wichtige atmosphärische Bestandteile in der unteren Stratosphäre wie die Profile von OH, HO_2, O_3, H_2O+Isotopologe und CO wurden von dem 1,8 THz-Kanal gemessen. Die Performanz des 1,8 THz-Empfängers und insbesondere einige erste DSB kalibrierte Spektren der Kiruna-Kampagne (2009) werden in dieser Arbeit vorgestellt.

Contents

Introduction

Scientists focus on a better understanding of the ozone destruction since the discovery of the ozone depletion in the mid-1970s due to the human-produced chemicals like chlorofluorocarbons (CFCs) used for refrigeration and air conditioning, industrial cleaning. The reduction of the ozone layer which resides mostly in the stratosphere demotes the health of the biosphere due to an increase of the ultraviolet radiation at the Earth's surface. The most severe ozone depletion called as "ozone hole" was discovered in springtime over Antarctica. To observe the ozone layer and the reactive species which causes the ozone destruction, remote sensing instruments were required.

A socalled "Dobson spectrophotometer" developed since 1920s by Gordon M. B. Dobson is a ground-based instrument utilized for a routine monitoring of total ozone [Fahey, 2006]. Nowadays a global network of about 100 sites of ground-based Dobson spectrophotometers is distributed throughout the world. Antarctica Satellite measurements of ozone started in the early 70's (Nimbus-7 satellite in 1978) [Sparling, 2001]. Currently, there are serveral different satellites measuring concentration of ozone and other atmospheric trace gases such as MLS, MAHRSI, GOME, GOME-2. Baloon- or air-born instruments can also be used for measuring trace gases in the lower stratosphere as well as validating the data measured by satellites.

The ozone destruction is formed by the reaction of the reactive species such as OH, NO_2, Cl, ClO, Br which act as catalysts. The Hydroxyl radical (OH) being one of the reactive species in the HO_x family is not only the significant catalyst to destruct the ozone but also influences other catalytic cycles and it is the focused trace gas of this work.

Since 1994, an observation of the OH was successfully done by using, a 2.5 THz heterodyne spectrometer on-board aircraft called THOMAS (TeraHertz OH-Measurement Airborne Sounder) which was developed by DLR. THOMAS was used to measure the hydroxyl and water vapour profiles in the stratosphere and mesosphere (1994-2000) [Krocka, 2002], [Titz, et al., 1994], [Englert, et al., 2000]

TELIS (TErahertz and submillimeter LImb Sounder) is the successive instrument of THOMAS. The TELIS instrument is a cooperation between DLR, SRON and RAL. The TELIS is a balloon-born heterodyne receiver which consists of three cryogenic heterodyne receivers: the 500 GHz channel developed by RAL, 450-660 GHz channel developed by SRON and 1.8 THz channel developed by DLR. The focus of the 1.8 THz channel is on the OH radical. Although the OH emission frequency at 2.5 THz is stronger than that at the 1.8 THz, the 1.8 THz was selected due to the limitation of the technology of the solid state local oscillator during the time of the development.

This doctoral work contains the development and characterization of the 1.8 THz cryogenic channel, the characterization of the autocorrelator spectrometer, the integration of the 1.8 THz cryogenic channel in the flight module cryostat and putting the instrument into operation in two TELIS/MIPAS campaigns (2008-2009) as well as the discussion of the results. Besides the development of several software packages developed for supporting the development and characterization in the laboratory, flight software used for operating and characterizing the 1.8 THz channel and for performing radiometric calibration for three cryogenic channels during the campaign was also successfully developed in this thesis.

The development of the 1.8 THz cryogenic channel continued from the prototype developed in the doctoral work of Dr. Ulrich Mair (2001-2005) [Mair, 2007]. In the present work, the cryogenic receiver installed on a 26 cm diameter optical bench utilizes a hot electron bolometer (HEB) as a highly sensitive mixer, a solid state local oscillator having a compact size, and a diplexer based on a MPI (Martin-Puplett Interferometer) used for coupling RF and LO signal into the mixer. Thus, the size of receiver could be reduced while the stability of the receiver was enhanced, since all components are cryogenically operated on a small optical bench. The 1.8 THz channel can operate at an LO frequency between 1780 GHz to 1880 GHz.

A test cryostat was used during the first period of the development and the characterization of the 1.8 THz channel. Devices used in the 1.8 THz channel and an digital autocorrelator spectrometer were at first individually characterized before they were afterward installed together and tested. The cryogenic channel was successfully integrated in the flight module cryostat, followed by a performance characterization of the complete flight receiver.

After a first test flight of the TELIS instrument in Terasina, Brasil, in May 2008, the performance of the instrument was further improved, and the TELIS instrument was successfully measuring scientific data in the first scientific campaign in Kiruna, Sweden in March 2009 where various important atmospheric constituents within the lower stratosphere such as H_2O+isotopologues, CO, O_3 were measured by the 1.8 THz channel.

This dissertation is subdivided into three parts. The first part consists of three chapters which introduce to the fundamentals of atmospheric science and remote sensing techniques. Chapter 1 introduces to some aspects of atmospheric science which focuses on the stratospheric ozone destruction by the OH radical. The basic principle of remote sensing and the current instruments available for measuring OH will be described in Chapter 2. The basic knowledge of the heterodyne spectroscopy such as the heterodyne technique, the HEB mixer which is used in the 1.8 THz channel as a key element and the digital autocorrelator spectrometer are introduced in Chapter 3.

The second part comprises an overview of the TELIS instrument and the development and characterization of the 1.8 THz channel including the IF backend and the autocorrelator spectrometer. The techniques applied for each cryogenic channel including the light weight cryostat and the integrating of the TELIS instrument on the gondola together with the MIPAS-B instrument will be shortly introduced in Chapter 4. Chapter 5

emphasizes on the setup of the 1.8 THz channel and the introduction to its significant components.

The third part is dedicated to the development, characterization and radiometric accuracy of the 1.8 THz channel. Chapter 6 describes the development, the characterization methods and the results of the characterization of the 1.8 THz channel such as the instrument sensitivity and stability. The radiometric accuracy of the 1.8 THz channel in was investigated by using gas cell measurements of opaque lines is discussed in Chapter 7.

Part four of this work consists of three chapters. An overview of two TELIS/MIPAS campaigns during 2008-2009 is given in chapter 8. The discussion of the results of the on-ground Characterization in both campaigns will be described in Chapter 9. The performance of the 1.8 THz channel and some quick-look results measured during the flight in Kiruna (2009) will be discussed in Chapter 10.

The summary of the results of all the work done in the context of this thesis and outlook will be discussed in Chapter 11.

Part I

Introduction to atmospheric physic

&

Fundamental of remote sensing measurement and heterodyne Spectroscopy

1 Aspects of atmospheric science

This chapter is a short introduction to some aspects of the atmospheric science. The atmospheric pressure and temperature profiles will be explained as well as the formation and the destruction of the stratospheric ozone by reactive species. In the ozone destruction, the emphasis is put on the OH radical, being the target species of the TELIS instrument.

1.1 Structure of the atmosphere

1.1.1 Atmospheric pressure and temperature profiles

The atmosphere is characterized by the variation of pressure and temperature with height. The vertical temperature profile is the criterion for distinguishing the different layers of the atmosphere. The five layers of the atmosphere are called troposphere, stratosphere, mesosphere, thermosphere and exosphere. The top of these atmospheric layers are called tropopause, stratopause, mesopause and thermopause respectively.

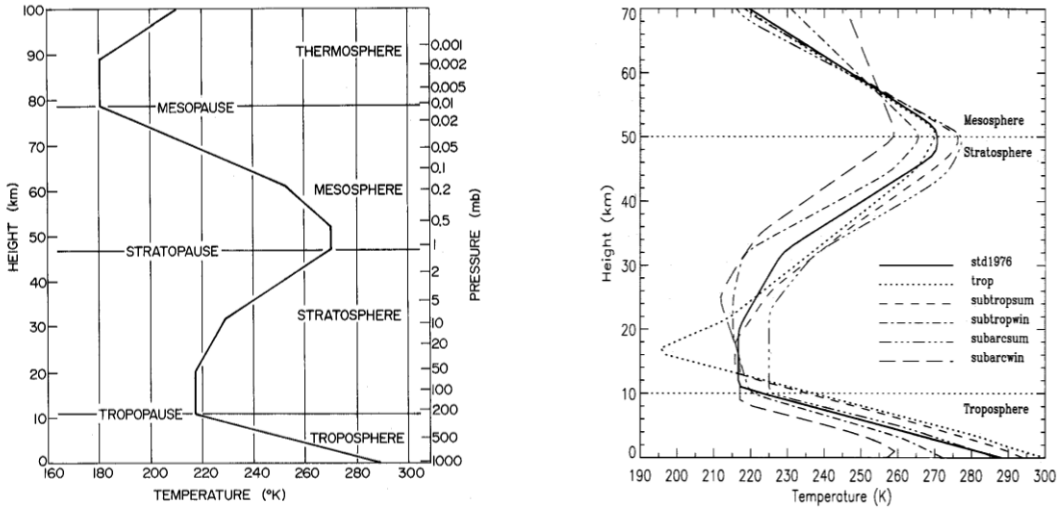

(a) (b)

Figure 1-1 : a) Vertical temperature profile for the U.S. standard atmosphere [Wallance, et al., 1977, p.23] b) Standard empirical model temperature profiles for various locations and seasons. The standard atmosphere in 1978 is the global mean. The tropical atmosphere is for latitudes less thand 30°; the subtropical atmosphere is for latitudes between 30°-45°: subarctical atmosphere for 45°-60° and the arctic on for 60°-90°. [Thomas, et al., 1999,p.12]

The vertical temperature profile of four of the atmospheric layers in the *homosphere*[1] is shown in figure 1-1a and the variation of the temperature profile depending on latitude and the seasons is shown in figure 1-1b.

With modern radiosonde systems the observation of the vertical temperature profile can be performed up to 40 km altitude. It is possible to monitor the temperature between 40 and 80 km by using a similar instrument together with acoustic sounding techniques borne aloft by rockets. The temperature structure at higher levels has been deduced indirectly from measurements of satellites [Thomas, et al., 1999].

The variation of pressure with height in the atmosphere can be easily described by using the hydrostatic equilibrium. The vertical pressure profile as shown in eq. 1-1 can be derived from the *hydrostatic equation*[2], the ideal gas law and two *geopotential heights (Z)*[3].

$$P(z) \cong P_0 \cdot \exp\left[-\frac{(Z_z - Z_0)}{H}\right] \qquad \textbf{eq. 1-1}$$

where H is the scale height which is equal RT_v/g_0, g_0 is the globally averaged acceleration due to gravity at the earth's surface (9.8 ms^{-2}). R is the gas constant and, T_v is the virtual temperature being the sum of the area over and under the actual temperature curve between two different pressures. Z_0 is the geopotential height at the sea level which is equal to the geometric height (z) at 0 km and P_0 is the pressure at the sea level ($1.013 \cdot 10^5$ Pa).

The vertical pressure drops off by a factor *e* in passing upward through a layer of the depth H. In the homosphere where the atmosphere is well mixed, the pressure and densities of the individual gases decrease with altitude and H correspondingly to the apparent molecular weight of the mixture [Wallance, et al., 1977].

1.1.2 Troposphere

The troposphere is the lowest layer of the atmosphere. It extends about 10 to 15 km from the Earth's surface up to the tropopause, depending on latitude and seasons. Typically, the temperature in the troposphere decreases with height, when the atmosphere in this layer is unstable, for example, in the afternoon, at which time the earth's surface is warm and the temperature at the surface is higher than that at the higher altitude. It is occasionally possible to have a temperature inversion near the ground (so-called surface inversion) during the night with the clear sky, where the temperature increases with hight.

---

[1] Homosphere is the region in the atmosphere that has the well mixed turbulences. This region is from the earth's surface up to about the base of the thermosphere (≅105 km).

[2] $dp/dz = -\rho g$

[3] The geopotential height (Z) is used as the vertical coordinate in atmospheric applications in which energy plays an important role. $Z \equiv \phi_{(z)}/g_0$, where the geopotential (ϕ) can be determined as integrating $d\phi = gdz$, z= geometric height and g depends on altitude and height. At the lower altitude (< 10 km) $z \cong Z$.

The troposphere is a layer with rapid turbulent mixing and contains all kinds of weathers. The study of change in atmospheric chemistry in the troposphere, or rather, in the lower atmosphere (up to 50 km) is therefore the key to the understanding of problems of air pollution, climate and the biosphere.

The water vapour (H_20) which is the majority of the gases in the troposphere is an important factor for the tropospheric chemistry [Mohanakumar, 2008], [National Research Council (U.S.). Global Tropospheric Chemistry Panel, 1984]. The property of *trapping radiative energy*[4] of water vapour and some minority species such as CO_2, methane (CH_4), the chlorofluorocarbons (CFCs) cause a greenhouse effect. Some important trace gases in the troposphere are hydroxyl (OH), carbon-monoxide (CO), methane (CH_4).

The OH radical is one of the important species of tropospheric chemistry since the degradation of trace gases and pollutants in the troposphere is dominated by their reaction with hydroxyl radicals (OH). A recent result of the measurement campaign over the Pearl River Delta, China 2006 done by [Hofzumahaus, et al., 2009] shows that concentrations of OH were three to five times greater than expected.

1.1.3 Stratosphere

The boundary layer separating the stratosphere from the troposphere is the tropopause. In the tropopause the *lapse rate*[5] is zero and the average temperature is constant with height. The stratosphere begins from the top of the tropopause and reaches up to about 50 km depending also on the latitude and season as shown in figure 1-1b. The most important trace gas of the stratosphere is ozone (O_3) which is the reason that the stratosphere is called the ozone layer. About 90% of the earth's atmosphere ozone is found in the stratosphere where it plays a significant role in keeping the earth warm [Ahrens, 2007].

The ozone gas causes an inversion (temperature increases with height) in the stratosphere because it absorbs the ultraviolet radiation from the sun and heats up the air. Therefore the stratosphere is very stable and the turbulent mixing transported from troposphere can only be slowly mixed with the atmosphere in this region. Furthermore the stratospheric ozone protects the biosphere from the dangerous UV-B solar radiation.

However since the 1970s it was found that the ozone depletion takes place and becomes larger due to the industrial gases e.g. the chlorofluorocarbons containing chlorine (Cl) and bromine (Br). The ozone holes occur at the Arctic and the Antarctic where the Polar Stratospheric Clouds (PSC) are formed and the ozone destruction process begins when the sunlight appears (in spring). It was found in 2009, that the ozone hole in Antarctica reached its 10th largest measured size since careful measurements began in 1979 [Scientific Committee on Antarctic Research (SCAR), 2009], [NASA, 2009].

[4] Water vapour and some other greenhouse gases have the dual property of allowing the shortwave solar radiation passing to the earth's surface while preventing the infrared radiation to release to space.
[5] Lapse rate is the rate at which the temperature decreases with height.

1.2 Stratospheric ozone

The stratospheric ozone absorbs the ultraviolet solar radiation of wavelengths 240-290 nm which is harmful to surface cells of higher plants and animals. It absorbs additionally the solar radiation of wavelengths between 290-320 nm (so-called UV-B) which causes skin cancer. An increase of the stratospheric ozone destruction leads to demote health of the biosphere. Approximately 1% of the stratospheric ozone destruction leads to a 2% increase in UV-B [Seinfeld, et al., 2006]. As depicted in figure 1-2, a maximum mixing rate in the stratosphere ozone measured at latitude 35°N is about 8 ppm at an altitude of 34 km. The mixing ratio depends on altitude and latitude.

The tropical region where the sunlight is intense has the greatest ozone production. However as shown in figure 1-2b the middle and high latitude is the region having the greatest ozone concentration because of the air circulation in the stratosphere. At the tropics, the deep cumulus convection is formed as the result of the high temperature and consequently the air brings the tropical ozone toward the poles. By the overall mass conservation, this stratosphere air must return back to the troposphere somewhere and this occurs at the middle latitudes.

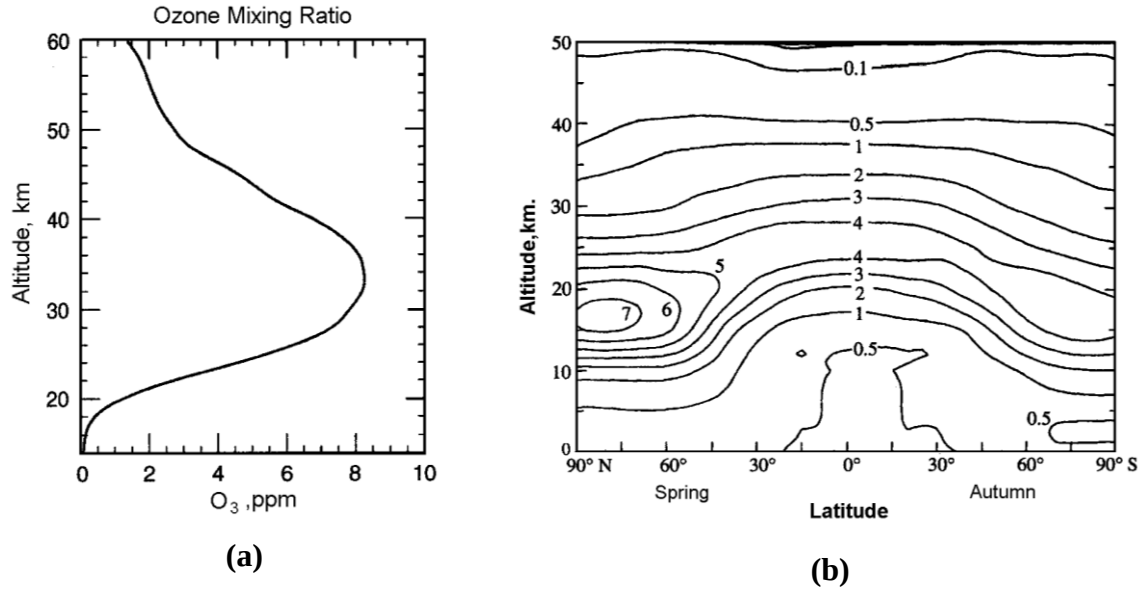

Figure 1-2 : a) Stratospheric ozone profile at midlatitude (35°N) measured in September 1996 by satellite with the Jet Propulsion Laboratory FTIR (Fourier transform infrared) spectrometer [Seinfeld, et al., 2006, p.53]. b) Zonally averaged ozone concentration (in unit of 10^{12} molecules cm^{-3}) as a function of altitude, March 22 (Johnston 1975).

It was concluded by [IPCC, 2007] that the global stratospheric ozone amounts since 1970 decreased, with the lowest values occurring during 1992-1993. Global ozone for the period 2000-2003 was approximately 4% below the 1964 to 1980 average values. Recently observed changes in ozone trends [Newchurch, et al.], [Weatherhead, et al.], 2006 are already indicative of recovery of the global ozone layer is not yet clear and requires more detailed attribution of the drivers of the changes.

1.2.1 Ozone formation

The stratospheric ozone is produced from the *photolysis*[6] of the molecular oxygen. This is the reason that the tropics are the greatest ozone-production region. The mechanism explaining the ozone formation in the stratosphere is called the "Chapman" mechanism proposed by Chapman (1930). This mechanism begins at the reaction of dissociating the molecular oxygen (reaction 1) with the ultraviolet solar radiation at wavelengths lower than 242 nm at about 25-30 km altitude.

$$O_2 + h\nu \xrightarrow{1} O + O \qquad reaction\,1$$
$$O + O_2 + M \xrightarrow{2} O_3 + M \qquad reaction\,2 \qquad \textbf{eq. 1-2}$$

M is the third molecule and in this case it means the air (either O_2 or N_2). Reaction 2 is the only one reaction to form ozone in the atmosphere. As mentioned in the previous section, the ozone absorbs the ultraviolet radiation at wavelengths in the range between 240 nm and 320 nm leading to decomposition of the O_3 back to oxygen as shown in reaction 3.

$$O_3 + h\nu \xrightarrow{3} O + O_2 \qquad (\lambda = 400 - 600\,nm) \qquad reaction\,3$$
$$\xrightarrow{3'} O(^1D) + O_2 \qquad (\lambda = 240 - 320\,nm) \qquad \textbf{eq. 1-3}$$
$$O + O_3 \xrightarrow{4} O_2 + O_2 \qquad reaction\,4$$

Reaction 3 occurs by radiation in the range of 400-600 nm and reaction 3' occurs at wavelengths lower than 320 nm. The $O(^1D)$[7] is the excited state of the oxygen atom and it can be quenched to the ground state (O) by reacting with M. Usually when reaction 1 begins (the O atom is produced), reaction 2 and 3 occur rapidly and repeated many times in cycle before reaction 4 can take place. It is useful to estimate the ozone concentration by looking at the partition of *odd oxygen*[8], or rather, the relationship between the O atom and the O_3 ($[O]/[O_3]$). It is clear that [M] decreases with the altitude, hence the $[O]/[O_3]$ ratio increases with the altitude. This means the oxygen atom (O) is dominant at the higher altitude and the ozone (O_3) is therefore dominant at the lower stratosphere with respect to the sum of odd oxygen.

1.2.2 Ozone destruction

The ozone destruction is formed by the reaction of the reactive species such as OH, NO_2, Cl, ClO, Br which act as catalysts. Therefore, the cycle causing the ozone destruction is called the catalytic cycle.

---

[6] Photolysis is the process to decompose molecules with the solar radiation.

[7] $O(^1D)$ represents the first electronically exited state of the oxygen atom. In some books it is termed as $O(^1\Delta)$.

[8] Odd oxygen consists of the oxygen atom (O) and the ozone (O_3) which are in the same chemical family (O_X).

Examples of the effective catalytic cycles are the Nitrogen Oxide Cycles (NO_x), Hydrogen Oxide Cycles (HO_x), and Halogen cycles, (ClO_x, Cl_y, Br_y). These reactive species come from both natural and anthropogenic (human) sources which are not removed by the precipitation in the troposphere. The chlorofluorocarbons (CFCs) are examples of the anthropogenic source and the methyl chloride (CH_3Cl) is the only natural source of the chlorine (Cl) in stratosphere. Two or more species that interchange rapidly with one another in the reaction are usually viewed as a chemical family and it is, in fact, easier to explain the catalytic cycles with the use of chemical families. Some important chemical families in the stratospheric chemistry are shown in table 1-1.

Table 1-1 : Some important chemical families in the stratospheric chemistry (edit from [Seinfeld, et al., 2006, p148]

Symbo	Name	Components
O_x	Odd oxygen	$O+O_3$
NO_x	Nitrogen oxides	$NO+NO_2$
NO_y	Oxidized nitrogen	$NO+NO_2+HNO_3+2N_2O_5+ClONO_2+NO_3+HOONO_2+BrONO_2$
HO_x	Hydrogen radicals	$OH+HO_2$
Cly	Inorganic chlorine	Sum of all chlorine-containg species that lack a carbon atom (CL+2Cl2O2)+HOCL+ClONO2+HCL+BrCl)
ClO_x	Reactive chlorine	Cl+ClO
CCl_y	Organic chlorine	$CF_2Cl_2+CFCl_3+CCl_4+CH_3CCl_3+CFCl_2CF_2Cl$ (CFC-113) $+CF_2HCl$(CFC-22)
Br_y	Inorganic bromine	Sum of all bromine-containing species that lack a carbon atom (Br+BrO+HOBr+$BrONO_2$)

1.3 Ozone destruction by OH

The OH radical is one of the reactive species in the HO_x family which is actually the result of the first catalytic cycle destroying the ozone. The production of the OH depends on the abundances of $O(^1D)$ reacting with the H_2O and CH_4 molecules, while the only source for producing $O(^1D)$ is the photolysis of ozone (O_3).

$$O(^1D) + H_2O \xrightarrow{1} 2OH \qquad \textbf{eq. 1-4}$$
$$O(^1D) + CH_4 \xrightarrow{1'} OH + CH_3$$

About half of the H_2O in stratosphere results from the oxidation of the methane entering through the tropopause from the troposphere, whereas the water vapour in the troposphere is trapped at the tropopause before transported to the dry stratosphere [Seinfeld, et al., 2006].

The tropical mean stratospheric H_2O mixing ratio is ≅ 3.5 ppmv from observations of [Engel, et al., 1996] and [Michelsen, et al., 2000], the stratospheric water vapor concentrations decreased by about 10% after the year 2000 [Solomon, et al., 2010].

$$\begin{aligned} HO_X \text{ cycle 1:} \quad & OH + O_3 \longrightarrow HO_2 + O_2 \\ & HO_2 + O \longrightarrow OH + O_2 \\ \textit{Net:} \quad & O_3 + O \longrightarrow O_2 + O_2 \end{aligned} \qquad \textbf{eq. 1-5}$$

The HO_x cycle-1 is effective at the upper stratosphere (altitude about 50 km) because at this altitude the oxygen atom is dominant with respect to partitioning of the odd oxygen. The HO_x cycle-2 is therefore very important at the lower stratosphere because of high concentration of the ozone. Because the OH radical can react with most trace gases, the mixing ratio of important trace gases can be assessed by monitoring the partitioning of the $[HO_2]/[OH]$.

$$\begin{aligned} HO_X \text{ cycle 2:} \quad & OH + O_3 \longrightarrow HO_2 + O_2 \\ & HO_2 + O_3 \longrightarrow OH + O_2 + O_2 \\ \textit{Net:} \quad & O_3 + O_3 \longrightarrow O_2 + O_2 + O_2 \end{aligned} \qquad \textbf{eq. 1-6}$$

The OH is not only the significant catalyst to destruct the ozone but also influences other catalytic cycles. For instance, the increase of the OH enhances the effectiveness of the ClO_x cycle [Weisenstein, et al., 1993], [Jucks, et al., 1995] whereas it decreases the effectiveness of the NO_x catalytic cycle by converting the NO_2 to the HNO_3 reservoir which is partly transported down to the troposphere.

1.4 Measurements of OH in the lower stratosphere

The demand of instruments having the capability to measure the OH radical has been increasing since the information of the change in $[HO_2]/[OH]$ is very useful to improve the atmospheric models. Instruments having the capability to measure OH in this region have been developed, using various techniques such as:

a) A balloon-borne lidar system for the measurement of ozone and hydroxyl radicals in the stratosphere constructed and flown by the Goddard Space Flight Center. The temporal variation of the hydroxyl radical concentration was measured in the 34–37-km altitude region, ranging from 40 parts/trillion shortly after noon to ~5 parts/trillion 2 h after sunset. [Heaps, et al., 1982]

b) The laser induced fluorescence technique [Stimpfle, et al., 1988] deployed on a balloon-borne gondola launched from Palestine, Texas on July 15, 1987. Midday stratospheric OH density measurements have been carried out within the altitude interval of 31 to 24 km in which the OH mixing ratio ranged from 16±5 ppt at 31 km to 4±3 ppt in the 27 to 24 km region

c) In October 1994 in the work of [Wennberg, et al., 1994], simultaneous in situ measurements of the concentrations of OH, HO_2, ClO, BrO, NO, and NO_2 demonstrate the predominance of odd-hydrogen and halogen free-radical catalysis in determining the rate of removal of ozone in the lower stratosphere during May 1993. Also it was found that a single catalytic cycle, in which the rate-limiting step is the reaction of HO_2 with ozone, accounted for nearly one-half of the total O_3 removal in this region of the atmosphere.

d) During the 1996 SUCCESS mission, the hydrogen radicals (OH and HO_2) were measured throughout the troposphere and the lower stratosphere with an instrument aboard the NASA DC-8 aircraft. It was found in the work of [Brune, et al., 1998] that typically midday OH was 0.1-0.5 pptv and HO_2 was 3-15 pptv.

e) In August 1997 during the second CRISTA/MAHRSI campaign, the OH observations were performed by an airborne-2.5 THz heterodyne spectrometer (THOMAS) developed by DLR. The measurement covered altitudes between 30 and 90 km over a full diurnal cycle. Comparison of the results to photochemical model calculations using standard chemistry and a 50% reduction in the rate coefficient for $O+HO_2 \rightarrow OH + O_2$ shows that neither model is capable of reproducing upper stratospheric and mesospheric OH concentrations simultaneously. There still are significant deficiencies in the understanding of middle atmospheric chemistry. [Englert, et al., 2000]

The OH concentration can also be derived from observed CH_4 and CO as shown in the study of [Warneck, et al., 1973] and [Jöckel, et al., 2002]. Nevertheless, to understand the chemical process in the atmosphere requires more observed data having better spectral resolutions and it becomes more important to develop better instruments as well as having more measurement campaigns in different latitudes and seasons.

2 Remote sensing measurements

Theories relevant to remote sensing measurements as the radiative transfer equation, line broadening will be shortly introduced in this chapter. In the remote sensing techniques, only the limb sounding technique will be described because TELIS instrument makes use of it.

2.1 Radiative transfer

The radiative transfer is responsible for exchanging energy between the atmosphere and the underlying surface as well as between layers of the atmosphere. It plays an important role in many of the chemical reactions especially in the upper atmosphere. The emission of the molecules can be monitored by the remote sensing techniques.

The incoming of the solar radiation and the outgoing of the terrestrial radiation are controlled by the atmosphere. The Earth's atmosphere consists of various gases which are selective absorbers in the infrared region. Thus, changes of the composition in the atmosphere lead to the change of the energy balance between the incoming solar radiation and the outgoing terrestrial radiation.

2.1.1 Radiative transfer equation

The *irradiance (F)*[9] received on a surface consists of parts of the irradiance coming from directions within the arc of solid angle (ω). The *spectral intensity* (I_ν)[10] or the instantaneous radiant power is defined by the net energy (d^4E) per unit area, per unit solid angle, per unit frequency ($d\nu$) and per unit time (dt) as shown in eq. 2-1 [Janssen, 1993],

$$I_\nu = \frac{d^4E}{\cos\theta \cdot dA \cdot dt \cdot d\omega \cdot d\nu} \quad [W \cdot m^{-2} \cdot sr^{-1} \cdot Hz^{-1}] \qquad \textbf{eq. 2-1}$$

where θ is the *zenith angle*[11] and the relative path length to the zenith angle is $1/\cos\theta$. Without considering scattering, the absorption of the beam radiation along the path from

[9] The irradiance is the radiant flux density received on a specific surface.
[10] It is sometimes called radiance and it refers to the radiant flux as a function of solid angle, crossing a surface perpendicular to the axis of the radiation beam.
[11] When the sun is directly overhead, the zenith angle (θ_0)= 0°.

the observed position (z_0), where an instrument is located, to the top of the atmosphere (z_{TOA}) can be described with the Beer-Lambert law as the following equation,

$$dI_{\nu,z_0} = -I_{\nu,z_{TOA}} \cdot \alpha \cdot dz \qquad \textbf{eq. 2-2}$$

where α [12] is the absorption coefficient which is proportional to the number of molecules per unit volume. By integrating eq. 2-2 the Beer-Lambert law can be formed as shown in eq. 2-3.

$$I_{\nu,z_0} = I_{\nu,z_{TOA}} \cdot e^{-\tau(z_0,\nu)} \qquad \textbf{eq. 2-3}$$

The optical depth (τ) as depicted in eq. 2-4 is integrated from the altitude z to the top of the atmosphere where the optical depth is usually assumed to be zero (no absorption and scattering).

$$\tau = \int_{z_0}^{z_{TOA}} \alpha(z',\nu)dz' \qquad \textbf{eq. 2-4}$$

At wavelengths of the terrestrial radiation (long wavelengths in infrared region) both atmospheric emission and absorption are equally important. Thus, the radiative transfer equation for the infrared radiation can be determined from the combination of absorption and emission (or sink and source) as shown in the following equation,

$$\frac{dI_{\nu,z_0}}{d\tau} = -\alpha I_{\nu,z_0} + S_{\nu,z} \qquad \textbf{eq. 2-5}$$

where $S_{\nu,z}$ is the source term which is equal to $\alpha B_\nu(T)$ and $B_\nu(T)$ is the Planck Function,

$$B_\nu(T) = \frac{2h\nu^3}{c^3 \cdot e^{h\nu/kT} - 1} \qquad \textbf{eq. 2-6}$$

At thermal equilibrium and with the *Kirchhoff law*[13], the equation of the emission of beam radiation from the surface can be treated in the same way as in eq. 1-2 by using the Planck Function for the emitted radian instead. Thus, the solution of the radiative transfer equation for none scattering can be determined by integrating eq. 2-5.

$$I_{\nu,z_0} = I_{\nu,z_1} \cdot e^{-\tau(z_1)} + \int_{z_0}^{z_1} B_\nu(T) \cdot e^{-\tau(z)} \cdot \alpha \, dz \qquad \textbf{eq. 2-7}$$

[12] Indeed, it should refer to the extinction coefficient (absorption and scattering coefficients) but in this case scattering is neglected. $\alpha = nS(T)F(\nu)$ where n=number density of absorber, $S(T)$=Line intensity, $F(\nu)$= Line shape function.

[13] E(absorption)=E(emission), therefore the emissivity = absorptivity

The path of the propagation of the beam radiation in eq. 2-7 starts from the observed position (z_0 : observed), extends through the medium and ends at a boundary (z_1 : origin). In general, the brightness temperature (T_b) is commonly used instead of the spectral intensity in the radiative transfer equation and has its unit in Kelvin. The brightness temperature is derived from the Planck function by making use of the Rayleigh-Jeans limit approximation ($h\nu << kT$). The eq. 2-8 shows the simple radiative equation in the form of brightness temperature whereby the Rayleigh-Jeans factor (T / T_b) is set to one and errors introduced by both Rayleigh-Jeans approximation and scattering are neglected.

$$T_b(\nu) = T_{b1} e^{-\tau(z1)} + \int_{z=0}^{z=z1} T(z) e^{-\tau(z)} \cdot \alpha dz \qquad \textbf{eq. 2-8}$$

Where $T_{bl(\nu)}$ is the background brightness temperature at the origin which is equal to $(\lambda^2/2k) \cdot I_{\nu,Zl}$. The approximation of the Rayleigh-Jeans becomes, however, more important at the low frequency. By knowing the atmospheric temperature and density profiles, the solution of the radiative equation can be calculated. In fact, the brightness temperature can be measured by remote sensing instruments but the atmospheric temperature structure and the opacity are usually unknown. Thus, the solution of the inversion problem in the radiative transfer equation is more complicated and it will not be discussed here.

2.1.2 Line broadening in the atmosphere

Two major causes for the broadening of spectral lines are the pressure and Doppler broadening effects. The natural broadening is practically negligible because its effect is much less in comparison to that of both pressure and Doppler effects [Vardavas, et al., 2007] due to the large lifetime of an atom in its ground state ($\Delta E \sim h/2 \cdot \pi \cdot \Delta t$: Δt=a definite lifetime). The pressure effect is significant at the altitude lower than 20 km whereas a combination of pressure- and Doppler broadenings prevail in the upper atmosphere.

Pressure Broadening:

The shape of the spectral lines [Liou, 2004] due to the pressure broadening in the infrared region is usually given by the Lorentz profile as expressed by the following formula

$$k(\nu) = \frac{S}{\pi} \frac{\alpha}{(\nu - \nu_0)^2 + \alpha^2} \qquad \textbf{eq. 2-9}$$

where k is the absorption coefficient, S is the line strength, α is the half width of the line at the half maximum being a function of pressure and temperature, ν_0 is the center frequency of the line (wave numbers).

Pressure broadening causes lines in infrared absorption bands to have considerably greater half widths in the lower layers of a planetary atmosphere than in the upper layers

as shown in the work of Strong [Strong, et al., 1950] where the net loss of heat by radiation from the various layers in the stratosphere was calculated.

Doppler Broadening:

The difference in thermal velocities of atoms and molecules causes the Doppler broadening and thus, it is sometimes called the thermal broadening. The line broadening ($\Delta\nu$) due to the Doppler effect is given by

$$\Delta\nu = \frac{\nu}{c}\left(\frac{2kT\ln 2}{m}\right)^{1/2} \qquad \textbf{eq. 2-10}$$

where m is the mass of the molecule, c is the speed of light and ν is the actual transition frequency. The shape of the spectral lines can be determined by the Gaussian profile in which the absorption coefficient $k(\nu)$ is expressed as the following equation [Liou, 1980].

$$k(\nu) = \frac{S}{\Delta\nu \cdot \sqrt{\pi}} \exp\left[-\left(\frac{\nu - \nu_0}{\Delta\nu}\right)^2\right] \qquad \textbf{eq. 2-11}$$

Both pressure and Doppler effects are significant at the altitude about 20 to 50 km. The Voigt profile [Armstrong, 1967], [Drayson, 1975] being the convolved profile between Lorentz and Doppler profiles is usually applied in the infrared transfer calculations in this region.

2.2 Limb sounding technique

TELIS instrument is a balloon borne sounder using limb sounding passive remote sensing technique. Limb sounding has advantages over vertical sounding. In addition, the cost of instruments carried on the balloon platform is much lower than the one on the satellite platform and the duration of the flight on balloon platform is longer than that on an aircraft. In comparison to ground based instruments, balloon borne sounders have the advantage of opacity independence.

Figure 2-1 presents the principle of limb sounding technique. The narrow field of view (FOV) of the instrument across the atmosphere layers is stepped in limb sounding and the tangent layer makes a major contribution of the measured spectrum. The instrument either on a satellite or a balloon locates at the observation point with the angle θ to the tangent line. The lowest altitude of the observation is basically limited by the tropospheric attenuation by water (vapour and liquid).

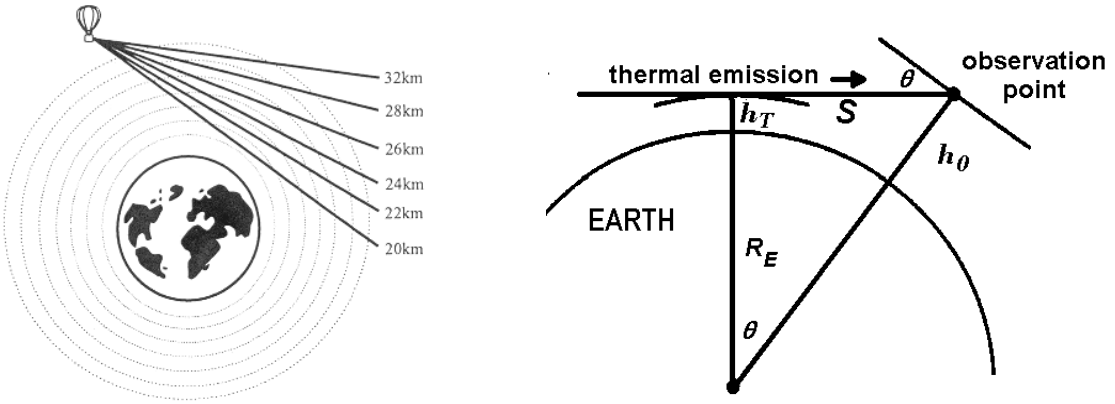

Figure 2-1: Left: illustrates the limb sounding measurement on a balloon platform in which the altitude resolution of the limb scan is 2 km. Right: At the observation point locates the instrument (either on the balloon platform or on the satellite). θ=the angle to the tangent line (pointing angle), h_T=the height of the instrument tangent point, S= the distance between observation point and the tangent point, R_E = Earth radian ≅6371 km., h_0=the height of the observation point above Earth's surface.

In the case of the TELIS instrument, $S \cong 550$ km and the pointing angle (θ) set by TELIS instrument must be corrected with the pitch angle of the balloon as well as the offset of the height (h_0). The data of the height of the balloon and the pitch angle is forwarded from the AHRS (Attitude and Heading Reference System) from MIPAS instrument (chapter 4.3.

At present, besides the TELIS instrument there are several types of instruments on the balloon- or space borne platforms which have a capability to measure the OH radical such as the BOH (Balloon OH instrument) built and operated by Dr. Pickett at JPL (Jet Propulsion Laboratory). It is a heterodyne receiver which operates at 2.5 THz and uses a methanol gas as a laser local oscillator [Drouin, 2004].

BOH can be used to validate with EOS-MLS (Earth Observing System-Microwave Limb Sounder) launched in July 2004. It is one of four instruments on the NASA' EOS Aura satellite. MLS observes thermal emission of the molecules including the OH radical (2.5 THz). It can scan from the ground to at the altitude of about 90 km.

SABER (Sounding of the Atmosphere using Broadband Emission Radiometry) one of four instruments on the NASA's TIMED mission (Thermospher Ionosphere Mesosphere Energetics Dynamics). It can measure earth limb emissions at the atmospheric region extended from 60 km -180 km. [Dyrland, et al., 2010],

3 Heterodyne spectroscopy

The chapter will introduce the basic principle used in the heterodyne system. It will start from an introduction to the heterodyne receiver, the parameter considerations of the heterodyne receiver, the HEB mixers and the Martin-Puplett Interferometer. In the aspects of the spectroscopy, the principle of radiometric calibration and the autocorrelator spectrometer will be shortly introduced.

3.1 Overview of an heterodyne receiver

The heterodyne technique is commonly applied for sensing very weak signals such as from the trace gas constituents in the atmosphere whose radiated frequencies are in a high frequency range extending from about 60 GHz to above 1 THz. The heterodyne detection systems will produce the shift-frequency output while preserving information such as the amplitude of the incident signal. A complete heterodyne detection system is usually called a *heterodyne receiver*. The detecting element in a heterodyne system is called *mixer* because it mixes two different input frequencies (f_{signal} and f_{LO}) and down-converts it to the intermediate frequency (IF).

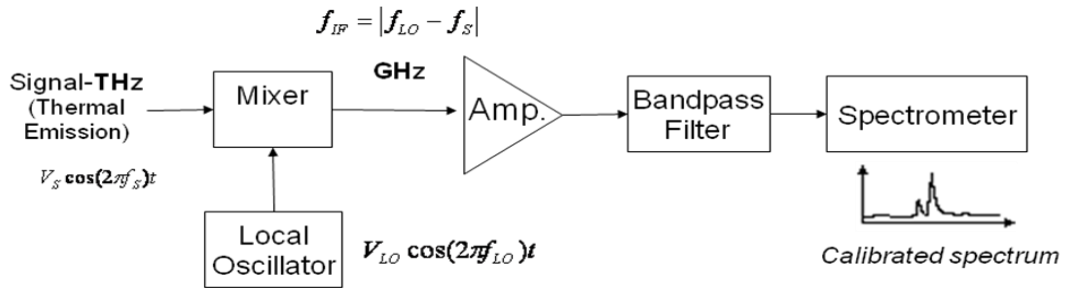

Figure 3-1 : Schematic diagram of the basic principle of a heterodyne receiver.

Figure 3-1 represents the basic principle of the heterodyne receiver. The local oscillator (LO) and the signal power are coupled into a mixer which is a nonlinear device (such as diode, bolometer). The detected signal frequency (f_S) is down converted by the mixer to intermediate frequency (IF) which consists of two side bands (upper [$f_S - f_{LO}$] and lower [$f_{LO} - f_S$] side-bands). The down-convertion at the mixer can be described with a square law principle ($I \alpha V^2$) as written in following equations,

$$I(t) \propto \left[V_{LO} \cos(2\pi f_{LO})t + V_S \cos(2\pi f_S)t\right]^2 \qquad \textbf{eq. 3-1}$$

$$I(t) = \frac{1}{2}\left\{V_{LO}^2 + V_S^2 + V_{LO}^2 \cos[2\pi(2f_{LO})t] + V_S^2 \cos[2\pi(2f_S)t]\right\} \quad \textbf{eq. 3-2}$$
$$\underbrace{+ V_{LO} \cdot V_S \cdot \cos[2\pi(f_{LO} - f_S)t]}_{\text{IF Signal}} + V_{LO} \cdot V_S \cdot \cos[2\pi(f_{LO} + f_S)t]$$

where *I(t)* is the mixer current, V_S and V_{LO} represents the signal and LO voltages. f_S and f_{LO} are the signal and LO frequency. The other high-frequency terms ($2f_{LO}$, $2f_S$, $f_{LO}\pm f_S$) are rejected by filtering at the output of the amplifier and only the amplified IF signal (f_{LO}-f_S, f_S-f_{LO}) is transferred to the spectrometer. In case of one side band (either lower or upper side band) is not suppressed by a single side band filter (SSB) preceding the mixer, the *heterodyne receiver* is operated in the double sideband mode (DSB).

3.2 Parameters consideration of a heterodyne spectrometer

The parameters considered in the development of any types of the heterodyne spectrometer/ radiometers are *sensitivity* and *drift* of the system.

Sensitivity of the radiometers/heterodyne spectrometer depends also on the *bandwidth*[14] and it can be defined in the term of a "*system noise temperature (T_{sys})"*. It is an equivalent noise temperature generated from all devices of the system and has its unit usually in Kelvin (K). The noise floor of the calibrated spectra (minimum detectable temperature) depends on the sensitivity of the instrument and it can be determined by using the *radiometer equation*. (see chapter 3.2.3).

Allan variance, a method applied in this thesis for characterizing the stability of the 1.8 THz channel, will be further described in chapter 3.2.4.

3.2.1 Receiver Noise temperature

T_{sys} of the heterodyne receiver can be separated into the mixer noise (T_M) and the noise generated by the IF chain (T_{IF}) such as the biasing electronics and the amplifiers.

In case of a bolometer cooled near absolute zero, thermal electric noise can be neglected. The shot noise depends on the mean current flowing through the detective element is thus dominant in the heterodyne system due to illuminating the mixer with the LO power ($P_{LO} >> P_S$) and thus the mean current flowing through the mixer increases.

The theoretical (ideal) noise temperature of the mixer (T_{mixer}) in the heterodyne system can be derived by using the shot noise and quantum theories and the signal to noise ratio (SSB) of the mixer can be defined as the following equation,

$$\left(\frac{S}{N}\right)_{SSB} = \frac{\eta P_s}{h\nu B} \quad \textbf{eq. 3-3}$$

[14] For a radiometer, a bandwidth means a RF bandwidth for a heterodyne receiver having an RF amplifier before the mixer. For a super-heterodyne receiver an IF bandwidth is considered instead.

where η=quantum efficiency and the maximum possible quantum efficiency is normally $\eta = 1$ (i.e. one electron per photon), B=Bandwidth and h=Planck constant and ν is a frequency midway between the signal and LO frequencies in which these two frequencies are very similar [Lesurf, 2002]. P_S= Signal Power which is simply equal to $P_S = k \cdot T_{Sig} B$. (λ_S is in Rayleigh-Jeans region) thus the eq. 3-3 can be rewritten as follows:-

$$\frac{S}{N} = \frac{T_{sig}}{T_{mixer(SSB)}} = \frac{\eta k T_{sig} B}{h\nu B} \qquad \textbf{eq. 3-4}$$

$$T_{mixer(SSB)} = \frac{h\nu}{k\eta} \qquad \textbf{eq. 3-5}$$

eq. 3-5 represents the lowest noise level of the receiver (quantum limit) when ignoring every possible noise generating mechanism except shot noise. The noise temperature is reduced by a factor of two in the DBS heterodyne receiver ($T_{mixer(DSB)} = h\nu / 2k\eta$) because the mixer responses to both input signal sidebands and thus $P_S = 2 \cdot k \cdot T_{Sig} B$. In eq. 3-5, h and k are constant, so the noise temperature in the heterodyne system is determined by the signal and LO frequencies and the quantum efficiency of the mixer. The mixer noise temperature tends to increase at the higher signal frequency.

A higher system noise temperature (T_{sys}) is expected in the practical heterodyne receivers due to the noise in the biasing elements and the amplifiers. The first amplifier connected after the mixer is normally cooled in which its noise arising from thermal noise can be reduced. Basically T_{sys} can be measured by using two specific black bodies in which it will be further described.

3.2.2 Noise temperature measurements

The output power from the heterodyne receiver is usually the sum of the detected signal power level and the noise power level generated by the receiver as shown in Figure 3-2.

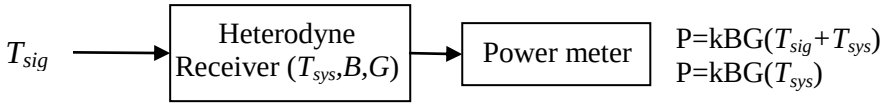

Figure 3-2: An idealized radiometer. The noise temperature generated from the receiver is added to the output power of the system.

By using two different thermal sources, the noise temperature of a heterodyne system can be conveniently determined by only looking at the output signal of the system as shown in Figure 3-3. The blackbody having the radiation of 300 K (room temperature) and the liquid nitrogen (77 K) are usually used as the hot and cold load respectively.

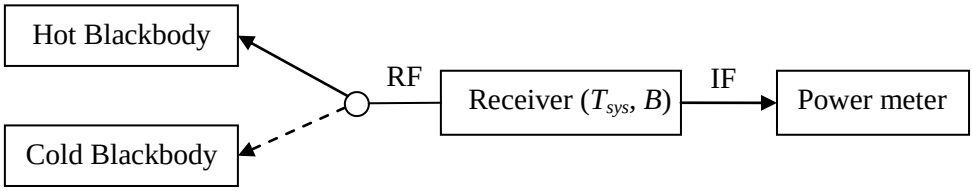

Figure 3-3: The principle of noise measurements with two different thermal sources. The hot and cold back bodies radiating two different powers at radio frequency (RF) coupled into the heterodyne receiver having the system noise temperature, T_{sys} and the bandwidth, B.

As shown in Figure 3-3, if a receiver is defined as a *two-port*[15] and it has an IF band pass filter, the power output from the receiver can be determined in the following equations,

$$P_H = kBG(T_H + T_n) \quad \textbf{eq. 3-6}$$

$$P_C = kBG(T_C + T_n) \quad \textbf{eq. 3-7}$$

where P_H and P_C are output powers measured while the receiver is switched to the hot and cold load respectively, k is Boltzmann's constant, B is a receiver's bandwidth, G is receiver's gain and T_{sys} is the noise temperature of the receiver. By dividing eq. 3-6 with eq. 3-7, the so-called Y factor can be determined in the following equation.

$$Y = \frac{P_H}{P_C} = \frac{T_H + T_n}{T_C + T_n} \quad \textbf{eq. 3-8}$$

Hence, the system noise temperature of the receiver can be expressed as eq. 3-9.

$$T_n = \frac{T_H - Y \cdot T_C}{Y - 1} \quad \textbf{eq. 3-9}$$

This method is called the Y-factor method and it is a precise method which is usually used for measuring the system noise temperature of the receiver (considering as a two-port).

[15] The two-port is linear. Although mixers are pumped nonlinear circuit elements, the process of shifting a signal from the RF to the IF is linear. Therefore, mixers are sometimes called a linear component.[14]

3.2.3 Radiometer equation

The fluctuation of the white noise power measured at the output of the heterodyne receiver with the bandwidth (*B*) limits ability to see the low (signal) power level. It is convenient to define the lowest signal power level that the receiver can detect in the same unit as the thermal source.

The smallest temperature change corresponding to a thermal source (K) that can be detected by a radiometer is called the *minimum detectable temperature (ΔT)*[16] and it can be calculated by the radiometer equation as expressed in eq. 3-10,

$$\Delta T = \frac{T_{sys}}{\sqrt{B \cdot \tau \cdot n}} \qquad \textbf{eq. 3-10}$$

where T_{sys} is the noise temperature of the receiver/system and its unit is usually in Kelvin (K), B is the IF bandwidth, and τ is the integration time of an individual measurement whereas n is the number of measurement averaged (dimensionless). The system noise temperature is constant, thus; the fluctuation of the detected power can be reduced by either increasing the IF bandwidth or the post detection integration time (τ).

The integration time provides a result of averaging over a period of time τ in which the white noise can be reduced. In practice, τ is limited at some number due to an increase in the drift with the integration time. In this case, by repeating the scan over and over (n) and averaging the results yield also the same result as increasing the integration time.

3.2.4 System drift and Allan variance

There are always three unwanted things added into the detected signal: white noise, 1/f noise and drift [Wilmshurst, 1990]. The white noise error can be reduced by increasing the integration time while 1/f noise is independent from integration time. The drift is usually increased as the integration time increases. This means that in case of the integration time is increased; the white noise error can be reduced while the drift is increased. A method which can characterize this combined noise is called the *Allan variance* and this method was used in this thesis for observing the best adjustment yielding the best stability of the THz channel.

Allan variance:

The advantage of Allan variance over the classical variance is that it can converge most common noise as discussed above whereas the classical variance does not. The integration time dependence of the Allan variance allows us to distinguish among various noise regimes. By using Allan variance [Allan, 1990], [Land, et al., 2007] the maximum effective integration time can be determined. In order to calculate the Allan variance, a long sequence of the detected signal is sampled (usually 10^3 to 10^4) and is divided into

[16] The minimum detectable temperature is sometimes called the radiometric sensitivity or radiometric resolution.

groups based on the integration time. Take the difference in averaging between successive groups, square this number, add them all up and divide by a rescale factor. After that increase the integration time and start the process over again. The Allan variance as a function of the integration time (τ) can be determined as expressed in eq. 3-11. The integration time (τ), of each group is $n \cdot t_0$ where t_0 is the time between each data point [Witt, 2001].

$$\sigma^2(\tau) = \frac{1}{2 \cdot p} \sum_{j=1}^{P} \left[y_{j+1}(\tau) - y_j(\tau) \right]^2 \qquad \textbf{eq. 3-11}$$

where y is an average value of the data points in group ($j=1..p$) of n points. The square root of Allan variance (σ) is called the Allan deviation.

3.3 Principle of radiometric calibration

By using three consecutive measurements of the two reference-black bodies, the unknown radiance field (the radiation of the signal of interest) can be determined by performing the calculation according to the following expressions.

$$P_H = C \cdot (T_H + T_{sys}) \qquad \textbf{eq. 3-12}$$

$$P_C = C \cdot (T_C + T_{sys}) \qquad \textbf{eq. 3-13}$$

$$P_S = C \cdot (T_S + T_{sys}) \qquad \textbf{eq. 3-14}$$

Where H,C,S are abbreviations of hot, cold and signal respectively, T_{sys} is the noise temperature of the heterodyne receiver, C is the instrumental properties such as losses and gains. By the calculation of these three equations, in the Rayleigh-Jeans limit, the brightness temperature measured by an instrument can be determined by the following equation.

$$T_S = \frac{T_H - T_C}{P_H - P_C}(P_S - P_C) + T_C \qquad \textbf{eq. 3-15}$$

In general, the actual spectra measured from the spectrometer consists of the frequency channels. The calibrated spectra can be determined conveniently by substituting the power of the signal in eq. 3-15 with the power of each channel in the spectrum measured from the spectrometer as the following expression:

$$S_i^{T_S} = \frac{T_H - T_C}{S_i^H - S_i^C}\left(S_i^S - S_i^C\right) + T_C \qquad \textbf{eq. 3-16}$$

where,

$S_i^{T_S}$ = *the signal temperature spectra*

T_H = *temperature at the hot blackbody*(K)

T_C = *temperature at the cold blackbody*(K)

S_i^H = *the element*(i) *of the hot spectrum*

S_i^C = *the element*(i) *of the cold spectrum*

S_i^S = *the element*(i) *of the signal*$(atmosphere)$ *spectrum*

3.4 Principle of a superconducting Hot Electron Bolometer (HEB)

Among various types of superconducting detectors being available at present, HEB mixers are the best choice for applying in THz frequency range due to their high sensitivity as shown in Figure 3-4. In fact, the noise temperature of the receiver in the real system is much larger than the quantum limit ($hf / 2k_B$: DSB, see chapter 3.2.1).

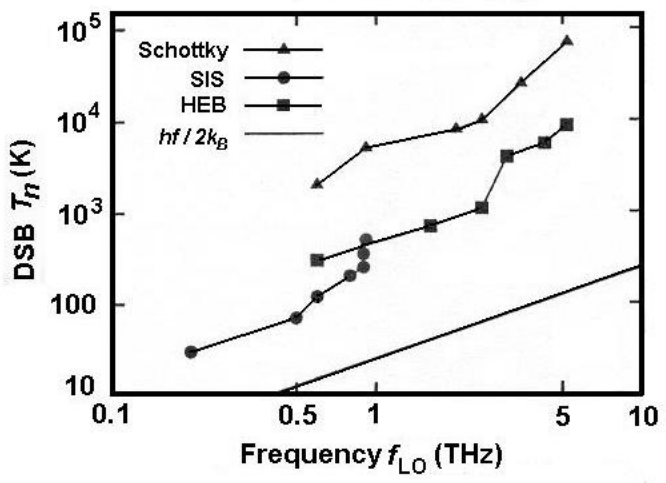

Figure 3-4 : The DSB receiver noise temperature of different mixer technologies in the THz frequency range. The straight line represents the idealized minimum noise temperature achievable with a DSB heterodyne receiver [Kroug, 2001].

The HEB device is a temperature detector whose resistance changes due to a change of the incident signal power. The HEB device is usually a thin superconducting film made of NbN or niobium (Nb). An advantage of HEB mixers over traditional bolometers is the shorter response time. HEB mixers are operated at superconducting temperature, where the coupling between free electrons and phonons is very weak; hence, free electrons can be easily excited. Therefore only free electrons in the hot electron bolometer are heated up instead of the whole bolometer media. As the result, the response time of HEB mixer is faster than that of traditional bolometers. In addition, the HEB mixers require low LO power which is usually lower than 100 nW.

At present, there are two types of the HEB mixer, diffusion cooled and phonon cooled types: *phonon cooled type and diffusion cooled type* [Prober, 1993]. The HEB applied in the 1.8 THz channel is the phonon cooled type.

The *phonon cooled type* uses an ultra-thin niobium film as a micro bridge. Hot electrons are cooled by an inelastic scattering with phonons in the film and subsequent heat transfer into a substrate. In the past years, the performance of several HEB mixers such as ones developed from Chalmers University or from JPL has been improved [Yagoubov, et al., 1998]. Their noise temperature is even close to twenty times the quantum limit and the IF bandwidth is wide.

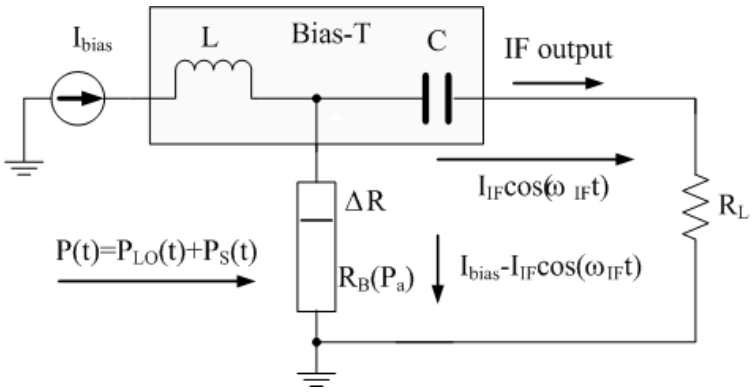

Figure 3-5 : The equivalent circuit of bolometer mixer. The inductance (L) and the capacitance (C) works as a "bias-T" which has a function to separate the DC bias supplied to a mixer from the IF frequency output. R_B is the bolometer resistance. ΔR is a change of the bolometer resistance which depends on a change of total power ($P_a = P_{LO}+P_S+P_{DC}$) provided on it.

Figure 3-5 shows the equivalent circuit of a HEB device. During operation, the device absorbs the LO and signal power as well as power from the DC bias supply. When the power increases, the electron temperature increases and the resistance of the device (ΔR) increases as expressed in the following equation.

$$\Delta R = \frac{dR_B}{dP} \cdot \Delta P \qquad \textbf{eq. 3-17}$$

The device impedance (R_B) is proportional to the difference of power between the LO and the signal. The device absorbs the LO and signal irradiance and modulates with $[\sin(\omega_{LO}t)+\sin(\omega_S t)]^2$ which results in a modulation at the difference frequency (IF). Usually the IF output from the HEB device is connected to the microwave components (such as an amplifier, a circulator) which have usually the load impedance (R_L) of 50 ohm.

The performance of a mixer is usually characterized by three parameters: the conversion loss, IF band width and noise figure. The conversion loss of a mixer (L_m) is defined by the inversion of the conversion efficiency (η_m) according to the following equation,

$$L_m = \frac{1}{\eta_m} \quad and \quad \eta_m = \frac{P_{IF}}{P_{Sig}} \qquad \textbf{eq. 3-18}$$

where P_{IF} is the IF power and P_{sig} is the signal power. Mixers have usually $\eta_m<1$; therefore, the conversion efficiency is sometimes called the conversion loss.

Superconducting HEBs have three states as indicated in

Figure 3-6. The HEB device is firstly cooled to the superconducting state and is pumped by the LO and dc power in which the gain of the HEB devices depends on the LO power pumped on it. In addition, the voltage reflection at the IF port causes fluctuations in the mixer gain due to an effect of the electrothermal feedback [Richter, 2005], [Kooi, et al., 2007] whereby the IF voltage across the load resistance R_L drives a current ΔI which adds to the dc bias I_0 through the bolometer. The IF power at the load resistance R_L depends on the HEB mixer's responsivity ($S\omega_{IF}$). The IF power as a function of the LO power can be determined by the following equation.

$$P_{IF} = V_{IF}^2(\omega,t)/4R_L \qquad \textbf{eq. 3-19}$$

$$V_{IF}^2(\omega,t) = S(\omega_{IF}) \cdot 2\sqrt{P_{LO}P_S}\cos\omega_{IF}t \qquad \textbf{eq. 3-20}$$

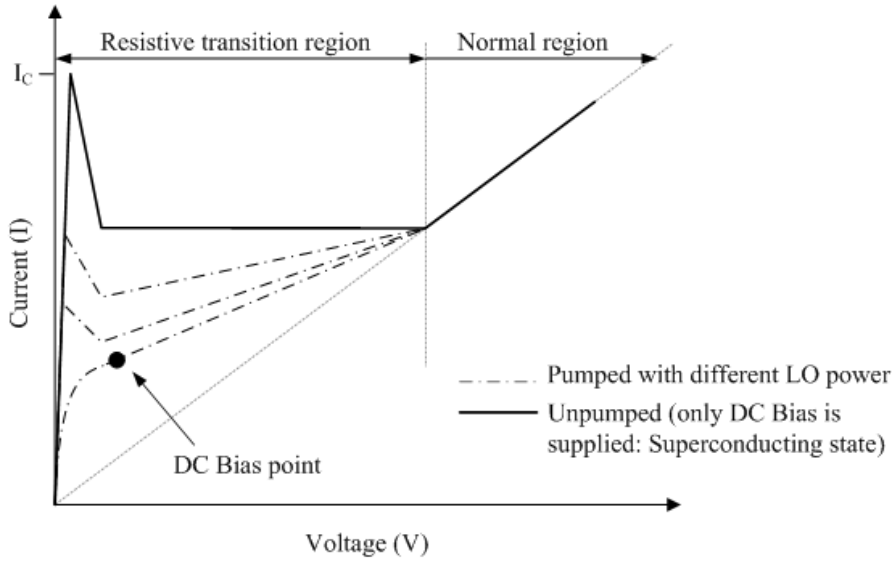

Figure 3-6 : The IV curve of a HEB mixer with three states: Superconducting, resistive transition and normal stat. I_C refers to the critical current.

3.5 Martin-Puplett Interferometer

Both diplexer and single side band (SSB) filter used in the 1.8 THz channel are based on the Martin-Puplett Interferometer (*Michelson polarizing interferometer*[17]*)* technique [Martin, et al., 1969]. The function of the diplexer is to couple both LO and the signal power into the HEB mixer while the SSB filter is applied for suppressing unwanted RF frequencies.

In comparison to the traditional Michelson interferometer, the MPI uses a polarizer at 45° (see "divider" in Figure 3-7) instead of the beam splitter and a so called "roof mirror" instead of the flat mirrors. By using the polarizer, the problems such as loss and frequency dependence of the beam splitter can be avoided. One roof mirror is movable and this allows the MPI to be employed for a wide range of the signal frequency by simply adjusting the position of the movable roof-mirror.

[17] The MPI Interferometer is a polarizing version of the Michelson interferometer , hence it is sometime called Michelson polarizing interferometer [Lesurf, 1990].

Matin-Puplett Interferometer as a diplexer:

The goal of the diplexer is to couple the maximum power of both signal and LO into a mixer. Figure 3-7 illustrates an optical circuit of the MPI employed as a diplexer. The signal beam is transmitted at the first polarizer whose grids align vertically while the LO beam is reflected. These two superposed beams which are orthogonally polarized enter the divider where these two beams are split into two combined components as shown in Figure 3-7 (A) [Polavarapu, 1998].

The first combined component which is perpendicular to the wires of the divider is a vectorial combination of S_T and L_T. The second combined component which is parallel to the wires is a vectorial combination of S_R and L_R. The one parallel to the wires will be reflected to a fixed roof mirror and the one perpendicular to the wires will be transmitted to a movable roof mirror.

The linear polarization of each combined component is rotated with the angle of 90° at the roof mirror. The roof mirror consists of two flat mirrors connected together on the edge with the angle of 90° as shown in Figure 3-7 (B). Both rotated linearly polarized components are recombined again at the divider.

An elliptically polarized wave is produced after both components are recombined at non-zero phase. Finally the analyzer (vertical/horizontal wire gird), divides the incident beam again into two linearly polarized components, the horizontally and the vertically polarized radiations, whose powers are monitored at a detector. If the interferometer is perfectly aligned, half of the incident power is detected at the detector.

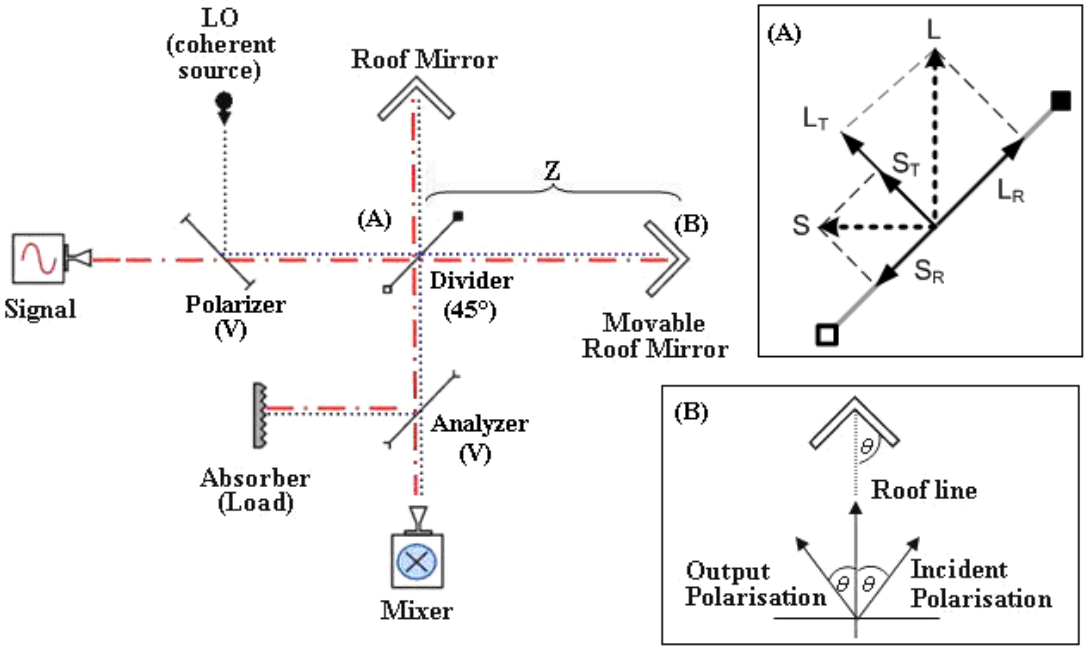

Figure 3-7 : The optical circuit of the Martin-Puplett interferometer used as a diplexer. The abbreviation "H", "V" and "45°" means their wires are aligned horizontally, vertically and 45° from the reference plane (horizontal) respectively. θ = 45°, S= incident Signal, L=incident LO, L_R and S_R are the reflected components of the incident LO and signal respectively, L_T and S_T are the transmitted components of the incident LO and signal.

By tuning the distance, Z, one can adjust the path difference. This yields the result of changing the polarization of the LO and the signal as well as changing both output powers coupled into the mixer.

At the mixer, the transmission of the signal at the wavelength λ_S and the transmission of the LO at wave length λ_{LO} can be expressed as the following equations,

$$T_S = \frac{1}{2}(1-\cos\frac{2\pi\Delta}{\lambda_S}) \quad \textbf{eq. 3-21}$$

$$T_{LO} = \frac{1}{2}(1+\cos\frac{2\pi\Delta}{\lambda_{LO}}) \quad \textbf{eq. 3-22}$$

where Δ is the optical path difference. As shown in eq. 3-21 and eq. 3-22, the transmission of the signal is maximal when $\cos(2\pi\Delta/\lambda_S) \cong -1$ at which the $\Delta_S = (n-½)\lambda_S$ and the LO transmission is maximal when $\cos(2\pi\Delta/\lambda_{LO}) \cong 1$ at which the $\Delta_{LO} = (n-1)\lambda_{LO}$. Thus, *n* which can fulfill this condition can be determined as follows:-

$$(n-\frac{1}{2})\lambda_S = (n-1)\lambda_{LO} \quad \textbf{eq. 3-23}$$

$$n = \frac{\lambda_S - 2\lambda_{LO}}{2(\lambda_S - \lambda_{LO})} \quad \textbf{eq. 3-24}$$

hence, the optimal path difference (Δ) can be written as follows :-

$$\Delta = (n-1)\lambda_{LO} \quad \textbf{eq. 3-25}$$
$$= \left(\frac{\lambda_S - 2\lambda_{LO}}{2(\lambda_S - \lambda_{LO})} - 1\right)\lambda_{LO} = \frac{\lambda_{IF}}{2}$$

The value of Δ depends upon the difference frequency ($|f_S - f_{LO}|$) which remains unchanged. Thus, the diplexer based on MPI can be applied for a wide range of the signal frequencies by slightly adjusting the path difference. In practice, the actual value of Δ can be determined by slightly adjusting the path difference until the power reaching the mixer is maximized.

Matin-Puplett Interferometer as a SSB filter:

The SSB filter is used for suppressing the unwanted sideband i.e. the image frequency. In principle, the MPI as a SSB filter works in the same way as the diplexer but only one polarized input signal incidents on the divider. At the mixer, the transmission of the wanted sideband should be maximal while the signal at the image sideband should be minimal as expressed in eq. 3-26 and eq. 3-27.

$$T_S = \frac{1}{2}(1-\cos\frac{2\pi\Delta}{\lambda_S}) = 1 \quad \textbf{eq. 3-26}$$

$$T_{im} = \frac{1}{2}(1-\cos\frac{2\pi\Delta}{\lambda_{im}}) = 0 \quad \textbf{eq. 3-27}$$

Hence, this yields the optimal path difference:-

$$\Delta_{SSB} = \frac{\lambda_{IF}}{4} \qquad \textbf{eq. 3-28}$$

3.6 Autocorrelator spectrometer

At present there are several types of spectrometers being considered for space based sub-millimeter heterodyne systems such as a digital autocorrelation, Chirp Transform, Acousto Optical, Filterbank spectrometers and digitizer. The advantages of digital autocorrelation spectrometers in comparison to other techniques are stability, compactness, high reliability and variability in bandwidth and resolution.

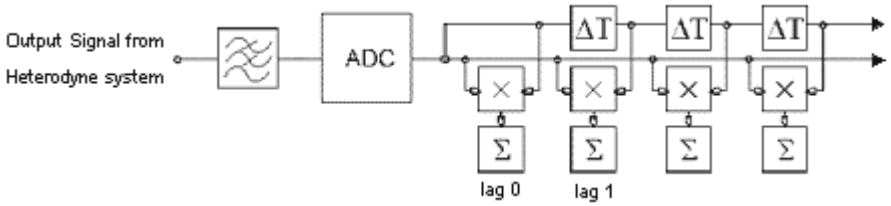

Figure 3-8 : The basic principle of the autocorrelator spectrometer.

The main processing part in the autocorrelation spectrometer (ACS) is done in the time domain. The signal is digitized with low precision (up to two-bit high speed digital electronics analogue to digital converters). The ACS for DLR channel of TELIS instrument is digitized with 1½ bit quantization levels. This ACS can provide 2048 spectral channels for 4 GHz with a spectral resolution (FWHM) of 2.4 MHz.

The basic principle of the autocorrelator is based on the autocorrelation function as shown in Figure 3-8. The input signal is digitized and correlated by shifting the signal as shown in eq. 3-29. The result after performing the correlation is stored in lags.

$$\sum_{k=0}^{N-1} X(k) * X(k+i) \qquad \textbf{eq. 3-29}$$

where, $i = discreteof\ samplevalue$

The Fourier-transformation of the autocorrelation results yields the desired spectrum. The number of lags is related to the spectral resolution while the sampling frequency yields the bandwidths.

Part II

Overview of the TELIS instrument and the 1.8 THz channel

4 TELIS Instrument overview

4.1 The TELIS Instrument

The TELIS instrument (TErahertz and submm LImb Sounder) is a new balloon borne cryogenic three channel heterodyne spectrometer for atmospheric research. The three channels are: the 500 GHz channel developed by RAL, the 450-660 GHz channel developed by SRON and the 1.8 THz channel developed by DLR.

TELIS is developed by DLR in co-operation with SRON, RAL and will be operated simultaneously with a FT spectrometer (MIPAS-B). The TELIS instrument is designed to be a compact, lightweight instrument and capable of providing broad spectral coverage and high spectral resolution. In order to fulfil these requirements, parts of the instrument such as the cryostat, spectrometer, shielding, the components of each heterodyne receiver have a special design to give high performance while their weight is reduced.

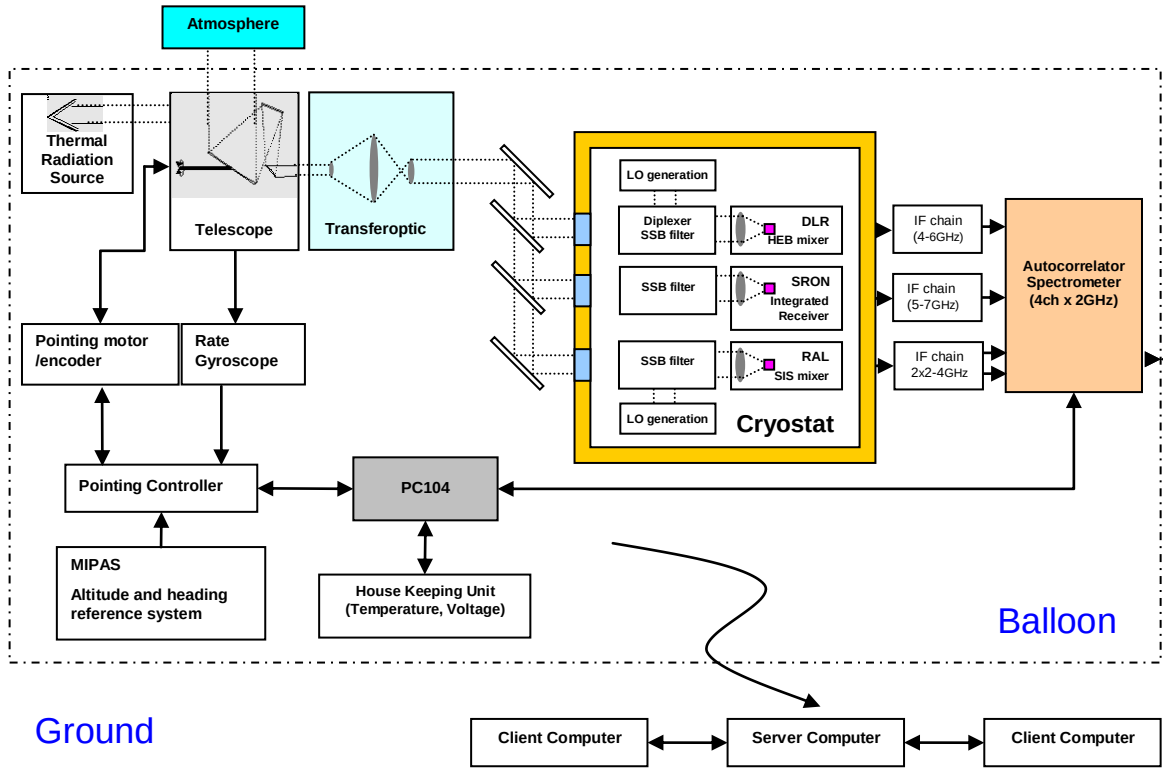

Figure 4-1 : Block diagram presents the construction of TELIS instrument. Cryostat consists of three heterodyne receivers (1.8 THz, 450-660 GHz and 500 GHz receivers).

The cryostat has the special design from RAL (by Mark Harman) which has the capability to install two optical benches inside. The weight of the cryostat is less than 20 kg. Both the 500 GHz and the 450-660 GHz channels are designed to be compact and share the same optical bench. The 1.8 THz channel is mounted on the second optical bench.

Hot Electron Bolometer (HEB) and superconducting tunnel junction (SIS) mixers are used for the 1.8 THz and 500 GHz and will be pumped by solid state local oscillators. A Superconducting Integrated Receiver (SIR) is used for the 450-660 GHz channel.

Figure 4-1 depicts the block diagram of the TELIS instrument. A dual offset Cassegrain telescope couples either the atmospheric radiation or the reference thermal radiation from the hot blackbody through the transfer optics into the cryostat. At the polarizer, acting as a beam splitter, the reflected beam is coupled to the 500 GHz channel and the transmitted beam having horizontal polarization is directed to the dichroic plate. It is used to separate the signals of the 1.8 THz and the 450-660 GHz channels and it was developed by RAL. A digital autocorrelator with 2 MHz resolution at 4 GHz bandwidth is provided as the backend spectrometer. The TELIS instrument is communicated and controlled by a computer (based on PC104) and the spectra will be retrieved via remote communication. The information of the pitch angle and the height of the gondola (balloon) are forward from the MIPAS to PC104 of the TELIS instrument. The pointing motor and encoder are used to control the telescope. All data measured during the flight are sent immediately to the ground server. In case of a failure the data is sent to the ground and all measured data is also stored on board (on the Flash-Rom with capacity of 8 GB).

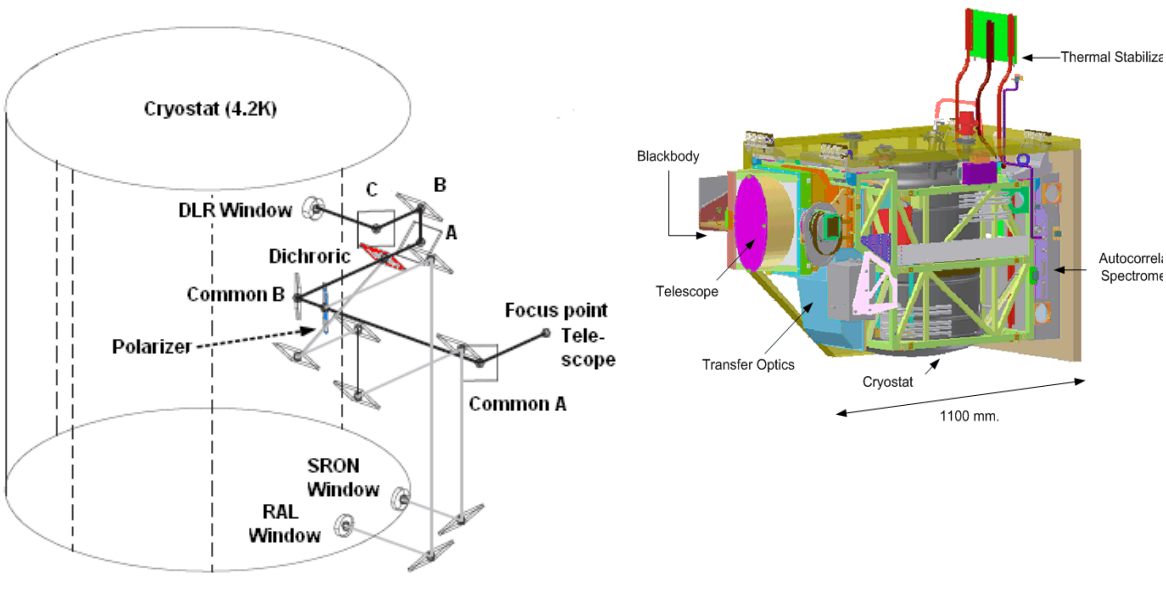

(a) (b)

Figure 4-2 : (a) Drawing of the transfer optics between the telescope focus point and three windows of the cryostat. The picture shows how the atmospheric signal is transported to each heterodyne channel (adapted from [Mair, 2007], p.73. b) 3D-drawing of the complete TELIS instrument (by Christian Sartorius, Forschungszentrum Karlsruhe).

500 GHz channel:

The highly compact 500 GHz channel is developed at Rutherford Appleton Laboratory (RAL), UK. The goal of the 500 GHz channel is to measure the concentration of ClO, BrO, N_2O and O_3 in the stratosphere within the frequency range from 497 to 504 GHz. The 500 GHz channel operates in single side band mode. The input signal (RF) is transmitted into the optical unit (see Figure 4-3a) having a dichroic plate filter (DCP) to separate the signal from the image sidebands. The image sideband is directed to a cold load (at 4.2 K) where it is rejected from the system. The selected signal is then directed towards a superconducting tunnel junction (SIS) waveguide mixer. The LO chain is formed by a phase locked dielectric tuned resonator at room temperature yielding the fundamental frequency of 32.3 GHz. This frequency is then up-converted to 484 GHz (the centre frequency of LO) by using two cascade multipliers: x3 and x5. These two multipliers are placed inside the cryostat but cooled to 77 K (see Figure 4-3b). The RF signal is then down-converted to 14-18 GHz and amplified with the low noise amplifier (LNA). The expected noise temperature of the 500 GHz channel is about 600 K (SSB).

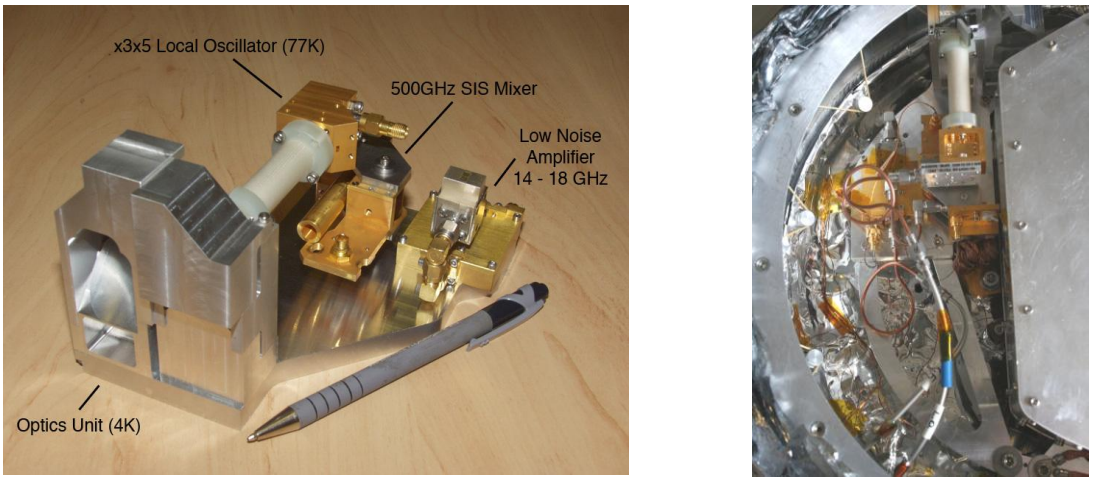

(a) (b)

Figure 4-3 : (a) Comparison of the highly compact 500 GHz channel with a pen. (b)The photo of RAL channel installed inside the flight module cryostat. (Courtesy of B. Ellison)

450-660 GHz channel:

The 450-660 GHz channel has been developed by the Netherlands Institute for Space Research (SRON) and Kotel'nikov Institute of Radio Engineering and Electronics RAS in Moscow (IRE RAS). The receiver based on a phase-locked Superconducting Integrated Receiver (SIR). SIR is an on-chip combination of a low-noise SIS mixer with quasioptical antenna, a superconducting Flux Flow Oscillator (FFO) acting as Local Oscillator (LO) and a SIS harmonic mixer (HM) [Yagoubov, et al., 2008]. Figure 4-4 shows schematics of the SIR with a phase-locked LO. The second SIS harmonic mixer (HM) is used for FFO phase locking. The frequency of the LO is locked by the phase locked loop (PLL) locating outside the cryostat. The free-running line width of the FFO can be up to 10

MHz. A wide tuning range of the FFO is an advantage in addition to its compact size. The 450-660 GHz channel operates in double side band mode with IF bandwidth of 4-8 GHz. Its noise temperature is about 120 K (DSB). The goal of the 450-660 GHz channel is to measure ClO, BrO, O_3, ClOOCl, HCl, HOCl, H_2O+isotopologues, HO_2, NO, N_2O, HNO_3, CH_3Cl and HCN.

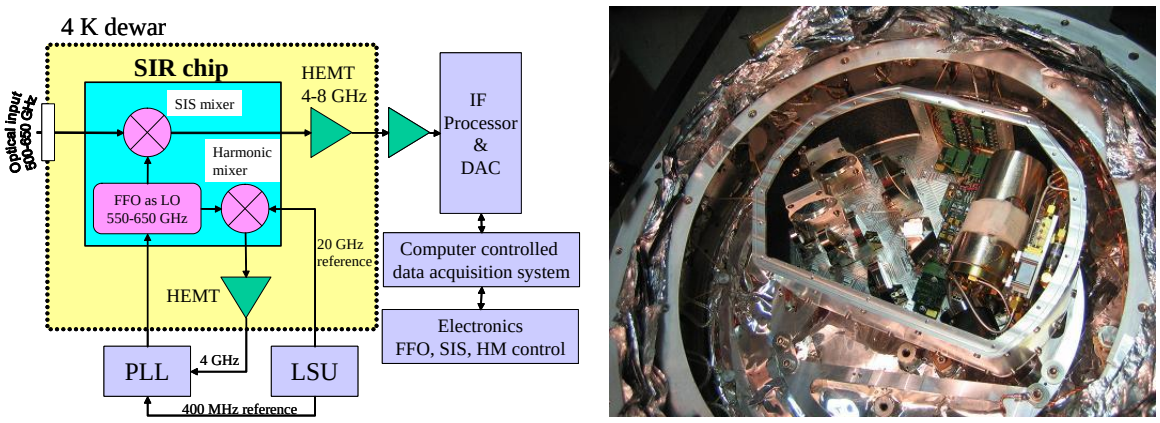

(a) (b)

Figure 4-4 : a) Schematics of the SIR with a phase-locked LO. b) A photo of 450-660 GHz receiver installed inside TELIS flight module cryostat.

1.8 THz Channel:

The 1.8 THz channel operates in double side band mode at frequency 1780-1880 GHz. Although the 1.8 THz channel focuses on OH, the other species such as HO_2, HCl, NO, NO_2, O3, H_2O+isotopologues, O_2, HOCl are also possible to be measured. Especially water isotopologues is an important key for understanding the changing of the partitioning of water vapour which is sources of OH in the stratosphere. In addition, with capability to measure at the same time with other channels and MIPAS instrument, the validation can be provided. The further detail of 1.8 THz channel is explained in Chapter 5.

4.2 Cryostat construction

Basically, the unit consists of a thin-walled vacuum vessel surrounding a liquid nitrogen cooled radiation shield which, in turn, surrounds a liquid helium pot. The nitrogen shield and the liquid helium pot are suspended via a Kevlar webbing structure (just visible in the picture) which is maintained under tension and retains the required internal alignment with minimal conductive heat leak into the cryogens. Liquid helium and nitrogen enters the cryostat through respective fill tubes and the instrument signals (including the sub-mm wave signals) enter the cryostat via a series of portholes located on the periphery of the vessel. The RAL and SRON channels (both channels mounted on the same optical bench) are attached to one end of the liquid helium pot (bottom) and the DLR channel to the other (top). Thermal contact to the liquid helium and the DLR channel is achieved via high conductivity conducting straps that are located inside the liquid helium pot. The liquid helium hold-time is about 24 hours for one fill (15 litres).

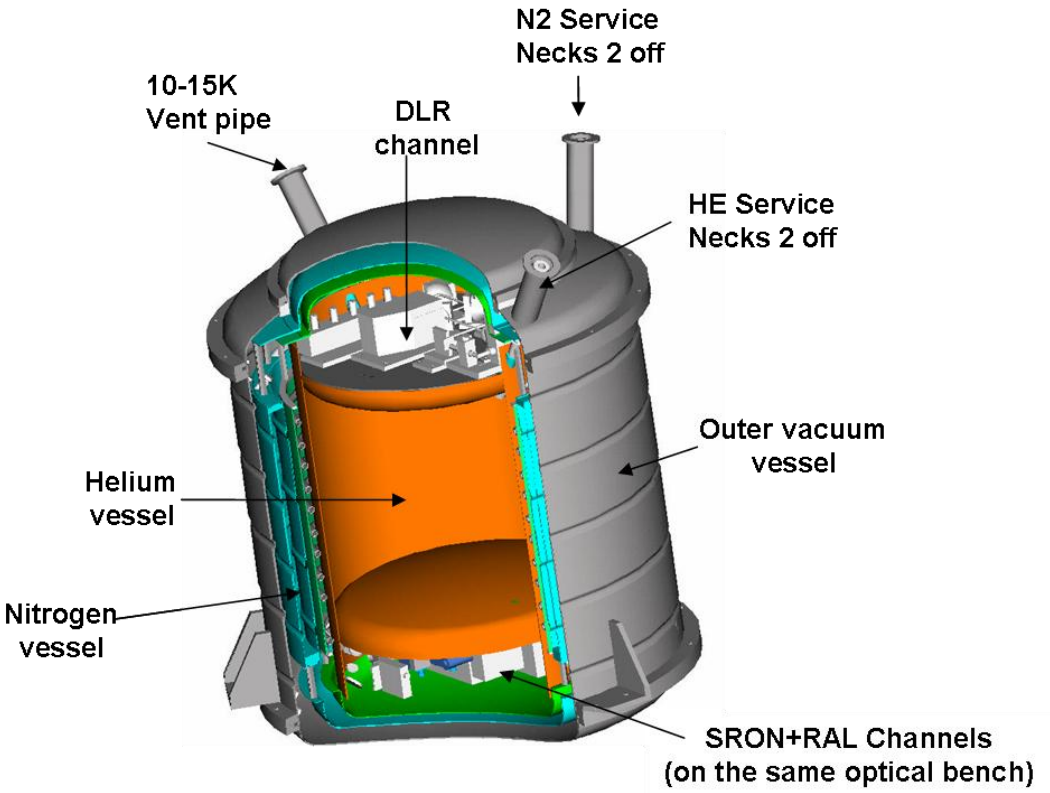

Figure 4-5: Illustration of the TELIS flight module cryostat, its components and the location of three heterodyne channels [Harman, 2002].

4.3 Multi-instrument remote sensing payload (TELIS/MIPAS/miniDOAS)

In cooperation with DLR, SRON, RAL, Universities of Bremen and Heidelberg, an advanced technology multi-instrument remote sensing payload on the same balloon platform has been qualified for first deployment in 2008 [Friedl-Vallon, et al., 2004]. The payload consists of three instruments: TELIS (DLR, SRON, RAL), MIPAS-B (IMK) and mini-DOAS (Universities of Bremen and Heidelberg). With this combination of sophisticated sensors is dedicated to remote sensing of radiation, atmospheric state parameters, cloud information and atmospheric composition. The sensors cover a wide range of the electromagnetic spectrum that can be used for atmospheric research. The broad spectral coverage offers large synergies as e.g. the cross-check of spectroscopic parameters, the cross-validation of measured parameters, the closure of chemical families, and improved detection of cloud parameters.

MIPAS-B (The balloon-borne Michelson Interferometer for Passive Atmospheric Sounding) is an advanced Fourier Transform Infra Red (FTIR) spectrometer specially tailored to the operation on a stratospheric balloon gondola. Equipped with suitable subsystems, MIPAS-B allows precise limb emission sounding of chemical constituents related to the stratospheric ozone problem and to the greenhouse effect. This method is appropriate to obtain vertical profiles of ozone and a considerable number of key radicals

(NO, NO_2), reservoir species (HNO_3, N_2O_5, $ClONO_2$, and HO_2NO_2) as well as source gases (CH_4, N_2O, H_2O + isotopologues, CFC-11, CFC-12, CFC-22, CCl_4, CF_4, C_2H_6, and SF_6) simultaneously, with an altitude resolution of 2 to 3 km.

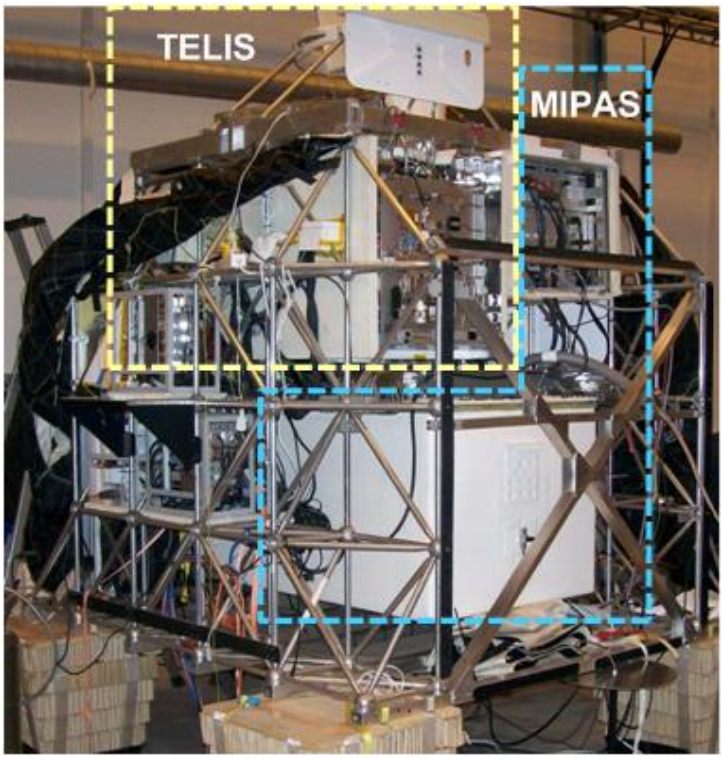

Figure 4-6 : The picture above depicts two instruments (TELIS and MIPAS) which were installed on the same gondola during the flight campaign in Kiruna, Sweden in March 2009. The photo below shows the design of the TELIS's optical module.

Mini-DOAS (Miniature differential Optical Absorption Spectrometer) is a two channel automated UV/VIS limb scanning spectrometer covering the wavelength range from 320 nm to 530 nm with FWHM spectral resolutions of 0.4 and 0.7 nm. The instrument is able to measure time dependent profile of UV/VIS absorbing atmospheric radicals, such as O_3, NO_2, CH_2O, $C_2H_2O_2$, HNO_2, Bro, IO. [Oelhaf, 2008].

5 The 1.8 THz cryogenic heterodyne receiver

In this chapter the 1.8 THz cryogenic heterodyne receiver is described in detail. An overview of the complete instrument of the 1.8 THz heterodyne receiver will be given first. The receiver consists mainly of its transfer optics, the 1.8 THz cryogenic channel and its back end instruments. A focus on the 1.8 THz cryogenic channel and its important components will be presented in the section 5.2

5.1 Overview of the 1.8 THz receiver

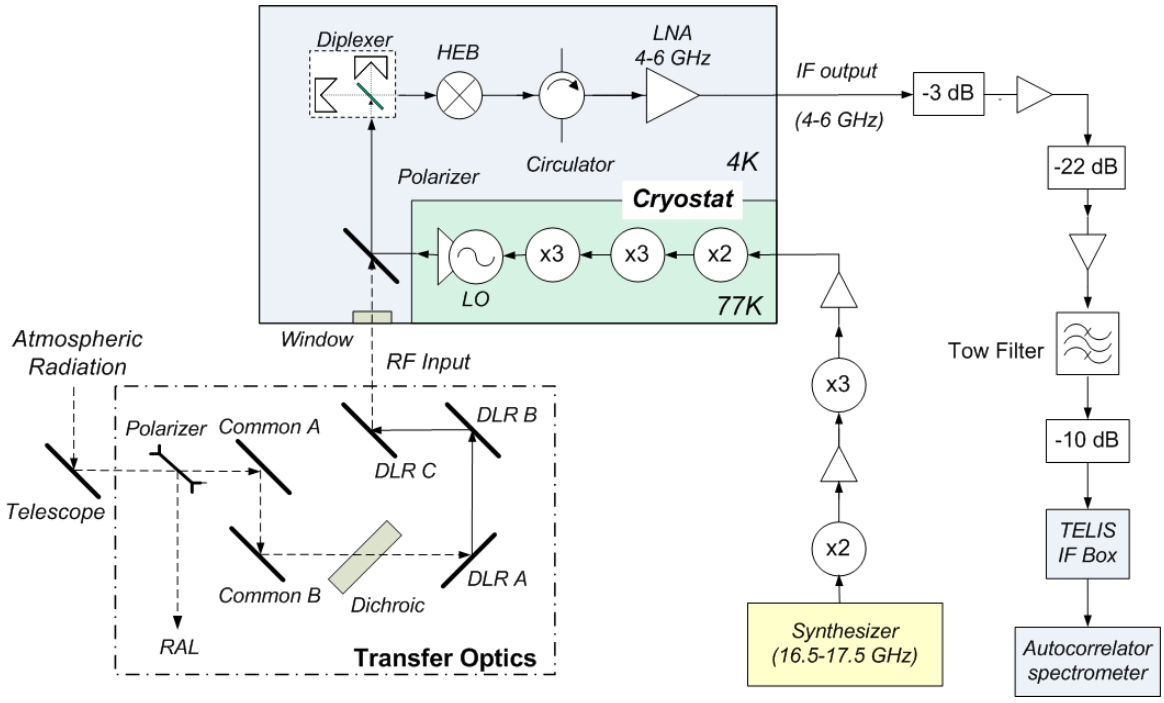

Figure 5-1: Schematics of the 1.8 THz Receiver

The incoming atmospheric radiation is transferred by a dual offset Cassegrain telescope through the common transfer-optics as shown in Figure 5-1. At the polarizer, the reflected beam having vertical polarization is coupled into the 500 GHz channel (RAL) and the transmitted beam having horizontal polarization is directed to the dichroic plate used to separate the signals of the 1.8 THz and the 450-660 GHz channels. The dichroic was developed by RAL and was tested at DLR by measuring it under 13° incidence angle. The

transmittance for the lower frequency limit (1780 GHz) is 82.3% and for the upper frequency limit (1880 GHz) is 92.5% as shown in Figure 5-2.

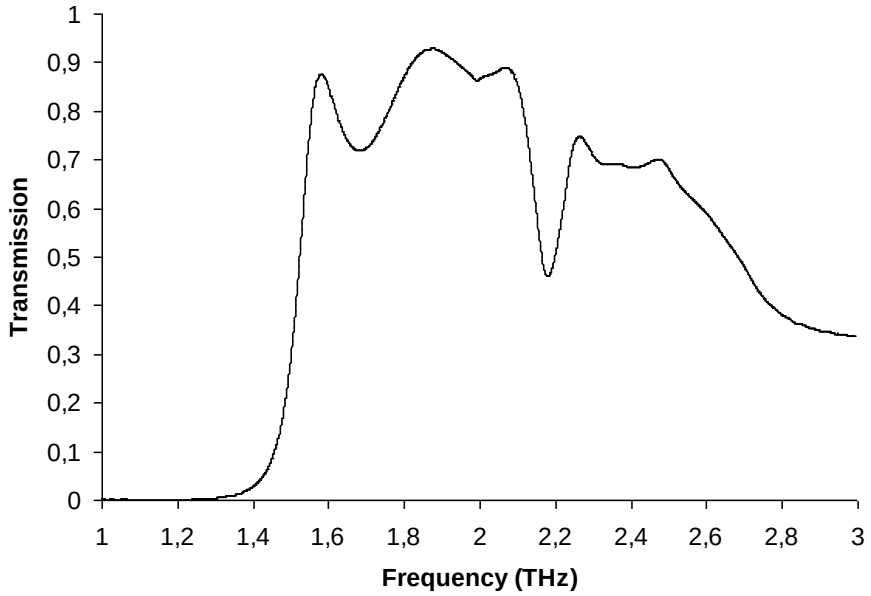

Figure 5-2: Transmissions of the dichroic measured at DLR with an incidence angle of 13° [Birk, et al., 2007].

The signal is coupled into the cryogenic heterodyne receiver by passing through the quartz window having average transmittances about 90% at 1.8 THz region. The transmitted signal is then down-converted to the intermediate frequency (IF) of 4-6 GHz. The IF signal is afterwards 70 times amplified by two low noise amplifiers. Because the sensitivity of the 1.8 THz channel is frequency dependent (worse sensitivity at the higher frequency), the frequency dependency of the output power of the cold channel (or input power of the autocorrelator) is not flat. As a result, the autocorrelator requires a tow filter in order to equalize the input power and this is placed in front of the autocorrelator spectrometer. An adjustable synthesizer which can be tuned from 16.5 GHz to 17.5 GHz is used as a source of the cryogenic LO. Along with frequency multipliers (doublet and triplet) based on the Planar Schottky Diode Technology, an output frequency of the cryogenic LO in the range of 1780 to 1880 GHz can be achieved.

5.2 The 1.8 THz cryogenic heterodyne receiver

The main target of the 1.8 THz receiver is the measurements of the OH radical. Further stratospheric species such as HO_2, HCl, NO, and NO, O_3, H_2O + isotopologues and HOCl and CO will also be measured in the frequency range of 1780-1880 GHz. The cryogenic receiver is installed on a 26 cm diameter optical bench. It utilizes a hot electron bolometer (HEB) based on a phonon-cooled NbN technology as mixer. In comparison to Schottky diode mixer technology utilized in the THz region the new superconducting mixer technology requires much less local oscillator power and thus allows using a cryogenic

solid state local oscillator (LO). Thus, the size of the receiver can be reduced while its stability is enhanced since all components are cryogenically operated on a small optical bench. The 1.8 THz heterodyne receiver operates in double side band mode and a diplexer based on a Martin-Puplett Interferometer (MPI) developed by SRON is used for coupling radio frequency (RF) and LO signal.

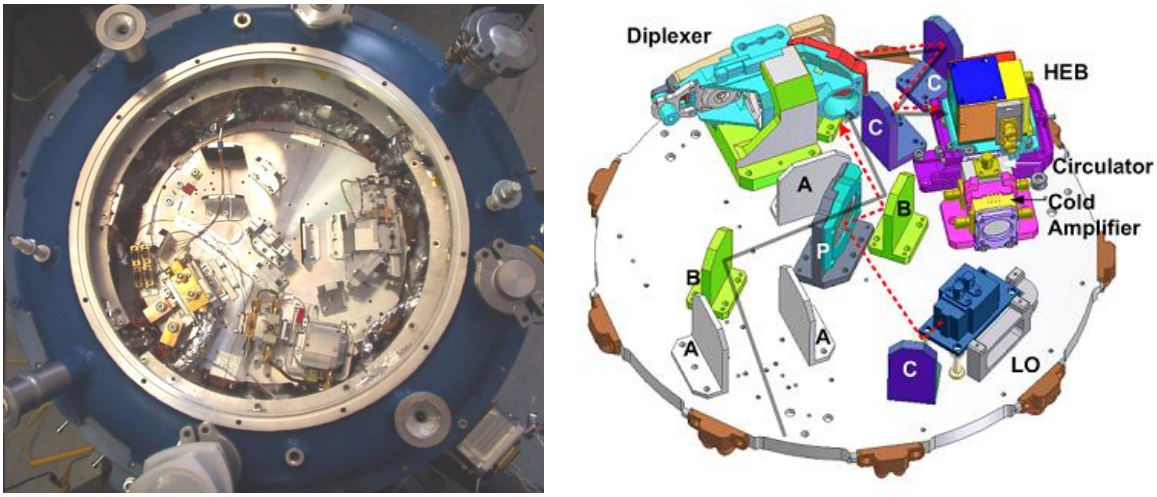

Figure 5-3 : a) A photo of the 1.8 THz channel in the flight module cryostat. b) 3D schematics of the 1.8 THz channel on the optical bench inside the flight module cryostat. "A" = Absorber, "B"=Flat mirror, "C" = Imaging mirror and "P" = Polarizer.

The schematics in Figure 5-3a) shows the 1.8 THz channel operating in double side band (DSB) mode. The atmospheric signal transmitted through the transfer optics (see Appendix H) is fed through the THz cryostat window and a blocking filter having a transmittance of about 70%. The horizontally polarized signal passes through the polarizer and is reflected by the flat mirror into the diplexer while the vertically polarized signal from the LO is reflected by the polarizer and the flat mirror to the diplexer. Both, signal and LO, are superimposed and horizontally polarized at the output of the diplexer. They are then reflected by two imaging mirrors to the HEB mixer where the RF signal is downconverted to 4-6 GHz (IF). The IF-output signal from the mixer is amplified and coupled into the IF backend (outside cryostat) where the digital autocorrelator is located.

The performance of the diplexer was tested with the FIR laser in a test cryostat. It has a very low leakage of about 0.7%. The highly sensitive HEB mixer developed by Chalmers University, Sweden, requires very low LO power (about 200 nW). It is a NbN phonon-cooled HEB mixer in which the electron phonon interaction (in the electron energy relaxation process) dominates over the electron diffusion [Ahrens, 2007]. The HEB mixer operates at a temperature of 4.2 K. The HEB together with a resistor network, Bias Tee and double slot antenna are integrated inside the same housing. The solid state local oscillator is heat-sinked to the 77 K shield in order to reduce the LO power dissipation to the optical bench (4 K). Basically, the output LO frequency is generated by a frequency multiplier chain. By multiplying the frequency from a synthesizer (16.5 GHz-17.5 GHz)

located at room temperature by 108, LO radiation at 1.8 THz can be generated. By using a solid state LO, the stability of the system is enhanced compared to a FIR laser source used for conventional Schottky mixers. Furthermore, the frequency can be tuned in the range of 1780-1880 GHz.

5.2.1 Diplexer

The diplexer based on MPI (Martin Puplett Interferometer) was developed by SRON. It has actually the same mechanical construction as the ones used for HIFI (Herschel-Heterodyne Instrument for the Far-Infrared), but grid spacing and OPD (Optical Path Difference) were adapted for the 1.8 THz receiver. The path difference is 29.98 mm, when the moving mirror is in the initial position. The diplexer consists of two main parts, the main structure being a fixed part and the rotating substructure being a movable part. The rotating substructure is used to move the roof top mounted on one side of it. In order to move the rotating substructure, a magnetic actuator is applied. The magnetic actuator consists of two parts, a magnet of a loudspeaker motor fixed at the main structure and a motor coil (mounted to the opposite side of the roof top) fixed on the rotating substructure. By adjusting the voltage supplied to the loudspeaker motor, the position roof top can be controlled. As a result, the path difference can be adjusted. The rooftop angle is within the tolerance of ±0.5 arcmin.

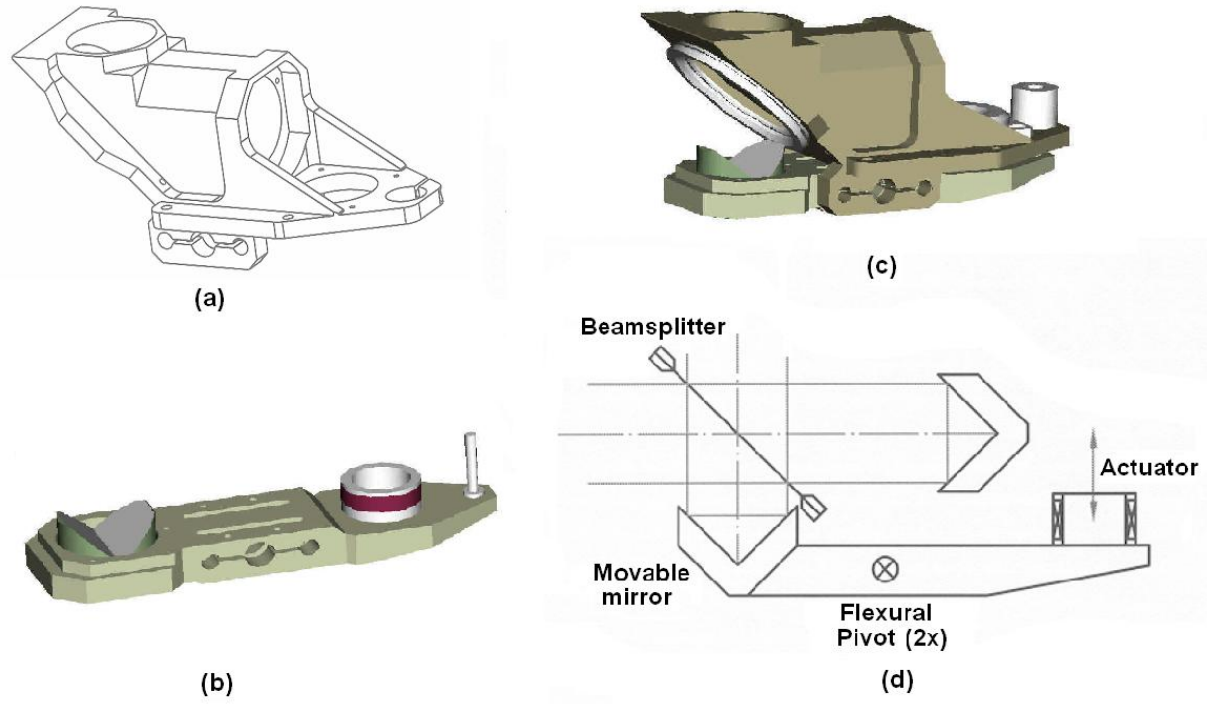

Figure 5-4 : (a) Main structure of a diplexer. On the right attachment holes for the LVDT body and motor body. One side of the clamps is shown at the bottom. (b) Rotating Substructure (c) 3D-Schematics of the complete diplexer. (d) Diplexer roof top optical mechanical configuration [Aalders, 2003]

The diplexer can be controlled in two modes, open- and closed-loop modes. In open loop control mode, only the bias of the actuator is adjusted but there is no feed back of the monitor signal. In contrast to the open loop control, the LVDT (Linear Variable Differential Transformer) is used in the closed loop control for detecting the current position of the roof mirror. The diplexer operated in the 1.8 THz channel is always controlled in the closed loop mode. By using this mode, the problem of the change of the roof mirror's position due to the vibration of the instrument can be neglected. However there are two disadvantages of using the closed loop control.

Firstly, the number of wires has to be increased due to the bias and communication with an LVDT. As a result, the power dissipation and the heat transfer to the optical bench (4 K) are also increased. Secondly, there is possibility of the electromagnetic interference. Further detail about diplexer characterization is in the chapter 6.

A LVDT is used for monitoring the position of the rooftop. In order to control the diplexer, a controller board communicating with the computer via RS485 is used. The inductance of the actuator is 110 mH and controlled by a 16 bit DAC (LTC1592). The DAC has to be set in the bipolar mode. A 24 bit data-stream is used for the communication at a clock frequency of 512 kHz. A digitally generated sine wave signal at a frequency from 1 kHz to 5 kHz with amplitude of 2 Volts is generated by the LVDT driver. The sine wave is generated by a 16 bit DAC (AD524BR) with 16 samples per period. The inductance at the primary coil of the LVDT (AC coupled) is 50 mH. The LVDT readout can be measured by the voltage sum/difference of two secondary coils of the LVDT. At the center position, the inductance is 70 mH.

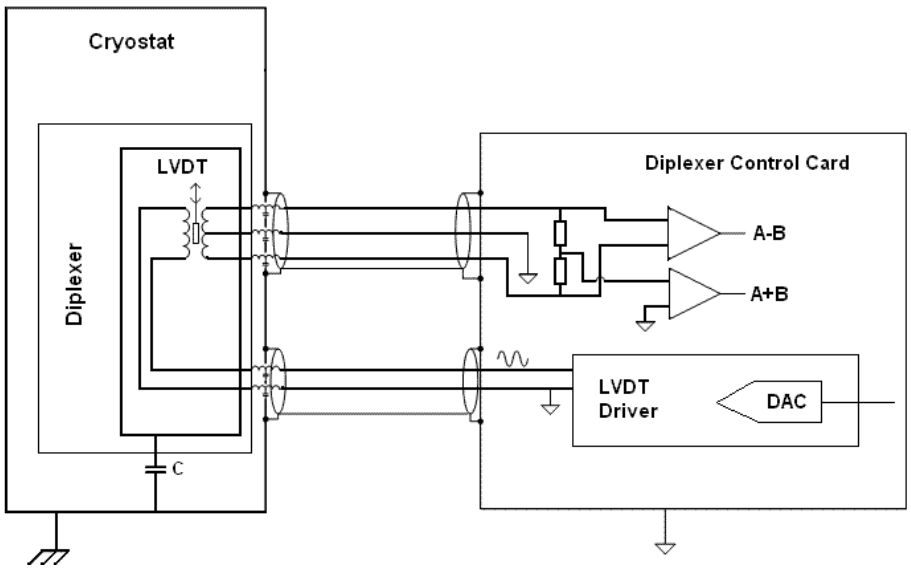

Figure 5-5: Schematic of the LVDT mounted with the diplexer. The LVDT consists of two secondary coils, "A-B" and "A+B". The voltage read out from both coils will be monitored and used to control the difference between the set point and the actual point. In closed loop control the motor coil will be automatically controlled by the LVDT position signal in order to maintain the setting position.

5.2.2 Mixer (Hot Electron Bolometer)

Phonon cooled HEB mixers with gold planar double slot antennas (DSA) were developed by Chalmers University of Technology. The antenna bandwidth of the mixer covers the RF frequency range from 1626 to 1910 GHz and the centre frequency lies at 1.8 THz. The mixer uses a quasi optic without mechanical tuning elements. The coupling to the optical beam is accomplished by a silicon lens. The mixer is designed to accept horizontally polarised radiation and its beam waist is 0.51 mm. The detector element is made of 3.5 nm thick niobium-nitride (NbN). The conversion of the mixer should be in the range of -10 to -20 dB. Actually the mixer used in the 1.8 THz channel has the same specification as the one developed for the HIFI instrument aboard the Herschel satellite having successfully launched in April 2009 [Graauw, et al., 2008],[Cherednichenko, et al., 2008]. Before it is delivered, the mixer noise temperature was tested at Chalmers University but it was tested with solid state LO at 1.6 THz instead of 1.8 THz. The measured mixer noise temperature is about 1500 K at IF output of 2 GHz and 2100 K at 4 GHz. The mixer was re-characterized at DLR by testing with the solid state LO at a frequency of 1.8 THz and the IF output range of 4-6 GHz.

The detail of the present characterization of the mixer and its performance used in TELIS flight module is in chapter 6. Figure 5-6 a. represents the HEB mixer unit. The silicon lens can be seen on the front of the mixer unit and connectors for a DC bias and an IF output are on the back side of the mixer unit. A large view of the detector is shown in Figure 5-6 b. The detector (HEB chip) is glued at the back of the silicon lens and is bonded to the IF board.

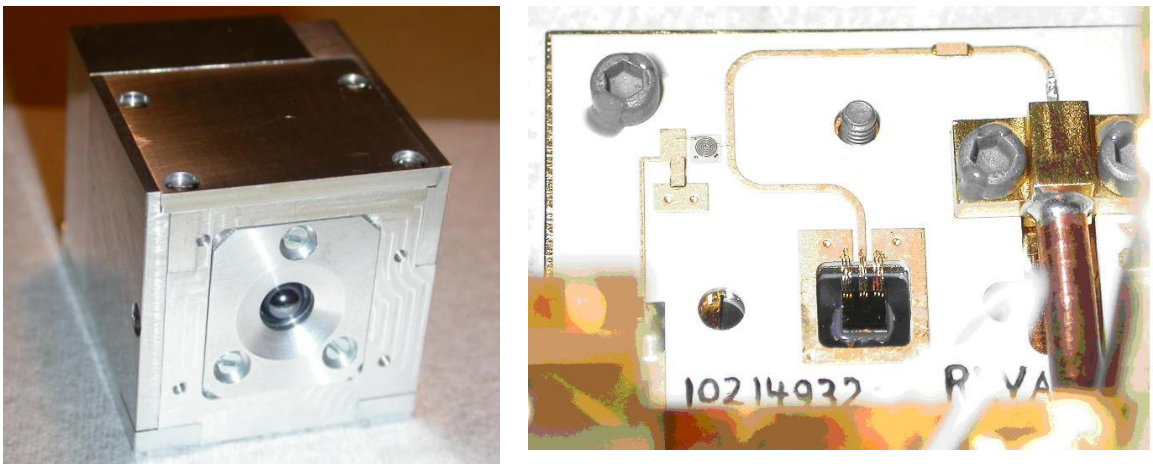

(a) (b)

Figure 5-6 : a) This picture shows a HEB mixer unit having the silicon lens on the front and the DC/IF connector are on the back of the mixer unit. b) A detector installed inside the mixer unit is shown at the middle of the picture. It is glued to the back of the silicon lens and bonded to the IF board. [Cherednichenko, et al., 2008]

5.2.3 Local Oscillator (LO)

The LO applied for the 1.8 THz channel is developed by RPG company. It is a solid state local oscillator being light weight. The output power of this solid state LO is in the

range of about 100 nW to 500 nW depending on the selected frequency. As shown in Figure 5-1 the input IF chain of the LO consists of two main parts; a set of multipliers and amplifiers mounted outside the cryostat under room temperature and a set of multipliers and its horn mounted on the optical bench inside cryostat. The solid state local oscillator is heat-sinked to a 77 K shield in order to reduce the LO power dissipation to the optical bench (4 K) as shown in Figure 5-7 (a). The warm part of the solid state oscillator and its bias supply is mounted outside the cryostat as shown in Figure 5-7 (b). The stability of the LO output power at the last state of the solid state oscillator (at 1.8 THz: 4 K) depends on the efficiency and the temperature of the LO's warm part. The upper limit temperature of the warm part of the local oscillator is 30°C.

More detail about the characterization of the solid state local oscillator will be shown in chapter 6.

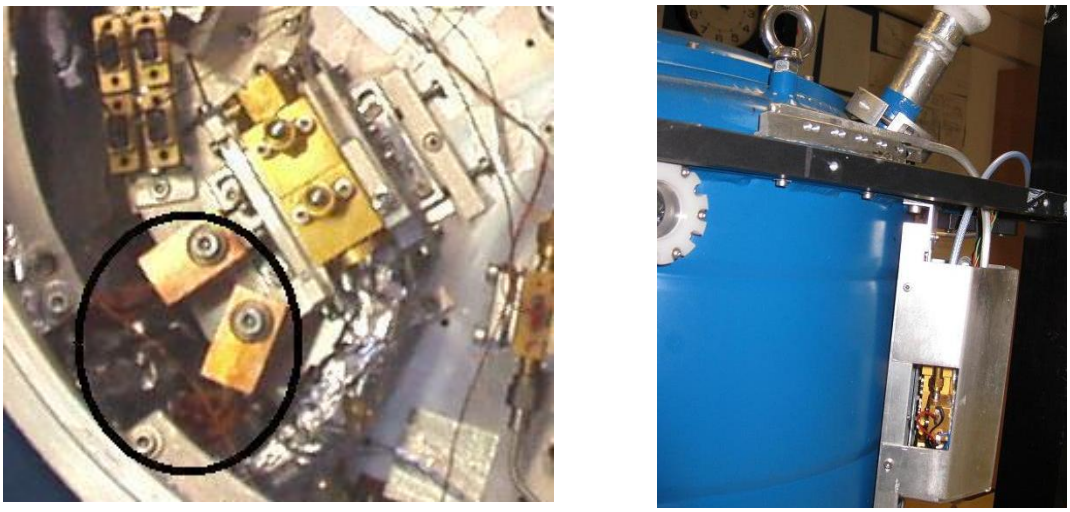

(a) (b)

Figure 5-7: a) A large view of the solid state local oscillator inside the TELIS cryostat and its heat sink interface to the 77 K shield of the cryostat (in the black circle). b) Warm part of the solid state oscillator mounted outside cryostat.

Part III

Development and characterization of the 1.8 THz channel, IF backend and the Autocorrelator spectrometer

6 Characterization of the 1.8 THz receiver

All devices operated in the 1.8 THz channel were firstly characterized individually before they were integrated together on the optical bench of the cryostat. All measurements for the characterization of individual devices were performed by using a test cryostat which is different to a flight cryostat. After that, the characterization of the 1.8 THz channel with completely integrated devices was carried out in order to determine the performance of the complete cryogenic channel. These characterizations of the cryogenic channel are shown in section 6.2.

The complete cryogenic channel on the optical bench was also firstly characterized by using a test cryostat. The whole optical bench having integrated with all cryogenic devices on it was then migrated into the flight module cryostat and re-characterized again. The characterization of the IF backend consisting of the IF chain (IF amplifiers, directional couples, RF detectors etc) and Autocorrelator spectrometer, will be discussed separately in the section 6.3.

6.1 Characterization of individual devices of the 1.8 THz channel

6.1.1 Window, blocking filter and polarizer:

The input IR signal transmitted into the cryogenic 1.8 THz channel is mainly attenuated by a vacuum cryostat window and a blocking filter. Therefore the selection of the material used for both components is considered. Two Zitex sheets (porous Teflon) are used as a blocking filter instead of an antireflection coated crystal quartz from Infrared Labs Inc. which had been used in the prototype tested in 2005 [Mair, 2007]. The crystal quartz blocking filter (ϕ 30mm.) has about 32% loss which is worse than the Zitex blocking filter. By using the Zitex sheet the loss is about 50% less. A wire grid polarizer [QMC Instruments, 2008] (Photolithographic Polarisers,[Auton,1967]) applied as a beam splitter on the optical bench (4 K) has a loss of about 1.3% (see Figure 5-3)

Cryogenic Window:

The cryostat window is made of the X-cut quartz material with antireflection coating (Parylene, [Parylene Engineering, 2009]) used for reducing the reflection loss. It has a diameter of 34 mm and a thickness of 1.5 mm. Cryogenic window transmission is measured at DLR by a FT-IR spectrometer (Bruker). Figure 6-1 shows transmission of the cryogenic window. The transmission in the frequency region of 1.8 THz is about 90%.

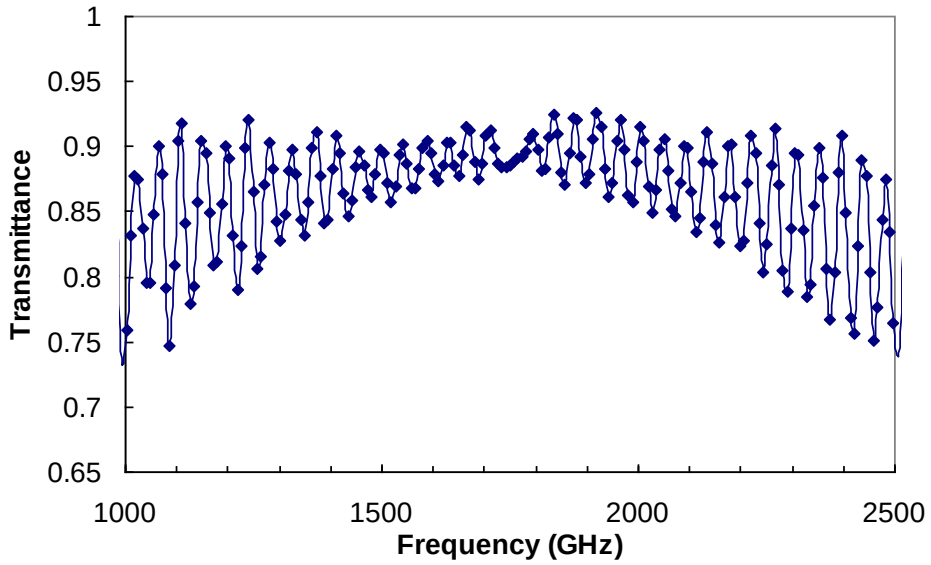

Figure 6-1: Transmittance of the cryogenic window.

Blocking filter:

A *blocking filter*[18] is used to block the unwanted IR radiation loading on cold optical elements. The Zitex sheet is used as a blocking filter because it can efficiently block the unwanted IR radiation while allowing the desired wavelengths to pass un-attenuated [Hunter, et al., 1996], [Kooi, et al., 1995]. Zitex is a porous Teflon sheet like a filter paper. It is an effective IR blocking filter with 1% transmission in 1-50 μm range while attenuating ≤ 10% at wavelengths longer than 200 μm. Moreover, Zitex has extremely low dielectric reflection losses (refractive index ca. 1.3). As a result, Zitex is a good choice as IR blocking filter in low-noise heterodyne receivers [Benford, et al., 1999], [Dominic, et al., 2003].

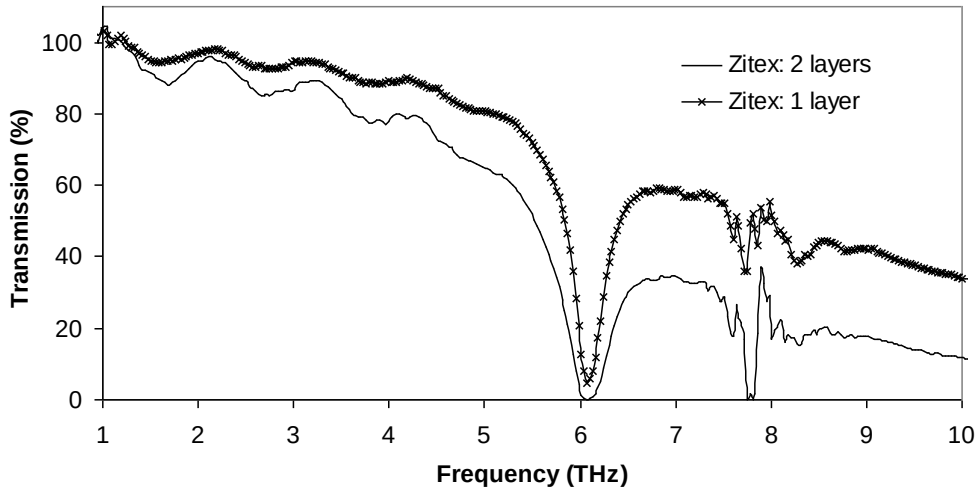

Figure 6-2: A comparison of the transmission of Zitex G104, one layer and double layers , across a frequency range from 1 to 10 THz. Transmission losses of the double layers at 1.8 THz is about 14%. (The measurement data is courtesy of L. de Jong, SRON).

[18] A blocking filter is sometimes called a heat filter.

The 1.8 THz channel uses two sheets of Zitex G104 (double layers) as a blocking filter. Each of them has about 7% loss (~0.3 dB) as illustrated in Figure 6-2. Double layers are used to reduce heat load. As a result the holding time of the cryostat can be extended and an undesired heating of the HEB above its transition temperature can be avoided. The diameter of the double layer Zitex is 20 mm. They are mounted on the 77 K (liquid nitrogen) radiation shield. Figure 6-2 shows the transmission of Zitex in the FIR range.

Polarizer:

Wire girds of the polarizer applied in the 1.8 THz channel are vertically tilted because it has to reflect the vertically polarized beam emitted from the LO while transmitting the horizontally polarized beam of the signal. The polarizer was tested at DLR with the FIR laser at 1.6 THz as shown in Figure 6-3. The transmission was obtained by measurements with and without the polarizer to be tested. The wire grid 1 was rotated with respect to the polarization plane to couple out about 10% for stabilizing the CO_2 laser. The wire grid 2 was used to adjust the FIR power and to select the polarisation. An Ecosorb sheet with an aperture of 1.5 mm was placed before the tested polarizer in order to simulate the real beam waist at the input of the polarizer (as it should be in the flight setup) while the Ecosorb was also used as an absorber to absorb an unwanted reflections. The transmitted power measured at Pyrometer 2 is about 98.7%.

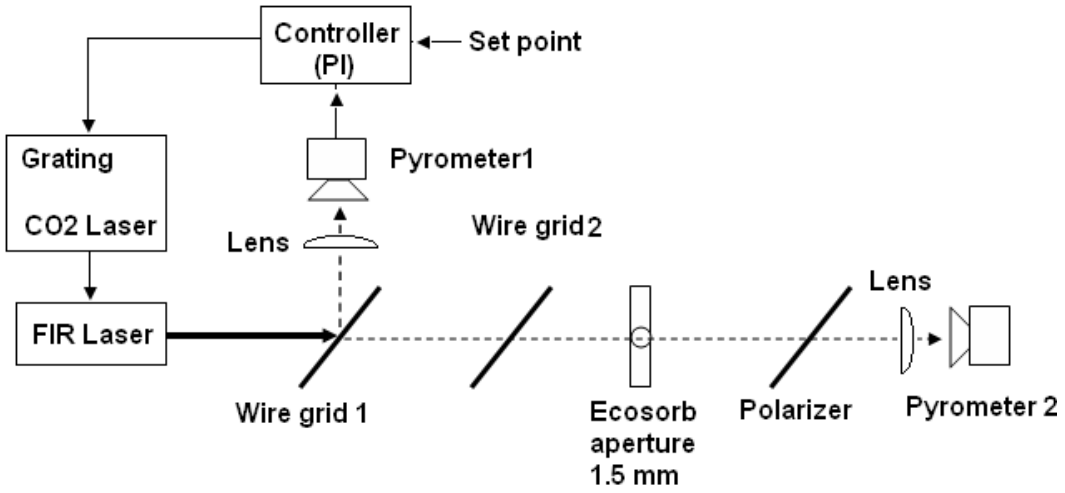

Figure 6-3: Measurement Setup for the polarizer's transmission test. The controller uses the so called "PI (proportional- Integral control)" technique.

6.1.2 Hot Electron Bolometer (HEB)

A copy of the HIFI flight model HEB developed by Chalmers University was selected to use as a mixer in the 1.8 THz receiver. The Chalmers HEB had good noise temperature, less antenna beam side lobes and a flatter IF bandwidth.

The mixer noise performance is specified in terms of a DSB noise temperature. This noise temperature can be measured by the Y-factor method (chapter 3.2.2) using room

temperature (300 K) and liquid nitrogen (77 K) cooled blackbody loads. Although the HEB mixer was tested at Chalmers University before delivery (by using the FIR laser at 1.6 THz and the solid state LO 1.5 THz), the DSB noise temperature had to be determined at DLR. The measurement was carried out by using the FIR laser at 1.6 THz and a flat mirror instead of the diplexer in the setup in Figure 5-3 (chapter 5.2).

The HEB was mounted on a holder and connected to the same cryogenic IF-chain as in the flight module cryostat. The IF semi-rigid cable connected to the IF output of the HEB is a copper semi-rigid cable with 0.75 cm diameter. The copper semi-rigid was selected because of its low attenuation while its higher diameter provides a better EMI shielding.

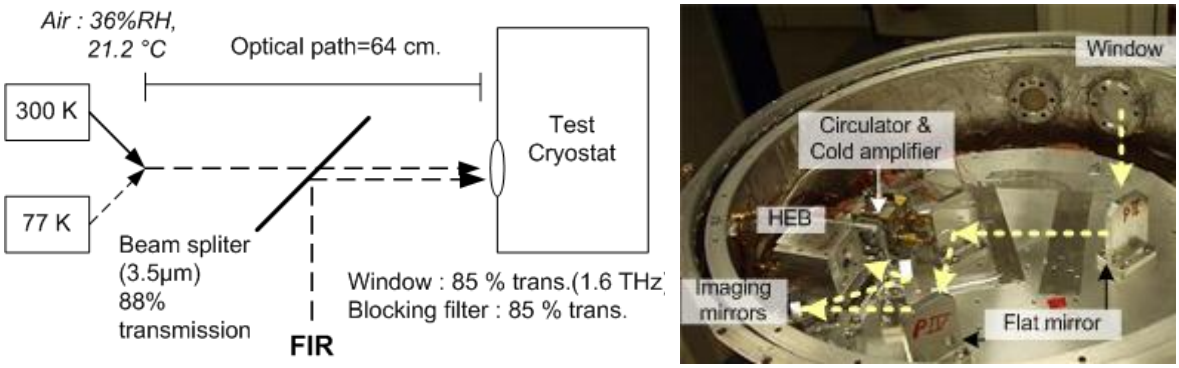

(a) (b)

Figure 6-4: a) The optical path, the setup for the measurement of the DSB noise temperature discrepancy and the optical losses are shown in the schematics. b) The setup inside the test cryostat is shown in the picture.

Two sheets of Zitex as blocking filter, having an attenuation of about 14.8% (0.6 dB) were mounted on the 77 K radiation shield. A 3.5 µm-beam splitter (milar) was used to couple the signal and LO beam into the test cryostat and it has a transmission of ~88%.

To calculate the water vapour absorption in the optical path, the relative humidity and temperature were measured. The total losses were determined to be about 67%. They consist of 20% loss from the water vapour in the optical path, 12% (at 300K) loss from the beam splitter, 15% loss of the Zitex blocking filter and 15% of the beam transmission losses by the window (at 1.6 THz). The IF-output from the cryogenic channel was connected to an autocorrelator spectrometer and a power meter. By using the Y-factor method, the noise temperature spectrum can be determined. Comparison of the HEB noise temperature measured at the Chalmers University and one measured at DLR are depicted in Figure 6-5. All spectra are corrected for all possible losses in the system. The noise temperature (NT) measured by the power meter is an averaged noise temperature from 10 individual noise temperature measurements. The NT spectrum measured by the ACS is averaged from 20 NT spectra.

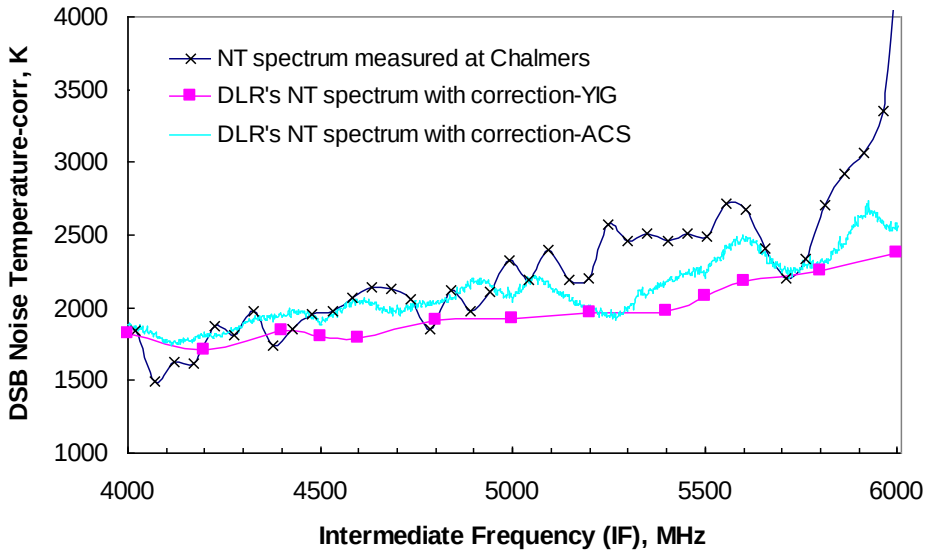

Figure 6-5: Comparison of the DSB noise temperature measured at the Chalmers University, the one measured at DLR by a power meter (using a YIG filter) and the one measured at DLR by a autocorrelator spectrometer (ACS). The FIR laser at 1.6 THz was used for the measurement. All spectra are corrected for the total losses in the system.

6.1.3 Local Oscillator Characterization

After the delivery of the solid state oscillator from RPG company, the LO output power with respect to its frequency was measured. The goal of this measurement is to observe the suitable frequency region which can be used to pump the HEB device. The LO power required to pump a HEB is dependent on the volume and thickness of its NbN film and for the device used for TELIS around 200 nW was required [Cherednichenko, 2007].

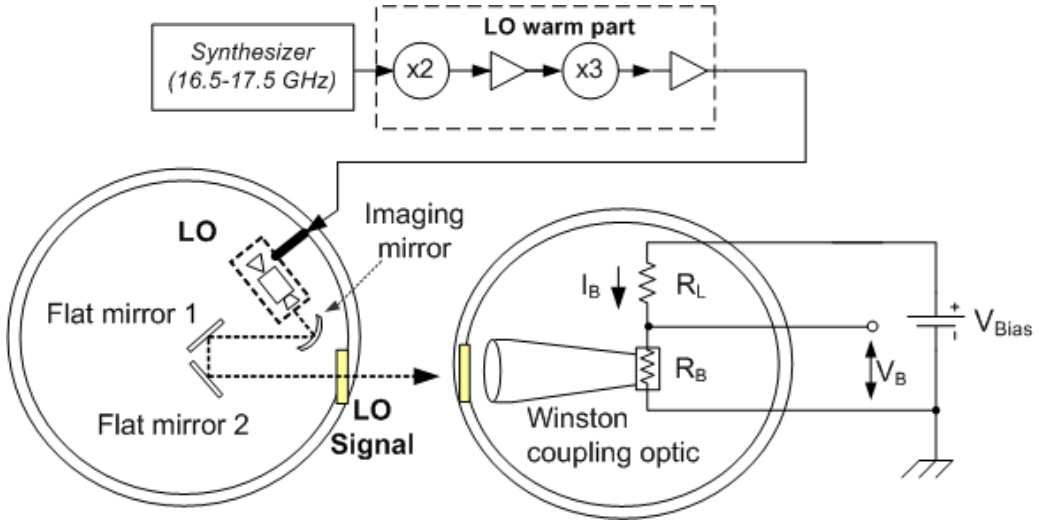

Figure 6-6 : The measurement setup for measuring the LO power spectrum on the THz channel optical bench in the test cryostat. A commercial helium cooled bolometer was used for power detection. The LO frequency was tuned from 1782 to 1890 GHz and the bolometer signal measured.

The output power of the LO was measured by pointing the LO beam to a bolometer and measuring the output absolute power. The measurement setup is depicted in Figure 6-6.

The optical bench was designed in such a way that one can turn the polarizer by 90° (horizontal direction counter clockwise, (see Figure 6-6) which can reflect the LO radiation through the cryostat window to outside the cryostat. The position of the solid state LO is aligned in the way that the LO beam profile (measured by FIR gas Laser) and the one measured from the solid state LO is on top of each other. As the result, the couple efficiency between LO and HEB is more than 90%.

The 4.2 K-Bolometer with a Winston cone optic [Infrared Laboratories, 1980] was used to measure the detected LO power. The voltage across the bolometer (V_B) was measured in this experiment and the current of bolometer (I_B) which is proportional to the voltage across R_L can be easily determined as follows:-

$$I_B = \frac{V_{bias} - V_B}{R_L} \qquad \textbf{eq. 6-1}$$

The LO power can be determined from the bolometer signal by calibration with 77/300 K Ecosorb blackbodies and corrected for all losses in the test cryostat consisting of 10% losses at the window, 15% losses at the Zitex blocking filter. The coupling efficiency of the LO beam into the Winston cone was estimated to be about 0.5. The result of the measurement is shown in Figure 6-7. The optimum LO power required to pump the HEB mixer is about 200 nW. Regions were the HEB power is larger than 200 nW are still valid since the LO power can be decreased by adjusting the gate voltage of the 33 GHz amplifier as described in Figure 6-18 (chapter 6.2.1.1).

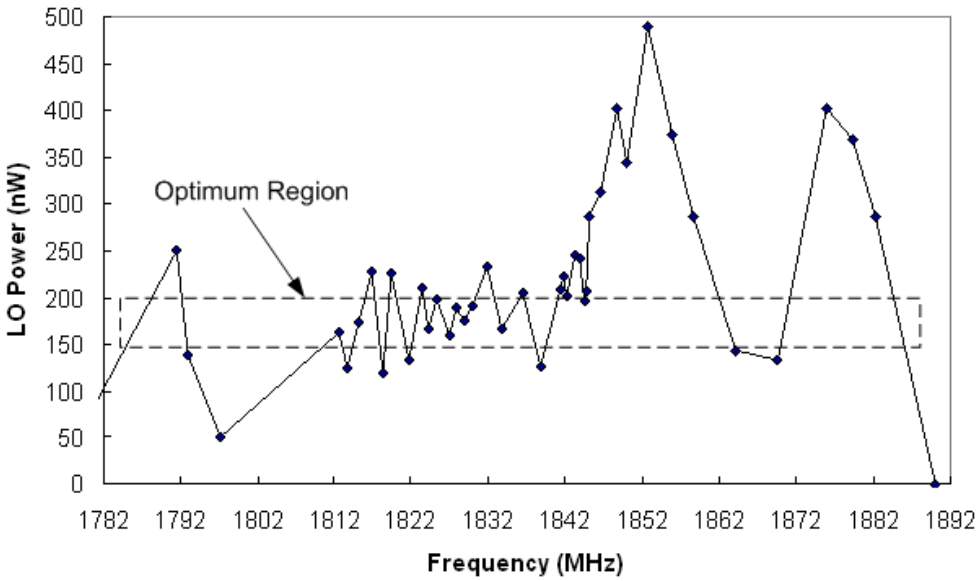

Figure 6-7: Measured LO output power as a function of frequency. The optimum region for operation of the TELIS HEB mixer is shown in this figure.

During the measurement for convenience a lab synthesizer was used instead of the TELIS synthesizer to drive the warm part of the LO for convenience. The TELIS synthesizer delivered in 2008 has very low spurious (<70dBc) noise. It provides an RF output frequency from 16520 MHz to 17370 MHz with a step size of 2 kHz. The synthesizer power output lies in the range of 10.6 dBm to 12.2 dBm.

6.1.4 Diplexer Characterization

In this section, the discussion will start with determining the leakage of the diplexer which was firstly done after the delivery to figure out the coupling efficiency of the diplexer. The diplexer misalignment being an important issue for the change of the side band ratio will be then further discussed. In the discussion of the diplexer misalignment, accuracy and repeatability of the diplexer control including the calibration error will be described. All diplexer characterisations were done at helium temperature (around 4 K).

6.1.4.1 Leakage of the diplexer:

With increasing diplexer losses, the sensitivity of the heterodyne receiver (the system noise temperature) decreases. The leakage of the diplexer was firstly tested by using the FIR laser (1.6 THz) due to the delay of the LO. The leakage was re-measured again later with the solid state local oscillator (1.8 THz).

Since the resistivity of the HEB mixer changes with the change of the DC bias and the incident radiation, by fixing the bias voltage applied to the HEB, the change of the LO power pumped on the HEB mixer can be easily measured by monitoring the HEB current. However due to the instability of HEB bias at under-pumped condition, the bias of HEB must be increased to 2 mV and assumed to be linear as shown in Figure 6-8.

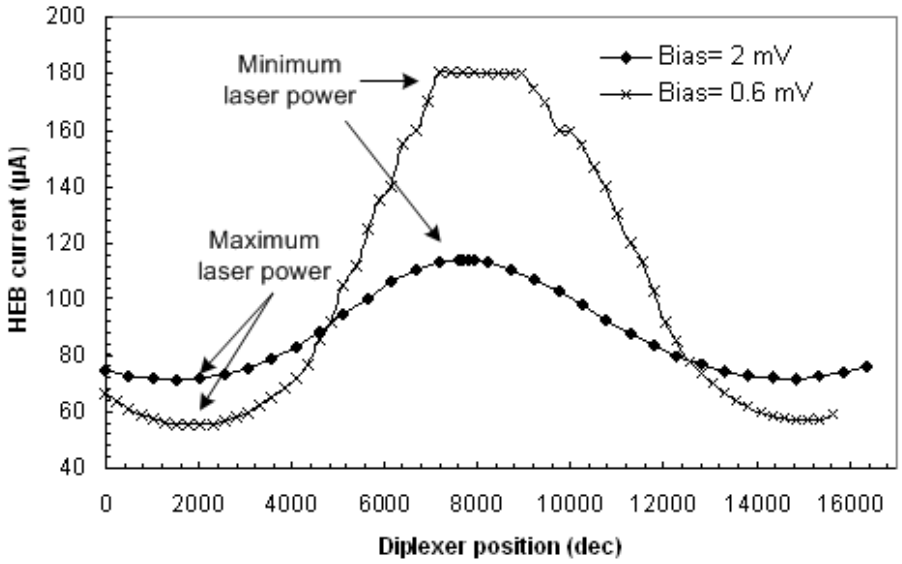

Figure 6-8: HEB current proportional to the LO power at two different HEB bias setting were measured and plotted on top of each other.

To determine the leakage of the diplexer, the diplexer was at first set to the position yielding the null laser power (= maximum HEB current). The readout of the HEB current with one second integration time during the measurement was very stable and repeatable. The HEB current was 114.4 µA after placing the Ecosorb to block the laser window (= no laser power coupled to the HEB mixer) which was 114.1 µA without Ecosorb. This gives 0.3 µA difference while the difference of the minimum and maximum HEB current was 42.2 µA. Thus the leakage in percentage of the diplexer is 0.7%.

The LO frequency in the measurement in Figure 6-8 was set at 1.6 THz (FIR laser). In Teresina before the flight, the leakage was re-measured at the LO frequency 1820.698 GHz and the leakage was about 0.8% which is coincided with the one measured in the laboratory with FIR laser.

6.1.4.2 Influence of diplexer misalignment on side band ratio:

The diplexer applied in the 1.8 THz channel is based on a Martin-Puplett interferometer as discussed in chapter 3. In order to couple the available input signal and LO into the mixer as efficient as possible, the optical path difference must be set correctly. At the output of the diplexer, the transmission with parallels (I_{Π}) and orthogonal ($I_{\perp}$) polarization can be determined as follows:-

$$I_{\Pi} = \frac{1}{2}\left(1+\cos\left(\frac{2\pi\Delta}{\lambda}\right)\right) \qquad \textbf{eq. 6-2}$$

$$I_{\perp} = \frac{1}{2}\left(1-\cos\left(\frac{2\pi\Delta}{\lambda}\right)\right) \qquad \textbf{eq. 6-3}$$

The partition in the output power depends on the wavelength (λ) and the optical path difference (Δ), whereas the smallest value of the optical path difference in case of $\lambda_{LO} << \lambda_{IF}$ is shown in eq.6-3.

$$\Delta \approx \frac{\lambda_{IF}}{2} \qquad \textbf{eq. 6-4}$$

$$\Delta = \lambda_{LO} \cdot m \qquad \textbf{eq. 6-5}$$

where m is an order of LO and it is an integer number. The LO used with the 1.8 THz channel is tuneable and the order of the LO depends on the selected λ_{LO}. The path difference (Δ) at the IF frequency 5 GHz (λ_{IF} = 5.99585 cm) is 2.9979 cm. Thus, at LO frequency of 1832.36796 GHz, the order should be 183.

The diplexer applied to the 1.8 THz channel can be adjusted to the maximum transmission with an uncertainty of about 60 decimal units, which yields of about 2% change in the sideband ratio at the margins of the detected spectral interval, whereas there is no change of the ratio at the centre frequency as shown in Figure 6-9.

The error of the diplexer adjustment comes from the accuracy and repeatability of the diplexer control and the error of the diplexer calibration function in which they will be further discussed.

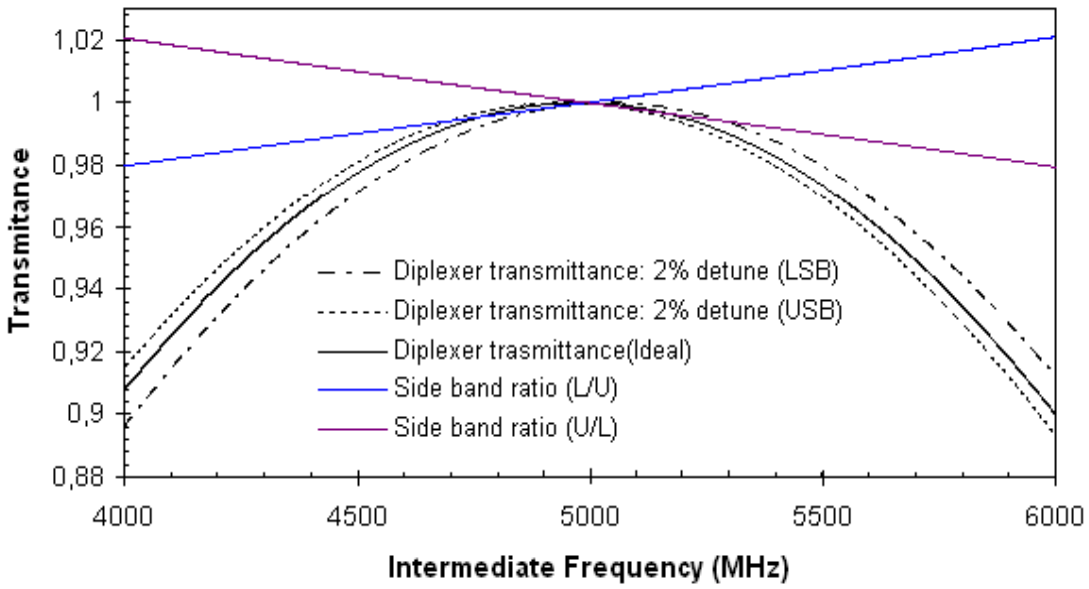

Figure 6-9: Effect of the diplexer misalignment by 2% on the side band ratio (at the edge). The LO frequency was set at 1830.3679 GHz.

6.1.4.3 Accuracy and Repeatability of the closed loop control of the diplexer.

Both accuracy and repeatability are taken from the measured data on 05.12.2007-13.12.2007. One important device which influences the accuracy and repeatability of the diplexer control is the LVDT applied as a sensor to monitor the position of the rooftop (see also chapter 5.2.1).

The readout from both LVDT coils consists of two digitized numbers related to the bias output of both secondary coils ("A-B" and "A+B") as described in Figure 5-5, chapter 5.2.1 and the ratio between both secondary coils of the LVDT (A-B/A+B) was used to calculate the read out of the diplexer position by means of a linear fit as shown in Figure 6-10.

Accuracy of the closed loop control of the diplexer:

Accuracy is defined as the difference between the actual readout and the set value. Due to the *hysteresis*[19] of the LVDT when moving forward and backward, the mean value calculated from the readout in both directions for each point is applied in the linear fit to determine the slope and the offset. The scan was done with step sizes of 256 decimal units and starts from 0 to 30000.

The slope and offset of the linear fit of the measured data was used later to interpret the readout from two secondary coils. To determine the accuracy of the closed loop control of the diplexer, the difference between the fitted readout and the setting was calculated.

[19] The hysteresis in this test was already considered inertia and readout from both secondary coils of the LVDT was done while the movement of the rooftop was expected to be stabilized.

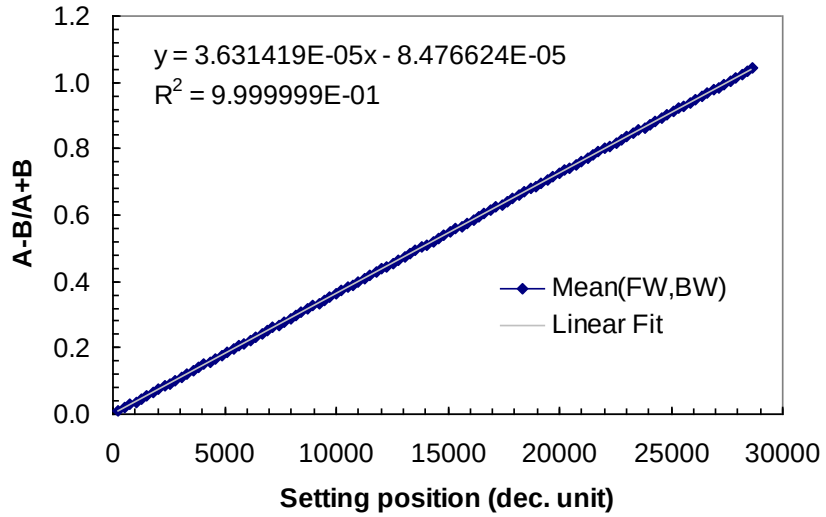

Figure 6-10: shows the linear fit of the read out from the LVDT. X-axis is the setting position set to the diplexer in decimal unit. Y-axis is a ratio between the readout of both secondary coils of the LVDT (A-B/A+B). Due to the hysteresis of the LVDT, the mean value between readouts in forward and that in backward direction was used for fitting.

Figure 6-11 shows the accuracy in decimal units of each diplexer setting from 0 to 30000 with step sizes of 256 decimal units. The deviation from the set position at the first 10000 decimal units (see region A in Figure 6-11) shows obviously a large deviation, so that this region should be avoided for diplexer operation.

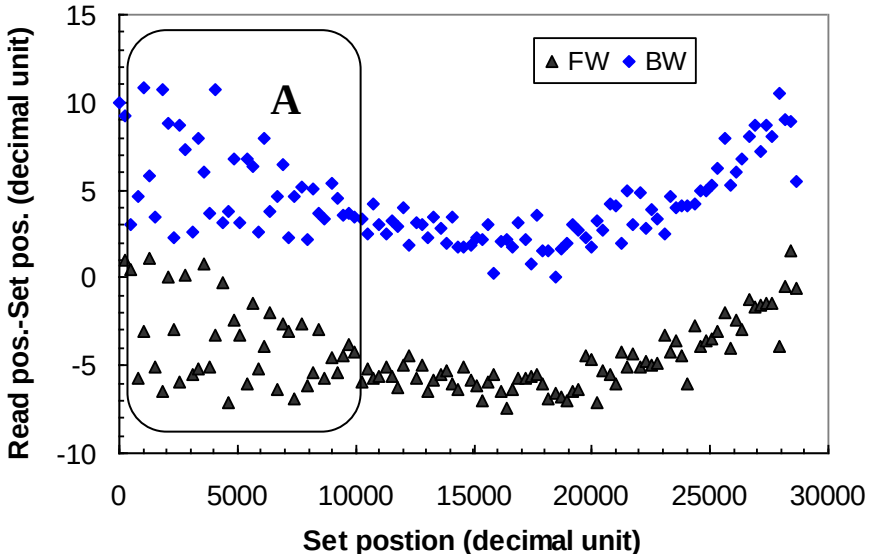

Figure 6-11: shows the accuracy of the closed loop control of the diplexer from 25 measurements. The plot shows the accuracy of each point with a step size of 256 decimal units in forward and backward direction. The accuracy is determined by means of the difference between the fitted readout from the LVDT and the set position. "A" is a region where large deviation from the set value and instability occurs.

Repeatability of the closed loop control of the diplexer:

Repeatability is defined as the difference between the largest deviation from the mean and the average of all data points (25 points) measured at the same position. It is useful for our application to define the repeatability in decimal units more than a percentage of reading because percentage of reading leads to misinterpret at the higher decimal number of the setting. Figure 6-12 shows the repeatability of two set positions at 10496 and 19712 decimal units measured 25 times in forward direction.

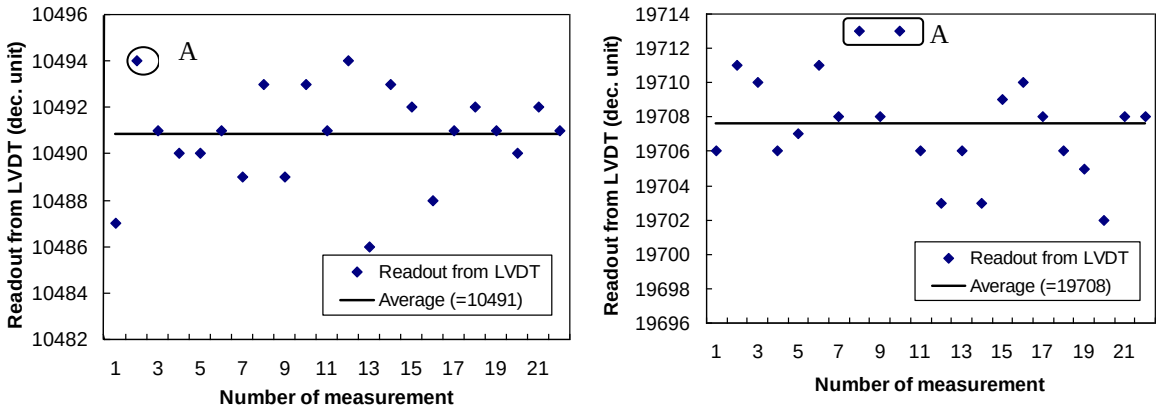

(a) (b)

Figure 6-12: Both plots are comparisons of the readout data from LVDT and the average value in two different diplexer settings. (a) The set position was at 10496 where the accuracy is -5 decimal units from the set position and the repeatability is +/- 3 decimal units. (b) The set position was at 19712, where the accuracy is -4 decimal units from the set position and the repeatability it +/- 5 decimal units. "A" is the maximum deviation from the mean value in which it is 10494 for (a) and 19713 for (b).

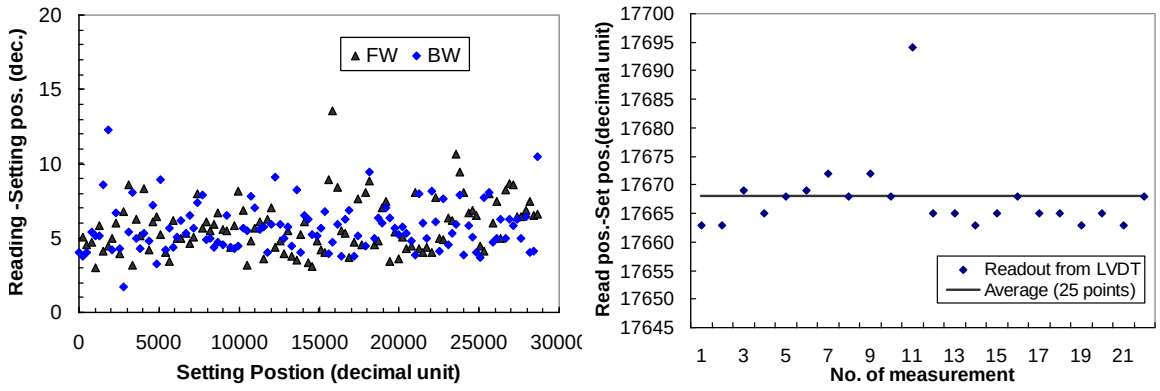

(a) (b)

Figure 6-13: (a) shows the repeatability of the diplexer setting from 0 to 30000 decimal units in the range of ±15 decimal units. (b) shows an occasionally largest deviation of one data point measured at 17664 at one setting position from 25 measurements.

A comparison of the repeatability from 0 to 30000 with a step size of 256 decimal units in forward direction and the one in backward direction are presented in Figure 6-13 (a). The worse repeatability for the whole range (0 to 30000) should be at about ± 15 decimal units. However there was occasionally one data point at 17664 having a larger deviation from the average value as shown in Figure 6-13 (b). Its deviation from the mean value is 30 decimal units.

In summary, it can be concluded that the accuracy of the diplexer setting is in the range of ±15 decimal units corresponding to 20.64 µm path difference change, and the repeatability is ±15 decimal units. It should be considered that the accuracy and repeatability were determined by using the readouts from the LVDT and with the assumption that the LVDT is reliable.

6.1.4.4 Diplexer Calibration

Method used to determine the setting of the diplexer:

To figure out the relationship between the optical path difference and the digital setting of the diplexer, LO radiation was coupled into the HEB mixer. However there are two individual parameters that can be used to detect the change of the LO power due to the change of the optical path difference of the diplexer: firstly the HEB current and secondly the HEB IF-output.

Although the accuracy of the HEB current reading is sufficient for measuring the leakage of the diplexer, it is too noisy to use it for determining the best adjustment of the diplexer. Furthermore the HEB current is sensitive to the standing wave in the cold optics (between the LO and the HEB mixer) which causes an asymmetric shape as shown in Figure 6-14.

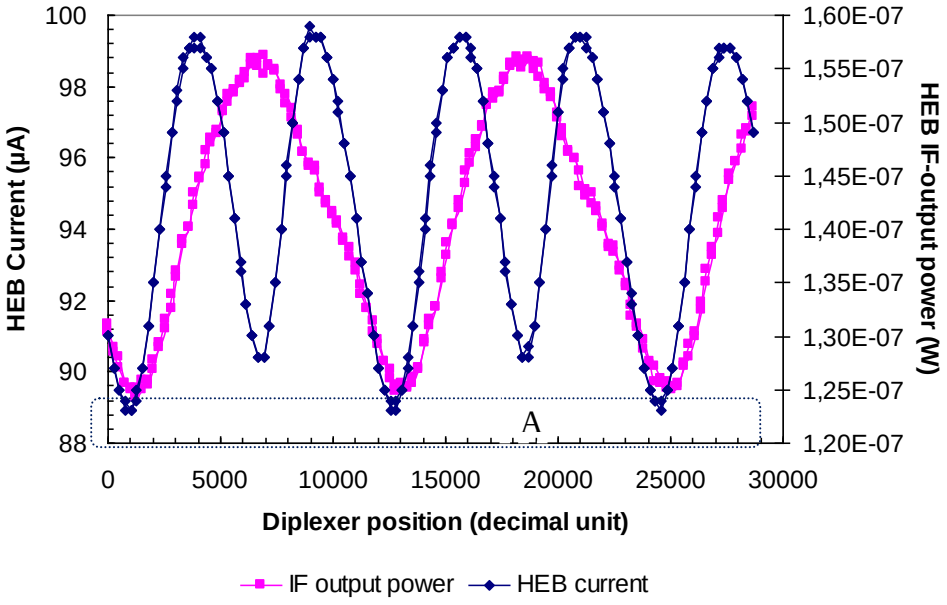

Figure 6-14: A comparison of the HEB current against the diplexer setting and the IF output power of the HEB against the diplexer setting. The measurement was done while the LO was set at a frequency of 1836.316 GHz and the HEB bias was set at 3 mV.

Figure 6-14 shows the relationship between the optical path differences, HEB current and HEB IF-output power. The optical path difference of the diplexer was tuned from 0 to 3000 decimal units while the HEB current and the IF output were recorded. The measured IF-output from the HEB mixer is obviously more stable and symmetric.

Even though the standing wave in the cold optics depending on the LO frequency affects the feature of the IF output, it still shows a symmetric feature. Thus, the HEB IF-output power is a well suited for determining the best adjustment for the diplexer.

The IF power dissipated in the matched load R_L (input impedance of the cold amplifier) can be determined by $P_{IF} = V_{IF}^2(\omega,t)/4R_L$ where $V_{IF}^2(\omega,t) = S(\omega_{IF}) \cdot 2\sqrt{P_{LO}P_S}\cos\omega_{IF}t$ (see chapter 3.4). Thus, the IF power is a function of the LO power level and the HEB mixer's responsivity ($S\omega_{IF}$) [Baubert, et al., 2003], [Ekström, et al., 1995]. The IF power decreases when the LO power increases above the optimal LO power level required by the HEB mixer. Thus, at the maximum LO power, the IF power is smallest as illustrated in Figure 6-14 [A].

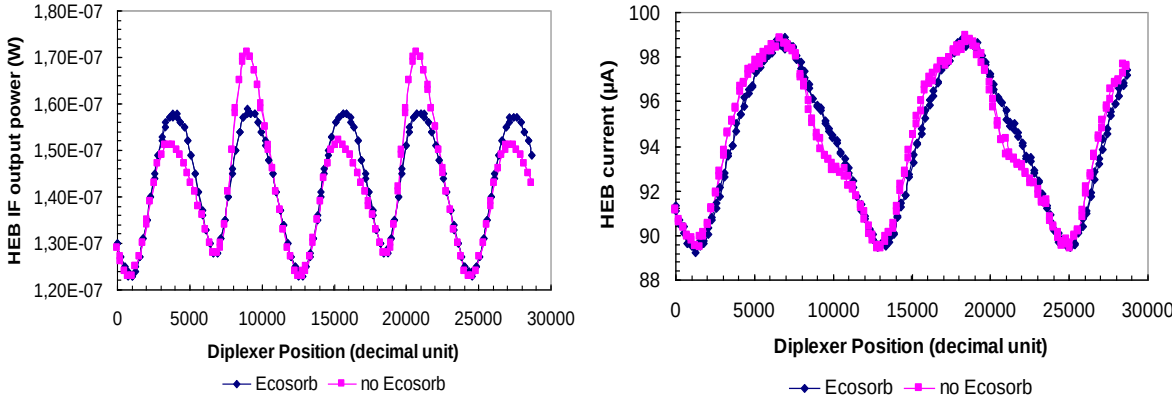

(a) (b)

Figure 6-15 : Fabry-Perot effect between cold and warm optics which modulates the incident LO power and changes the IF output. Ecosorb was used in front of the window of the cryostat to decrease standing wave effects. (a) depicts the effect on the HEB IF output power and (b) shows the Fabry-Perot effect on the HEB current.

Another important effect to be considered is the Fabry-Perot effect between cold optics and warm optics because it causes the modulation on the incident LO radiation fed to the HEB mixer. As a result, the IF output changes. In this case, placing the Ecosorb in front of the cryostat could help to decrease the standing wave between the cold and warm optics as shown in Figure 6-15. Nevertheless, the minimum of the curve corresponding to the best adjustment for the diplexer doesn't change and is symmetric. By fitting the curve, the accurate minimum of the curve can be determined.

However one single diplexer scan takes time, so that scanning the diplexer at all LO frequencies during the THz characterization (see Parameter surface in 6.2.1) would take hours. Hence a method to predict the best adjustment for the diplexer was developed and will be referred to as the *diplexer calibration function*.

Diplexer calibration function:

To calibrate the diplexer, the best fitted minima from diplexer scans (HEB IF-output power against the OPD of the diplexer) in both forward and backward directions at different LO pumped frequencies are required. Each scan with a step size of 256 decimal units was firstly done close to the minimum of the diplexer curve as shown in Figure 6-16 (a) in order to reduce the scanning time.

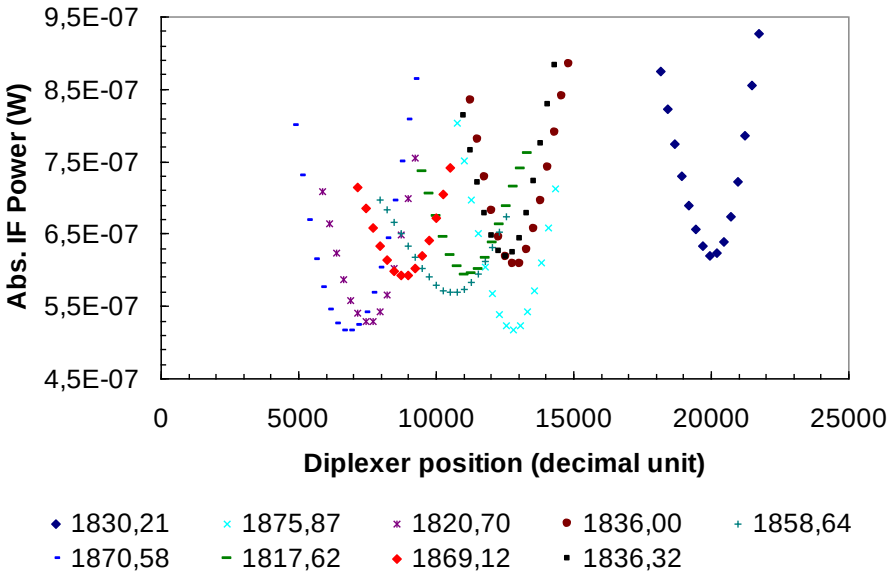

(a)

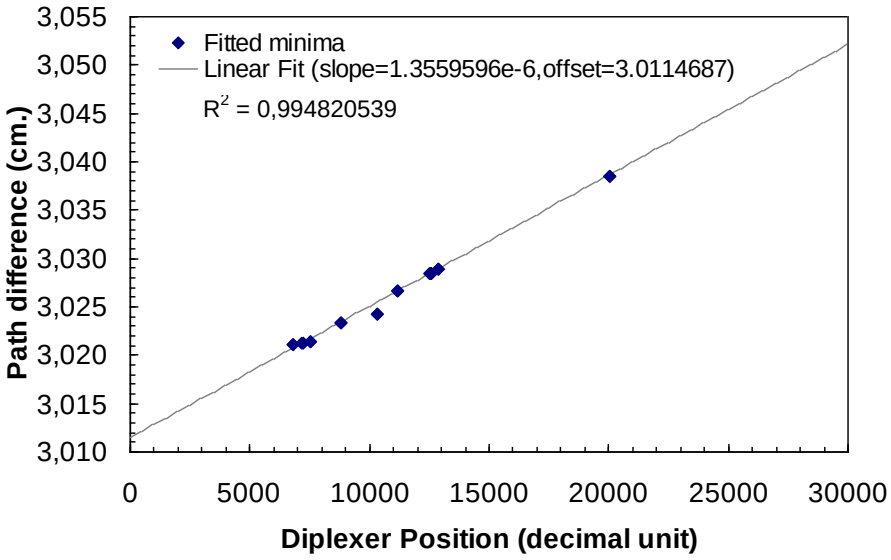

(b)

Figure 6-16: (a) the graph shows diplexer curves (HEB IF-output power against the OPD of the diplexer) at different LO pumped frequencies. (b)Y-axis: the calculated path difference of the total power of the minimum of the diplexer curve; X-axis: the diplexer position in decimal units. Fourteen fitted minima (Newton-Raphson) were used to determine the slope and offset of the linear fit. Both plots use measured data on 05.12.2007

Next, the diplexer curves were fitted with 4th order polynomial and the minimum of each curve was determined by means of the Newton-Raphson method [Ortega, et al., 2000]. The offset and slope of the linear fit were calculated by applying all fitted minima in the first order polynomial as shown in Figure 6-16 (b). The calibration function [Birk, et al., 2008] was firstly developed by using the measured data on 05.12.2007.

The LVDT readout as discussed in 6.1.4.3 shows a repeatability of ±15 decimal units; thus, at the beginning of implementing the diplexer calibration function, set positions were used for the fitting. A decimal number used for setting the diplexer is determined as shown in eq. 6-6.

$$dec\_pos = \frac{(m + 0.5) * \lambda_{LO} - offset}{slope} \qquad \textbf{eq. 6-6}$$

where ***dec_pos*** is a decimal number used to adjust the diplexer corresponding to the best adjustment of the OPD of the diplexer at that LO frequency. ***m*** represents a mode (integer number) $\boldsymbol{\lambda_{LO}}$ is the wavelength of the LO frequency.

The term, (m+0.5)*$\boldsymbol{\lambda_{LO}}$, yields the path difference of the total power minimum. The zero path difference corresponds to the maximum power of the diplexer curve whereas the 0.5 lambda (=90° phase shift) is the minimum power of the curve. With this calibration function the best setting for the diplexer in decimal units can be calculated by using only a known LO wavelength and its correct mode.

Estimated error of the diplexer calibration function:

To estimate the error of the diplexer calibration function, the residuals of the 4th order polynomial were observed as a quality check in which the calculated total power from the 4th order polynomial was compared with the measured total power retrieved from the power meter, yielding a difference of about ± 0.6%.

The further error estimation is the difference between the minimum of the diplexer curve calculated from the 4th order polynomial of the measured data and the one calculated from eq. 6-6 which yields an error of about ±30 decimal units.

Diplexer in different cooling cycles:

Another consideration for the diplexer characterization is the repeatability of the diplexer setting in different cooling cycles. The minima of the diplexer curve were found to be shifted in different cooling cycles as shown in Figure 6-17. The first assumption for the minimum shift is due to the aging of the LVDT. Thus, the diplexer has to be re-calibrated in every cooling cycle before operating the 1.8 THz channel.

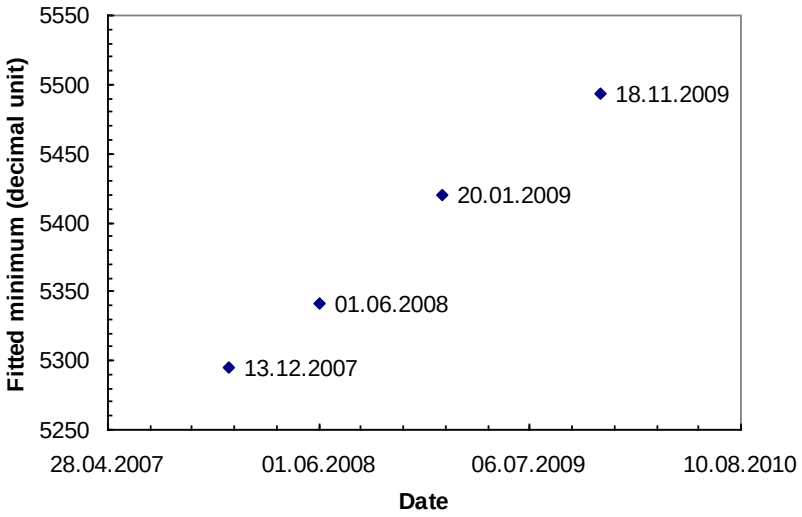

Figure 6-17: shows the shift of the minimum in different cooling cycles. All diplexer calibration functions use the measured data retrieved from the power meter.

Summarization of the diplexer characterization:

The accuracy of the diplexer setting is in the range of ±15 decimal units while the repeatability is ±15 decimal units (20.64 µm path difference change). The leakage of the diplexer (at 1.8 THz) measured in Teresina is about 0.8%. The error estimation for the diplexer calibration function by making use of the measurement data on 5-13.12.2007 is about ±30 decimal units (41.26 µm path difference change).

In the same cooling cycle, the accuracy of the side band ratio of the THz channel is about 2% (at the edge) which is proportional to detuning in the range of +/- 60 decimal units (82.48 µm path difference change). However, at the center the accuracy is better than 1%.

The diplexer calibration method described above make only use of a few data points for fitting; hence, the diplexer calibration function can be improved by increasing the number of data points [Suttiwong, et al., 25.02.2009]. Furthermore, observing the behaviour of the LVDT in each cooling cycle as discussed in 6.1.4.3 selection of the best stable region for setting the diplexer can be improved which results in a better diplexer calibration function.

In different cooling cycle cycles, the diplexer must be re-calibrated due to the aging of the LVDT.

6.2 Characterization of the 1.8 THz channel

The complete characterization of the 1.8 THz channel was done after transferring the cryogenic channel into the flight module cryostat. This section begins with the investigation of the parameter surface forming the relationship between HEB bias, LO power and system noise temperature followed by a detailed description how the 1.8 THz channel was characterized during the flight campaign.

After that the sensitivity of the 1.8 THz receiver (cryogenic channel, IF backend and the autocorrelator) and the effect of changing the gate voltage (corresponding to the change of LO power level) on the stability of the 1.8 THz channel will be described.

The further discussions in this section refer to the filtering applied for improving the stability of the HEB bias and the gate voltage, the calculation of the heat transfer of the cryogenic channel and the results from the antenna beam profile measurement obtained for the 1.8 THz channel.

The 1.8 THz channel was also characterized in SSB mode during the development of the channel in the test cryostat. However technical problems arose so that the 1.8 THz channel was operated during the first two flights in DSB mode only. The results from the characterization will be shown and problems mentioned above will be further discussed.

6.2.1 Parameter surface of the THz channel

To achieve the lowest system noise temperature, one has to optimize the power (DC power and LO power: see chapter 3.4) fed to the HEB mixer which can be achieved by changing the following two parameters: the HEB bias and LO power level.

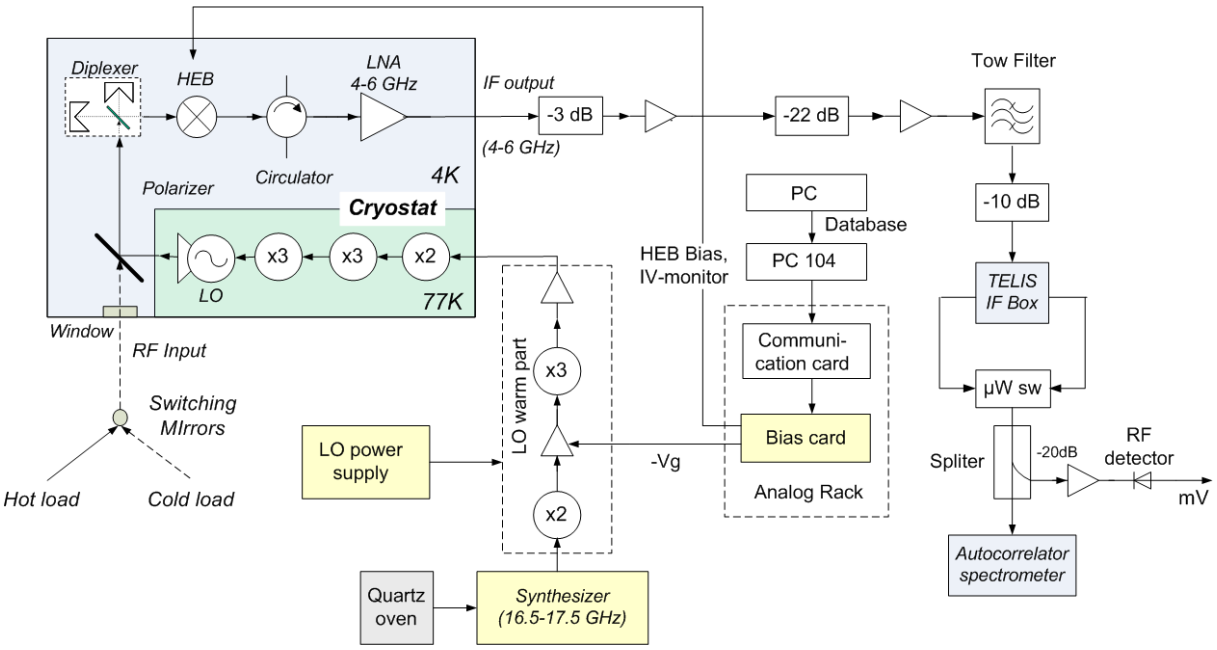

Figure 6-18: The schematic shows details of the complete 1.8 THz channel and its IF backend. The LO warm part has two different bias supplies: LO power supply and the gate voltage are directly controlled from the PC via a bias card

As illustrated in Figure 6-18 LO power can be adjusted by changing the gate voltage of the first amplifier (33 GHz) which can be adjusted by the computer via a bias card. The same bias card is also used to control the HEB bias voltage as well as to retrieve the DC current (I_0) and DC voltage (V_0) of the HEB mixer. Read out of the HEB-IV curve can be used to monitor the absorbed LO power level as well as the absorbed DC power.

However there are fluctuations of the LO power level due to the Fabry-Perot effect between the HEB mixer and the LO. In addition, the LO power drifts due to the temperature drift of the LO's warm part and different cooling cycles. These effects were carefully observed during the development and will be firstly discussed.

6.2.1.1 LO power

In order to obtain a rough estimation of the relationship between the pumped HEB current and the LO output power, the approximate absolute LO power in the frequency range between 1780 and 1880 GHz measured by a 4.2 K-Bolometer with a Winston cone optics (see 6.1.3) is compared with the pumped HEB current as shown in Figure 6-19.

The coupling efficiency of the HEB mixer [Cherednichenko, 2007] is influenced by the impedance mismatch between its antenna and its IF circuit. The antenna of the HEB mixer is a double slot antenna which impedance strongly depends on the frequency. The couple efficiency is fitted by using polynomial of the forth order and the couple efficiency at 1.8 THz is 100% as illustrated in Figure 6-19.

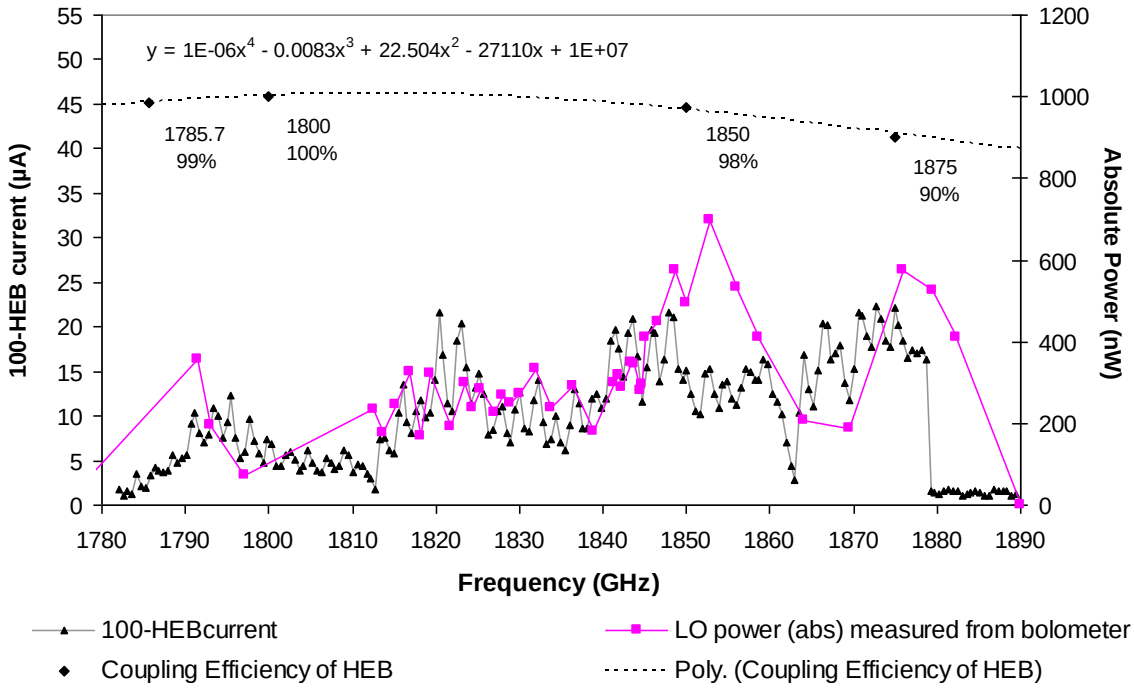

Figure 6-19: Comparison between the absolute power measured directly from the LO by the bolometer, the 100 (µA) - HEB current (µA) and the coupling efficiency between the double slot antenna of the HEB to the HEB mixer.

The "100-HEB current" is simply the inverse scale by subtracting the monitored HEB current from 100 µA in order to make the comparison easier (higher LO power is at the top and lower LO power is at the bottom). During measuring the HEB current, the HEB bias was fixed at 3 mV and the gate voltage was set at -0.7 Volts (at the maximum LO power)

The region having too low LO power might be difficult to use for pumping the HEB mixer and this must be considered for the LO frequency selection. The region having too high LO power is however valid because the LO power level can be reduced by decreasing the gate voltage.

LO power at different gate voltages:

The frequency of the solid state local oscillator applied in the 1.8 THz channel can be tuned from 1780 to 1890 GHz and its power is also adjustable by changing the gate voltage of the first amplifier at the LO warm part located outside the cryostat (see 5.2.3 and Figure 6-18). All graphs in Figure 6-20 show the change of HEB current at different LO frequencies (1782 GHz to 1890 GHz) due to the change of the gate voltage.

Figure 6-20 (a) shows the difference of the HEB current when changing the gate voltage within its operating range (-0.7 Volt to -1.02 Volt). The small graph enlarges the change of HEB current in the range of 1830.5 GHz to 1832 GHz. The more the gate voltage is increased, the more power is provided by the LO. Decreasing the gate voltage less than -1.02 Volt causes the drift and instability of the LO power as shown in Figure 6-20 (b). Figure 6-20 (c) shows the completely switched off of the LO power when the gate voltage is less than -1.1 Volt. The HEB current has an uncertainty of about ± 2µA due to the noise of the HEB bias voltage in the feedback loop. To improve the stability of the HEB bias, the noisy signal in the ground loop must be better filtered.

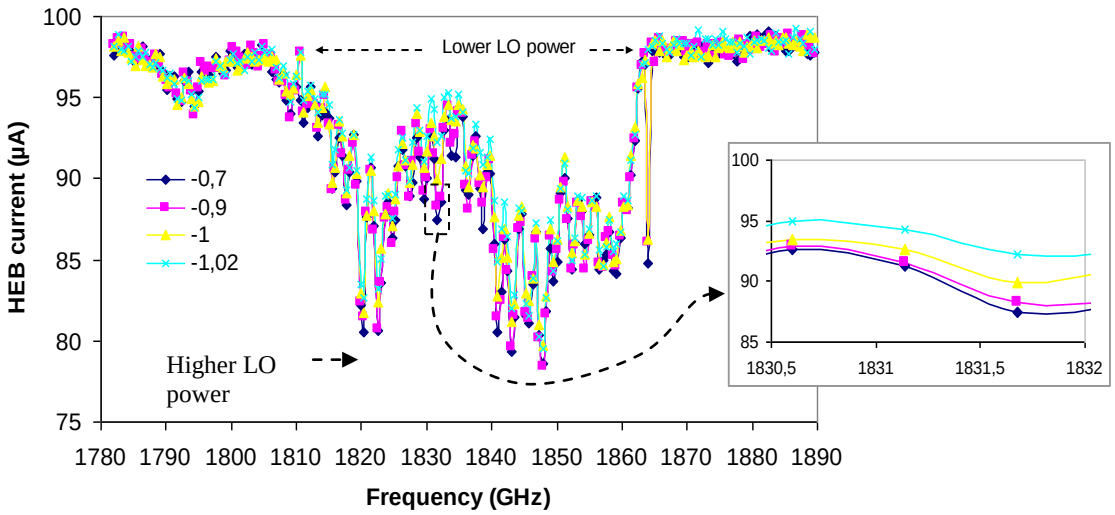

(a)

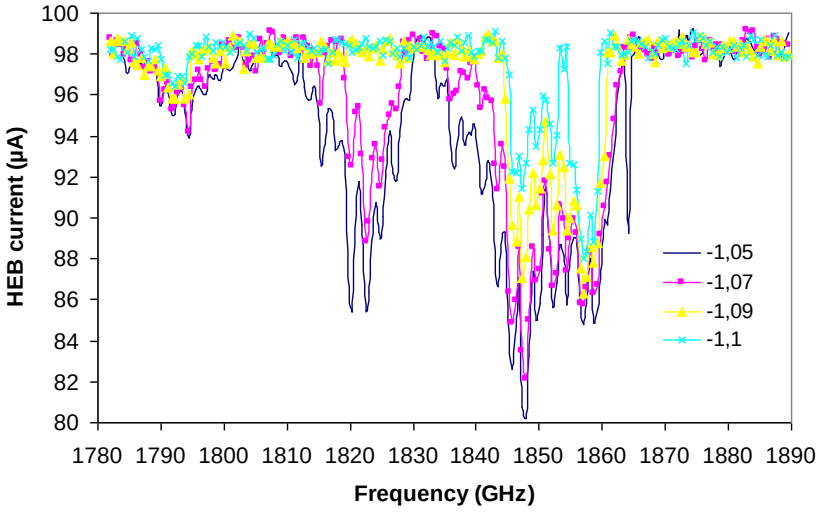

(b)

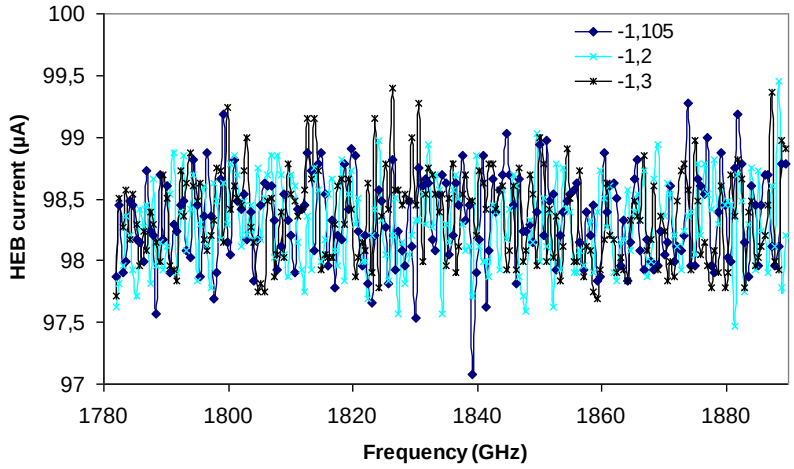

(c)

Figure 6-20 : shows the HEB current corresponding to the LO power coupled onto the HEB mixer at an LO frequency of 1782 GHz to 1890 GHz at different LO gate voltages from -0.7 Volt to -1.3 Volt.

Effect of temperature on the warm part of the LO (in the same cooling cycle):

The critical temperature of the LO warm part is above 30°C. At lower temperature the active amplifiers of the LO warm part could have higher gain; as a result, the power output of the multiplier state of the LO increases.

Figure 6-21 shows a comparison of the HEB current (corresponding to the LO power) measured at different temperature of the LO warm part. All measurements were done in the same cooling cycle of the cryostat. At the operating range (20°C to 27°C) the LO power was almost constant (deviation = ±1µA), so this temperature range was selected to be best suited for operation. The LO power starts increasing strongly when the temperature of the LO warm part is lower than 15°.

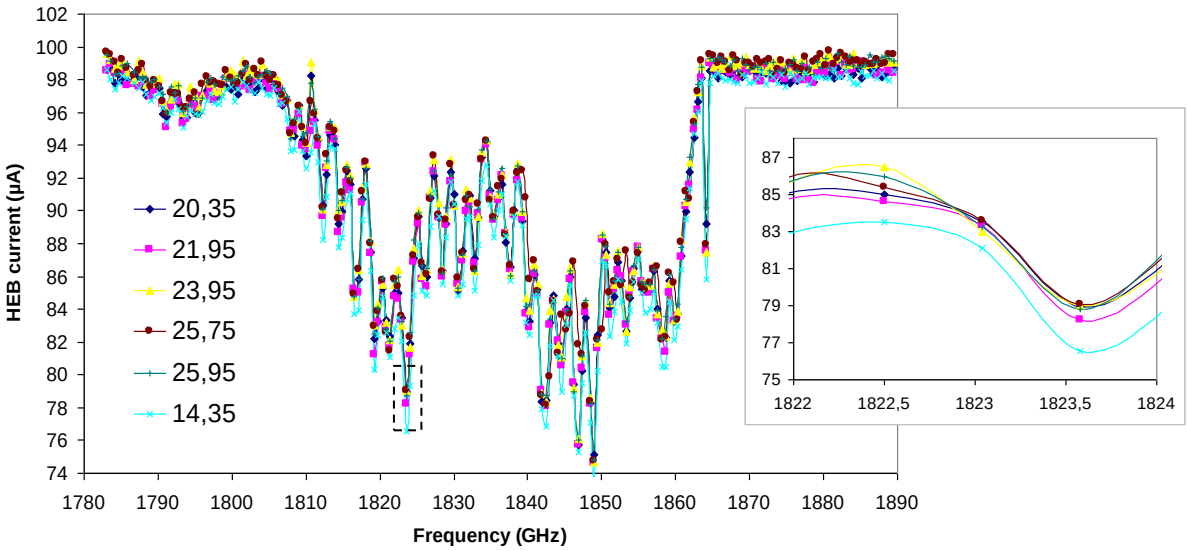

Figure 6-21: Comparison between the LO power across frequency range from 1782 GHz to 1890 GHz measured at different temperatures of the LO warm part. The LO frequency was set at 1830.1 GHz.

Change of LO power in different cooling cycles:

Figure 6-22 (a) depicts the HEB current against the LO frequencies from 1782 GHz to 1890 GHz. Each measurement was done in a different cooling cycle. The feature of the LO power at different frequencies as shown in graph (a) is reproducible and can be used as a first analysis for system monitoring. Figure 6-22 (b) presents the comparison of the HEB current measured at different LO frequencies from 1829.35 to 1830.24 GHz for four different cooling cycles. The small step scan was not performed during the flight in Kiruna (on 10.03.2009) due to the lack of measurement time.

In each LO scan, the HEB bias was usually set to the low sensitive region (2 mV -3 mV) in order to avoid the unstable HEB current readout due to the low pumped LO power on the HEB mixer. It is clear that the LO power changes in different cooling cycles as shown in Figure 6-22 (b). Even though three measurements on 15.03.2008, 30.05.2008 and 24.10.2008 were using different HEB bias, a drift of the LO power can clearly been identified. The drift of the LO power is supposedly caused by the change of electrical grounding and the drift of the warm part's temperature

Figure 6-22 (b) illustrates the Fabry-Perot effect observed in all LO measurements. It can calculate by $1/2\sigma$, where σ is a wave number. The frequency 300 MHz yields a wavelength of about 1 meter and thus 0.5 λ is 50 cm which corresponds to the distance between the HEB mixer and the LO. It might be proposed to reduce this effect in the future by putting a gray absorber between the LO and the coupling polarizer.

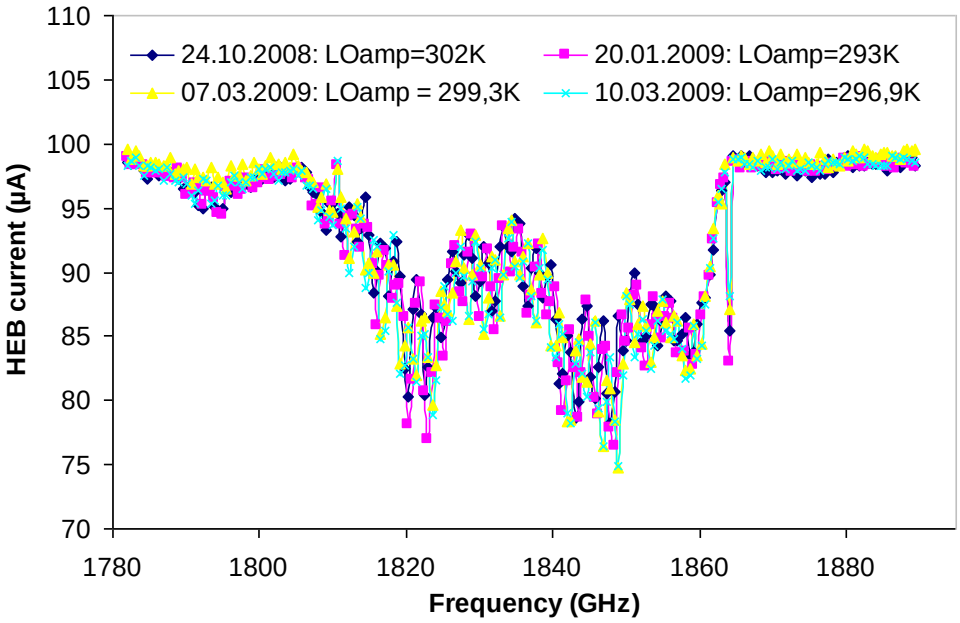

(a)

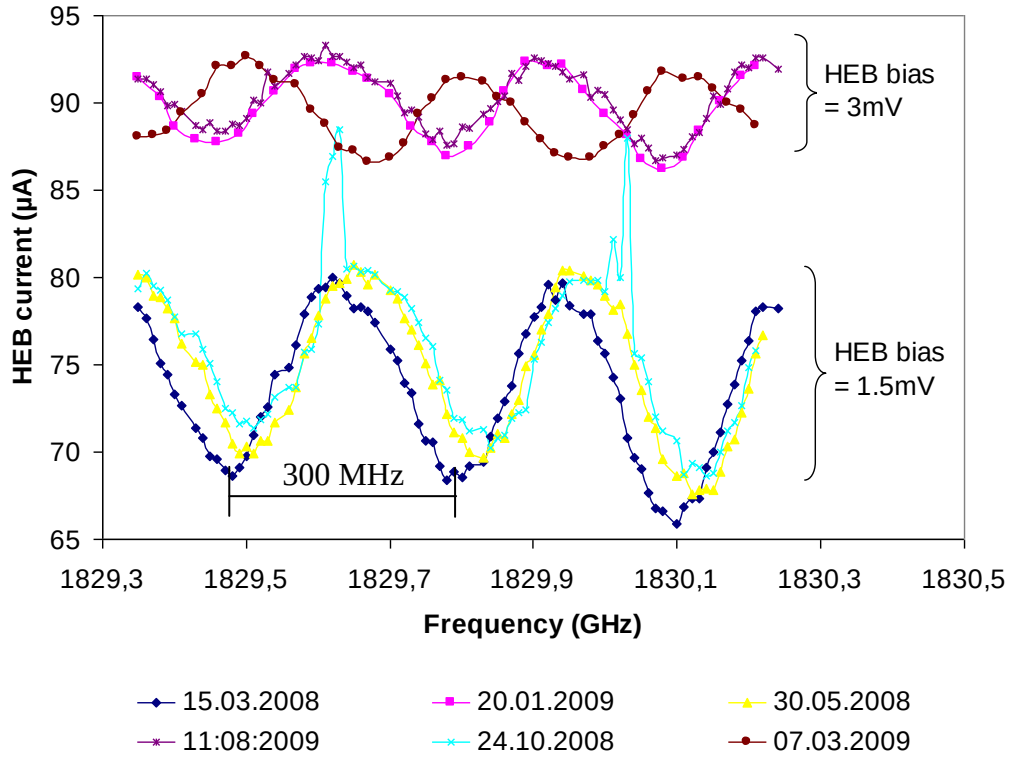

(b)

Figure 6-22: (a) Comparison between LO power measured during four different cooling cycles. The temperature of the LO warm part for each measurement is in the operating range 20° to 29°. (b) Comparison of the LO power in the LO frequency range of 1829.35 GHz to 1830.25 GHz.

LO power in the same cooling cycle:

LO power measured in the same cooling cycle, with the same temperature of the LO warm part and no change in grounding during the measurement is reproducible as shown in Figure 6-23. The grounding problem would appear when the TELIS instrument is moved or transported after which the instrument has to be reconnected. It effects directly to the HEB monitoring and causes the reduced accuracy of the readout from the bias card.

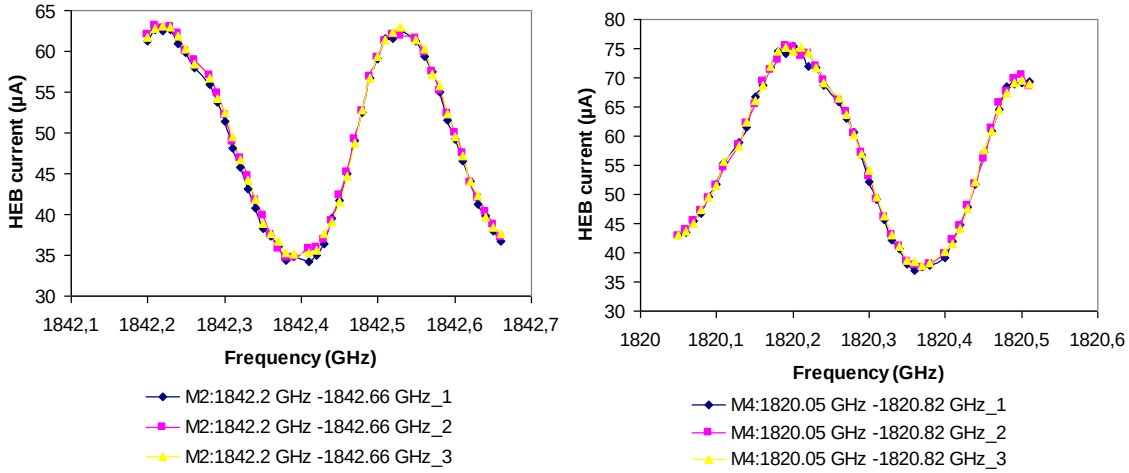

Figure 6-23: Left: comparison between three HEB current against the LO frequency in the range of 1842.2 GHz to 1842.66 GHz Right: a comparison between three HEB currents against the LO frequency in the range of 1820.05 GHz to 1820.82 GHz. All measurements were measured at the same temperature (30°C) and in the same cooling cycle. Time between each measurement was about 30 minutes

6.2.1.2 HEB Bias:

The HEB mixer applied to the 1.8 THz channel has a critical current (I_c) of about 220 μA and the sensitive region for setting the HEB bias is usually in between 0.4 mV and 0.8 mV. However at some LO frequencies which provide very low LO output power (see Figure 6-7), the HEB bias might be increased in order to optimize the pumped power of the HEB mixer. Nevertheless, the bias should not be set higher than 1.5 mV because then the HEB mixer starts to have less sensitivity in this bias range.

The optimum HEB bias can be determined by observing the system noise temperature at different HEB bias voltages while the LO power was kept stable. A result from such a measurement is shown in Figure 6-24 (a). The LO frequency was set at 1820.51 GHz and the measurement was redone four times by setting the diplexer at different orders. The HEB bias yields the best noise temperature as well as the best stability is at 0.5 mV. The repeatability of the system noise temperature measurement depending on the stability of the LO and the HEB bias is ±2-3% of the measured system noise temperature [20].

Figure 6-24 (b) presents the result of the hot-cold measurement used for calculating the system noise temperature in which the absolute power was retrieved by the RF detector.

[20] This number is calculated by averaging ten successive system noise temperatures.

For the 1.8 THz channel operation, the stability is more important than the absolute system noise temperature; therefore, the best operating point is the one with the best stability. The stability is determined by calculating the standard deviation from 10 points of the absolute power measured with the switching mirror pointed to the (cone) hot load. The hot load was used to be a reference blackbody for determining the stability of the readout of the IF power due to its backscattering which is below -70 dB [Murk, 2005]

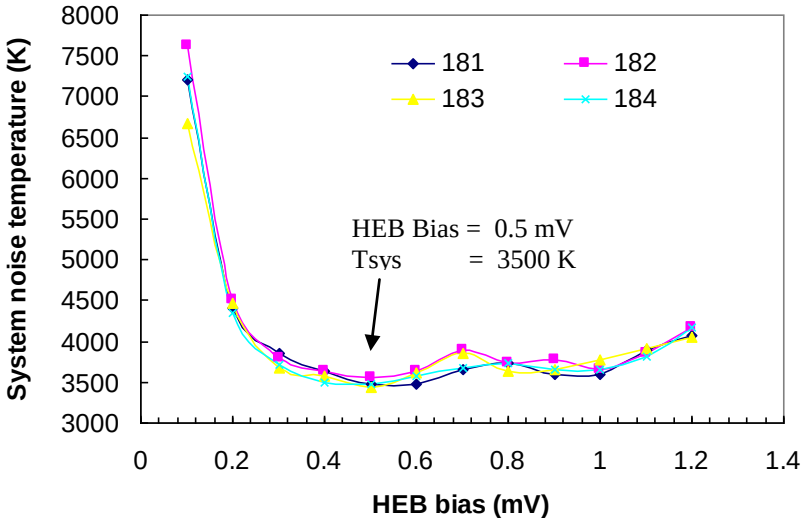

(a)

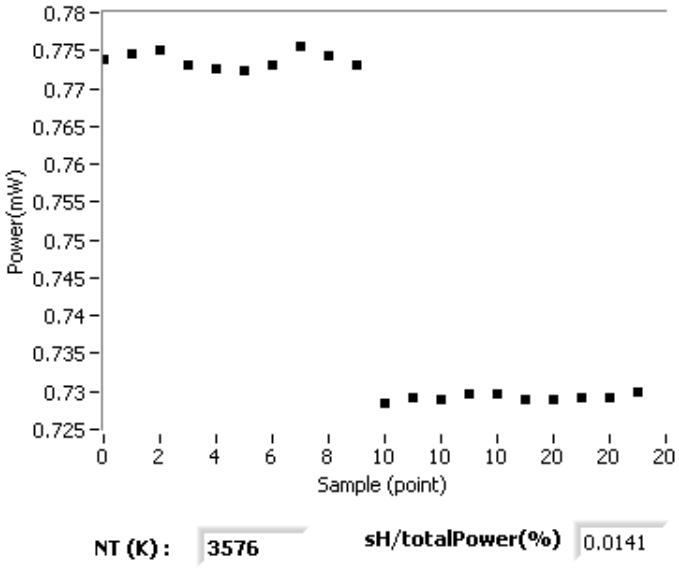

(b)

Figure 6-24: shows the system noise temperature measurement. In this measurement the LO frequency was set at 1820.51 GHz and the LO power was fixed (the gate voltage = -0.7 V). The HEB bias was the only one parameter changed from 0 mV to 1.5 mV with the step size of 0.1 mV. (a) The plot of the HEB bias against the system noise temperature. (b) The measured power while the switching mirror was pointed to hot and cold respectively. "NT(K)" is the system noise temperature calculated from the averaged hot and cold measured power. "sH/totalPower (%)" is the standard deviation from the total power in percentage calculated from ten points of the hot power.

6.2.1.3 Parameter surface characterization (HEB Bias, LO power, NT):

The parameter surface of the THz channel can be investigated only under the condition that the temperature at the LO's warm part is stabilized and with no drift or offset in the grounding. To characterize the operating point, at first the level of the pumped HEB-IV curve corresponding to the optimum LO power level should be estimated.

Figure 6-25 shows how the optimum HEB IV curve is determined from an unpumped and a pumped HEB IV curve. The experimental operating point (V_0, I_0) is the one yielding the best system noise temperature. Theoretically for a line of linear resistance R_0, the absorbed LO power can be written as,

$$P_{LO} = R_0 (I_u^2 - I_0^2) \qquad \textbf{eq.6-7}$$

where I_u is the current when no LO power is applied [Kroug, 2001]. This pumped HEB IV curve was selected by considering the operating point on the pumped IV curve which gives the R_0 close to the one of the unpumped curve.

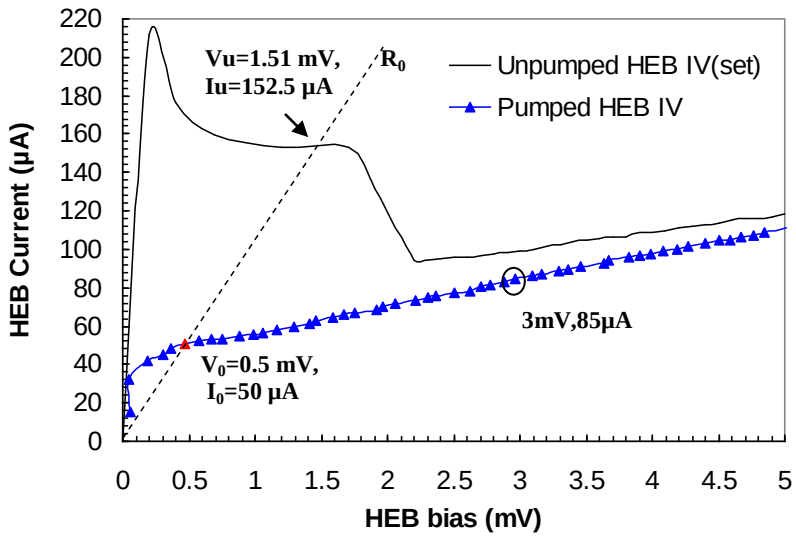

Figure 6-25: illustrates the pumped HEB IV curve corresponding to the optimum LO power (~200nW) by using a line of linear resistance R_0.

By assumption that the R_0 is almost constant and ignoring the effect of the *electro-thermal feed back voltage*[21] [Ekström, et al., 1995], the calculated absorbed LO power is about 206 nW which is in good agreement with the information of the HEB mixer received after the delivery. Thus, this level of the pumped HEB IV curve should be the best choice for the optimum LO power level.

[21] An electro-thermal feedback mechanism causes by an IF voltage reflection modulates the mixer's inhomogeneous non-linear 'hot spot' region. (≡this current adds to dc bias current I_0 through the bolometer).

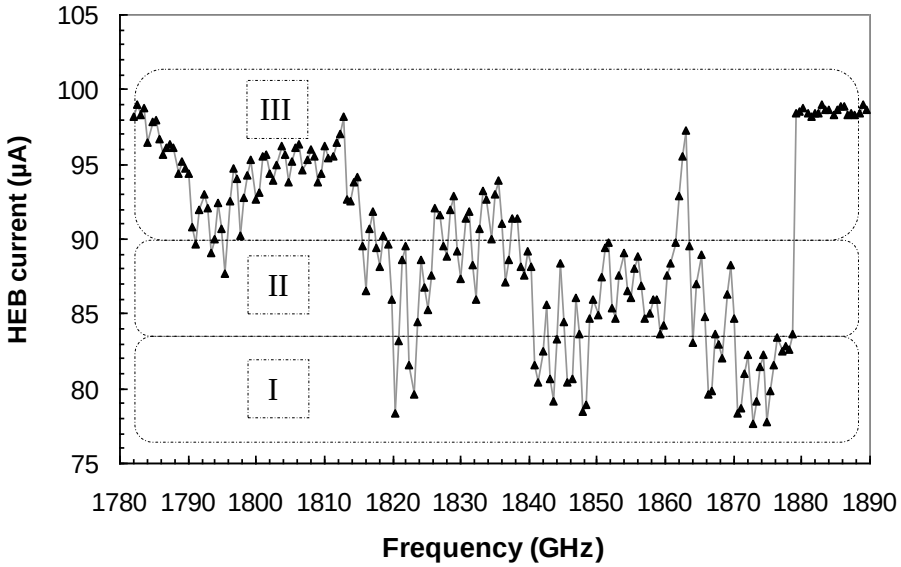

Figure 6-26: depicts the HEB current at different LO frequencies from 1780 GHz to 1880 GHz with 5 MHz step size measured while the HEB bias voltage was fixed at 3 mV. The measurement was done at the maximum LO power amplification (gate voltage = -0.7 Volts). "I" = LO frequencies having high LO power, "II"= LO frequencies having LO power close to optimum LO power, "III"= LO frequencies having too low LO power for pumping the HEB mixer.

Usually, the LO power is observed by monitoring the HEB current and the HEB bias voltage is set at 3 mV to avoid an unstable readout when the HEB is not sufficiently pumped as shown in Figure 6-26. The LO frequency having the optimum LO power should be the one having a HEB current close to 85 µA (**region II**). LO frequencies in **region I** have too high LO power which is still valid because the LO power can be reduced by reducing the gate voltage. The power of LO frequencies in **region III** is too low for pumping the mixer efficiently.

After the optimum LO power has been selected, the optimum DC bias for the HEB can be determined by measuring the system noise temperature as described in chapter 6.2.1.2. By using the characterization software (see Appendix G.2) the characterization can be done in short time and more convenient. The software provides the possibility for searching the LO frequencies yielding the optimum LO power, and for the optimum HEB bias yielding the best system noise temperature and system stability.

Figure 6-27 shows the effect of the change of LO power on the system noise temperature. At a HEB bias voltage of 0.6 mV the optimum LO power is at 50µA ±5µA. This graph is shown the HEB current against the system noise temperature at three different LO frequencies. The results in Figure 6-27 are not corrected for water vapour absorption. The system noise temperatures measured at the LO frequencies from 1842.20 GHz to 1842.70 GHz (M2) have the highest noise temperature due to 15% absorption of water vapour in the optical path (an optical path of 50 cm and an relative humidity of 43%). After correction for all losses, the system noise temperature will be around the same for all frequencies.

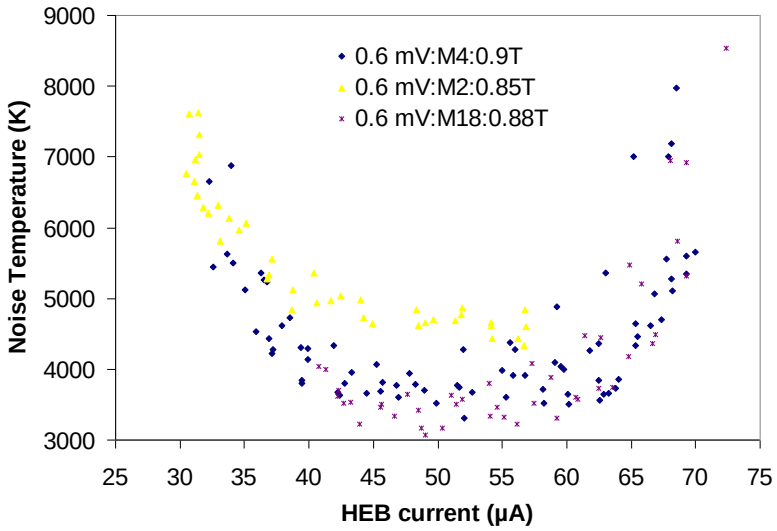

Figure 6-27: A comparison of the system noise temperature measured at different LO output power (proportional to the HEB current). The HEB bias voltage was set to 0.6 mV for all measurements. LO frequencies at M4 are from 1820.05 GHz to 1820.85 GHz. LO frequencies at M2 are from 1842.20 to 1842.70 and LO frequencies at M18 are in the range of 1823.7 to 1824.3. The signal transmission due to the optical path of M4, M2 and M18 are 90%, 85% and 88% respectively. "M2, M4, M18" are indexes of Microwindow: see in Appendix B.

Summarization of parameter surface:

The optimum LO power corresponding to the HEB current at the optimum HEB bias between 0.4 mV and 0.6 mV is about 50μA ± 2 μA. It should be noted that the accuracy of the HEB current monitor is not better than ±2μA and the accuracy of the HEB bias is about ±30 μV. The repeatability of the system noise temperature depending on the stability of the LO and the HEB bias is ±2-3% from the measured system noise temperature.

The accuracy of the gate voltage is about ±0.001 V. The LO power changes slightly with the change of the temperature at the LO warm part in which the LO power increases obviously at a temperature lower than 20°C. The operating range of the gate voltage is recommended to be -0.7 Volt to -1.02 Volts. Some LO frequencies having very high LO power are still suited for operation even though the gate voltage is less than -1.02 Volts. (see Figure 6-20). LO power reaches a zero value when the gate voltage is less than -1.1 Volts.

Even though with the Fabry-Perot effect between the HEB and LO (~50 cm.), the LO power (as a function of LO frequency) absorbed at the HEB mixer is reproducible in the same cooling cycles. The LO power level changes in different cooling cycle and it drifts due to the temperature change of the LO's warm part.

6.2.2 Radiometric sensitivity of the 1.8 THz receiver (system noise temperature)

Setup of the noise temperature measurement and the results of the measurements:

The noise temperature of the HEB mixer applied to the DLR channel as discussed in section 6.1.2 was measured by using the FIR gas laser at 1.6 THz. The system noise temperature was fully characterized again in the 1.8 THz region (1780-1880 GHz) after transferring the cold channel in the flight module cryostat. The measurement setup for measuring the system noise temperature by using the flight setup was shown in Figure 6-28.

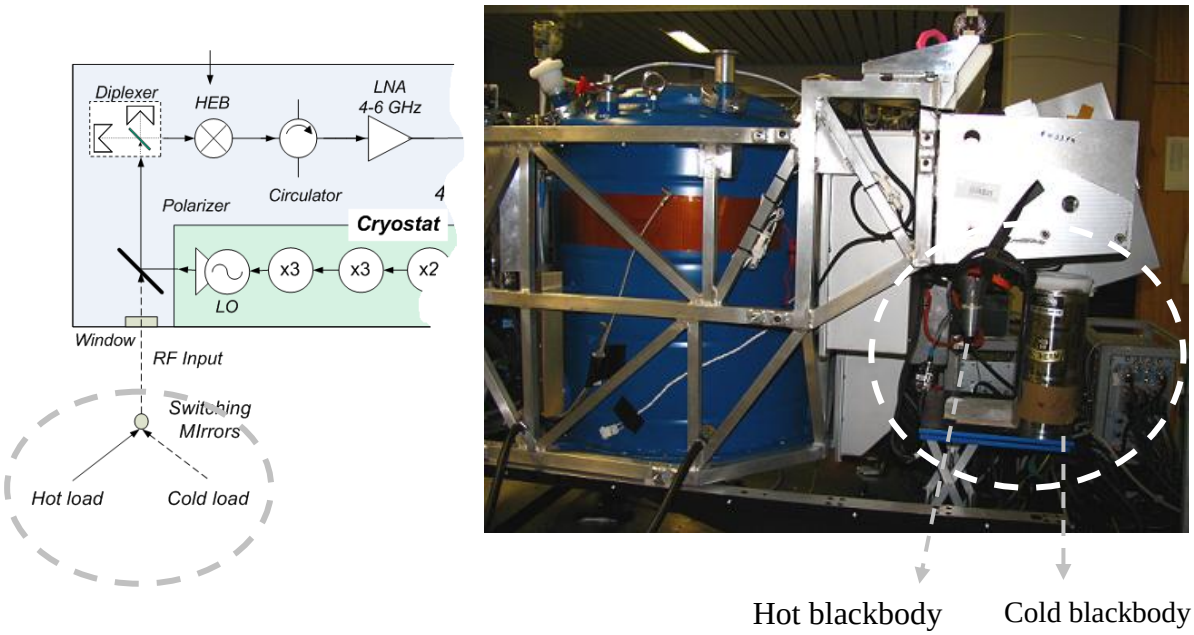

Figure 6-28: A photo illustrates the position of a hot blackbody (flight module) and a cold blackbody. The hot blackbody is a cone blackbody which has a backscattering below -70 dB.

Figure 6-29 depicts the photo of a hot blackbody and a cold blackbody applied in the setup of the characterization on ground. The cone-hot blackbody has a backscatter below -70 dB [Murk, 2005]. The cold blackbody is formed by a small dewar containing liquid nitrogen (77 K). It is possible to calculate the system noise temperature by using either the absolute power measured from the RF detector mounted at the microwave backend, as shown in Figure 6-18, or the noise spectra measured from the Autocorrelator spectrometer. The switching mirror chops between the hot and cold blackbody (300 K and 77 K, respectively). The optical path length from the blackbodies to the window of the flight module cryostat has a length of 720 cm.

Figure 6-29 illustrates the system noise temperature spectra calculated by using the Y-factor method. The system noise temperature spectra are corrected for the attenuation of water vapour in the optical path (720 cm.).

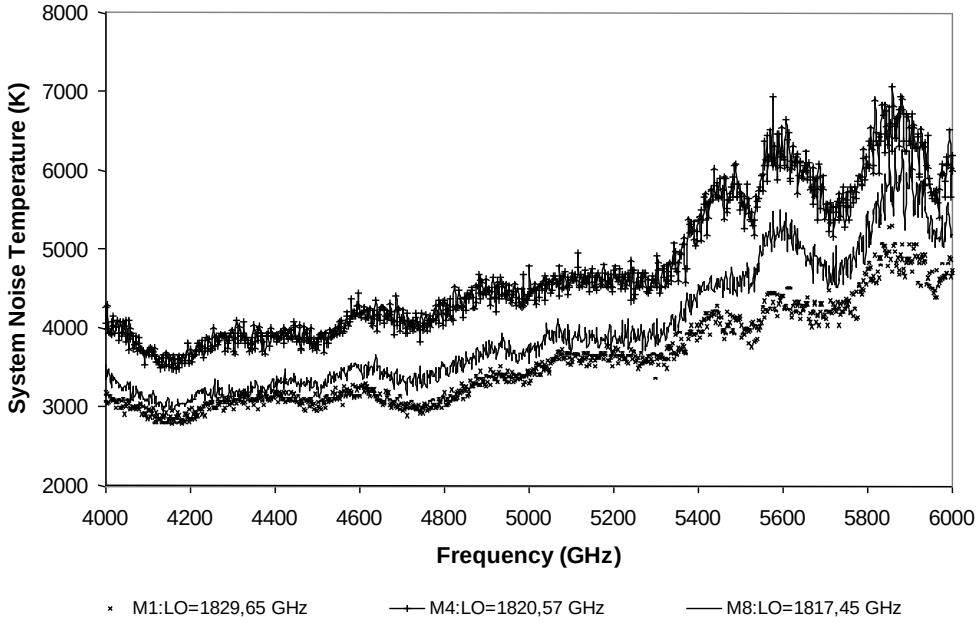

Figure 6-29 : The graph shows noise temperature spectra (only water absorption has been corrected) with different LO frequencies measured from the autocorrelator spectrometer. X-axis is the IF frequency which is down converted from the HEB mixer. Y-axis represents the system noise temperature (the sensitivity to the system) having a unit of Kelvin. They were measured during the flight campaign (on-ground characterization) in March 2009 in Kiruna, Sweden.

The system noise temperature depends on the LO power pumped on the HEB mixer and the LO power depends strongly on the LO frequency (due to the standing wave in the IF chain) and the temperature of the LO warm part as discussed in chapter 6.2.1. The average system noise temperature for all LO frequencies having the optimum LO power is about 3000 K.

Conversion loss of the HEB mixer:

In the previous section, the system noise temperature of the whole system (optic, mixer and IF backend) was presented. In order to determine the conversion loss of the HEB mixer, all losses and the noise contributions of all components in the system have to be calculated.

Figure 6-30 a) shows all components in the heterodyne receiver path. Two major losses in the signal path are the optical losses (L_{opt}) and the mixer conversion losses (L_M). The power output is amplified with a LNA (low noise amplifier) and the HEMT amplifiers before passing through the band pass filter (2 GHz bandwidth). P_{out} is proportional to various parameters and can be described as the equation below.

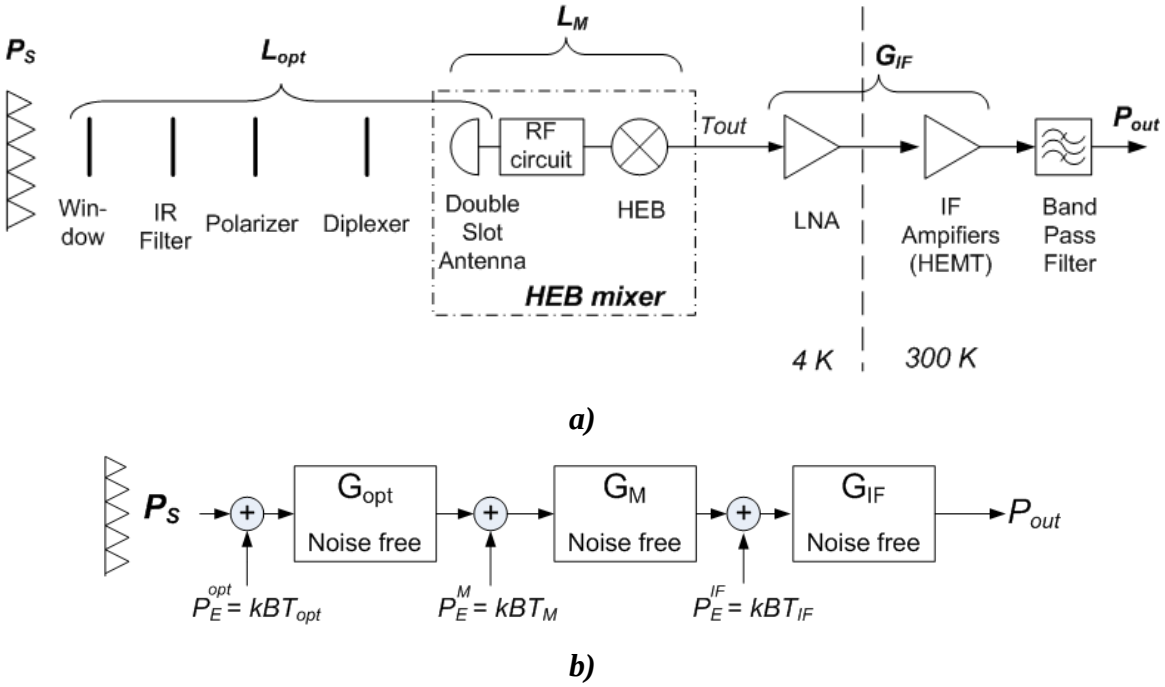

Figure 6-30: ***a)*** **The IF chain and two losses in the path: the optical losses (L_{opt}), the RF losses of the mixer (L_M), are depicted.** ***b)*** **The block diagram presents the equivalent input noise power of cascade devices in the heterodyne receiver. G_{OPT} (=1/L_{OPT}) and G_M (=1/L_M) represent the optical gain and the mixer conversion gain. G_{IF} is the gain of IF chain. T_{OPT}, T_M and T_{IF} represent the noise temperature of the optics, mixer and IF chain respectively. P_S represents the power of the source. P_{SO} and P_{no} are the power of the signal and the noise at the output. k is Boltzmann constant and B represents the bandwidth (2 GHz) and P_E is the equivalent noise power.**

$$P_{out} \alpha T_S \cdot G_M(V_0, P_{LO}) \cdot G_{IF}(V_0) + T_{opt} G_M(V_0, P_{LO}) G_{IF}(V_0) + T_{out} G_{IF}(V_0) + T_{IF} G_{IF}(V_0) \quad \textbf{eq.6-8}$$

T_{out} is the mixer output noise which depends on the mixer bias and the LO power and it is equal to $T_M \cdot G_M$. The gain of the HEB mixer (G_M) depends on the DC bias (V_0) and the LO power (P_{LO}). The gain of the IF amplifiers depend on the drain bias and are assumed to be constant at a constant temperature (LNA at 4 K, HEMT at 300 K). The noise temperature of the HEMT amplifiers at room temperature dominates the whole noise temperature of the IF amplifier's chain (T_{IF}) and is less than 110 K.

Figure 6-30 b) is a block diagram presenting the input equivalent noise of a cascaded system of the 1.8 THz receiver. The power output can be calculated by the equation below and the total system noise temperature is equal to the total equivalent noise temperature as shown in eq. 6-10 .

$$P_{out} = \left(G_{opt}G_M G_{IF}\right)\cdot P_S + \left(G_{opt}G_M G_{IF}\right)\cdot P_E^{opt} + \left(G_M G_{IF}\right)\cdot P_E^M + G_{IF}\cdot P_E^{IF} \qquad \textbf{eq.6-9}$$

$$= \left(G_{opt}G_M G_{IF}\right)\cdot k\cdot B\cdot\left(T_S + T_E^{opt} + \frac{T_E^M}{G_{opt}} + \frac{T_E^{IF}}{G_{opt}\cdot G_M}\right)$$

$$T_{sys} = T_E^{opt} + \frac{T_E^M}{G_{opt}} + \frac{T_E^{IF}}{G_{opt}\cdot G_M} \qquad \textbf{eq.6-10}$$

where T_S is the source temperature, T_E^{opt}, T_E^M, T_E^{IF} are equivalent noise temperatures of the optics, mixer and the IF chain, respectively. The summarization of all optical losses of the 1.8 THz channel is shown in Table 6-1. Basically, losses in the RF chain consist of losses from the RF circuit (impedance mismatch between the antenna and the HEB) [Kroug, et al., 1997] and the conversion loss of the mixer itself. It is difficult to measure losses in the RF circuit; therefore these cannot be separated from the mixer conversion loss.

Table 6-1 : Summarization of all optical losses. Tn represents Noise temperature of a device.

Optical devices	Device Temp (K)	Loss (dB)	Tn (K)
Quartz window	300	-0.46	33.33
Zitex blocking filter	77	-0.66	12.53
Polarizer	5	-0.04	0.05
Diplexer (leakage)	5	-0.03	0.04
Silicon lens, reflection	5	-1.50	2.06
Silicon lens, absorption	5	-0.10	0.12
lens antenna	5	-0.46	0.56
total optical loss		-3.24	48.69

The noise figure of each device applied in the 1.8 THz channel is presented in Table 6-1. Optical losses can be calculated in form of the noise figure (dB) and the noise temperature (Tn) [Skou, 1989]. The total optical losses of the 1.8 THz channel are about 50 K. The conversion loss of the mixer cannot be measured directly, but can be calculated by using the measured output power of two specific sources and the measured system noise temperature:

$$P_{Hout} = kB\cdot\left(T_{Shot} + T_{sys}\right)\cdot G_{IF}\cdot G_M \qquad \textbf{eq. 6-11}$$

$$P_{Cout} = kB\cdot\left(T_{Scold} + T_{sys}\right)\cdot G_{IF}\cdot G_M \qquad \textbf{eq. 6-12}$$

$$P_{Hout} - P_{Cout} = \Delta P_{out} = k\cdot B\cdot G_{IF}G_M\cdot\left(T_{Shot} - T_{Scold}\right) \qquad \textbf{eq. 6-13}$$

$$G_M = \frac{\Delta P_{out}}{kBG_{IF}\cdot\left(T_{Shot} - T_{Scold}\right)} \qquad \textbf{eq. 6-14}$$

T_{Shot} and T_{Scold} are the temperature radiated from a hot (300 K) and cold (77K) blackbody within a given bandwidth which follows the Callen-Welton law [Callen, et al., 1951].

The mixer conversion loss is in the range of -14 dB to -18 dB due to the HEB bias and the LO power. Using the measured output power at the measured system noise temperature of 2900 K (corrected with the water absorption loss of the optical path between the switching mirror and the cryostat window), the mixer conversion loss calculated from eq. 6-14 is about -15 dB. Substituting the system noise temperature in eq. 6-10 yields a mixer noise temperature T_E^M of about 1600 K. Therefore, the mixer output noise temperature (Tout) is about 50 K.

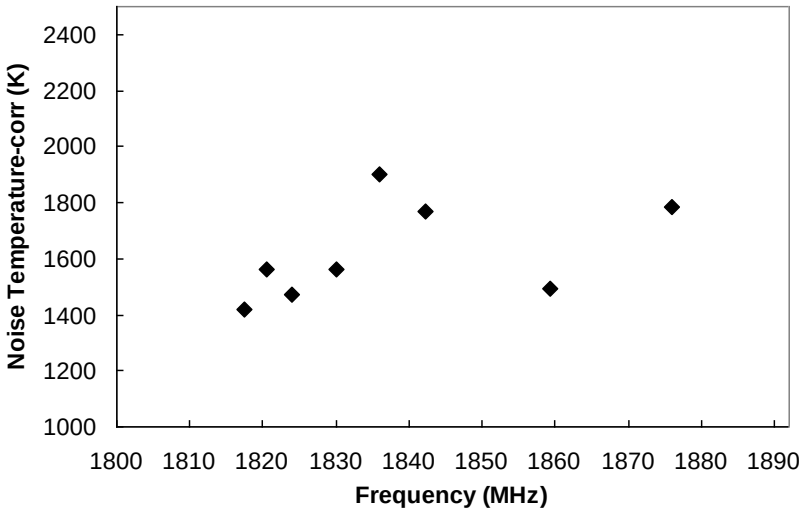

Figure 6-31: Mixer noise temperatures of the HEB mixer applied to 1.8 THz channel measured by the RF detector (absolute power) with respect to different LO frequencies are depicted.

The setup for measuring the system noise temperature is shown in Figure 6-18. The absolute output power of the 1.8 THz channel can be measured by a RF detector while the power spectrum across 2 GHz of IF bandwidth can be measured by the autocorrelator spectrometer. From the measurements, the averaged mixer noise temperature at various LO frequencies (from 1840 GHz to 1890 GHz) are about 1600 K. The accuracy of the system noise temperature as shown in Figure 6-31 is about ± 200 K due to the temperature drift of the LO warm part (thus, the LO power drifted) and the DC bias noise of the HEB mixer during the measurement and the temperature drift of the autocorrelator spectrometer (1% / K).

6.2.3 Stability of the 1.8 THz channel

The Allen variance (see. chapter 3.2.4) is used for determining the stability of the 1.8 THz channel. The stability of the cryogenic channel was separately tested by using the power meter to measure the IF output of the 1.8 THz channel directly. The results showing the effect of the LO power on the stability of the cryogenic channel will be at first discussed.

The further discussion in this section focuses on effect of a change of the stability of the cold channel and IF backend in case that the LO gate voltage is changed. These tests were conducted to figure out if the stability of the cold channel changes when the LO power is adjusted to the optimum level by changing the gate voltage.

Effect of LO power level on the stability of the 1.8 THz channel:

The measurement was performed by measuring the power output of the cold channel directly from the power meter, and by calculating the Allan Variance according to the equation 3.11. The measurement setup for the stability measurement is shown in Figure 6-32.

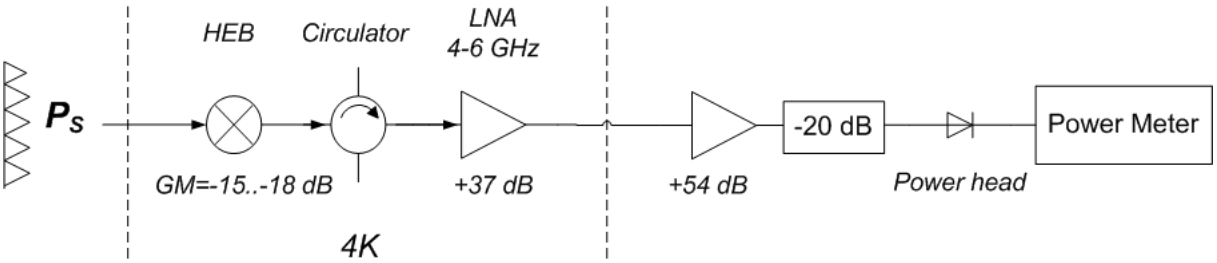

Figure 6-32: The measurement setup for the stability measurement with the power meter. "Ps" is the source power, "GM" is a mixer gain and "Power head" is basically a diode used to convert the IF power into voltages.

As shown in Figure 6-33, the white noise error of the lower curve (63 µA, 3900 K) is reduced when the integration time is increased to 500 ms (Allan variance follows the radiometric equation). At an integration time between 500 to 1000 ms, the slope follows the 1/f noise-floor region whereas an increase of integration time doesn't affect the stability of the system. When the integration time is set higher than 2000 ms, the cold channel starts to drift. It must be considered that the bandwidth used to calculate the Allen variance is 4 GHz; thus, at the lower resolution (the resolution of the autocorrelator = 2 MHz) the integration time can be increased according the radiometric equation (3.10.).

Figure 6-33 shows also the effect of changing the LO power level on the stability of the cold channel. The cold channel has a reduced stability when the gate voltage of the LO warm part was set lower corresponding to a reduced LO power. Thus, the system noise temperature is about 600 K worse than the other. The drift of the Allan plot at 75 µA presents the drift since the integration time is at about 700 ms. It is noted that the temperature of the LO warm part was stable (at 299 K) during this stability measurement.

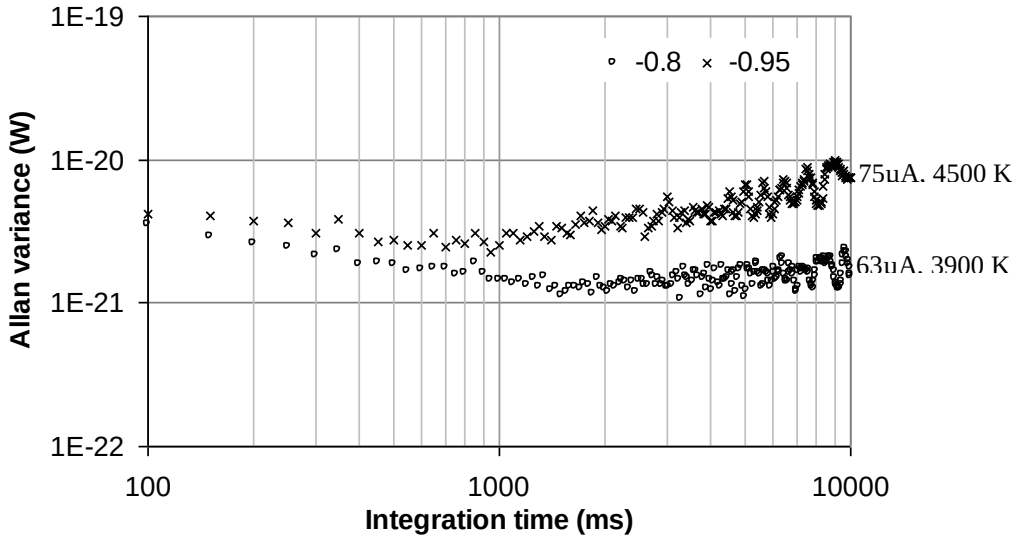

Figure 6-33: Comparison of the stability of the 1.8 THz channel at different LO power level. The LO power was adjusted by changing the gate voltage. The temperature of the LO warm part was stabilized at 299 K during the measurement.

Effect of changing the gate voltage on the stability of the 1.8 THz channel:

In this test, the stability of the THz channel at the gate voltage between -0.7 and -1.05 Volts were measured. The gate voltage was firstly adjusted, and only LO frequencies having the optimum power corresponding to the HEB current of about 50 µA (see. 6.2.1.3) were selected.

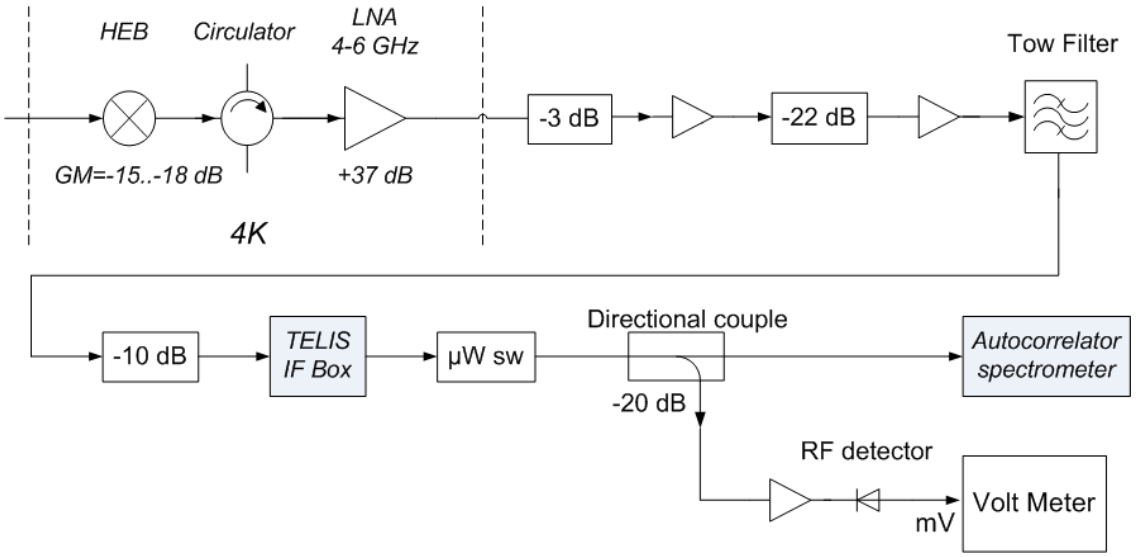

Figure 6-34: Measurement setup for measuring the stability of the 1.8 THz channel and the IF backend chain in front of the Autocorrelator spectrometer.

Figure 6-34 shows the measurement setup for measuring the stability of the 1.8 THz channel and IF backend in front of the Autocorrelator spectrometer. Thus, the results of the test will show not only the stability of the THz channel, but will also include the stability of the IF backend in front of the Autocorrelator. The Allan Variance was

calculated from the measured voltages (see eq. 3-11). The HEB bias was fixed during the measurement.

Figure 6-35 shows the results of the Allan Variance measurements. A gate voltage lower than -0.85 V, influences the stability of the input power of the Autocorrelator spectrometer. The stability of the system is not reproducible at the gate voltage lower than -0.85 Volts.

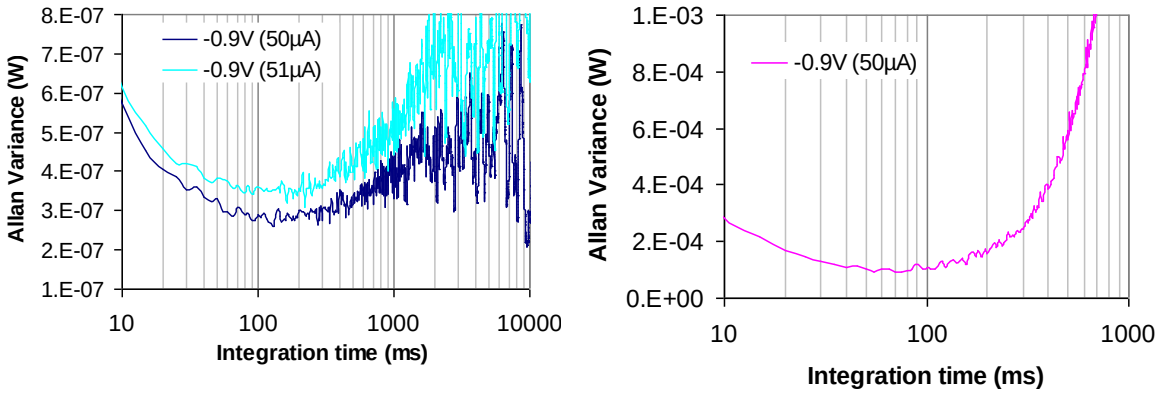

Figure 6-35: Allan Variance showing that the input power of the Autocorrelator is unstable and not reproducible when the gate voltage was set lower than -0.8 V. In the graph is the result of the gate voltage at -0.9 V which starts to be unstable and not reproducible.

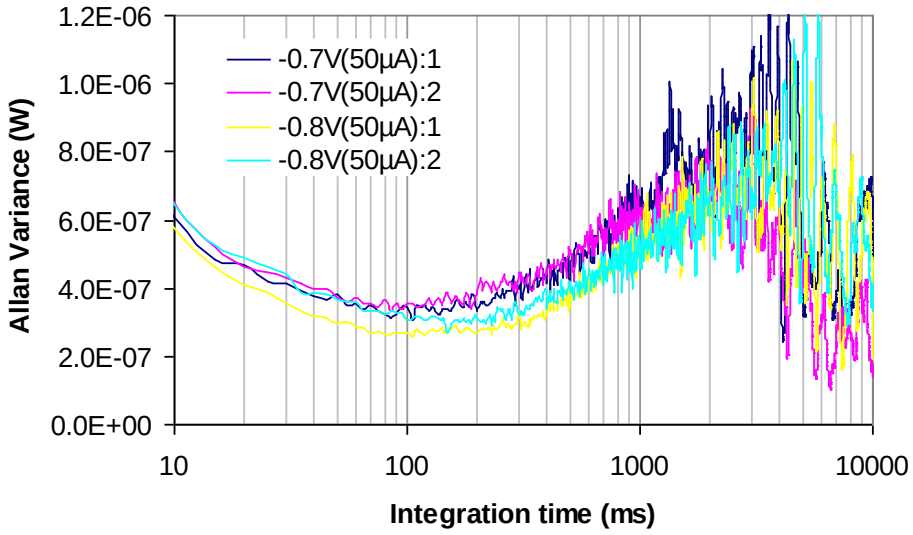

Figure 6-36: A comparison of the Allan Variances measured while the gate voltage of the LO was set at the -0.7 V and -0.8V. The Allen variance at each setting was measured two times to check the repeatability of the measurements.

Figure 6-36 depicts a comparison of the Allen Variances with two different gate voltages: -0.7V and -0.8 Volts. It shows that at a gate voltage of -0.7 V the stability was good and reliable. At the setting of the gate voltage of -0.8 V, even though the Allen Variance is better, it was not really reproducible. Therefore the gate voltage of -0.7 V was the best choice for controlling the 1.8 THz channel during the flight campaign in Teresina (2008) and Kiruna (2009).

The best integration time from the Allan variance plot measured after the IF backend is shorter than the one measured directly after the THz channel. The system (THz receiver and the IF backend) starts to drift after increasing the integration time more than 100 ms.

Summarization of the receiver sensitivity and stability:

Sensitivity of the 1.8 THz channel is in the range of 3000 K in case of the LO power is adjusted close to the optimum LO power (~50 µA) required by the HEB mixer.

The LO power level influences the stability of the 1.8 THz channel whereby less LO power pumped on the HEB mixer leads to the worse stability of the cold channel.

From the stability measurement of the cold channel with the IF backend, the best integration time on the Allen variance plot should be about 100 ms. It should be noted that the measurement was done at 2 GHz bandwidth. However the integration time depends on the bandwidth whereas the resolution bandwidth of the Autocorrelator (2 MHz) is 1000 times smaller; thus, the integration time of the autocorrelator can be set at 1.5 seconds.

The gate voltage of -0.7 V should be the best choice for 1.8 THz channel because its stability and reliability. The stability of gate voltages lower than -0.85 V is not reliable.

6.2.4 Filters for gate voltage and HEB monitoring

The stability of the bias voltage to the gate of the first amplifier of the LO warm part and the bias and monitoring of the HEB mixer were improved during the development by filtering. In the real system, there is much electromagnetic interference (EMI) induced in the ground return path. Filtering is a method to reduce this problem. Two Filters were designed and built for the bias voltage of the gate of the LO warm part's amplifier and the HEB monitors (see Appendix E).

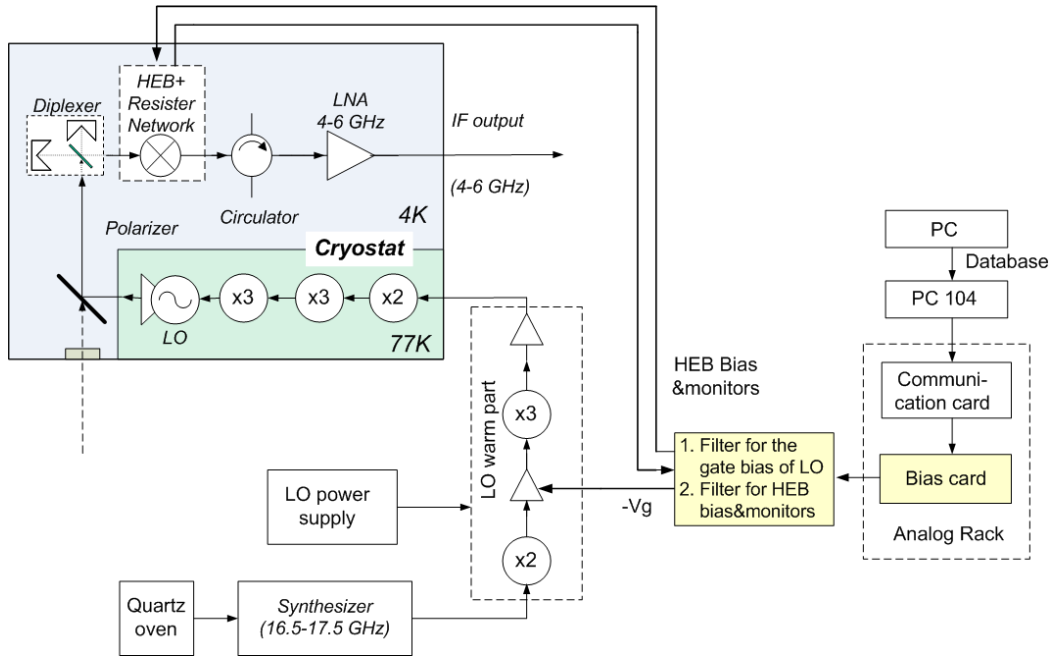

Figure 6-37: Schematic showing the connection of filters (yellow colour) in the bias system. Both filters were built on the same PCB and shielded.

Filter for the gate bias of the LO:

The filter was designed to be maximally flat and thus a third order RC passive filter (Low pass filter: LPF) was built in. An advantage of the third order LPF is to attenuate higher frequencies more steeply (-60dB / decade). In order to determine the losses of the filter, a transfer function of the circuit is calculated. By using Kirchhoff's voltage law (KVL), three equations (eq.6-8, 6-9, 6-10) can be formed and the invert matrix is applied to solve the equations.

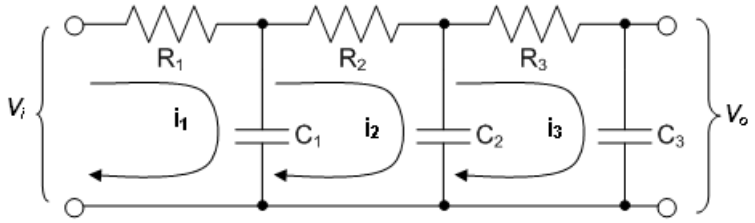

Figure 6-38: A third order RC passive circuit filter. It is a low pass filter built for filtering the high frequency interference at the gate voltage.

KVL Loop i_1 : $V_i(s) = \left(\frac{R_1C_1s+1}{C_1s}\right)I_1(s) - \left(\frac{1}{C_1s}\right)I_2(s)$ **eq. 6-15**

KVL Loop i_2 : $0 = -\left(\frac{1}{C_1s}\right)I_1(s) + \left(\frac{R_2C_1C_2s^2 + (C_1+C_2)s}{C_1C_2s^2}\right)I_2(s) - \left(\frac{1}{C_1s}\right)I_3(s)$ **eq. 6-16**

KVL Loop i_3 : $0 = -\left(\frac{1}{C_3s}\right)I_2(s) + \left(\frac{R_3C_2C_3s^2 + (C_2+C_3)s}{C_2C_3s^2}\right)I_3(s)$ **eq. 6-17**

And : $V_0(s) = -\left(\frac{1}{C_3s}\right)I_3(s)$ **eq. 6-18**

where $R_1 = R_2 = R_3 = R$ and $C1 = C_2 = C_3 = C$ the transfer function of the third order RC passive low pass filter can be determined as follows :-

$$\frac{V_o(s)}{V_i(s)} = \frac{1}{(RCS)^3 + 5(RCS)^2 + 6RCS + 1}$$ **eq. 6-19**

The transfer function is equivalent to the impulse response when Vi(s) = 1. [Dorf, et al., 2001]. The impulse response should be converted into the frequency domain (Fourier Domain) in order to find the magnitude and phase response of the filter. A cut off frequency of this LPF is designed at 550 Hz; thus $\omega = 2\pi fc = 17.73$ rad/sec and R=1200 Ω, C=47 nF. The filter characteristic is not influenced by the load resistance of the gate, because it has a very high impedance.

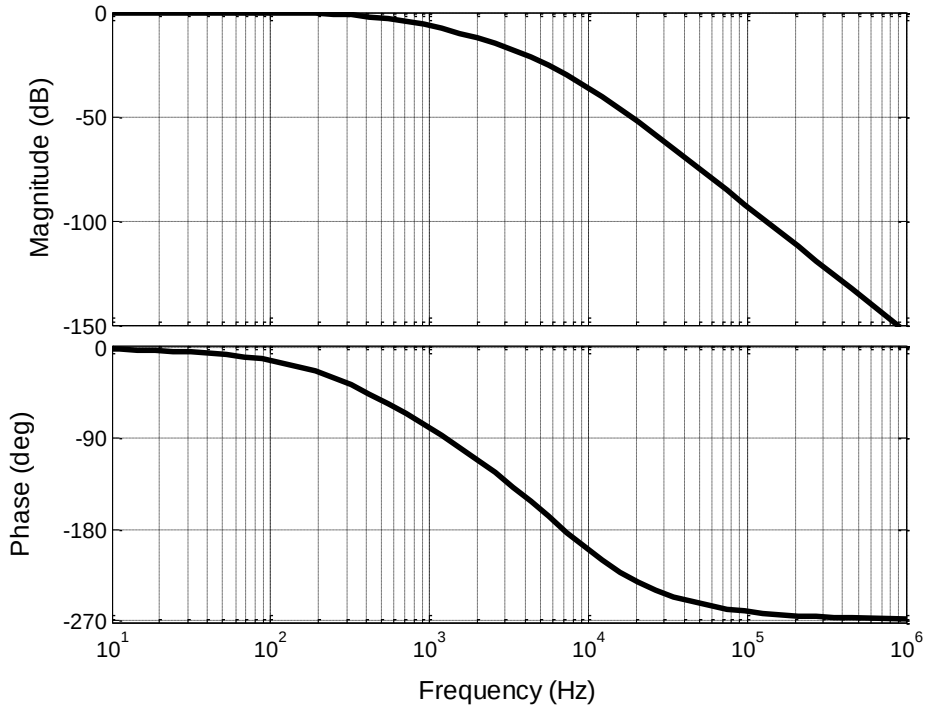

Figure 6-39: Magnitude and phase response of the third order RC passive low pass filter for the gate bias of the LO.

Filter for HEB monitors:

Since filtering of the feed back voltage to the bias board should be not lower than 10 kHz [Vries, 2007]; thus, the cut off frequency of two HEB monitors (voltage and current monitor) is designed to be about 34 kHz with first order passive RC (R=100 Ω, C=47 nF). eq. 6-21 is a Fourier transform of the transfer function in eq. 6-20. The gain and phase response are shown in Figure 6-40.

$$\frac{Vo}{Vin} = \frac{1}{RCs + 1} \qquad \textbf{eq. 6-20}$$

$$Vo = \frac{1}{\sqrt{1 + \omega^2 R^2 C^2}} \cdot Vin \qquad \textbf{eq. 6-21}$$

Summarization of filtering:

Without the filtering, the cold channel could not be controlled due to the ground loop and EMI between channels. The filters designed reduce the ripple at the gate bias down to ±20 mV_{p-p} and increase the stability of the HEB readout to ΔI=±2μA, ΔV±30μV. Hence, the cold channel is efficiently controlled. The grounding design of the whole TELIS instrument and the EMI reduction should be improved in order to get a better accuracy of the controlled bias of the cold channel (HEB and LO). As a result, not only the sensitivity of the 1.8 THz channel can be improved, but also the cold channel can be better stabilized.

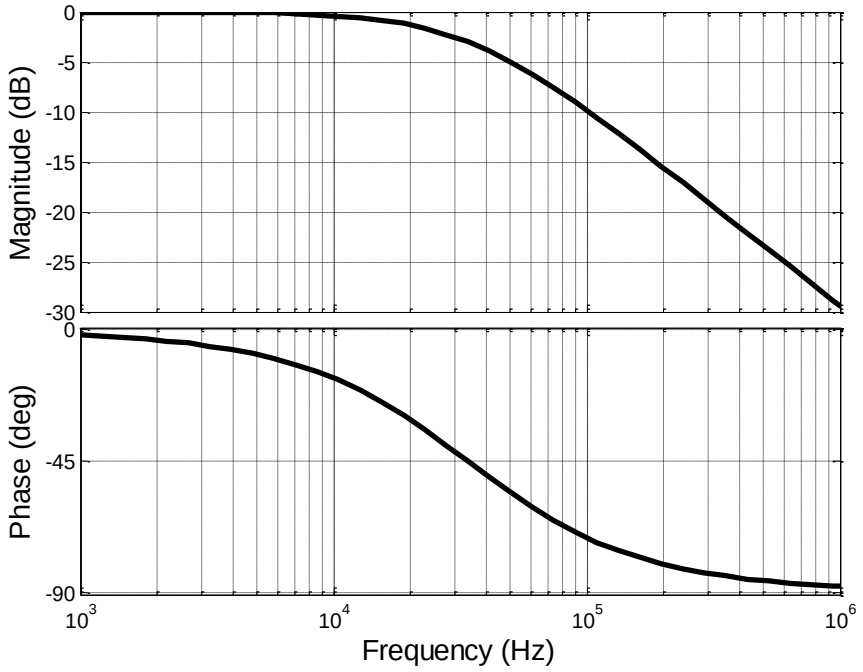

Figure 6-40 : Magnitude and phase response of the first order RC passive low pass filter of two HEB monitors (Voltage and current)

6.2.5 Heat transfer of the 1.8 THz channel

How long the cold channels can operate during the flight, depends on the holding time of the cryostat because the HEB mixer works at the superconducting transition temperature. Therefore all cables applied to the 1.8 THz channel were designed [Suttiwong, 2006] to minimize heat transfer in order to increase the holding time of the cryostat. The largest heat losses are caused by the heat transfer from 300 K to 4 K and the power dissipation in the wires. The heat capacity of devices installed inside the cryostat is negligible compared to these two parameters because the temperature can be kept constant after minutes.

Heat transfer of wires:

The power loaded to 4 K due to the heat conduction of wires can be determined from the following equation.

$$P = \frac{A}{L}\int_{T1}^{T2} q dT \qquad [W/m] \qquad \textbf{eq. 6-22}$$

where P is the power loaded to 4 K due to the heat conduction having unit in watt per meter. A is the area of a wire having unit in quadrant meter and L is the length of a wire having unit in meter. The specific heat, q, is integrated from T_1 to T_2. The power dissipation (P) produced from the current (I) flowing into wires can be calculated by the following equation.

$$P = I^2 \cdot R \qquad [W]$$
$$R = \rho \frac{L}{A} \qquad [\Omega] \qquad \textbf{eq. 6-23}$$

The resistance of wires (R) depends on the diameter, length, resistivity (ρ) and material of wires. The Phosphor bronze (ϕ=125 μm) and Manganine (ϕ=250 μm) with isolation are used for bias and sensing wires because their heat conductivity is very low and they can be applied at superconducting temperature. Due to the temperature dependence of the resistivity and the specific heat, two temperature ranges (300 K-77 K and 77 K-4 K) were separately calculated as shown in Figure 6-41.

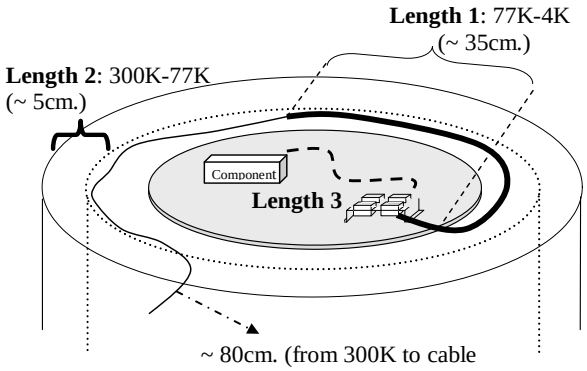

Figure 6-41: The schematic shows the length of wires at two different heat gradients, 300 K to 77 K and 77 K to 4 K.

Figure 6-41 represents the heat transfer from outside the cryostat (at 300 K) to the cable bench being on the THz channel-optical bench (at 4 K). The heat transfer from 300 K to 77 K is 96.10 mW and the heat transfer from 77 K to 4 K is 6.10 mW. The overall heat transfer of wires from 300 K to 4 K is the sum of the heat transfer calculated from two different heat gradients which is about 102 mW (see Appendix D).

Heat transfer of the SMA cables:

The SMA Cable connected to the output of the HEB mixer is another additional heat load. To reduce the heat transfer between 300 K and 4 K while trying to have a lower signal attenuation, the stainless steel SMA cable (30 cm.) having very low heat conductivity (but poor electrical conductivity) together with the copper SMA cable (50 cm.) having very good electrical conductivity (good heat conductivity) are applied. Both SMA cables have 2.2 mm diameter. The stainless steel SMA cable is connected between 77 K and 4 K while the copper SMA cable is connected between 300 K and 77 K. In this way, the heat transfer from 300 K is reduced, while the electrical conductivity is improved by 70% with respect to using only stainless steel SMA cables. The heat transfer of two combined SMA cables was separately measured in the test cryostat. The sum of the power loaded at 4 K due to the SMA cables yields about 20 mW.

6.2.6 Antenna beam profile of THz channel

The method was developed by Herb M. Pickett at JPL for the characterization of the 2.5 THz MLS channel [Pickett, 2006]. Using a copy of the telescope in front of the TELIS telescope, an image of the TELIS telescope focus is created containing the field of view information.

The azimuthally collapsed beam profiles of the three cryogenic channels of the TELIS instrument were measured by mean of placing a slit source in the focus of the *compact range*, scanning the TELIS telescope and measuring the total IF power. In this thesis only the measured results of the 1.8 THz channel are presented. The *compact range* has a copy of the primary and the secondary mirror of the TELIS telescope but no tertiary mirror as shown in Figure 6-42. The slit is positioned in the focus of a horizontally extruded elliptical cavity with the mercury arc lamp in the other focus. The mercury arc lamp has a cylindrical shape with a 15 mm horizontally and 5 mm vertically extended 2500 K hot plasma [Birk, et al., 2009]. The schematic of the antenna beam profile measurement is shown in Figure 6-43

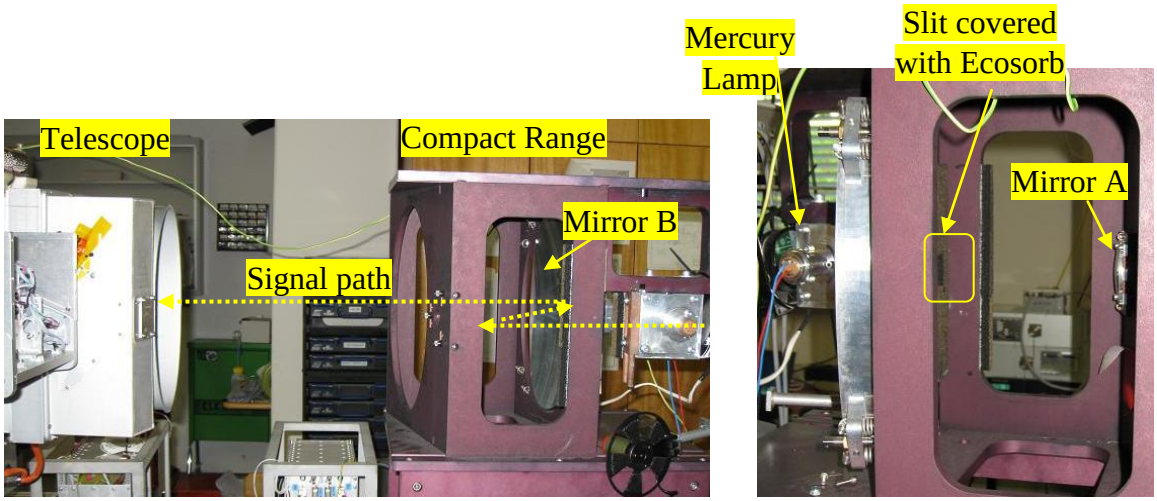

Figure 6-42: illustrates photos of the setup for the optics and components applied in the optical path. The signal path starts from the light source (mercury lamp) through the slit and is reflected at the mirror A (small mirror: a copy of the secondary mirror of TELIS telescope) and the mirror B (big mirror: a copy of the primary mirror of TELIS telescope) before the light beam is coupled to the telescope of the TELIS instrument.

The effective focal length of the telescope is 1329 mm. The image of the slit source was examined (the mercury arc lamp emits visible light) at the telescope focus and the telescope angle was adjusted to center the image on the (geometrical) optical axis corresponding to a telescope angle of -0.12°±0.02°.

The beam profile measurement was conducted with 0.8 mm and 1.6 mm slit width. A software tool was implemented to control the telescope and retrieve the readout of the IF total power. There are two possibilities to retrieve the power: retrieving the readout power directly from the power meter (direct measurement) and retrieving the voltage difference

via a lock-in amplifier. By placing a chopper in front of the slit source and detecting the signal via a lock-in amplifier, the signal-to-noise ratio can be improved.

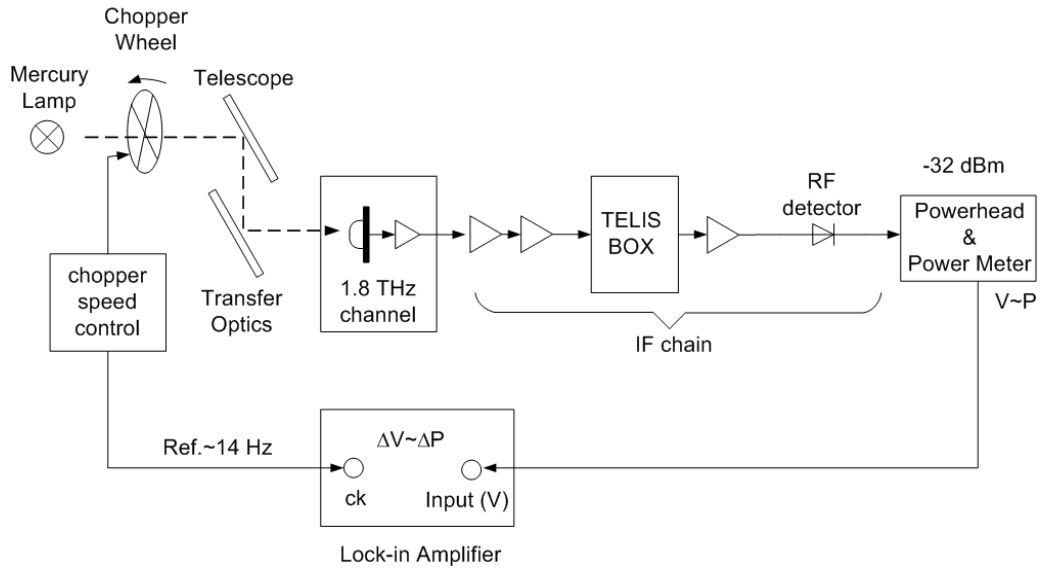

Figure 6-43: shows the schematic of the measurement setup and how the power output is retrieved.

Three consecutive readouts within a step were retrieved. The readouts were done after the movement of the telescope was stabilized whereas the time constant of 0.2 seconds was set after positioning the telescope. The step increment for the beam profile measurement of the 1.8 THz channel is 0.01°. Upwards and downwards stepping sequences were measured to detect and correct for any time- or direction-dependent effects in the measurement. Two different LO frequencies were used to ensure that the LO frequency was not influencing the measurement.

Figure 6-44 (a) is a comparison of the beam profile measured with 0.8 mm slit width during the telescope was scanned upwards and downwards. The comparison of the beam profile scanned upwards and downwards with 1.6 mm. slit width is shown in (b). Nevertheless all beam profiles scanned in the same direction are reproducible as shown in Figure 6-44 (c) and (d). The maximum of the beam profile is at -0.05 degree.

The results are plotted in linear scale as shown in Figure 6-44 in which the setting angle of the telescope was used instead of the actual angle of the telescope (the angle readout) ;therefore, the profiles with upwards and downwards direction show the scan direction and the angle dependency where it can be later calibrated by using the calibrated offset calculated by means of the readout from the angular sensor mounted at a motor of the telescope and the time stamp during the readout retrieved.

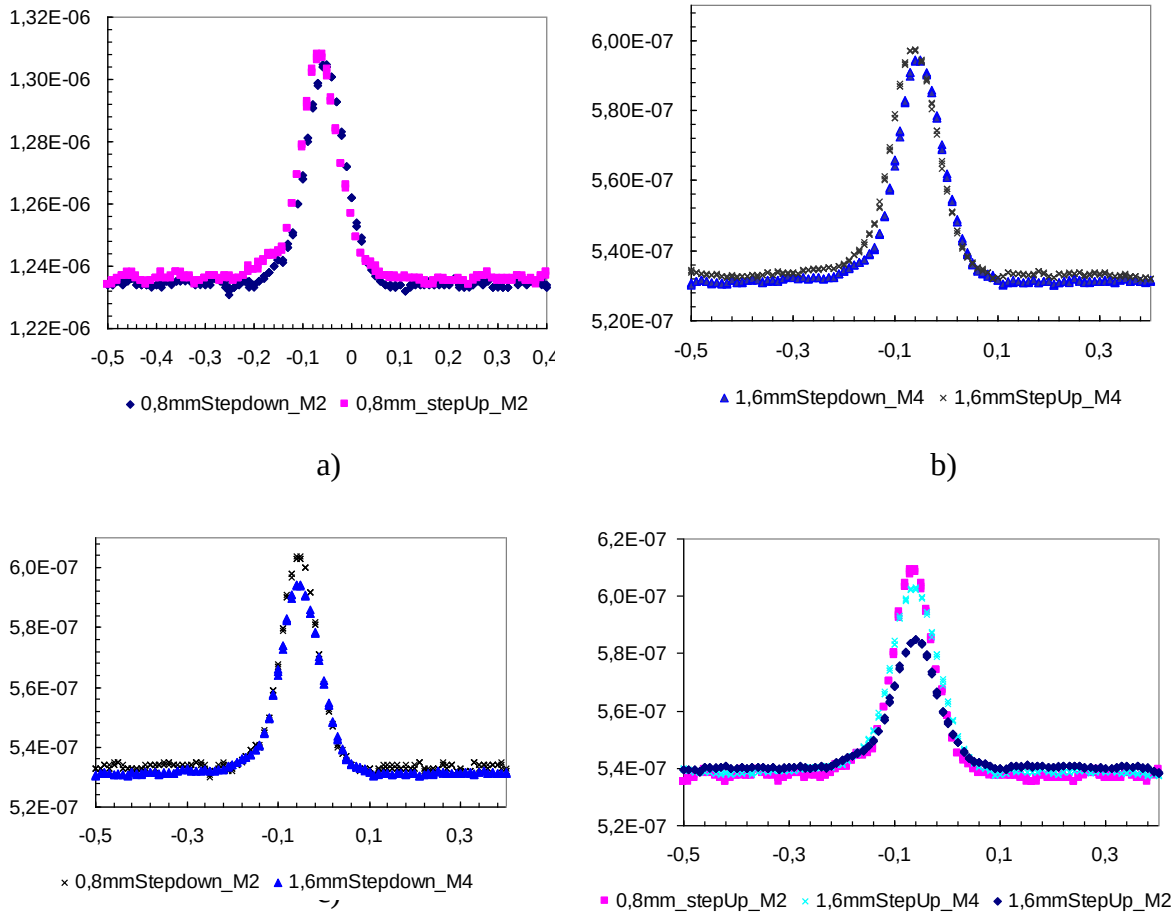

Figure 6-44: (a) A comparison of the beam profile measured while the 0.8 mm-slit was installed inside the compact range and the telescope was scanned in both upwards and downward directions. (b) A comparison of the beam profile scanned upwards and downwards while the 1.6 mm-slit was installed. (c) and (d) show the repeatability of the telescope while it scanned in the same direction.

After correcting the measured beam profiles with the calibrating offset [Birk, et al., 2009] and fitting with a Gauss function, upward and downward scans are in good agreement. The full wave half maximum (FWHM) of the beam profile of the 1.8 THz channel is 0.1043° (6.3').

6.2.7 Characterization of the 1.8 THz channel in Single Side Band mode (SSB)

All measurements described above were conducted in Double Side Band (DSB) mode. In Single Side Band (SSB) mode, an unwanted side band is suppressed by using the SSB filter based on the Martin-Puplett Interferometer (MPI). The difference between SSB and DSB devices is just the path difference. The diplexer has a path difference which two times larger than the SSB. The SSB filter was installed and tested in the test cryostat with the FIR laser at 1.6266026 THz due to the delay of the solid state LO during the test period. By using the autocorrelator spectrometer the system noise temperature spectra across 2 GHz bandwidths (4-6 GHz) can be measured.

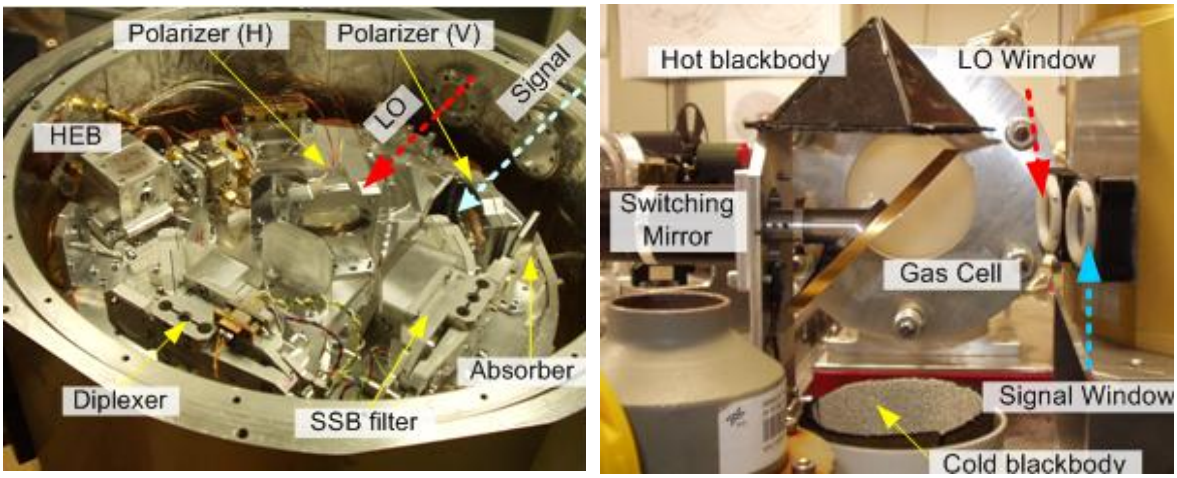

a) **b)**

Figure 6-45: a) a photo showing the setup of 1.8 THz channel inside the test cryostat. b) The photo presents the optical setup of the noise temperature measurement.

The signal path is 27.5 cm. and has a loss of about 20% due to the water vapour in the air. The loss of a quartz window is 10% and that of two layers of Zitex blocking filter is 15%. The total loss in the optical path is 45%. The test cryostat has two separate windows: one for coupling the FIR laser and the other for coupling the signal from the hot- and cold load. The hot load being the Ecosorb is glued inside the special roof top for reducing the standing wave in the optical path.

Table 6-2: The line center of the signal and its side band. LSB is lower side band and USB is upper side band.

#	Side band	Signal frequency (GHz)	IF frequency (MHz)
1	LSB	1621,8099	4793
2	LSB	1621,9270	4676
3	LSB	1622,0961	4506
4	USB	1632,4826	5880
5	USB	1632,5611	5958

In Table 6-2 are the frequencies of the methanol lines which can be measured at the (FIR) laser 1.6266026 THz. Figure 6-46 illustrates the results of the methanol measurement in which the IF frequency of the line centre is as expected. However the feature of both NT spectra is different. The feature of the system noise temperature spectra changed when the SSB filter was detuned as shown in Figure 6-47.

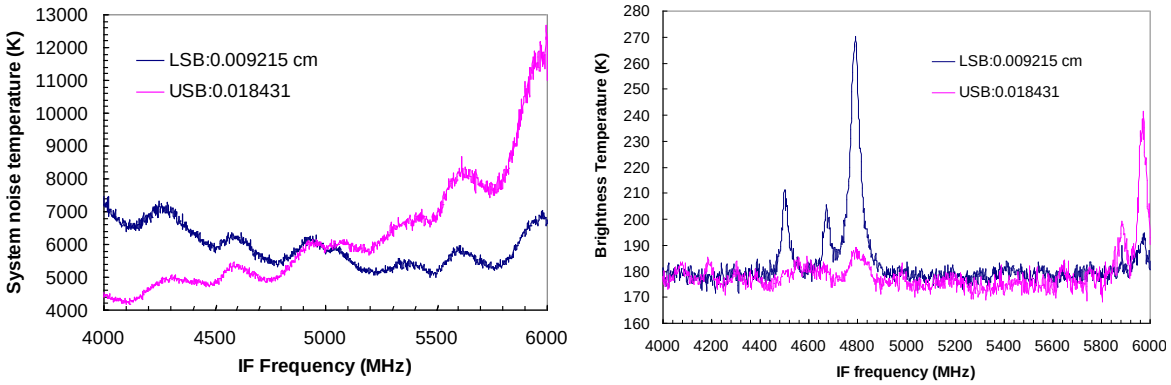

(a) (b)

Figure 6-46: (a) A comparison of the LSB and USB noise spectrum. (b) The methanol line was measured while the SSB filter was tuned to LSB and USB.

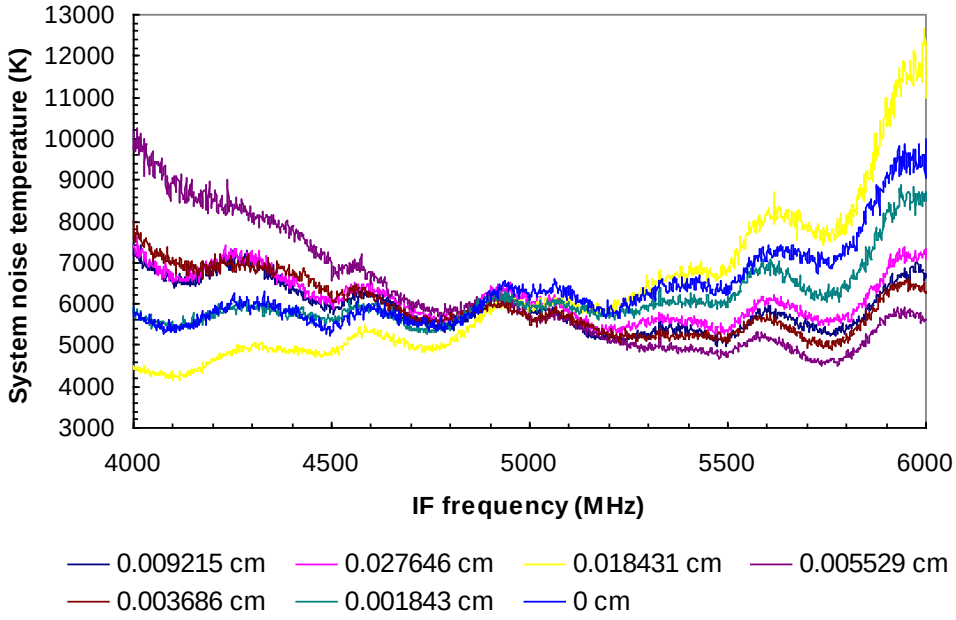

Figure 6-47: System noise temperature spectra at different detuning of the SSB filter at ΔOPD 0cm = 1.50667296450677 cm.

However, the averaged noise temperature across 2 GHz bandwidth of each NT spectrum is about 6200 K as expected. The first assumption for describing the change of the NT spectrum feature could be the Fabry-Perot effect. Nevertheless, this problem was not further investigated because it was found that there was a problem with interference of low frequency (20-20 kHz) in the cryogenic channel in which it disturbed the measurement. It is possible that the low frequency interference was generated by the LVDT of the SSB filter feedback electronics. Due to the limitation of time before the first flight in Teresina, it was decided to operate the 1.8 THz in DSB mode.

6.3 Autocorrelator and microwave backend characterization

The Autocorrelator plate (ACS plate) is located at the backend of the TELIS instrument. It consists of the microwave backend, connected to the IF output from the HEB mixer, and the autocorrelator spectrometer as shown in Figure 6-48. The IF output signal from the HEB mixer (4-6 GHz) is downconverted to 1.75 to 3.75 GHz by using another mixer and a LO at 7800 MHz which are both located inside the TELIS box.

This section will start with explaining the design of the Autocorrelator followed by an explanation of the consideration for operating the Autocorrelator and the strategy used for initializing the Autocorrelator during the flight. Then the calibration of the RF detector used for monitoring the input power of the Autocorrelator, and finally the results of the linearity and the stability will be discussed.

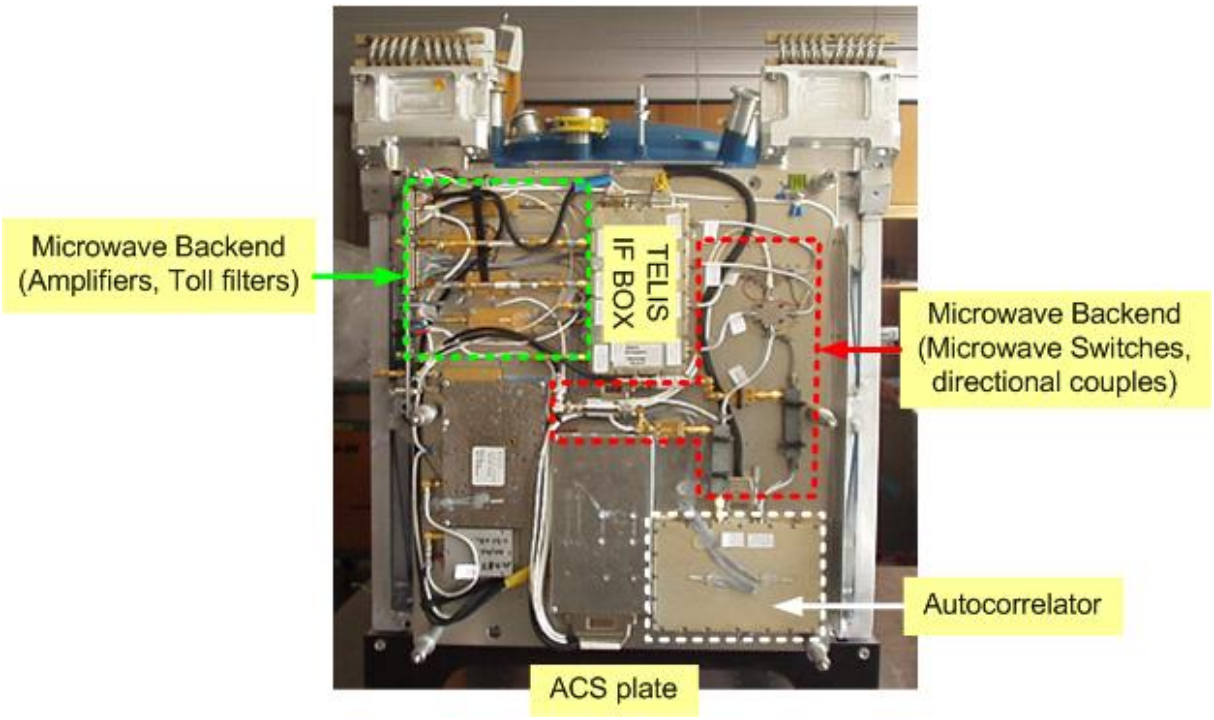

Figure 6-48: shows the back view of the TELIS instrument which locates the ACS plate (autocorrelator spectrometer plate). On the ACS plate, several microwave backend components are installed (for instance amplifiers, two *toll filters*[22], two directional couplers, microwave switches etc.)

6.3.1 Design of the autocorrelator spectrometer

The autocorrelation spectrometer (*ACS*[23]) of the TELIS instrument consists of three subsystems which are the TELIS IF box, the TELIS Spectrometer and the 4G Spectrometer. The 4G Spectrometer is provided for the RAL channel (RAL1 and RAL2) which handles the IF frequency from 2 GHz to 4 GHz. In the IF box is only amplification but no frequency conversion in case of the RAL channels. The TELIS Spectrometer consists of two channels, DLR channel and SRON channels. The SRON channel operates

[22] The toll filter is an equalizer.
[23] The ACS for DLR channel of the TELIS instrument is developed from Omnisys Instruments company

at an input frequency from 5 GHz to 7 GHz. The DLR channel operates at an input frequency from 4 GHz to 6 GHz (2 GHz bandwidth). Figure 6-49 (a) shows the block diagram of the TELIS IF box for the DLR and SRON channels. The output signal from the heterodyne receiver of both channels will pass through a very steep band pass filter (not shown in the figure) before reaching the TELIS IF box. The input power levels after the heterodyne receivers should be -10dBm/GHz. The signal will be mixed with the local oscillator at 7800 MHz and 8800 MHz at the DLR and SRON channels in order to down-convert these two input signals to 1.75-3.75 bandwidths. The output signal from the TELIS IF box will be passed to the TELIS spectrometer to perform the correlation.

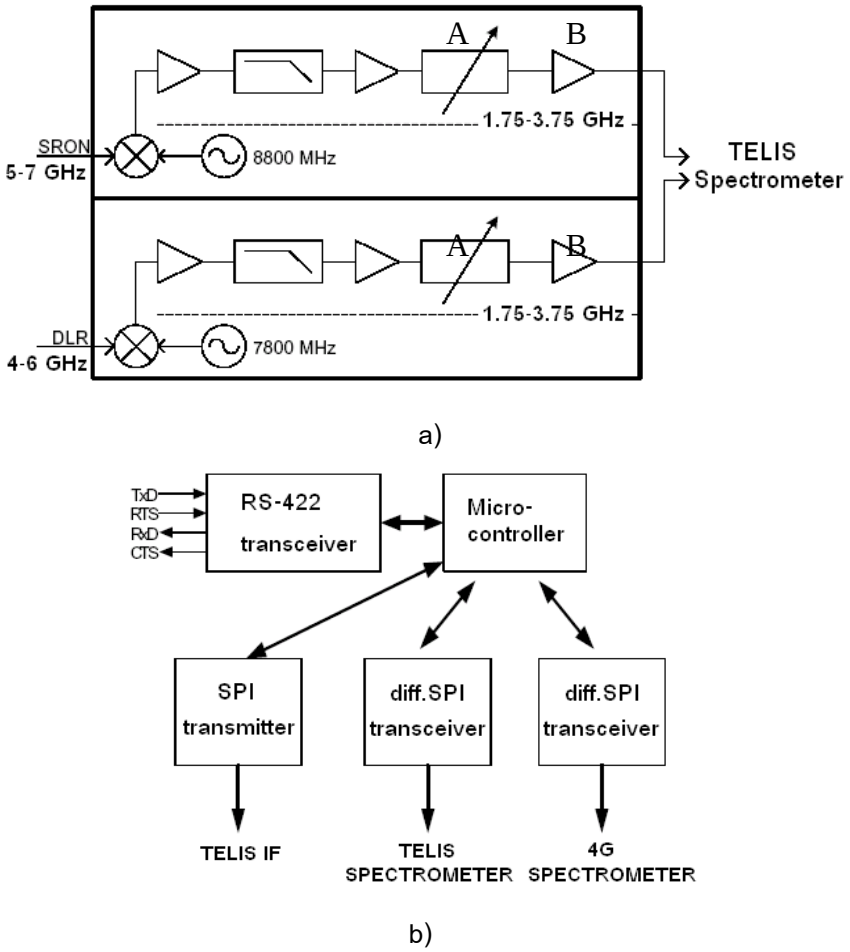

Figure 6-49 : (a) block diagram of the IF of the DLR channel of the TELIS IF box. "A" is an programmable attenuator controlled by a Microcontroller. "B" is the last amplifier inside the TELIS box. (b) Block diagram of the communication board of the TELIS IF box.

Figure 6-49 (b) is the block diagram of the communication board of the TELIS IF box. A Microcontroller is the processor to perform the communication between the IF signal, the spectrometers and the computer. The communication between the TELIS IF and the spectrometers is performed by the serial peripheral (SPI) interface. The communication between the TELIS IF box and the computer is performed via RS-422/RS485 interfaces. Omnisys developed a LabVIEW code for the PC for controlling the IF-box and

spectrometers. A further MATLAB tool was supplied by Omnisys for further data analysis such as quantization correction and Fourier-transformation.

The IF signals, after down-converting from the TELIS IF box to 1.75-3.75 GHz bandwidth, are fed into the TELIS spectrometer. The spectrometer is divided into three major subsystems, the IQ down-converters, the correlator section, and the supporting power subsystem as shown in the Figure 6-50. The IF-box is shown in the left part of the figure. The two input signals are each fed to four IQ down-converters which each processes 500 MHz of the 2 GHz wide input band. Each IQ converter will perform two 250 MHz wide I and Q signals and feed these into the correlator part. Since the local oscillator frequency is different for each of the down-converters the full bandwidth of 2 GHz is covered. Very steep 250 MHz filters truncate the signal for obtaining the desired spectral interval. Due to the IQ processing, the input signal is converted into two signals with 90° phase shift, and is later on digitized with two separate 1.5 bits A/D converters. This yields a spectral range from –250 to +250 MHz for each converter, thus with a sampling rate of 500 MHz a spectral range of 500 MHz results.

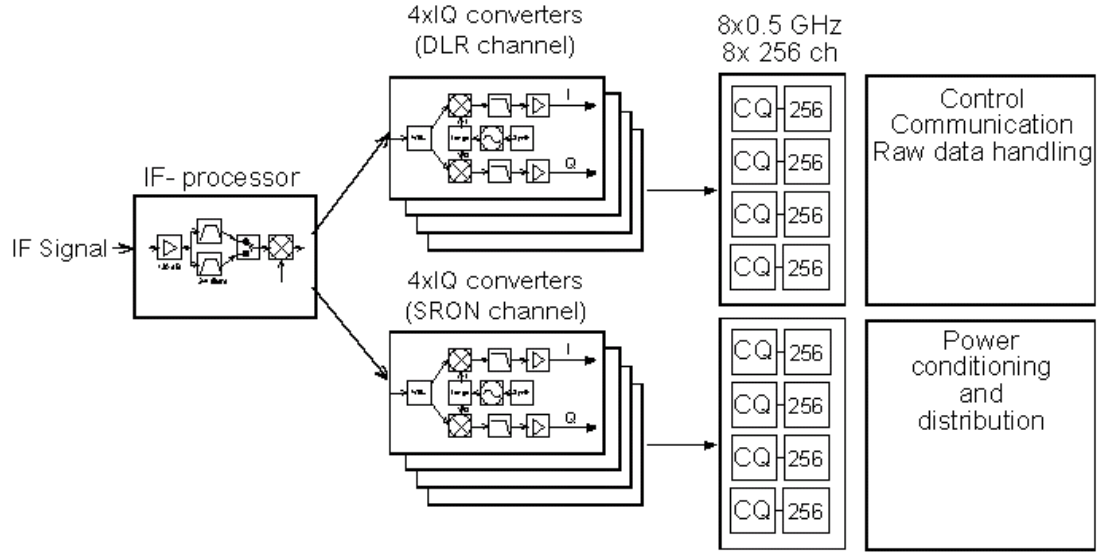

Figure 6-50: The system architecture of the TELIS spectrometer [Omnisys Instruments AB, 2004].

The correlator part consists of two 1.5 bit analog to digital converters for each correlator chip (CC). The two I and Q signals are digitized and fed to 128 lags autocorrelator chips. Each lag has 4 chips collecting I^2, Q^2, I*Q and Q*I. The correlation data is read and the processed data stream is stored in local memory, before it is transferred to the external control computer via the TELIS IF box. The Fourier-transformation of the 4*128 correlation data yields 256 spectral channels [Suttiwong, 2004].

6.3.2 Considerations for operating the Autocorrelator and strategy for initializing the Autocorrelator spectrometer

Two parameters of the Autocorrelator which must be properly adjusted before operating the Autocorrelator in order to avoid the nonlinearity are the input power of the autocorrelator and the *reference levels* of the 1.5 bit ADC.

The input power of the Autocorrelator can be adjusted by changing the *programmable internal attenuator* located inside the TELIS box (see Figure 6-49 "A" and "B"). The optimum input power which yields the counts of the ADC monitor around 25% was carefully determined and it should not drive the last amplifier above the 1 dB compression gain or rather into saturation (-7dB). By using the directional coupler and the RF detector (see Figure 6-48), 1% coupling power from the input power of the spectrometer can be monitored and the *internal attenuator* setting corresponding to the optimum input power of the autocorrelator is possible and can be adjusted automatically by software.

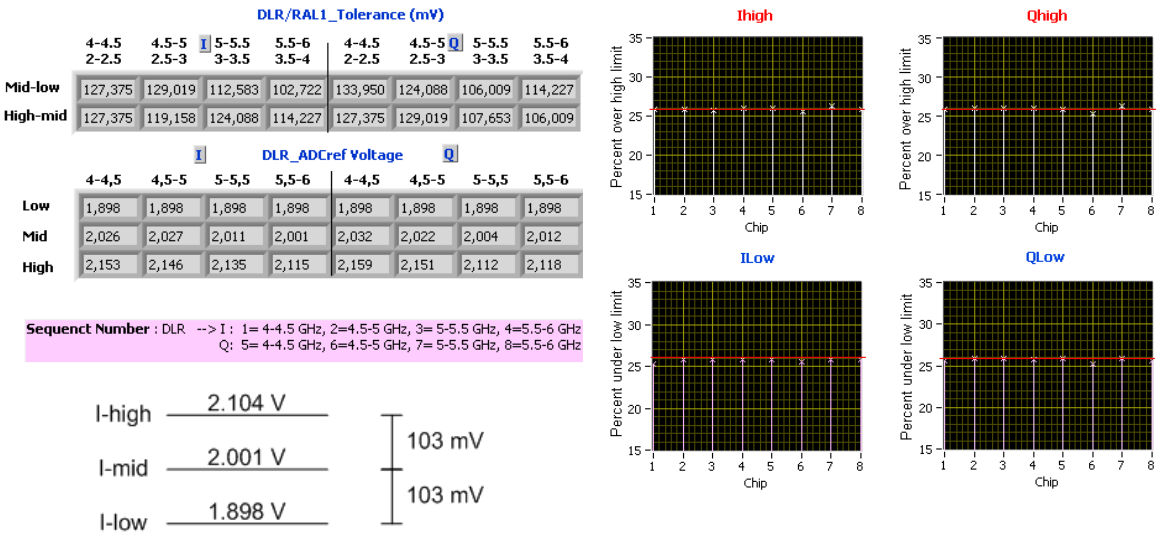

Figure 6-51: (a) The ADC reference monitor for each ADC chip having 500 MHz bandwidth. The graph shows the tolerance of the reference level of the ADC (mid-low and high-mid). (b) Counts in percentage over the high limit and under the low limit of the I and Q signal. The red horizontal line shows the upper limit of the counts.

The *reference voltages* of the 1.5 bit ADCs can be optimized either manually or automatically via a "*autocalibration*" command. Using the command *autocalibration* the *reference voltage* of each 1.5 bit ADC chip is calculated from the analog input power dissipated on it (500 MHz). Thus, in case of optimal input power, the *reference voltages* of the 1.5 bit ADC chips can be adjusted automatically with the command *autocalibration.* The optimized reference voltages should be within a tolerance of a voltage of 103 mV ±30 mV [Stenman, March 2006] as shown in Figure 6-51(a).

The process of optimizing the *ADC reference level* by using the command *autocalibration* can be shortly described as follows. The output 1-bit stream of the sigma-delta ADC must be firstly monitored before adjusting the reference level by using a digital to analog converter (DAC). The ADC monitor consists of counters, each monitoring the number of samples in each output state [Omnisys Instruments AB, 2005]. This information would then be processed and used to adjust the ADC reference levels through a DAC. The adjustment can be made in real-time or as a part of an auto-calibration procedure.

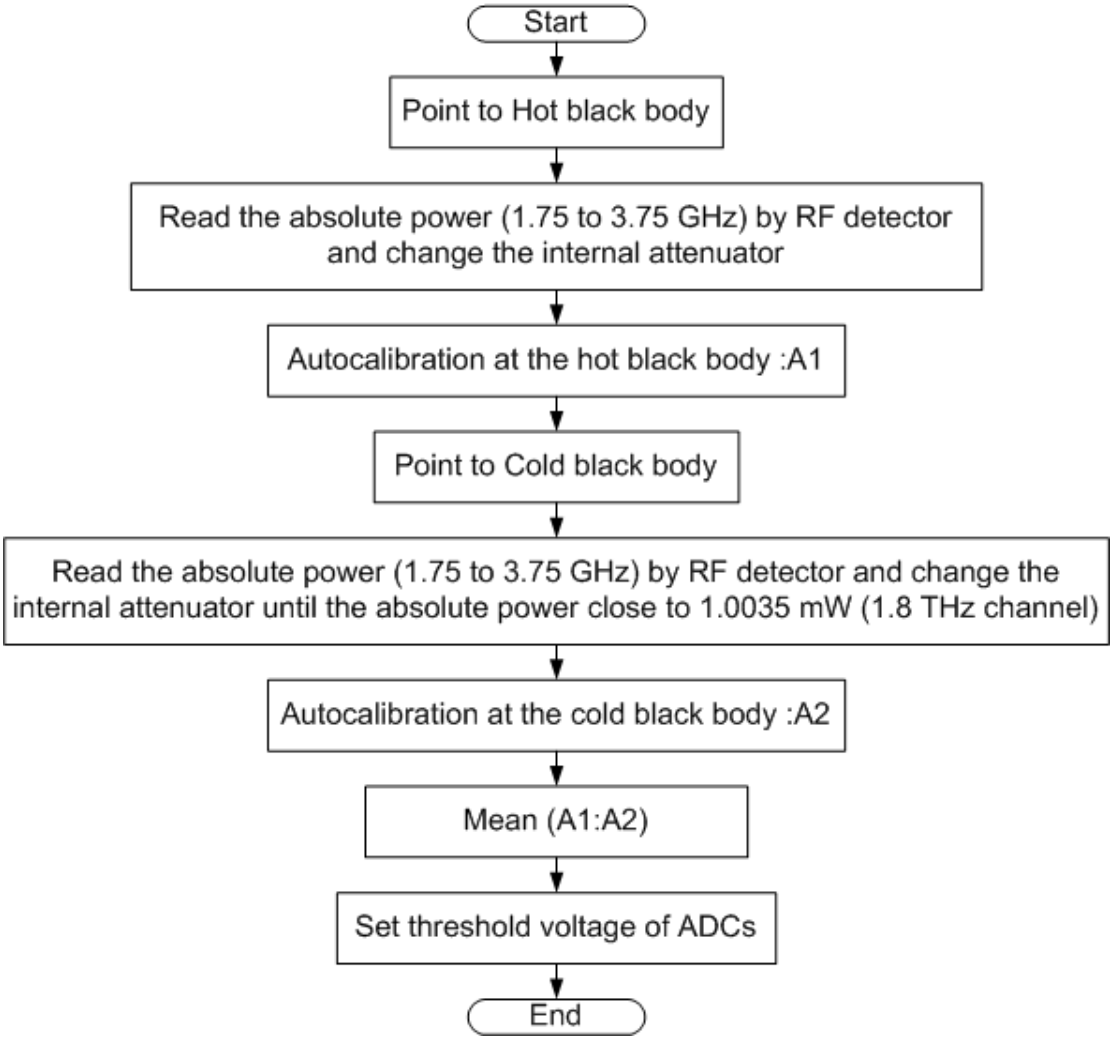

Figure 6-52: Flowchart represents the auto-calibration process operated automatically by the autocorrelator flight software.

Due to the fact that the reference voltage of the ADC chips must be optimized before starting the radiometric measurement (Hot-Limb1-Limb2-…Cold-Hot-Limb1-Limb2…), the extra software for initializing the autocorrelator on the flight plays an important role. The process to optimize the reference voltage of the ADC chips called "auto-calibration" and the autocorrelator must be auto-calibrated before starting the measurement. In the radiometric calibration, the radiometric spectra are calculated from three different spectra measured from different temperatures radiated from blackbodies (two referent

blackbodies and one signal). During the flight the telescope together with the switching mirror are used to switch between three sources. As a consequence, the power input of the autocorrelator spectrometer changes as the telescope switched from one source to another. The optimal reference voltage for the ADC chips is then calculated from the mean of two optimal reference voltages while the telescope is switched to the hot blackbody and to the cold blackbody (deep sky is used as a cold blackbody during the flight) as shown in the flowchart in the Figure 6-52.

During the flight, the initialing process must be redone when the input power of the Autocorrelator drifts more than ±1 dB (from the initialization). The drift of the power is automatically detected in the flight software. The RF detector is applied to monitor the drift of the input power of the Autocorrelator. Each channel has an individual RF detector and they were carefully calibrated which will be further described.

6.3.3 RF detector calibration.

The heart of the detector circuit of a typical RF detector is a diode, whose non-linear behavior is applied for detecting the incident radio frequency. The diode rectifies the incident power, providing a signal that is of one polarity to the bypass capacitor, with amplitude proportional to the input power level following the square law [Smith, 1998]. For a certain range of power levels, a detector output voltage is proportional to its incident power measured in watts.

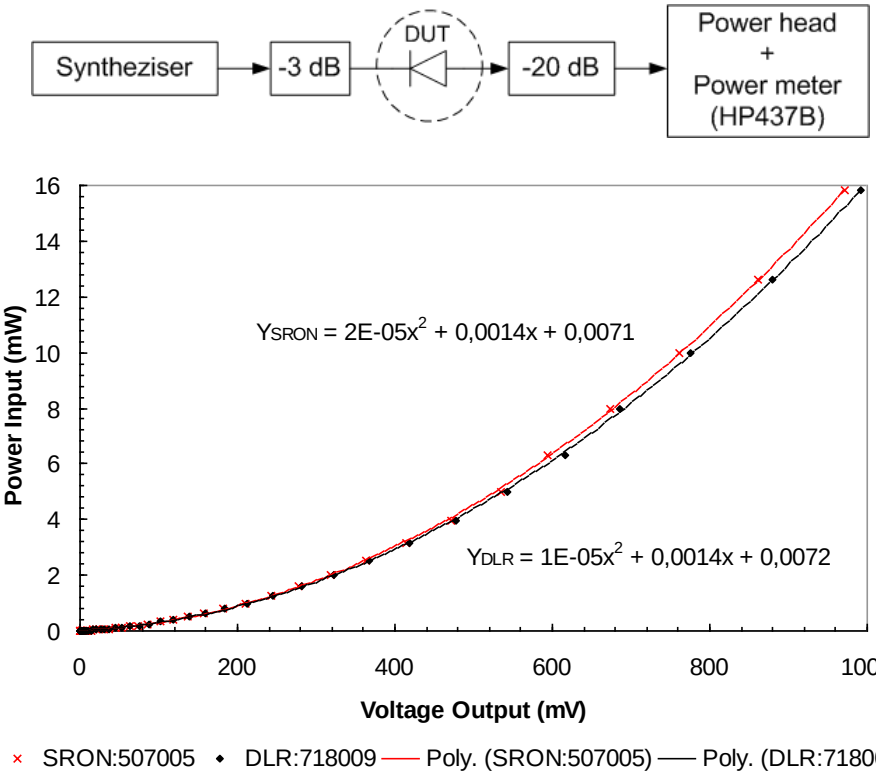

Figure 6-53: The calibration curve of two RF detectors applied for the 1.8 THz channel (DLR) and 600 GHz channel (SRON)

The RF detectors are used in the TELIS instrument to monitor the absolute power at the input of the autocorrelator and each of them was individual calibrated before using. Figure 6-53 shows the calibration curve of two RF detectors applied to the DLR channel and SRON channel and the measurement setup for measuring the output voltage being proportional to the incident input RF power.

The sensitivity of the RF detector is also temperature dependent and this issue must be considered because the temperature could be down to -10°C during the flight. In the flight setup, the total load resistance is in MΩ by which the sensitivity of the RF detector could slightly increase up to 0.5 dB at the temperature lower than 25°C according to the typical sensitivity change of the RF detector from Anritsu [Anritsu, 2006]. However, during the first two flights the temperature on the RF detector was not possible to detect directly due to a technical problem. Therefore the RF detectors were mainly used for pre-monitoring of the input power of the Autocorrelator before the manual *autocalibration* was carried out (at the surrounding temperature lower than 0°C)

For the ground calibration, degradation of the RF detector must be taken into account and degradation is usually caused by either static discharge or its lifetime. The noise temperature calculated directly by the absolute power measured from the RF detector can be changed due to the degrading of the RF detector.

6.3.4 Linearity of the microwave backend

The linearity of the IF chain and the *autocorrelator spectrometer*[24] is an important issue for the radiometric calibration. The linearity experiment of the autocorrelator was done before the first flight in Teresina (Brasil), in order to determine the accuracy of the input power at the autocorrelator with the same auto-calibration which can be used in the radiometric calibration and doesn't get nonlinearity. In the experiment the absolute power measured from both the autocorrelator and the RF detector at different temperatures of the source was measured.

Figure 6-55 depicts the setup of the experiment for the linearity measurement. The liquid nitrogen was applied as a liquid source at temperature of 77 K. Isopropanol mixed with the liquid nitrogen (198.12 K, 200.84 K, 242.92 K, 247.56 K, 293.52 K, and 294.32 K) was used as the liquid source for the temperatures higher than 200 K. Methyl-Cyclohexan (146.42 K, 146.61 K) was used as the liquid source for the temperatures lower than 200 K. A 50 Ω - terminator (SMA) was immersed in several liquid sources and the power proportional to the equivalent noise temperature (thermal noise) generated from the 50 Ω - terminator together with the equivalent noise temperature of the rest of the system was monitored by the autocorrelator and the RF detector simultaneously.

[24] The microwave backend of the TELIS instrument starts from the output of each heterodyne channel until the autocorrelator spectrometer. This microwave backend consists of several microwave components, for instance the MDM amplifiers, equalizer, mixers etc. Many microwave components locates inside the TELIS box are another heterodyne system which is applied for down-converting the 1.8 THz channel from 4-6 GHz to 1.75-3.75 GHz.

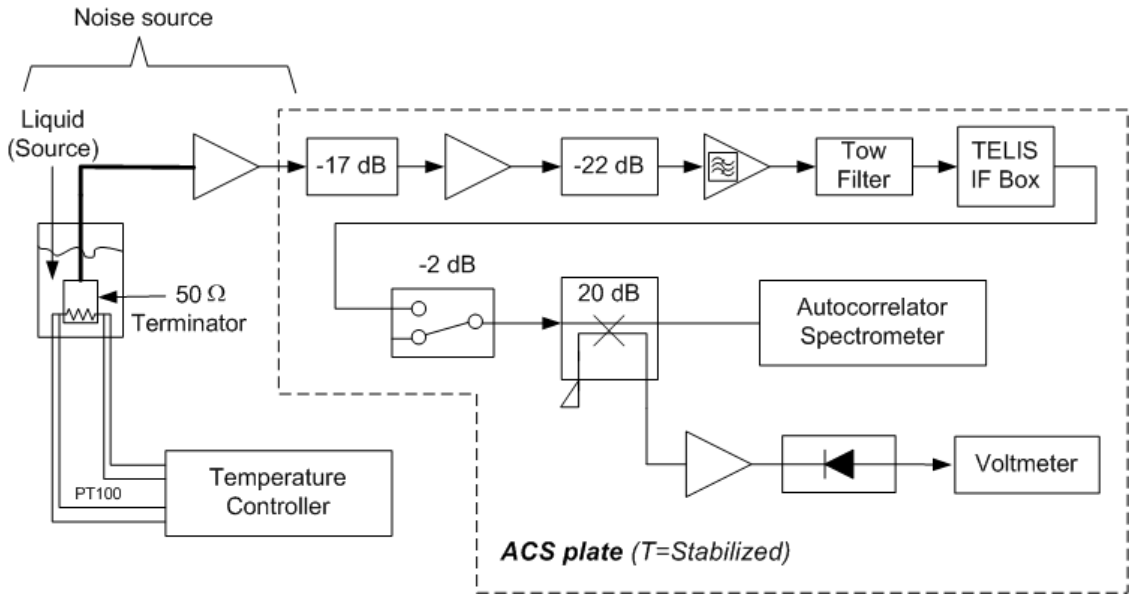

Figure 6-54: The schematic shows the experiment setup for testing the linearity of the autocorrelator comparing with that of the RF detector.

The power measured at the output is a contribution of two main noise sources: The 50 Ω - terminator as a thermal noise source and the noise generated from the rest of the system. The 50 Ω - terminator is a conductor which has an impedance of 50 Ω. According to the standard theory of thermodynamics, the kinetic energy of an electron is proportional to its temperature, and these random motions of the electrons produce fluctuations in the electric charge which produce voltage fluctuations [Ulaby, et al., 1981]. The noise voltage generated by the resistor is called the thermal noise and can be written as the following equation: [Nyquist, 1928]

$$V_{rms}^2 = \overline{V_n^2(t)} = 4RkTB \qquad \textbf{eq. 6-24}$$

$$P_n = \frac{V_{rms}^2}{4R} = kTB \qquad \textbf{eq. 6-25}$$

V_n is the noise voltage generated by the resistor and its root mean square (V_{rms}) value is not zero. Where k is Boltzmann's constant and B is called the noise bandwidth which is determined by the filter at the third amplifier (2 GHz). T represents the temperature at the 50 ohm terminator depending on the liquid sources. P_n represents the power generated from the 50 ohm terminator which depends on its temperature and the bandwidth.

Basically the output noise power measured by the RF detector and the autocorrelator is the sum of the noise power generated from the 50 Ω terminator and the noise power of the rest of the system (or called *the system noise*). *The system noise* was assumed to be constant due to the temperature stabilization of the autocorrelator plate and constant biases of the microwave components. Therefore, the total noise power output can be

approximated by the following equation whereas the temperature of the 50 Ω - terminator (T_{res}) dominates the change of the output power (P_{out})

$$P_{out} \cong 4R(T_{res} + T_{sys}) \qquad \textbf{eq. 6-26}$$

A standing wave can occur due to the impedance mismatch caused by the resistor change due to the change of the temperature of the 50 Ω terminator. There was no input-matching-network between the noise source and the IF chain. Nevertheless, only the absolute power across the 2 GHz bandwidth was considered, and the standing wave problem was ignored. A comparison of the absolute power measured by the RF detector and the one measured by the autocorrelator is shown Figure 6-55. The absolute power measured by the autocorrelator is calculated from the sum of all channels of the spectrum (926 channels) and its unit is arbitrary. During the measurement, the autocorrelator was auto-calibrated and set at one fix internal attenuator (7 dB) being *the optimal setting for the ADC chips*[25].

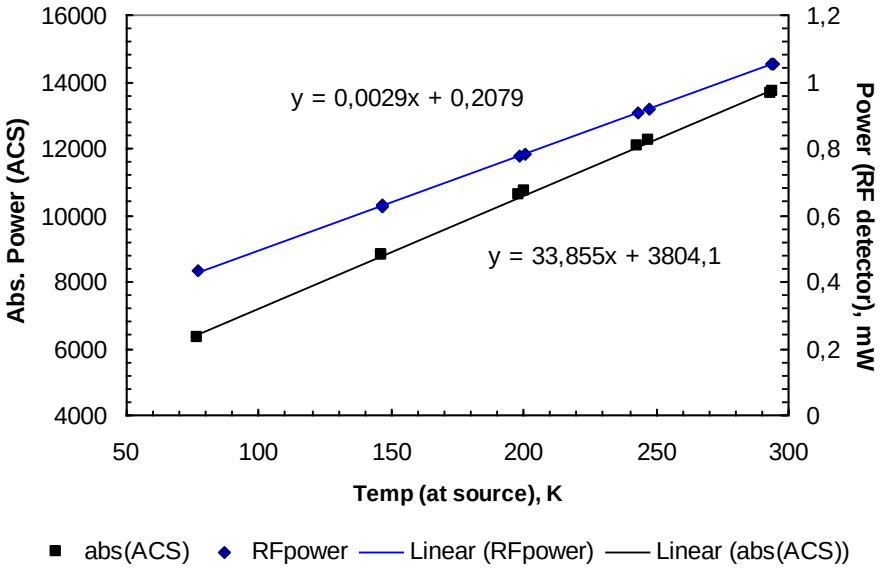

Figure 6-55: A comparison of the absolute power measured by the RF detector and by the autocorrelator spectrometer. X-axis indicates the temperature of the sources.

Figure 6-56 depicts the result of the linearity measurement in dB. X-axis represents the power generated by the 50 Ω terminator as eq. 6-25 by using the power generated at 249.92 K as a reference (at zero *dB*[26]). Y-axis; power measured by the autocorrelator and by the RF detector, shows the output power which is the sum of the change of the power

[25] The optimal threshold voltage for the 1.5 bit ADC chip is specified for the voltage having a tolerance ±30mV from the reference voltage (103 mV). The value of the internal attenuator varies according to the input power in front of the TELIS box.

[26] $dB = 10 \cdot \log \frac{P}{P_{ref}}$, P_{ref} = the power calculated at the temperature 242.92 K.

at the 50 Ω terminator due to the temperature of the liquid sources and the system noise expected to be constant.

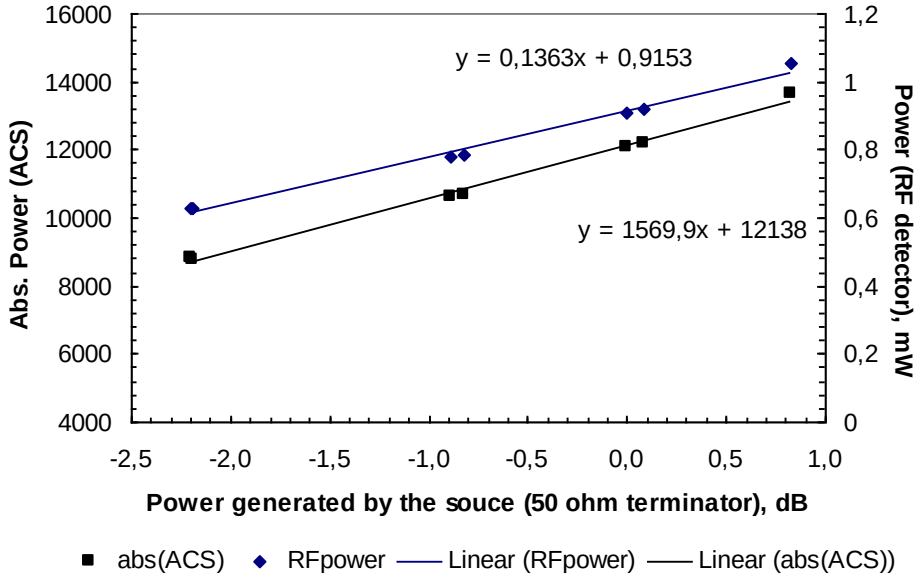

Figure 6-56: A comparison in dB of the absolute power measured by the RF detector and measured by the autocorrelator. The X-axis presents the power generated by the 50 ohm terminator at different temperature in dB. The power generated at 249.92 K is used as a power reference (=0 dB).

The results of the linearity experiment show good dynamic range as shown in Figure 6-56. The autocorrelator was still linear although the drift of the input power was -2 dB /+1 dB from the reference (the initial input power at 249.92 K) where the *autocalibration* was set. The linearity calculated from the power measured by the RF detector is however in coincidence with the one measured by the autocorrelator. Thus, the RF detector can be applied for monitoring the drift of the input power of the spectrometer during the radiometric measurement.

It was concluded from this experiment that the radiometric measurement can be done without the nonlinearity problem as long as the drift of the input power is not above +1 dB and below -2 dB of the initialization. To be sure that nonlinearity effects will not occur during measurements, the measurement in the flight will be stopped when the drift of the input power of the autocorrelator is more than ±1 dB from the initialization value.

6.3.5 Stability of the autocorrelator spectrometer and 1.8 THz channel and IF backend

An experiment was carried out to determine how long the complete receiver, the 1.8 THz channel and the microwave backend including the autocorrelator, are able to operate without nonlinearity effects to occur. The setup of the experiment is shown as in Figure 6-18 above in section 6.2.1 (Flight setup) and the result of the stability measurement is depicted in Figure 6-57.

Figure 6-57 shows a comparison between the stability of the whole system (the 1.8 THz channel, the microwave backend components and the spectrometer) and an ideal system having no drift. During the measurement the temperature of the autocorrelator plate, which locates all microwave backend and the autocorrelator spectrometer, was stabilized at a temperature of 10°C by a cooler. The deviation from the mean value of the ideal system is calculated from $(\tau \cdot B)^{-0.5}$ where τ is the integration time of the spectrometer being 2 seconds and B is the bandwidth being 2 GHz. From the result of the stability measurement, the drift of the whole system in 25 minutes after the initialization is about 0.8% which is much lower than the critical point (at ±1 dB or 16% from the initialization value).

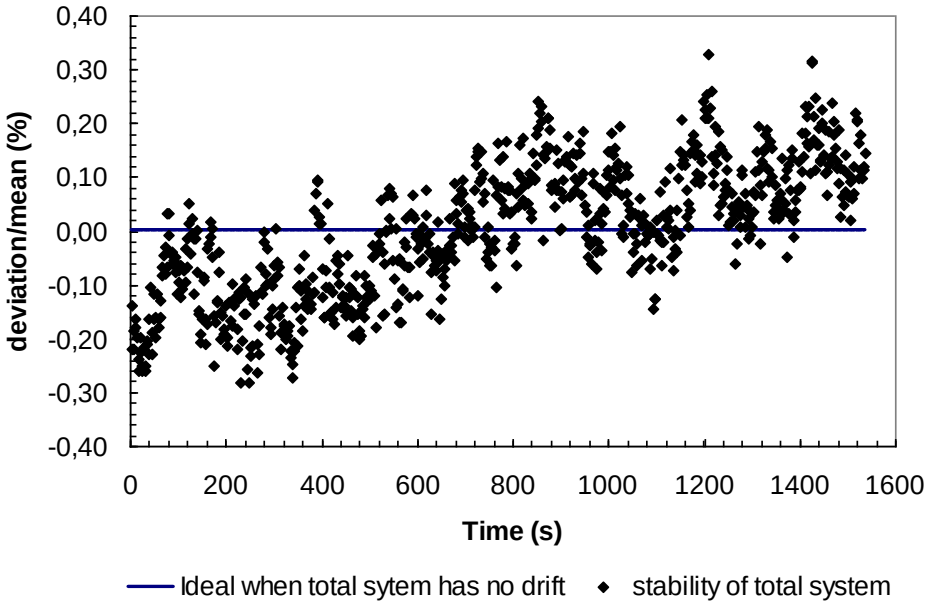

Figure 6-57: A comparison of the ideal system which has no drift and the stability of the whole system (the 1.8 THz chanel, the microwave backend and the spectrometer) in 25 minutes. The temperature of the autocorrelator plate was stabilized at 10°C by the cooler.

Summarization of the linearity and stability of the microwave backend and the autocorrelator:

In order to avoid the nonlinearity problem the power in front of the spectrometer should not drift more than ±1 dB from the initial power where the radiometric measurement starts. The total time used for one radiometric measurement (H..L_1..L_2…..C) up to half an hour is possible during the flight with the condition that the temperature at the ACS plate is stabilized. However the autocorrelator spectrometer (IQ chain and correlator chips) itself shows a temperature drift as well which is caused by the temperature drift of 1% /K [Omnisys Instruments AB, 2004] which has to be taken into account.

The degradation of the RF detector and temperature dependence must be taken into account during the flight operation because the readout from the RF detector is used for adjusting the internal attenuator automatically. However, the user can also adjust the internal attenuator manually during the flight by monitoring the counts of the ADCs (see Figure 6-51).

7 Radiometric accuracy of the 1.8 THz channel

The radiometric accuracy of the 1.8 THz channel in DSB mode was investigated in a laboratory before the first flight in Teresina, Brasil in which gas cell measurements of opaque lines was carried out as a quality assessment. The LO frequency was selected by which one opaque line from each sideband superimposed at the same IF frequency. Thus, the brightness temperature of the line centre of the superimposed lines must be the hot load temperature and it is independent from the side band ratio (gas was at same temperature as hot load). The radiometric check for this method is however limited to very few IF points for different line frequencies [Birk, 2008].

7.1 Measurement setup and methanol spectra measurement

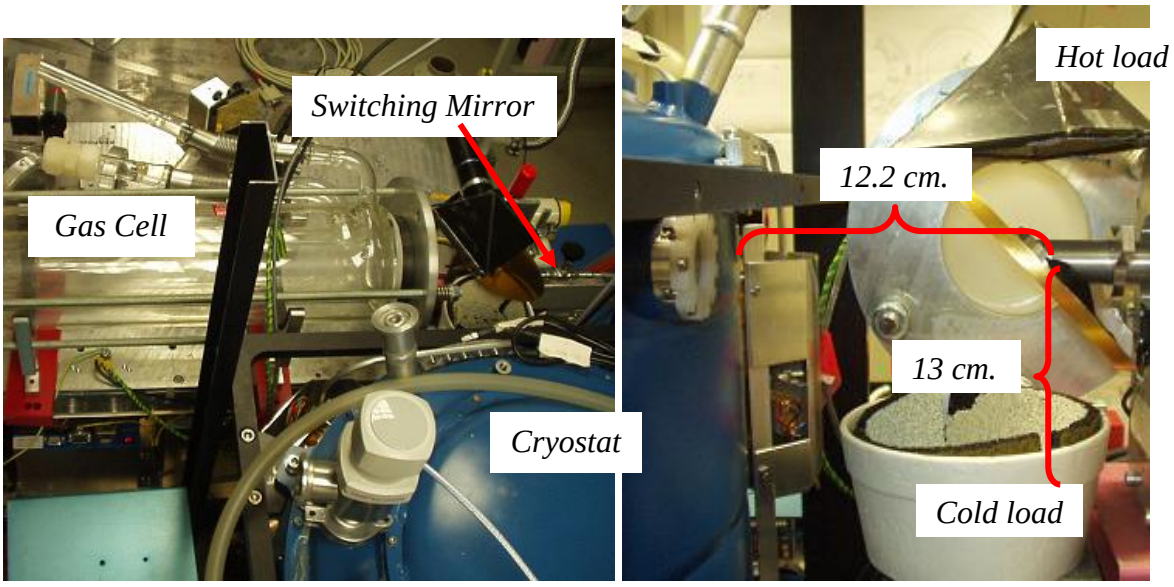

Figure 7-1: The photos show the optical setup of the gas cell measurement. The distance from the window of the cryostat to the middle of the switching mirror is about 12 cm. and that from the middle of the switching mirror to 80% full of the liquid nitrogen is about 13 cm.

The 1.8 THz channel in double side band mode (DSB) being installed in the flight module cryostat (blue colour) as shown in Figure 7-1 was removed from the frame and the flight-transfer optics. In the experiment, the switching mirror was applied in stead of the flight-switching mirror and the telescope. Figure 7-2 shows the schematic of the

whole measurement including the IF setup and the detail of the optics. The room temperature was stabilized at 28°C and the humidity during the experiment was 42%RH.

The gas cell was filled with the methanol gas (CH_3OH) and the length of the gas cell is 50 cm. The material of the cell windows is the Low Density Polyethylene (LDPE) and the gas cell is made out of the Borosilicate glass. To avoid the Fabry Perot reflexion between two windows, both windows were built so that they were tilted about 0.3° to the optical axes.

The leakage of the cell is another consideration which could limit the total measurement time. In this experiment, the leakage of the gas cell was fairly low about 0.0009 mbar per second. The longest total measurement time was about 10 minutes at which the total leakage of the gas cell is about 0.009 mbar. The gas cell was evacuated and refilled with methanol gas in each measurement.

In a radiometric calibration as discussed in chapter 3, three consecutive measurements of two reference black bodies and the signal radiance field are used for calculating one calibrated spectrum as eq. 3-16.

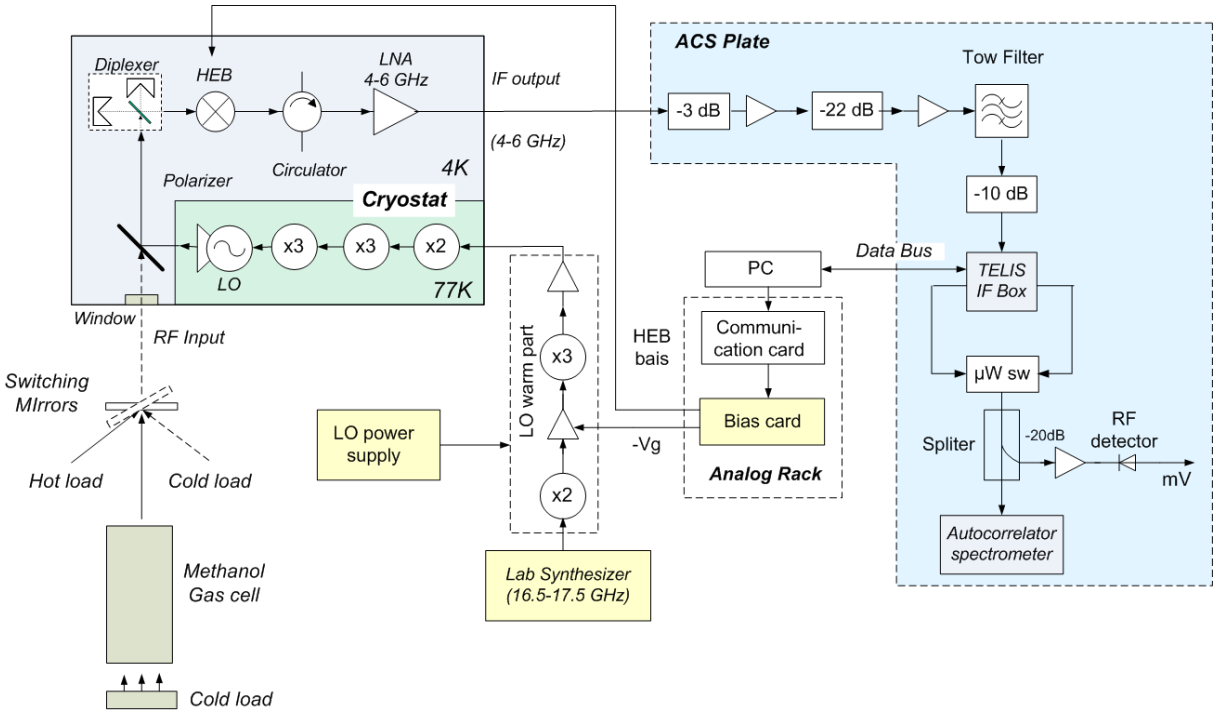

Figure 7-2: Schematic of the measurement setup for measuring methanol lines by the 1.8 THz channel installed inside the flight module cryostat. The spectra measured from the autocorrelator are retrieved directly by the laboratory computer.

Two black bodies are used in this experiment one is warm Ecosorb sheets as a hot black body (300 K) and a liquid nitrogen (77 K) dewar coated with Ecosorb is used as a cold black body. The sequence of the measurement is Hot-Methanol-Cold-Methanol-…. The

integration time for each spectrum (the hot, signal and cold spectrum) was set to 1.5 second and the total measurement can be taken up to 30 minutes where the drift of the whole system should not more than ±1dB from the initialization.

Figure 7-2 presents the optical and IF setup of the measurement. Measurements were controlled directly by the laboratory computer with special laboratory software for controlling the instrument and making the radiometric calibration. Another cold load (77 K) was used after the methanol cell to produce radiance contrast for the methanol gas.

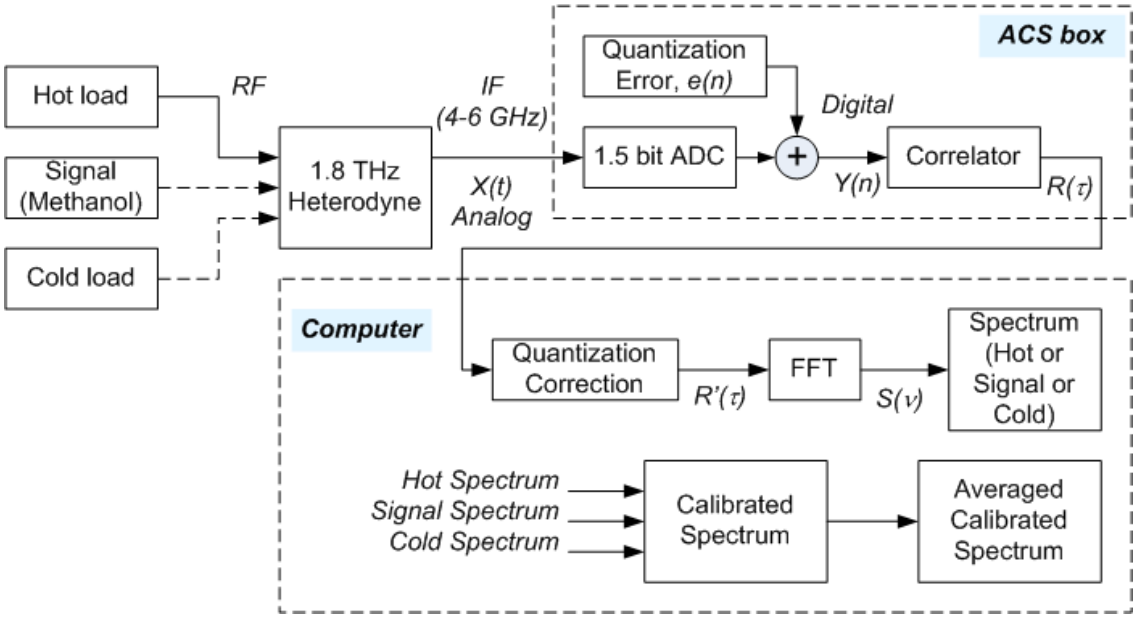

Figure 7-3: Block diagram presents the process of the radiometric calibration. *X(t)* is an analogue signal in time domain which is downconverted from the HEB mixer of the 1.8 THz channel. *e(n)* is an quantization error being an error from the quantizer of the 1.5 bit ADC. *Y(n)* is the digitized signal at the output of the 1.5 bit ADCs. R(τ) is the autocorrelation in time delay which is fed to the computer. *R'(τ)* is the correlated data whose quantization error is corrected and S(ν) is the power in frequency domain.

The schematic in Figure 7-3 shows the sequence of the data processing in the radiometric calibration. The radiometric calibration starts from measuring the RF signal radiated from the sources: hot load, Methanol gas cell and cold load. A switching mirror was used to switch between loads. The IF analogue signal which is downconverted from the mixer of the 1.8 THz channel is fed to the ACS box consisting of two major parts: ADCs and correlators. The analogue signal is digitized by 1.5 bit ADCs where the quantization error occurs [Omnisys Instruments AB, 2005]. The quantization correction is however carried out later after the correlation. The correlated data is sent to the computer where the quantization correction and the Fourier Transformation are performed. A spectrum with the quantization correction is resulting after FFT. With three spectra measured from different sources (hot, methanol and cold), the calibrated spectrum can be

calculated by using eq. 3-15. In order to reduce the noise floor of the calibrated spectrum, calibrated spectra are averaged.

7.2 Discussion of the methanol measurement results

Figure 7-5 shows an opaque line from each side band on top of each other at the same IF frequency (4756 MHz). Using the Kirchhoff's law, the power radiation which is detected at the HEB mixer can be written as eq. 7-1.

$$P_L(f) = [((P_C \cdot t_{W1} + (1-t_{W1}) \cdot P_{CT}) \cdot t_M + (1-t_M) \cdot P_{CT}) \cdot t_{W2} + (1-t_{W2}) \cdot P_{CT}] \qquad \textbf{eq. 7-1}$$

Where P_C is the radiation power emitted from the cold source located after the cell, P_{CT} is the radiation power at the cell temperature. t_{W1}, t_{W2} and t_M is the transmission of two windows of the cell and the methanol transmittance. The baseline corresponds to the radiation power from the windows of the cell with no gas (no absorption due to the Methanol gas, t_M =0) plus the cold load can be written as follows:

$$P_{baseline} = [P_C \cdot t_{W1} + (1-t_{W1}) \cdot P_{CT}] \cdot t_{W2} + (1-t_{W2}) \cdot P_{CT} \qquad \textbf{eq. 7-2}$$

Base line measurement:

The base line was checked by measuring the radiation power from the cell without Methanol gas. The base line is at 170 K ± 2 K (Δ = 4000 K × (2 s × 2 MHz)$^{-0.5}$ = 2 K) and in good agree ment with the base line measured with methanol gas shown in Figure 7-5.

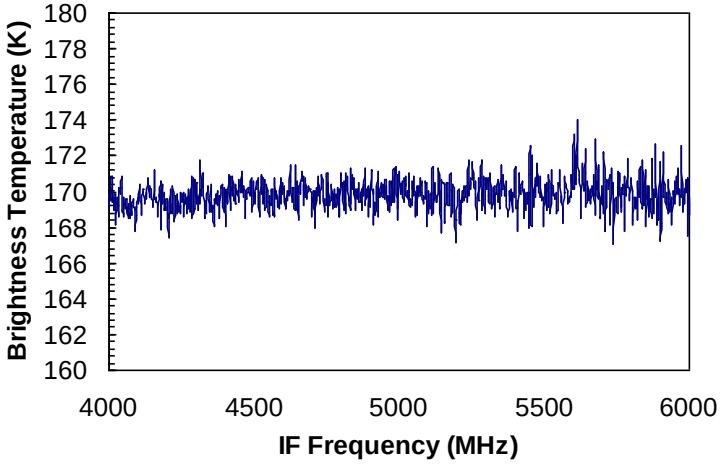

Figure 7-4: illustrates the base line averaged with 50 calibrated spectra. The radiation power from the cell without Methanol gas was measured. The noise of the base line is ± 2 K.

The brightness temperature of the peak of the line was 15 K too high. In order to investigate whether the 12% error in the radiometric accuracy is dependent on the input power, four PE plates similar to the cell window were placed in front of the cryostat window.

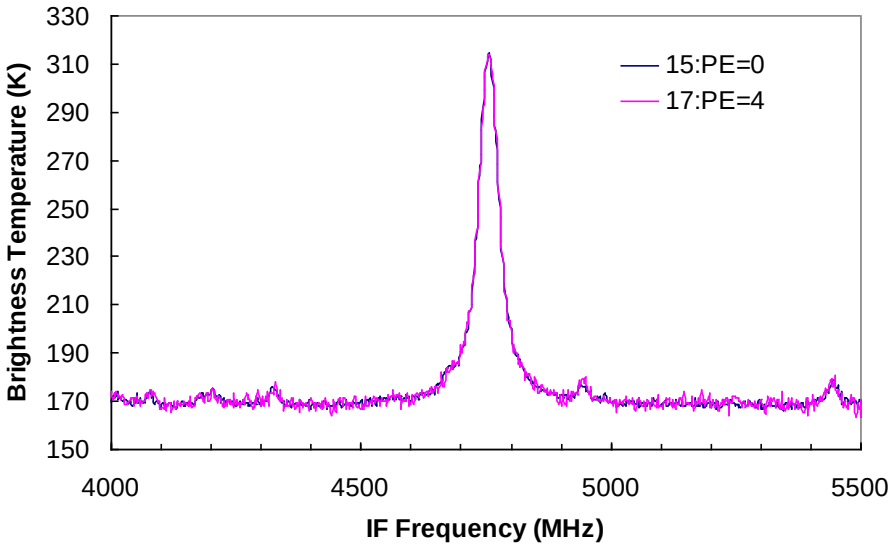

Figure 7-5: Two calibrated spectra plot on top of each other. Both calibrated spectra were averaged from 50 calibrated spectra. PE=4 is the calibrated spectrum measured while four Polyethylene plates placed in front of the window of the THz channel in which the noise floor of the calibrated spectrum was increased by a factor of 2.

The result in Figure 7-5 (PE=4) shows higher system noise temperature propagated on the noise floor of the calibrated spectrum ($\Delta T=2\cdot T_{sys}/(n\cdot\tau\cdot B)^{-0.5}$) as expected. From this result, one can conclude that a problem with the autocorrelator's digital part can also be excluded because a change in signal level must give a different error propagated into the calibrate scene. The nonlinearity at the IF backend (amplifiers, programmable attenuator and IF components inside TELIS IF box) in front of the spectrometer can be excluded since the results from the linearity test measured by the RF detector was linear (see 6.3.4).

This radiometric accuracy problem was also investigated with the SRON channel (4580-660 GHz) by using the OCS gas in the gas cell measurements of opaque lines. The same radiometric error of about 15% was also occurred [Birk, et al., 2010]. The cause of the error in radiometric calibration is further investigated in the ongoing doctoral thesis.

Part IV

TELIS/MIPAS Campaign

8 Overview of TELIS/MIPAS campaign

TELIS and MIPAS are integrated on the same balloon platform with the total mass of about 750 kg. The first campaign which was a first test flight for the TELIS instrument took place in Teresina, Brasil. The balloon campaign was held by CNES. The second balloon campaign which being the first scientific flight of the TELIS instrument was organized by Esrange Space Center in Kiruna, Sweden.

8.1 TELIS/MIPAS Campaign in Teresina, Brasil (June-May 2008)

This large balloon campaign was organized by CNES in the frame work of the SCOUT-O3 project in collaboration with the ENVISAT validation campaign. This campaign consisted of seven different payloads having abilities not only to investigate transport from the tropical tropopause layer into the stratosphere and to study the role of deep convection on the transport of species into the stratosphere but also to investigate the microphysics of aerosols and clouds and their impact on the composition of this atmospheric region.

The flight of MIPAS/TELIS/mini-DOAS was on 5/6 June 2008 with the flight duration of more than 19 hours. The gondola landed short before sunset of the next day inside the rain forest [Oelhaf, 2008].

An objective in this campaign was to test the performance of the instrument. Thus, this campaign was a test flight for TELIS instrument. MIPAS and mini-DOAS worked perfectly while the TELIS instrument encountered two significant problems which can be summarized as follows:-

1. Problem with insulation: The TELIS instrument was insulated with a Mylar foil. Therefore, the instrument was cooled down very fast during ascent to 240 K which was much colder than expected. As a result, the cable applied between the moving part and the rigid part of the telescope was stiff while the angle of the telescope was looking down to 10-20°C and the flip mirror was also stuck. Thus, calibration was not possible.

2. Leakage of the cryostat: Due to the strong cooling of the instrument (<240 K), Viton O-rings sealing the vacuum tank of the cryostat got stiff and a leak developed and the thermal insulation of the helium vessel failed. Thus, the helium inside the TELIS cryostat evaporated quickly and channels warmed up within 3 hours after launch.

Problems occurred on the 1.8 THz channel such as the oscillation on the HEB IV curve, which were also discovered after ascent. The time for observing of the performance of the 1.8 THz channel during the flight was however limited because the telescope and the 1.8 THz channel cannot be commanded simultaneously. This is also one weakness of the design of the server for the flight operation. The investigation of the movement of the telescope required pretty long time and it was highest priority. Therefore, the investigation of THz channel performance was done only three times of five minutes. The short explanation of problems on THz channel will be discussed in chapter 10.

Further in-flight characterization of the TELIS system was not possible because the telescope, switching mirror was stiff. Therefore, only the HEB IV curve and two spectra were measured.

8.2 TELIS/MIPAS Campaign in Kiruna, Sweden (January 2009)

Thermal concept of the TELIS instrument and the performance of the 1.8 THz channel were improved after the campaign in Teresina. By covering the TELIS instrument with an insulation it was prevented that the moving air reached the instrument during ascent. PE foam glued by Mylar foil on one side is applied as insulation. The cable connected between the fix and moving part of the telescope used during the flight in Teresina was replaced with flexible Kapton PCBs as they are used in printers to connect the moveable printer head to the fixed electronics. A sample was tested down to -110°C and no obvious change in flexibility was found [Birk, et al., 2008].

The optimization method used for the 1.8 THz channel was also improved after the campaign in Teresina. Several problems of the 1.8 THz channel such as a drift on LO's warm part, IF chain and the oscillation on the HEB IV curve during the flight were carefully observed [Suttiwong, 2008]. Furthermore, additional housekeeping for observing parameters relevant to the hardware of the THz channel was implemented in the flight-software.

The flight in Kiruna was the second flight of the TELIS instrument which was *the first scientific flight*. The TELIS instrument functioned properly and various trace gases such as OH, CO, water isotopologes were measured. The recordings of OH and ClO will result in profiles that change over time and will be used to constrain atmospheric models.

MIPAS/TELIS balloon was launched at 23:18 UT on 10 March in Kiruna, Sweden. After about 2 hours 25 Minutes the altitude at about 34.5 km was reached. The flight took about 9 hours and the payload landed south east of the Finnish town *Kemijärvi* [Widell, 2009].

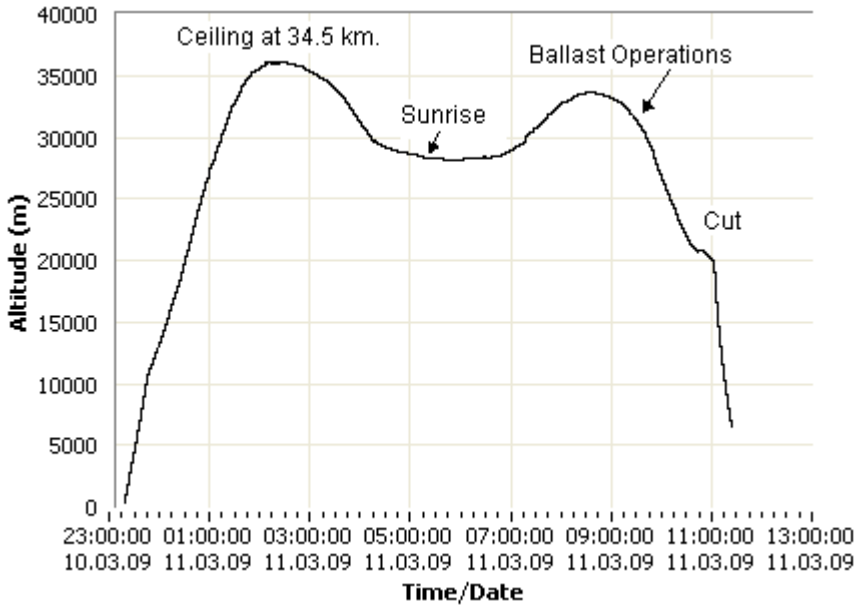

Figure 8-1: MIPAS/TELIS flight profile on 10/11.03.2009 (UTC). The balloon was launched in Kiruna (latitude 67.888513°, longitude 21.08222°) and it reached the ceiling at 34.5 km. The sunrise was at 05:08 am. The balloon was taken down in Finnish town (Kemijärvi: latitude 65.928948, longitude 28.35564). The flight duration was about 9 hours.

During the flight in Kiruna, TELIS instrument performed flawless. Although a few technical problems occurred, they could be solved in a few minutes and the measurement could continue smoothly.

9 On-ground characterization

Because the local oscillator's drift obviously occurs from one cooling cycle to another cooling cycle, the re-characterization in every cooling cycle is necessary. Therefore, the THz Channel's pre-characterization shortly before the flight was required. This pre-characterization was done on the ground and it will be called in this thesis "on-ground characterization". The on-ground characterization is the measurement utilized to determine all optimization parameters for operating the THz channel such as the path difference setting of diplexer, the HEB bias etc.

9.1 Result of the on-ground characterization in Teresina-Campaign

In the on-ground characterization of the THz channel, parameters of interest are the local oscillator power as the function of frequency, the HEB bias, the HEB current and the system noise temperature. These parameters were determined by searching the LO frequency having the optimal power the HEB mixer required, then calculating the diplexer position (see chapter 6.1.4.4) and searching the HEB bias voltage yielding the best noise temperature and stability (see chapter 6.2.1). In each micro-window has the specific range of the LO frequency as shown in Appendix B. The summary of parameters for setting up the channel is illustrated in Table 9-1.

Table 9-1 : Summary of parameters for each micro-window selected during the flight.

µW ID	Spiecies	Line Center (GHz)	Side band	Order Sel.	LO Freq (GHz)	Dip_ min (Hex)	Vg (-V)	HEB bias (mV)	HEB (uA)	NT (K)	sigmaH
1	OH	1834,75	USB	184	1830,10	1F9E	-0,7	0,4	59,69	3830	1,72E-02
2	OH	1837,80	LSB	186	1842,23	4469	-0,7	0,5	55,57	4040	2,56E-02
3	$H_2{}^{17}O$	1880,75	USB	190	1876,19	5E92	-0,7	0,5	46,36	3360	-
4	$H_2{}^{18}O$	1815,85	LSB	183	1820,54	1DE0	-0,7	0,5	50,42	3338	9,49E-03
5	$H_2{}^{16}O$	1840,15	USB	186	1835,93	62BE	-0,7	1,2	66,56	4169	7,78E-03
6	HDO	1853,90	LSB	188	1858,38	5591	-0,7	1	52,12	5954	7,51E-03
7	$^{16}O^{18}O$	1875,04	USB	188	1870,10	1E0D	-0,7	0,6	51,12	3290	-
8	HO_2	1821,80	USB	183	1817,58	2C2B	-0,7	0,4	59,48	3904	1,15E-02
9	CO	1841,36	USB	185	1836,26	319A	-0,7	1,2	70,13	4688	1,21E-02
18	HDO	1818,50	LSB	183	1823,94	0D77	-0,7	0,4	50,93	3299	8,45E-03

"µW ID" is an index of each microwindow (see Appendix B). "Line center" presents the center frequency of observed species. "Order sel." shows the selected order of the diplexer setting (see chapter 6.1.4.4). "LO Freq." represents the LO frequency selected.

"Dip_min" is the setting of the diplexer in hexadecimal unit. "Vg" and "HEB bias" are a gate bias voltage and a HEB bias voltage, respectively. "HEB (μA)" shows the readout HEB current. "NT" and "sigmaH" is a system noise temperature and standard deviation which calculated from the measured hot power.

The system noise temperature of each micro-window illustrated in Table 9-1 was corrected for the attenuator in optical path from the water vapour between the blackbodies (hot cone and the liquid nitrogen) to the window the 1.8 THz channel (see Appendix C).

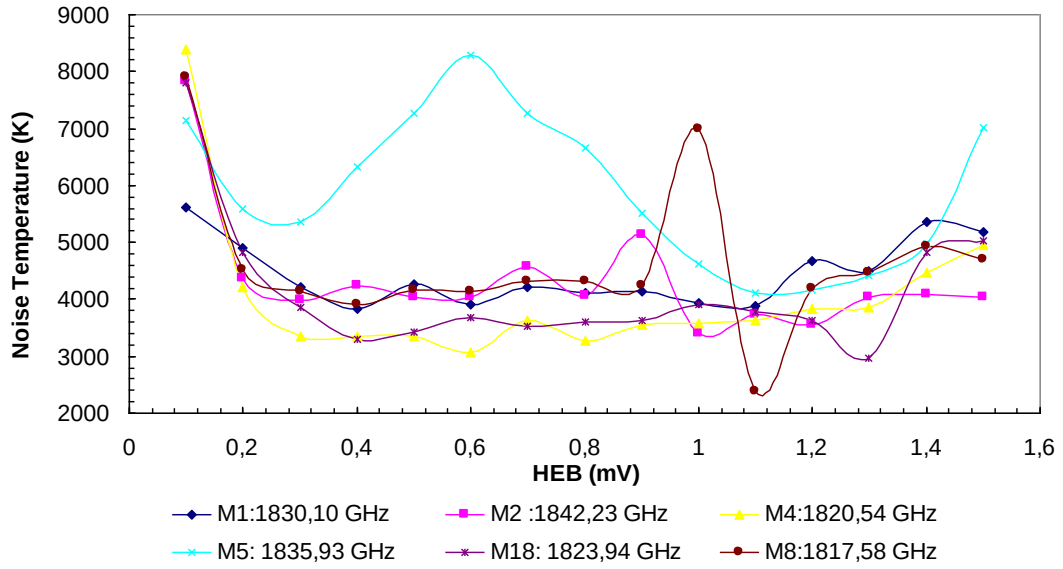

Figure 9-1 : Comparison of the noise temperature measured before flight for different LO frequencies.

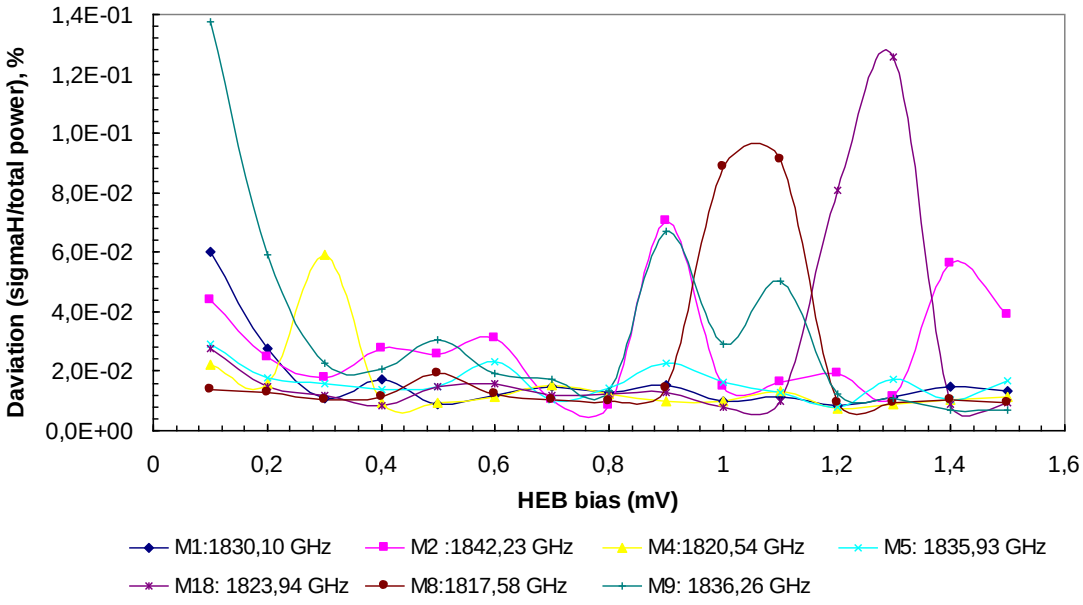

Figure 9-2 : Comparison of the standard deviation of total power at different frequencies. Each point is calculated from 10 points of absolute power measured while the swiching mirror was pointed to the hot load.

During this noise temperature measurement, the gondola was sealed in order to keep the instrument dry. Water vapour, however, still influenced the measurement in the microwindows that have low water transmittance, for instance in microwindows 3 and 7. Therefore, the noise temperature in these two microwindows had to be measured manually with warm and *cold Eccosorb*[27] directly at the cryostat's window, thus avoiding the long optical path to the calibration (cone) blackbody via the flip mirrors used in the automatic process.

Figure 9-1 shows how noise temperature, HEB bias and LO frequency are related to each other. In order to choose the best optimised parameters for each microwindow, stability also has to be taken into account. Figure 9-2 shows the standard deviation of total power which was calculated from 10 points while the mirror pointed to the hot load. One can recognize that the HEB bias voltage which shows a corresponding low noise temperature is not always the one that simultaneously shows the best stability.

9.2 Result of the on-ground characterization in Kiruna-Campaign

The preparation for the flight in Kiruna started since the middle of January 2009. Due to the weather conditions, the flight took place at the middle of March (10-11.03.2009). Several tests such as the radiometric calibration, the stability during the calibration, the standing wave in the optic and functionality of the software were performed in January.

The stability of THz channel during the radiometric calibration test (January):

Figure 9-3 shows the stability of THz channel measured by the autocorrelator spectrometer. Consecutive measurements of the hot source were taken and the spectral power evaluated. Each point in the graph is calculated from the sum of 926 channels in one hot spectrum. This measurement took about half an hour. The deviation from the reference is about ±0.8% for the THz channel.

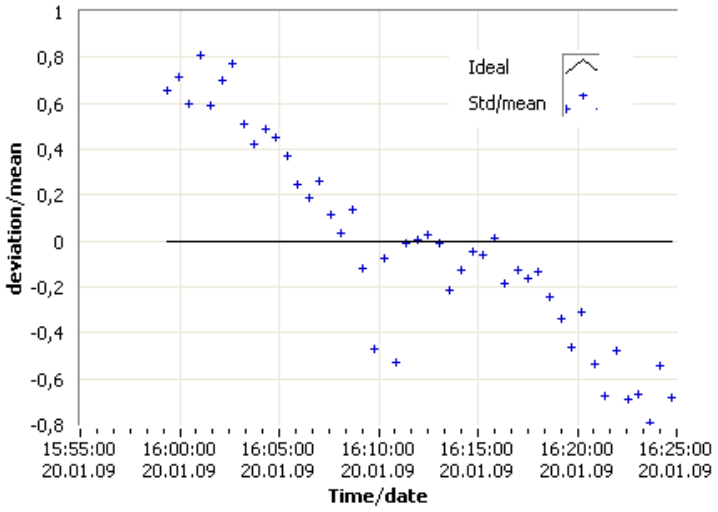

Figure 9-3: shows the deviation from the mean over time in percent for the THz channel. Each point in the left graph is calculated by summing of all channels in single hot spectrum.

[27] Ecosorb immersed into the liquid nitrogen

The drift is about 1.6% from the initialization being about 10 times lower than 1 dB (see Chapter 6.3.5). The drift of the output power of THz measured by the RF detector for DLR channel [Suttiwong, et al., 25.02.2009] was ≈ 0.1 dB from the initialization which is in coincidence with the drift calculated by the absolute power of the autocorrelator.

On-Ground characterization of THz channel:

The characterization for all micro-windows used during the flight campaign in Kiruna was done during the same cooling cycle as the flight. The summary of parameters for each micro-windows selected during the flight is shown in Table 9-2.

Table 9-2 : Summary of parameters for each micro-window selected during the flight.

µW ID	Species	Line Center (GHz)	Side band	Order Sel.	LO Freq (GHz)	Dip_ min (Hex)	Vg (-V)	HEB bias (mV)	HEB (uA)	NT (K)	sigmaH
1	OH	1834,75	USB	184	1829,65	20FE	-0,7	0,9	63,6	3234	1,11E-02
2	OH	1837,8	LSB	185	1842,41	1377	-0,7	1	53,01	3287	8,43E-03
3	$H_2{}^{17}O$	1880,75	USB	188	1876,08	151	-0,7	0,8	48,03	6224	4,61E-02
4	$H_2{}^{18}O$	1815,85	LSB	183	1820,48	1D63	-0,7	0,8	38,76	3148	7,88E-03
5	$H_2{}^{19}O$	1840,15	USB	186	1835,8	627F	-0,7	0,8	66,89	3151	1,90E-02
8	HO_2	1821,8	USB	183	1817,45	2C06	-0,7	1,1	63,23	2925	8,09E-03
9	CO	1841,36	USB	184	1836,39	00BE	-0,7	1	61,86	3214	1,09E-02
27	$H_2{}^{20}O$	1818,5	LSB	183	1824,06	0D54	-0,7	0,6	59,36	3002	6,53E-03

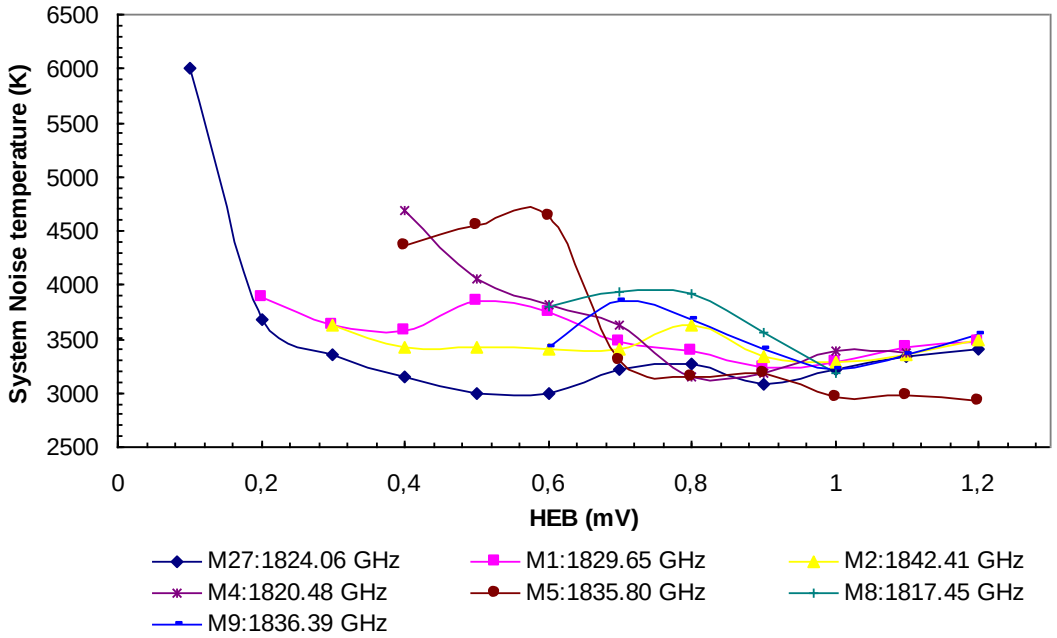

Figure 9-4: Comparison of the system noise temperature as a function of bias voltage measured before the flight in Kiruna for different LO frequencies.

The system noise temperature of each micro-window shown in Figure 9-4 was measured by means of placing a cold Ecosorb directly in front of the window of the 1.8 THz channel as a cold blackbody and a hot cone as a hot blackbody. The parameters yielding the best stability were selected as shown in Table 9-2.

During the rehearsal before the flight the radiometric calibration was tested on ground with a flight macro. The aim of the test was to check for undesired standing waves in the optical setup, the functionality of the software, hardware and software macros which were used during the flight. In this test four different calibrated spectra at different tangent heights as shown in Figure 9-5 (a) were measured while a warm Ecosorb sheet was placed in front of the telescope. The measurement took about 10 minutes and the liquid nitrogen was applied as a cold load (77 K) while the temperature at the hot load was about 300 K. Figure 9-5 (b) depicts the deviation of the absolute power of each hot spectrum measured by the autocorrelator.

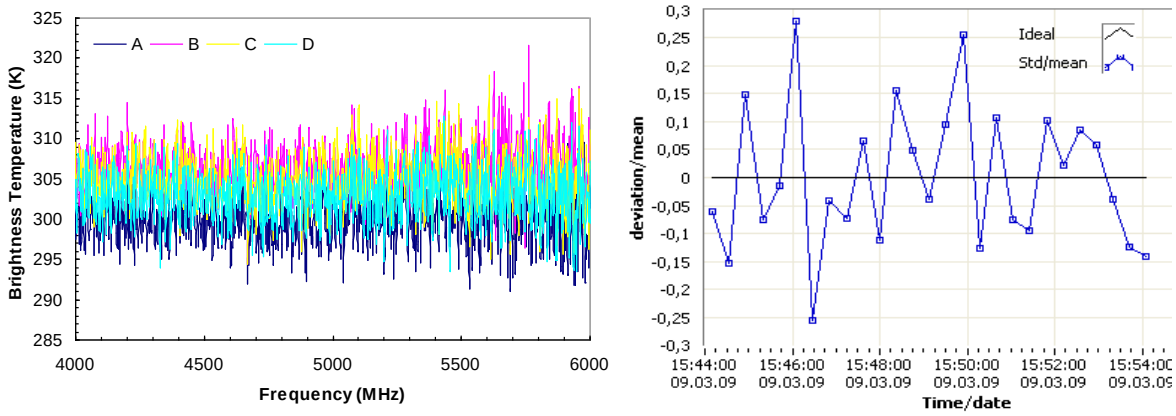

(a) (b)

Figure 9-5: (a) Measured calibrated spectra for different pointing angles during the rehearsal on the ground in Kiruna. Four different tangent heights were set during this measurement. (b) The graph illustrates the deviation of the absolute power of each hot spectrum measured by the autocorrelator spectrometer.

The results from the measurement of the 1.8 THz channel shows the deviation from the mean over time is about ±0.3% which was stable (see chapter 6.3.5). The measured calibrated spectrum in Figure 9-5 (a) shows also less effect of the standing wave in the warm optics (transfer optics, see Figure 5-1) in which it could be concluded that the 1.8 THz channel was ready for the flight.

10 Discussion of the performance of the1.8 THz channel during flights

In this chapter both stability and system noise temperature of the 1.8 THz channel during the flight will be discussed, followed by some quick-look results measured during the scientific flight in Kiruna 2009.

Stability of THz channel during the flight in Kiruna:

The stability of THz channel during flight depends on the temperature of the relevant hardware such as the warm part of the LO located at on the side of cryostat, the IF amplifier, LO synthesizer and the autocorrelator located on the ACS plate. Thus, the temperature drift during the flight must be considered before the stability of THz channel can be examined as illustrated in Figure 10-1. About 02:43 AM when the gondola reached the ceiling at an altitude of about 34.5 km, the temperature was stabilized.

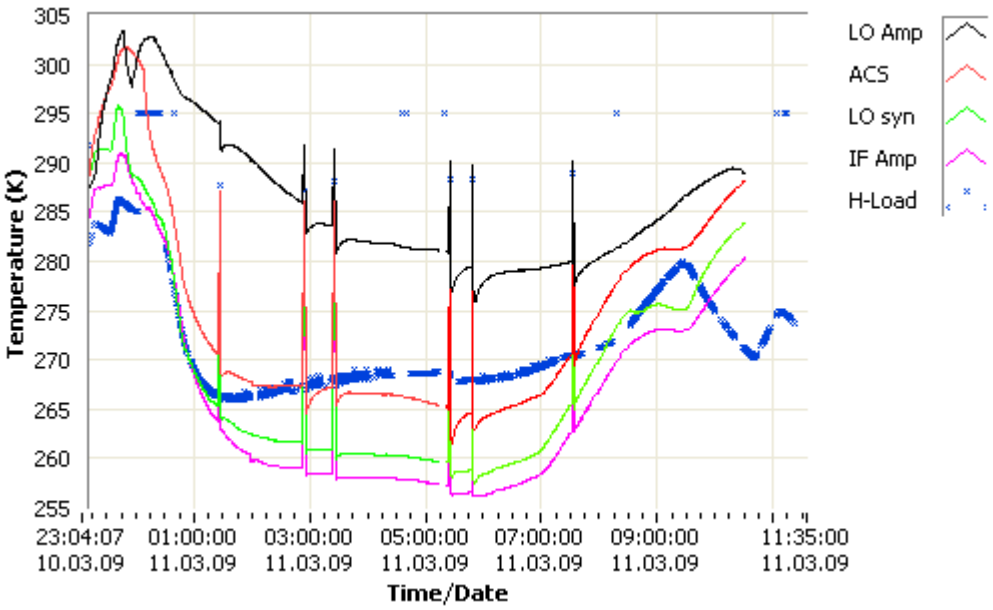

Figure 10-1: The temperature drift of components relevant for the THz channel (local time). PT-100s temperature sensors were used to measure the temperature of the relevant components. "*LO Amp*" is the temperature at the warm part of the LO, "*ACS*" is the temperature at the autocorrelator box, "*LO syn*" is the temperature at the synthesizer of the LO located on the ACS plate, "*IF Amp*" is the temperature at the two IF amplifier and "*H-Load*" is the temperature at the TELIS hot black body (clone).

The stability and the system noise temperature spectra of one measurement (10 limb sequences with 1.5 km altitude resolution) while the gondola was at 33 km altitude are shown in Figure 10-2. The quick look results from this measurement are shown in Figure 10-3.

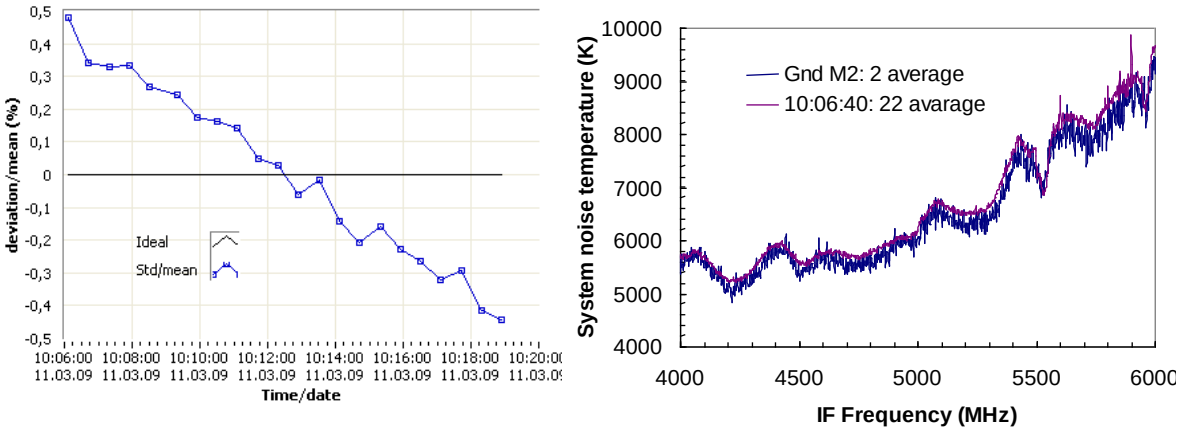

(a) (b)

Figure 10-2: (a) depicts the drift of the system of one measurement during the flight. (b) A comparison between the system noise temperature spectrum measured on ground and during flight at an LO frequency of 1842.41 GHz.

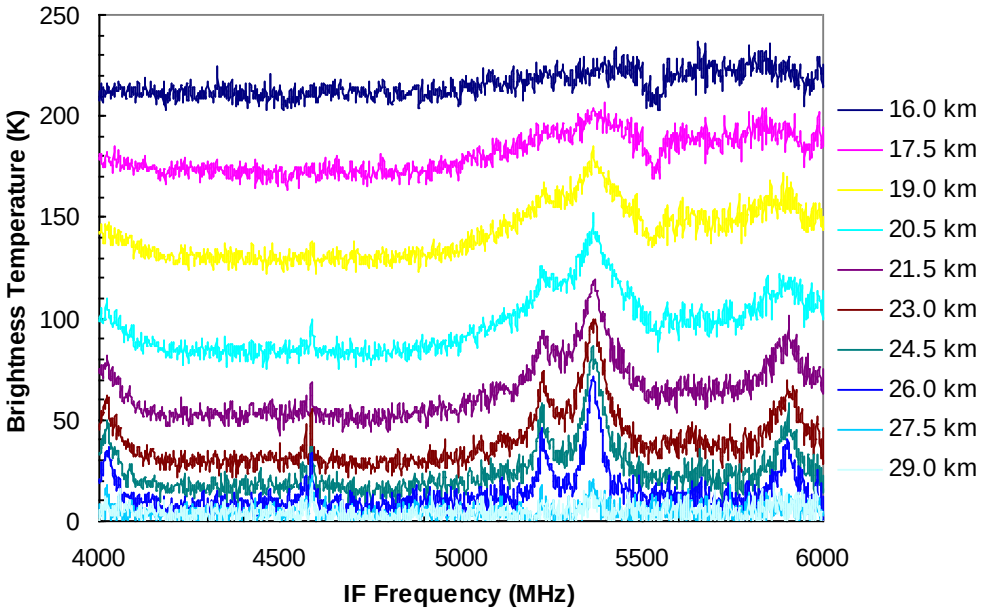

Figure 10-3: Double sideband quick look spectra of THz channel OH (LSB). The LO frequency was set to 1842.41 GHz. Tangent altitude at 16 km. to 29 km with altitude resolution of 1.5 km.

Reproducibility of the diplexer during the flight:

The reproducibility of the diplexer curve (see chapter 6.1.4.4) at the same LO frequency was rechecked during the flight by a comparison with the one measured on the ground as illustrated in Figure 10-4:. Two diplexer curves which were scanned in forward and backward direction during the characterization on the ground are compared with two curves measured in flight. The curve was fitted with a 4th order polynomial and the fitted minima were compared. The deviation of both minima was within 80 decimal units which is a good reproducibility yielding the side band ratio (at the edge) accuracy within 3%.

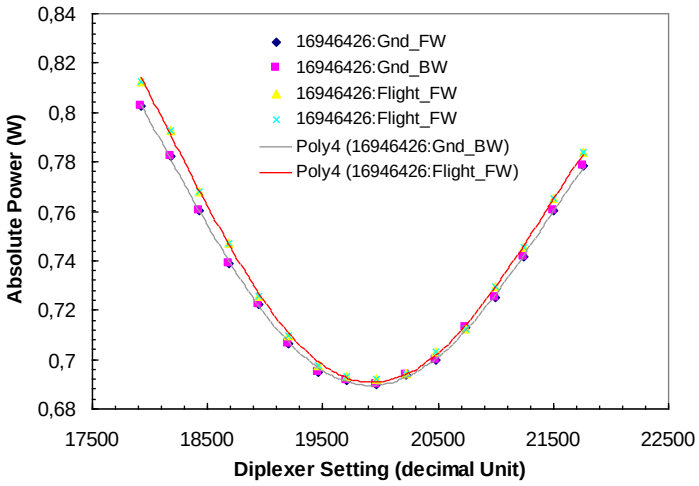

Figure 10-4: A comparison of the diplexer curves (forward and backward directions) measured during the on-ground characterization at an LO frequency of 1830.214 GHz (=16946426 KHz set at the first state amplifier of the LO chain, see Figure 6-18) and the ones measured during flight. "Gnd_FW" and "Gnd_BW" refers to a diplexer curve measured during the instrument was on ground in forward and backward direction, respectively. "Flight_FW" refers to a diplexer curve measured during flight. "Poly4" represents a fitted curve with 4 order polynomial.

System noise temperature of the THz channel during the flight:

Figure 10-5 illustrates a comparison of the system noise temperature of the 1.8 THz channel measured by the RF detector and the autocorrelator spectrometer during flight. The system noise temperature increased by a factor of two at an altitude of 30-35 km compared to the ones measured during ascent. Possible reasons for this increase are a higher LO power provided to the HEB mixer, an influence of low temperature on the sensitivity of components in IF chain of the 1.8 THz channel and possible ice layer on the telescope.

Due to the stability of the LO during the flight, the drift of the LO power due to the low temperature at this altitude which would overdrive the output power at the last state of the LO can be excluded.

The problem of the IF backend and the autocorrelator spectrometer due to low temperature also can be excluded because the change of the system noise temperature of the SRON channel which was simultaneously measured with the THz channel was only up to 16% higher than measured on ground.

Another interesting factor is the altitude. The system noise temperature changes obviously with the altitude (see also Figure 8-1) and thus, only THz channel had this effect during the flight. It is feasible to have an ice layer at the telescope at this altitude in which it attenuates the signal coupled into the THz channel.

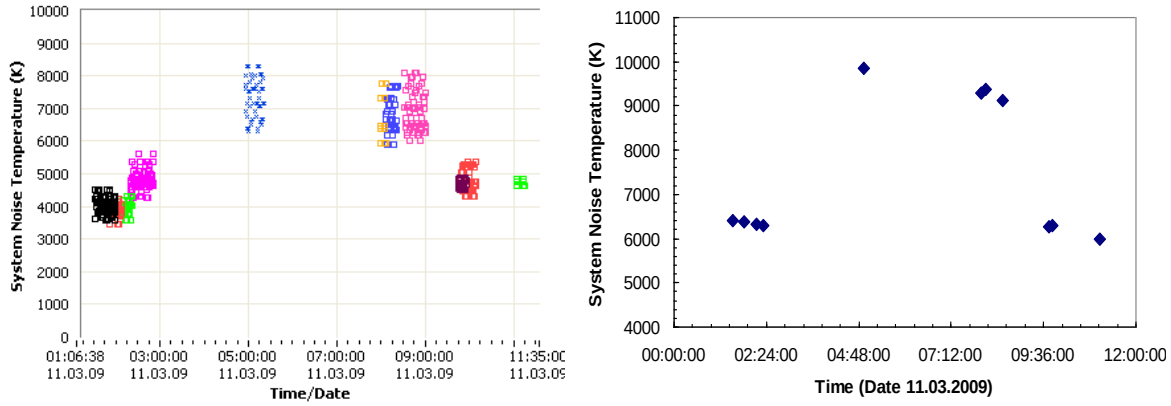

(a) (b)

Figure 10-5: (a) the system noise temperature of the 1.8 THz channel during the flight. All system noise temperature is calculated from the power measured by the RF detector. Each color represents the system noise temperature measured in different tangent heights in the same microwindow. The LO frequency set for all measurement presented in this figure was 1829.65 GHz. (b) System noise temperature of the same microwindow measured by means of the autocorrelator. Each was calculated from the sum of all channels of an averaged noise temperature spectrum of each measurement.

Quick look result measured by the 1.8 THz channel during the flight (Kiruna 2009):

Some DSB (quick-look) calibrated spectra measured by the 1.8 THz channel during the Kiruna (2009) campaign are illustrated in Figure 10-6, 10-7 and 10-8. The measured calibrated spectra shown in these three figures are without a correction of a pointing offset. The measured results are compared to the model spectrum using the HITRAN spectroscopic database [Rothman, et al., 2009]. The forward model calculations were done with FASCODE [Anderson, et al., 1994] assuming a pencil beam profile. The calibrated spectra shown in Figure 10-6 and Figure 10-8 are measured at the same OH Microwindow. The OH in Figure 10-8 was not appear in the measured spectra since this measurement was done before sunrise.

Figure 10-7 presents the measured results of the CO microwindow measured after the sunrise on 11.03.2009 at the tangent height between 16 and 30 km while the gondola was at 34.963 km altitude.

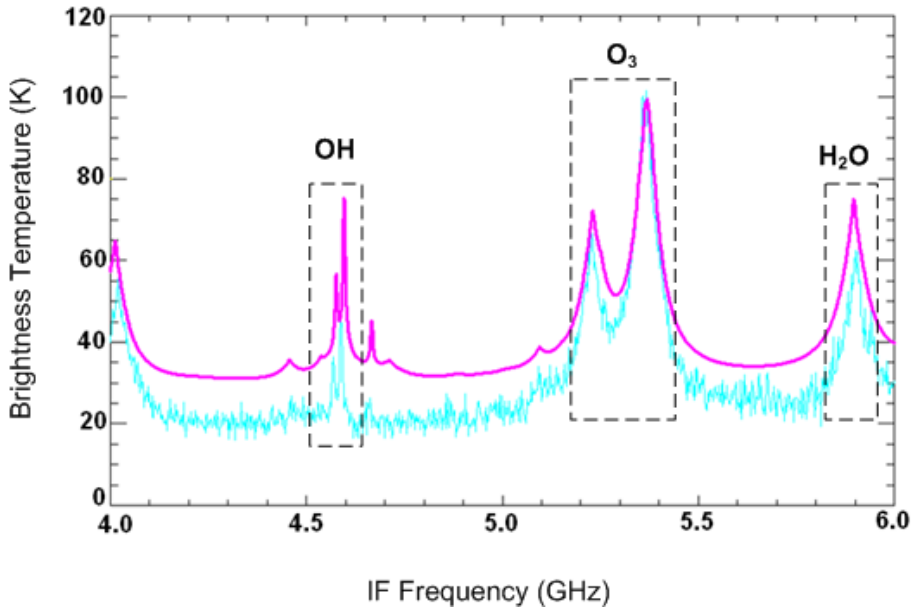

Figure 10-6: The DSB (quick –look) calibrated spectra measured by the 1.8 THz channel during the flight in Kiruna 2009 while the gondola was at 32.17 km altitude. The LO frequency was set at 1842.41 GHz and the measurement took placed at 8:50 AM on 11.03.2009 at a tangent height of 26.5 km. The blue line shows the measured spectrum, and the magenta line shows the modeled spectrum using HITRAN database+FASCODE (SAW) climatology.

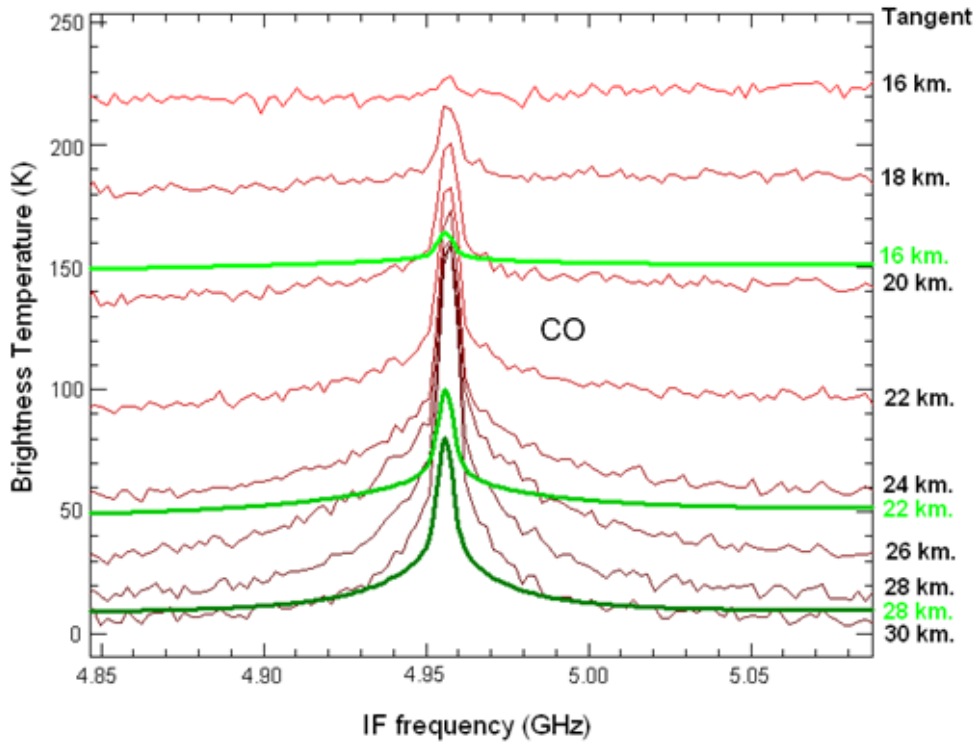

Figure 10-7: The DSB (quick –look) calibrated spectra of CO measured by the 1.8 THz channel while the gondola was at 34.963 km altitude. The LO frequency was set at 1836.39 GHz and the measurement took placed at 07:17 AM on 11.03.2009 at a tangent height from 16 to 30 km. The red line shows the measured spectrum, and the green line shows the modeled spectrum using HITRAN database+FASCODE (SAW) climatology.

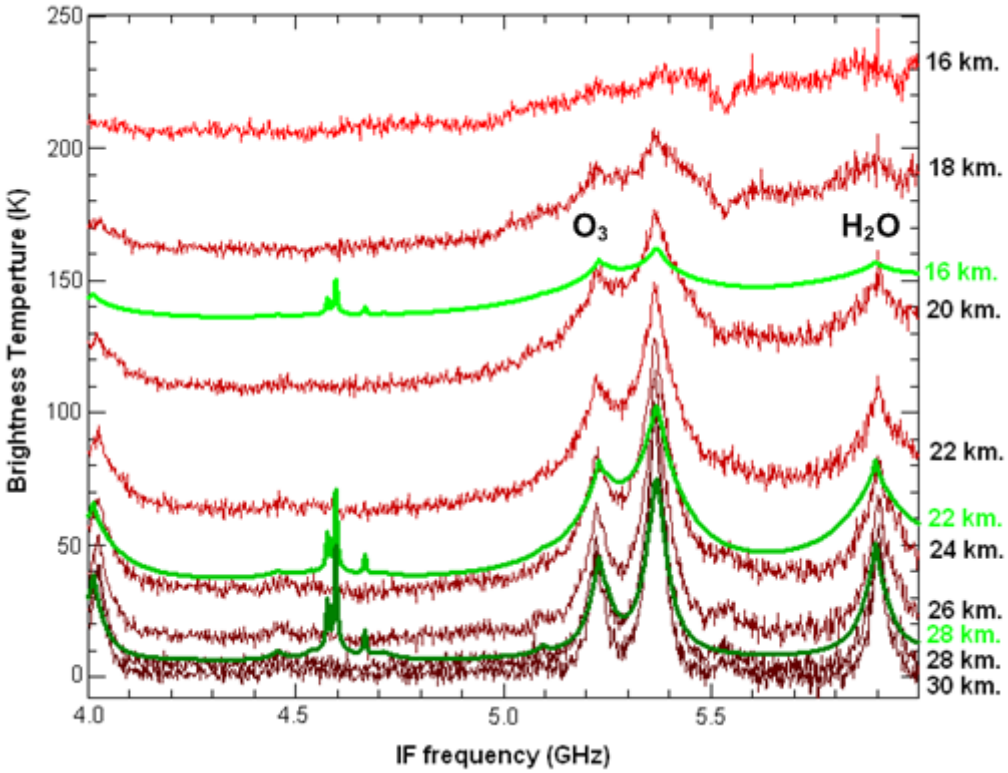

Figure 10-8: The DSB (quick –look) calibrated spectra measured by the 1.8 THz channel while the gondola was at 35.788 km altitude. The LO frequency was set at 1842.41 GHz and the measurement took placed at 03:44 AM on 11.03.2009 at a tangent height from 16 to 30 km. The red line shows the measured spectrum, and the green line shows the modeled spectrum using HITRAN database+FASCODE (SAW) climatology.

Figure 10-9 illustrates the DSB quick look spectra (OH Microwindow) measured by the 1.8 THz channel during the Kiruna (2009) campaign while the gondola was at an altitude of 35.788 km. The base line has already been corrected for a pointing offset of 1.5 km to achieve a better match of the line contrasts at the different tangent heights. The forward model used the HITRAN spectroscopic database and temperature, ozone and water profiles measured by the MIPAS instrument at the same time in the same airmass [Wetzel, 2009]. The forward model calculations were done with FASCODE assuming a pencil beam profile. The modeled spectra was then converted into double sideband spectra by and IDL tool (developed by Wagner and Birk, 2008) assuming a sideband ratio of 1.

While the measured line contrast is in good agreement with the theoretical calculations, the base line is still too high at lower altitude. The offset of the base line could be caused by an error in spectroscopic parameters, especially by the pressure broadening parameters of strong water lines and their temperature dependence.

A detailed radiometric analysis and correction is subject of an ongoing investigation. The resulting data product will be used for the retrieval of concentration profiles of the different species investigated.

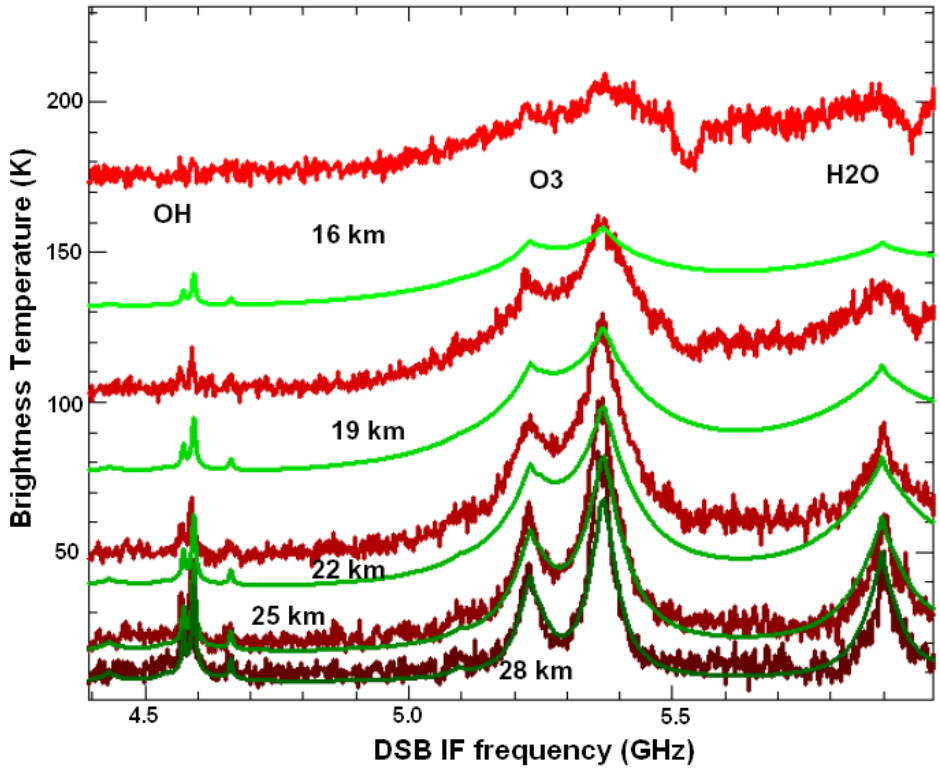

Figure 10-9: The DSB (quick –look) calibrated spectra measured by the 1.8 THz channel during the flight in Kiruna 2009 while the gondola was at 35.788 km altitude. The LO frequency was set at 1842.41 GHz and the measurement took placed at 03:44 AM on 11.03.2009. The red line shows the measured spectrum, and the green line shows modeled spectra using HITRAN database+FASCODE SAW climatology as well as the measured profile from MIPAS instrument [Schreier, et al., 2009].

11 Summary and Outlook

Summary

The work of this doctoral thesis started from the development of the 1.8 THz heterodyne channel which continued from the prototype developed by Dr. Ulrich Mair (2001-2005) [Mair, 2007]. The work covered the characterization and the integration of the channel in the flight module cryostat, and putting the 1.8 THz channel and the IF backend including the Autocorrelator spectrometer into operation in the flight campaigns. The results of this thesis can be summarized as follows:-

1. **The improvements of the 1.8 THz channel applied in the flight module cryostat comparing to the prototype:**

   - The absolute **system noise temperature** across 2 GHz IF-bandwidth (4-6 GHz) was reduced by 7000 K.
   - The **solid state local oscillator** has successfully been characterized and integrated into the flight module cryostat.
   - The **cold IF chain** was improved by the new design of cabling (bias wires and semi-rigid cable) and relevant connectors.
   - The **diplexer** was re-characterized at 5 K, thus the diplexer was more accurately characterized. The leakage of the diplexer at 1.8 THz is 0.8%. The accuracy of the diplexer setting is in the range of ±15 decimal units while the repeatability is ±15 decimal units (20.64 µm path difference change). In addition, the diplexer calibration function was also developed in order to predict the best adjustment for the diplexer (see chapter 6.1.4.4) in which the power output of the HEB mixer is used to determine the setting of the diplexer instead of the HEB current. The accuracy of the diplexer calibration function is ±30 decimal units (41.26 µm path difference change). In the same cooling cycle, the accuracy of the diplexer setting is in the range of ± 60 decimal units (82.48 µm path difference change) which is proportional to the error of the side band ratio (at the edge) of about 2%.
   - Two Zitex sheets (porous Teflon) are used as a blocking filter instead of antireflection coated crystal quartz from Infrared Labs Inc. By using the Zitex sheet the loss is about 50% less. (from32% to 14% loss)

- The **heat concept** was improved and carefully calculated in which the holding time of the cryostat is longer as well as the HEB mixer is better cooled close to the critical temperature (~0.6 K better: from 5.6 to 5 K). The overall heat transfer of wires from 300 K to 4 K of the 1.8 THz channel which is the sum of the heat transfer calculated from two different heat gradients is ~102 mW.
- The **control of the 1.8 THz channel** was changed from manual to automatic (remote) control where the HEB mixer, the diplexer, SSB, the LO gate bias voltage and the LO frequency are controlled more conveniently by a computer via SSB and SIS cards instead of the bias voltage from the laboratory power supplies.

2. Characterization of the 1.8 THz channel:

The characterization was at first done in the test cryostat but was redone after migrating the cold channel into the flight module cryostat, due to a change of the hardware such as power supplies, monitor and grounding.

The HEB mixer was separately tested after delivery with an FIR laser as LO due to the delay of the LO delivery. Thus, a new test with the solid state LO was required afterward. The mixer noise temperature at 1.8 THz measured after migrating the channel in the flight module cryostat was 1600 K ± 200 K.

The output power of the LO was measured after delivery by mounting the LO in the test cryostat, pointing the LO beam to a bolometer and measuring the output absolute power (chapter 6.1.3). The result from this measurement yields a rough estimation for the LO output power generated by the solid state LO as a function of its frequency.

The 1.8 THz channel was successfully characterized before the first test flight in Teresina, Brasil. The method, algorithms and software for characterizing the cold channel in flight was developed and implemented (chapter 6.2.1 and Appendix G.2). The filtering for the bias voltage of the HEB mixer and the LO gate was additionally built due to the EMI between channels. The summery of the parameters used for characterizing is as follows:-

- The optimum LO power corresponding to the HEB current at the optimum HEB bias between 0.4 mV and 0.6 mV is about 50 µA ± 2 µA.
- The accuracy of the HEB current monitor is ± 2µA and the accuracy of the HEB bias is ±30 µV. The repeatability of the system noise temperature depending on the stability of the LO and the HEB bias is ± 3%.
- The accuracy of the gate voltage is ±0.001 V, where the LO power changes slightly with the change of the temperature at the LO warm part in which the LO power increases obviously at a temperature lower than 20°C. The operating range of the gate voltage is recommended to be -0.70 Volt to -1.02 Volts.

3. Characterization of the Autocorrelator spectrometer:

The results of the characterization in the laboratory which was done before the flight in Teresina, Brasil are used for specifying criteria for working with the autocorrelator spectrometer which can be summarized as follows:-

- The optimized reference voltages for initializing the autocorrelator should be within a voltage of 103 mV ±30 mV.
- The optimum input power of the autocorrelator spectrometer can be determined by RF detectors. The sensitivity of the RF detector is temperature dependent and increases up to 0.5 dB at a temperature lower than 25°C which could take into account for the operation during the flight because the temperature will be down to -10°C.
- The linearity of the autocorrelator was tested by using liquid sources at different temperature (see chapter 6.3.4). To be sure that nonlinearity of the autocorrelator will not occur during the measurement, the measurement during flight should be stopped when the drift of the input power of the autocorrelator is more than ±1 dB from the initialization value.
- The stability of the autocorrelator was tested in the laboratory with the condition that the temperature of the autocorrelator plate was stabilized at 10°C. The result showed that the drift of the whole system in 25 minutes after the initialization is about 10 times lower than 1 dB. Thus, the total time used in one radiometric measurement (H..L1..L2…..C) up to half an hour is possible during the flight with the condition that the temperature at the ACS plate is stabilized. However it must be considered that the autocorrelator spectrometer itself has a temperature drift of 1%/K.
- The reference voltage of the ADCs for the radiometric calibration was optimized by taking the mean value between the reference voltage calibrated with the hot blackbody and that with the cold blackbody instead of calibrating the reference voltage with the signal level. As a result, the reference voltage for the ADCs is optimized for all signal levels (= signal limb sequence) between two specific blackbodies.

4. The flight software:

The flight software for operating the 1.8 THz channel (Appendix G) and performing the radiometric calibration were required shortly before the first flight due to a change of the software concept. It was successfully developed and operated in both campaigns. The main functions of the flight software can be summarized as follows:-

- General tools for monitoring and biasing the HEB mixer, the LO. All housekeeping data relevant to the operation of the 1.8 THz channel such as the temperature, voltages, current consumption are also presented on the graphic interface of the flight software. Also the software covers the ability to calibrate the diplexer separately either on the ground or in flight (see Appendix G.1).

- Characterization tool for the 1.8 THz channel allows all parameters used for the control the 1.8 THz channel (chapter 6.2.1) to be determined conveniently (see Appendix G.2).
- ACS tools for initializing and operating the autocorrelator. The main purpose to develop this tool is to perform the radiometric calibration (for three channels) during the flight in which the calibrated spectra of all limb spectra can be presented on-line (without quantization correction). As well all raw data measured during the flight are saved into the database to allow for performing the post processing later (see Appendix G.3).
- A post processing tool was implemented in order to redone the radiometric calibration with the (min/mid/maximum) quantization correction which is the time consuming process.

5. Performance of the 1.8 THz channel in the campaigns:

During the campaign in Kiruna the 1.8 THz channel could successfully measure trace gas profiles of OH, $H_2{}^{17}O$, $H_2{}^{18}O$, $H_2{}^{19}O$, HO_2, $H_2{}^{20}O$ and CO.

The 1.8 THz channel was successfully operated in the campaigns with a system noise temperature of about 3500 K. The feature of the system noise temperature spectrum measured during the flight is the same as the one measured on the ground. However the system noise temperature was about double increased at the higher altitude of 30-35 km. The first assumption for this issue is an ice layer at the telescope at this altitude which attenuates the signal radiation coupled into the THz channel.

The drift from the initialization of the 1.8 THz channel including the IF backend which is calculated from the power measured while the gondola was at 33 km altitude, where the temperature was stabilized, was 0.13 dB.

The reproducibility of the diplexer at the same LO frequency was checked during flight by a comparison with the one measured on the ground. The deviation of the diplexer position was within 80 decimal units (109.96 µm path difference change) in which it still shows a good reproducibility yielding the side band ratio accuracy (at the edge) within 3%.

Outlook

An important issue which must be further investigated is the problem of the radiometric accuracy. As discussed in chapter 7, it was found that there is a 12% error in the radiometric accuracy. Furthermore, the results from the campaign in Kiruna 2009 show that the base line is still too high at lower altitude.

The problem of the twice as high system noise temperature at higher altitude should be further investigated. The heater should be mounted at the telescope in order to observe if an ice layer is really the reason of this problem.

Based on the results of this thesis, further improvements of the 1.8 THz channel for increasing the stability, sensitivity of the channel should be as follows :-

- The stability of the bias voltage of the HEB mixer should be further improved by improving the stability of the feedback voltage monitor.
- The temperature at the LO warm part should be better stabilized by adding an additional cooler and heater at the case of the LO warm part.
- The temperature sensors should be mounted at both RF detectors allowing for a better calibration of the power output of the RF detectors during the flight.

The command for monitoring the diplexer position, HEB current and bias including the temperature at the SSB/SIS boards should be added in the measurement macro for convenience.

Appendix A: Abbreviations

Abbreviations	Meanings
ACS	Autocorrelator Spectormeter
ADC	Analog to Digital Converter
AHRS	Attitude and Heading Reference System
CNES	Centre National d'Etudes Spatiales
CRISTA	Cryogenic Infrared Spectrometers and Telescopes for the atmosphere
DAC	Digital to Analog Converter
DAC	Digital to Analog Converter
DAS	Double Slot Antenna
DC	Direct Current
DLR	Deutschen Zentrums für Luft- und Raumfahrt
DSB	Double Side Band
EMI	Eletro-Magnetic Interference
Envisat	Environmental Satellite (an Earth-observing satellite built by the European Space Agency)
FASCODE	Fast Atmospheric Signature Code
FFO	Flux Flow Oscillator
FIR	Far InfraRed
FOV	Field Of View
FT	Fourier Spectrometer
FT-IR	Fourier Transform Infra Red
GOME	Global Ozone Monitoring Experiment satellite
HEB	Hot Electron Bolometer
HEMT	High Electron Mobility Transistor
HITRAN	High Resolution Transmission
HM	Harmonic Mixer
IDL	Interactive Data Language
IF	Intermediate Frequency
IMK	Institut für Meteorologie und Klimaforschung
JPL	Jet Propulsion Laboratory
LDPE	Low Density Polyethylene
LNA	Low Noise Amplifier
LO	Local Oscillator
LSB	Lower Side Band
LVDT	Linear Variable Differential Transformer

Abbreviations	Meanings
MAHRSI	Middle Atmosphere High Resolution Spectrograph Investigation
MIPAS	Michelson Interferometer for Passive Atmospheric Sounding
MIPAS-B	Interferometer for Passive Atmospheric Sounding on a stratospheric balloon gondola
MLS	Microwave Limb Sounder satellite
MPI	Martin-Puplett Interferometer
NASA'EOS	NASA's Earth Observing System
NASA's TIMED	Thermospher Ionosphere Mesosphere Energetics Dynamics
NT	Noise Temperature
OPD	Optical Path Difference
PLL	Phase Locked Loop
RAL	Rutherford Appleton Laboratory
RF	Radio Frequency
RPG	Radiometer Physics GmbH
SAW	Sub Arctic Winter
SCOUT-O3	Stratospheric-Climate Links with Emphasis on the Upper Troposphere and Lower Stratosphere
SIR	Superconducting Integrated Receiver
SIS	Superconductor Isolator Superconductor
SMA	SubMiniature version A
SRON	Netherlands Institute for Space Research
SSB	Single Side Band
TELIS	Terahertz and submm Limb Sounder
THOMAS	TeraHertz OH-Mesurement Airborne Sounder
USB	Upper Side Band
UTC	Superconductor-Insulator-Superconductor
YIG	Yttrium Iron Garnet filter

Appendix B: Microwindow

Table A-1 illustrates the micro-windows specification of the 1.8 THz channel and the frequencies in Table A-2 are alternative LO frequency for all micro-windows which can be used in case of the LO power is not reached the optimum power (lower or higher than the optimum power).

Table A-1: Micro-windows of the 1.8 THz channel

No.	Species	Line center GHz	LOrange(min) GHz	LOrange(max) GHz	Side band
M1	OH	1834.75	1829.35	1830.25	USB
M2	OH	1837.80	1842.20	1842.70	LSB
M3	$H_2{}^{17}O$	1880.75	1875.65	1876.55	USB
M4	$H_2{}^{18}O$	1815.85	1820.05	1820.85	LSB
M5	$H_2{}^{19}O$	1840.15	1834.70	1836.00	USB
M6	HDO	1853.90	1858.10	1859.60	LSB
M7	$^{16}O^{18}O$	1875.04	1870.04	1870.84	USB
M8	HO_2	1821.80	1817.40	1817.70	USB
M9	CO	1841.36	1836.10	1836.56	USB
M10	HCl	1873.40	1868.15	1869.05	USB

Table A-2: Micro-windows of the 1.8 THz channel (alternative)

No.	Species	Line center GHz	LOrange(min) GHz	LOrange(max) GHz	Side band
M11	OH	1834.75	1839.75	1840.20	LSB
M12	OH	1837.80	1833.50	1833.60	USB
M13	$H_2{}^{17}O$	1766.20	1770.70	1771.00	LSB
M14	$H_2{}^{18}O$	1800.50	1804.65	1805.65	LSB
M15	$H_2{}^{18}O$	1815.85	1810.05	1811.65	USB
M16	$H_2{}^{19}O$	1783.40	1788.35	1788.80	LSB
M17	$H_2{}^{19}O$	1840.15	1844.20	1844.35	LSB
M18	HDO	1818.50	1823.70	1824.30	LSB
M19	HDO	1818.50	1813.80	1814.30	USB
M20	HDO	1853.90	1849.10	1849.70	USB
M21	$^{16}O^{18}O$	1875.04	1880.34	1880.74	LSB
M22	HO_2	1805.50	1810.08	1810.13	LSB
M23	HO_2	1821.80	1826.45	1826.55	LSB
M24	HO_2	1847.25	1842.68	1842.75	USB
M25	CO	1841.36	1846.00	1846.10	LSB
M26	HCl	1873.40	1877.60	1878.40	LSB
M27	HDO	1818.50	1823.95	1824.10	LSB

Appendix C: Water vapour absorption

The water vapour absorption between the loads (hot/cold) and the window of the 1.8 THz channel can reduce the intensity of the measured signal. Thus, to calculate the system noise temperature, the water vapour absorption in the optical path should be taken into account. Figure B-1 shows the model of the water vapour at 1 bar in three different absorption paths which was used during the measurement in the laboratory.

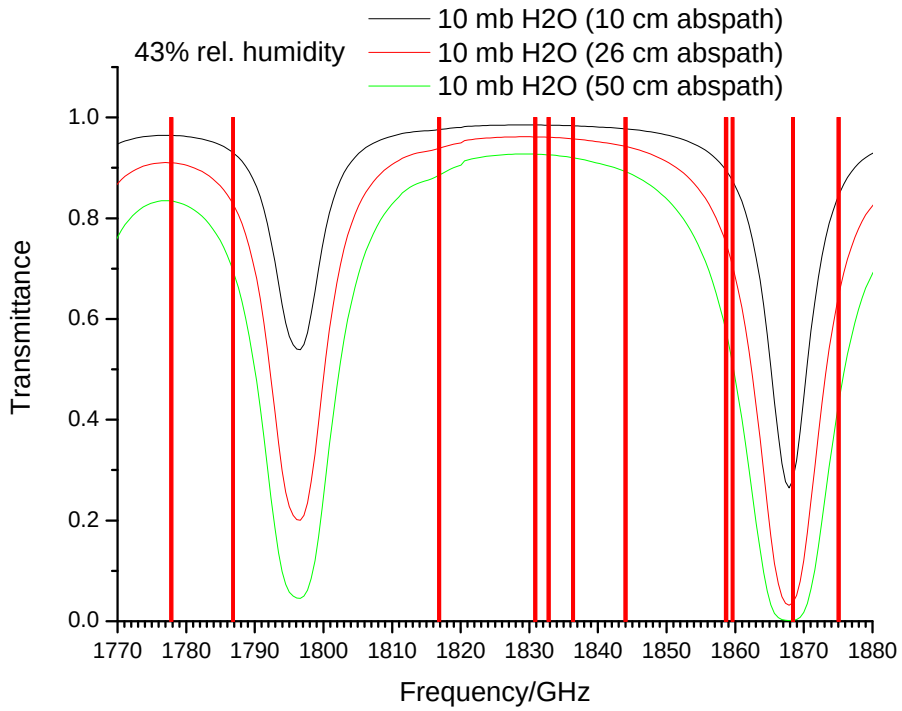

Figure B-1: Water absorption cross sections at 1000 mb were modelled applying Hitran2000 database. Note water frequencies differ from the newest JPL version by about 6 MHz which, however, is uncritical here, due to the large line width at ambient pressure [Birk, 2007]. The red bars are the LO frequencies from the micro-window specification [Birk, et al., April,2008].

Appendix D: Summary of total heat transfer and power dissipation

The summary of the heat transfer (HT) and the power dissipation (PD) of all cables wired between the devices applied to the 1.8 THz channel at the temperature ~4 K and the connector mounted outside the cryostat at temperature 300 K is illustrated in Table C-1, C-2 and C-3. “HT” and “PD” refer to heat transfer and power dissipation, respectively.

Table C-1: Heat load between 300 K and 77 K

No.	Devices	HT+PD (mW)
1	HEB	16,50
2	LO	16,50
3	Diplexer	20,90
4	SSB	20,90
5	Cold Amplifier	10,80
6	Temperature Sensors (DT670x2)	10,50
	Sum	**96,10**

Table C-2: Heat load between 77 K and 4 K

No.	Devices	HT+PD (mW)
1	HEB	0,30
2	LO	0,30
3	Diplexer	1,60
4	SSB	1,60
5	Cold Amplifier	2,10
6	Temperature Sensors (DT670x2)	0,20
	Sum	**6,10**

Table C-3: Summary of the heat load between 300 K and 4 K

No.	Devices	HT+PD (mW)
1	HEB	16,90
2	LO	16,90
3	Diplexer	22,20
4	SSB	22,20
5	Cold Amplifier	12,90
6	Temperature Sensors (DT670x2)	10,70
	Sum	**101,80**

Appendix E: Schematic diagrams

E.1 Filtering Adapter

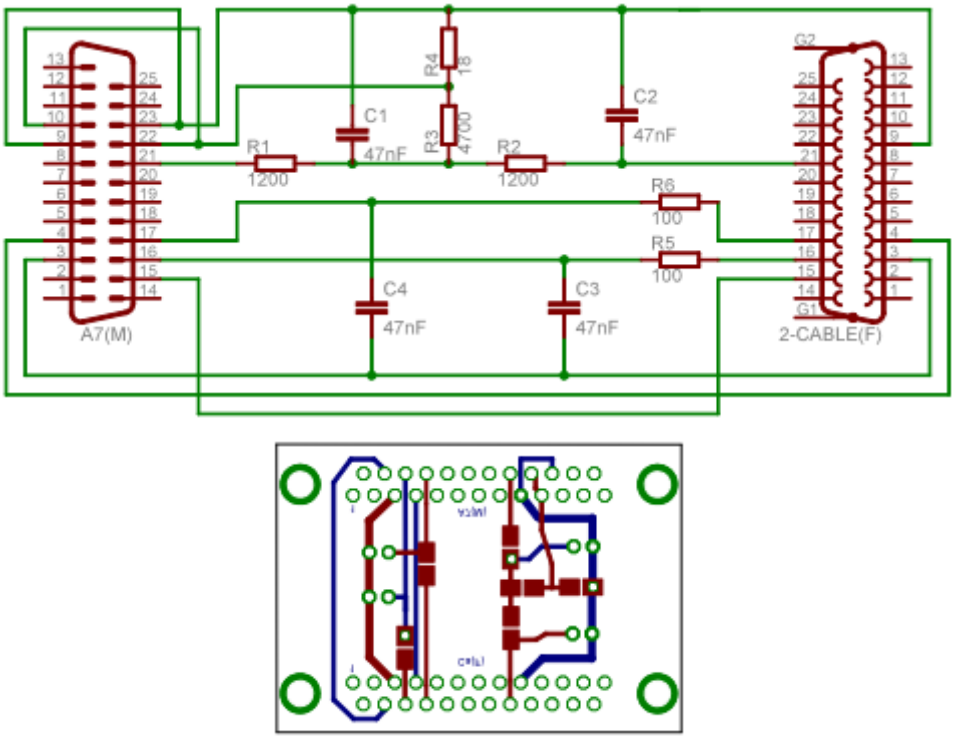

Figure E-0-1: Schematic diagram and the layout of the filtering for HEB bias-monitor and the LO gate bias voltage.

SIS bias board : Bias settings and ranges for the LO gate.

set range	+/-	**2600**	mV
R2		**18**	ohm
R1		4662	ohm

R1		**4700**	ohm
R2		18	ohm
set range	+/-	2621,11	mV
set resolution		79,990	uV/bitstep

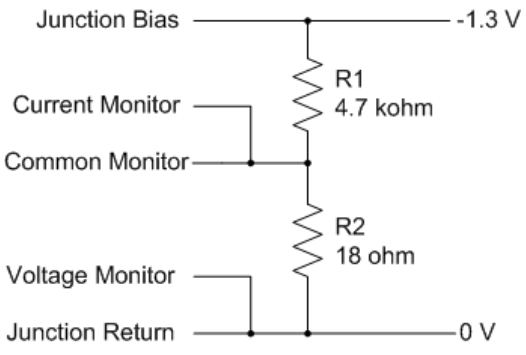

Figure E-2: Range and resolution of the setting for the LO gate bias voltage.

E.2 Bias and monitor of the cold amplifier

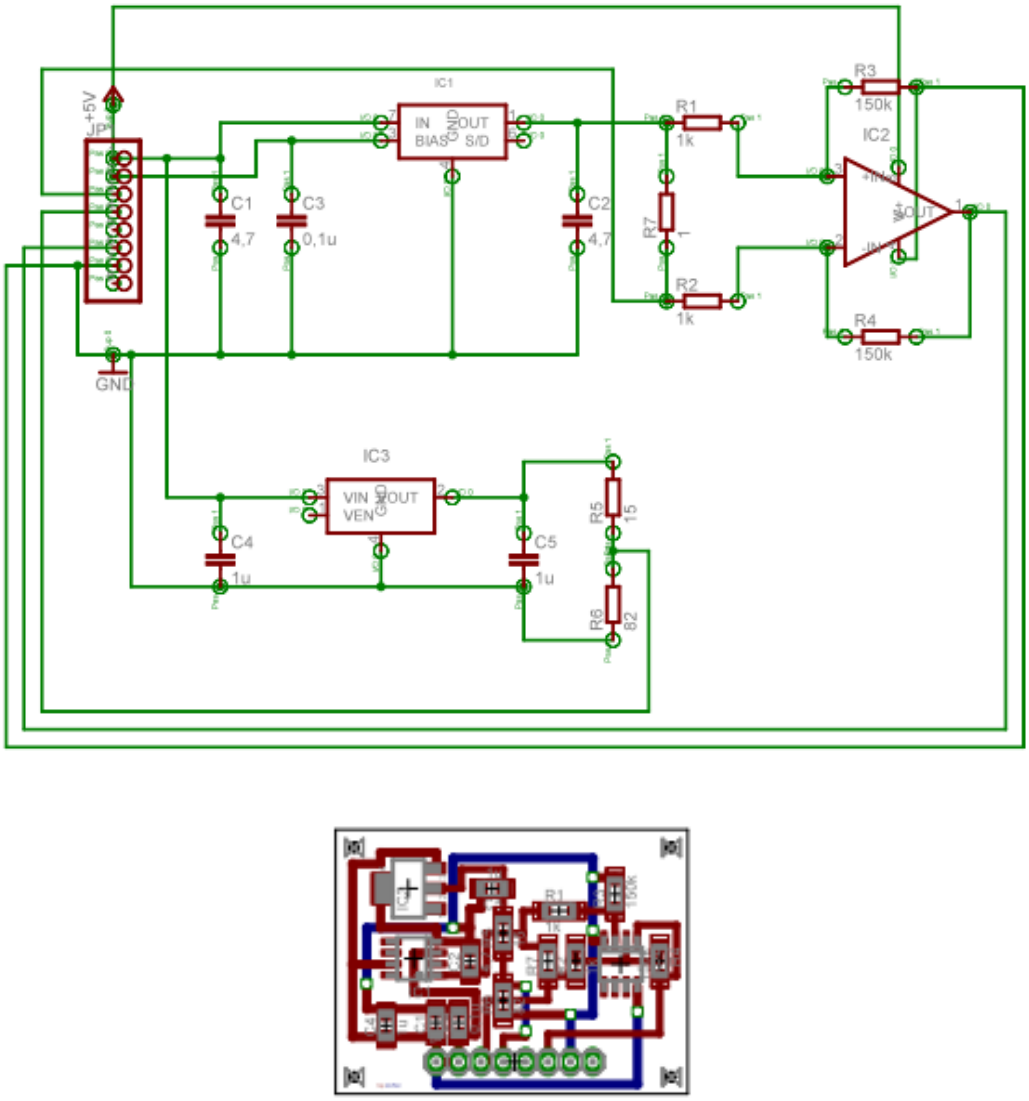

Figure E-3: Schematic diagram and the layout of the bias and monitor of the cold amplifier.

Appendix F: Lab-Software

Most laboratory software are complicated than the flight software due to the direct communication to the devices over different bus system. Thus, more necessary functions must be additional implemented and separately tested. All functions implemented in laboratory software are very important since they are later used a commands and macros in the TELIS database (Flight version).

During the development, several laboratory software were implemented, however only two of them are selected to publish in this Appendix: Software for measuring the antenna beam profile and cell measurement.

F.1 Antenna beam profile measurement

This software is used for measuring the antenna beam profile by control the position of the telescope via the TELIS database and read out the data from either a lock-in amplifier or a power meter.

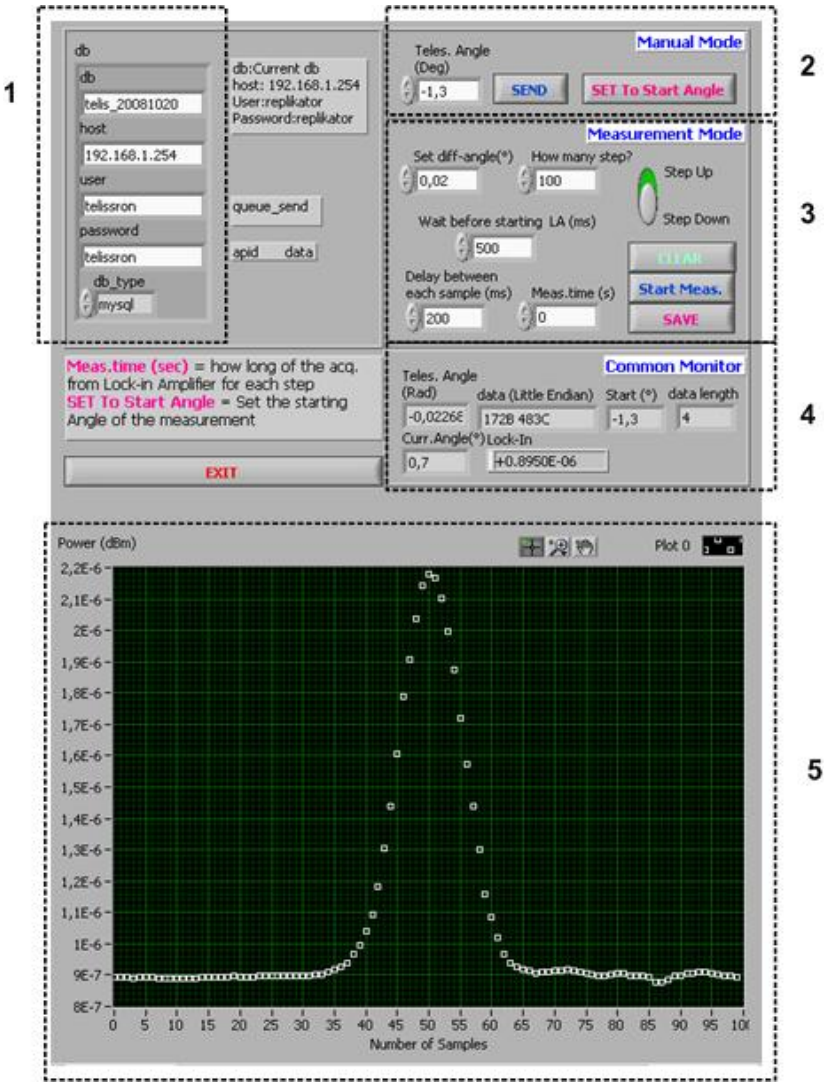

Figure F-0-1: Graphic User Interface of the antenna beam profile software.

No.1: used for specifying the currently database and type of the database (over "mysql" or "OBDC").

No.2: Define the telescope angle which used as a starting position in the scan routine. The number of an angle is in degree. The degree will automatically changed into radian before sending the command to the TELIS database.

No.3: "Measurement mode" used to define the delay time before starting the measurement, delay between each acquisition, measurement time, direction of scanning (upwards or downwards) and save the measured data into txt-file.

No.4: "Common Monitor" is used to monitoring the current angle of the telescope and other important factors.

No.5: A graph shows the result of the measurement. X-axis refers to the number of samples and Y-axis refers to the power measured by ether a lock-in amplifier (in Volts) or a power meter (in Watts).

F.2 Cell Measurement

This software was developed not only for performing the radiometric calibration but also for measuring the noise temperature spectrum, spectra and Y-factor by means of the autocorrelator spectrometer. The software gives also an opportunity to search for suitable positions of a switching mirror used as a switch between different blackbodies. It provides as well a possibility to initialize and calibrate the autocorrelator spectrometer.

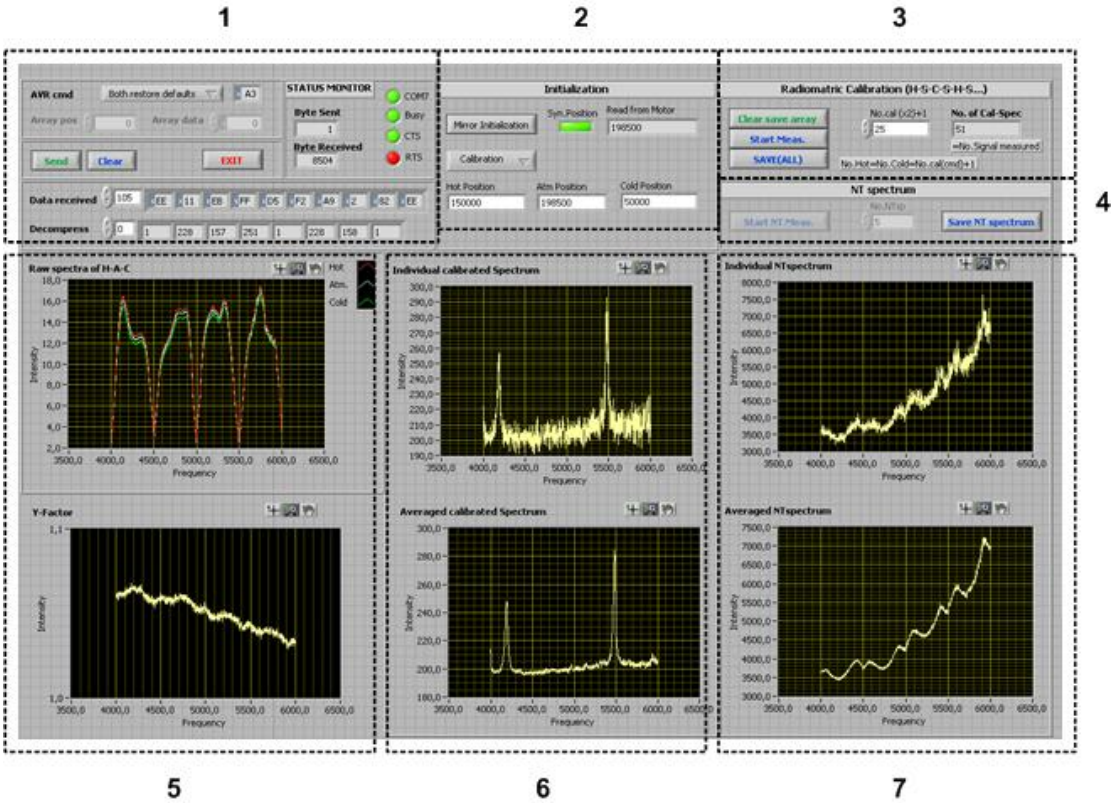

Figure F-2: Graphic User Interface of the software for cell measurement.

No.1: Buttons and indicators in this group are used for initializing and calibrating the autocorrelator spectrometer. LEDs indicate the status of the RS488 bus.

No.2: Define suitable positions for a switching mirror. The speed of the mirror was already calibrated and fix as a constant value in the software.

No.3: "Radiometric Calibration" Buttons and controls here serve as a tool for performing the radiometric calibration. Measurement time is defined by a number of the calibrated spectrum where it depends also on the integration time of each spectrum which can define in No.1.

No.4: "NT spectrum" is used to performing the noise temperature measurement. Measurement time depends also on a number of noise temperature spectrum.

No.5: The upper graph shows hot, signal, cold spectra of each calibrated spectra during the measurement. The lower graph shows a Y-factor which is calculated by hot and cold spectra of a current measurement.

No.6: The upper graph shows an individual calibrated spectrum. The lower graph shows an averaged calibrated spectrum of this measurement routine.

No.7: The upper graph shows an individual noise temperature spectrum of the current measurement. An averaged noise temperature spectrum is shown in the lower graph.

Appendix G: Flight-Software

Structure of the flight software (last update 2009):

The flight software comprises of the software on the PC104 which uses to communicate directly with instruments on the balloon and the ground softwares. The heart of the ground software is the ground server (developed by Dr. Michael Krocka) which communicate with the TELIS instrument on the balloon via the sender/receiver. The technique of the (radio) sender/receiver depends on the organization of the scientific balloon campaign for instance in the scientific balloon campaign in Terasina, Brasil (2008) organized by CNES and the ETNA was utilized for the sender/receiver.

The IDL tool developed by Dr. Georg Wagner and Dr. Manfred Birk is used for the pointing purpose as well as the quick look of the limb spectra with simulation for the 1.8 THz channel.

The Labview Tools were developed by Nopporn Suttiwong during the frame work of this thesis consists of the tool for communicating/testing/initializing the 1.8 THz channel (F.1) as well as characterizing the 1.8 THz channel (F.2), the tool for performing the radiometric calibration for three cryogenic channels including (automatic/manual) initializing the autocorrelator (F.3) and the tool for performing the post processing utilized for redoing the radiometric calibration (F.4). Due to the plenty of the functions available in each software tools, only some main functions of each tool will be introduced.

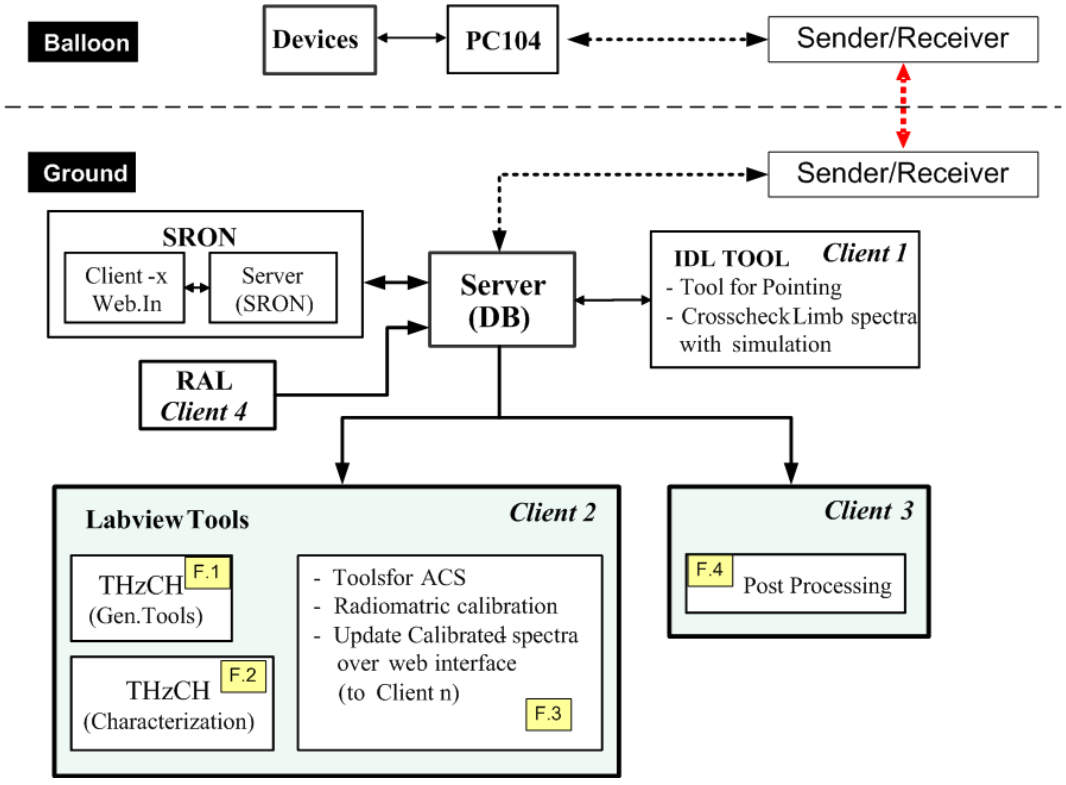

Figure G-1: The schematic shows the flight software structure of the TELIS instrument.

G.1 General Monitor/Control for the1.8 THz channel

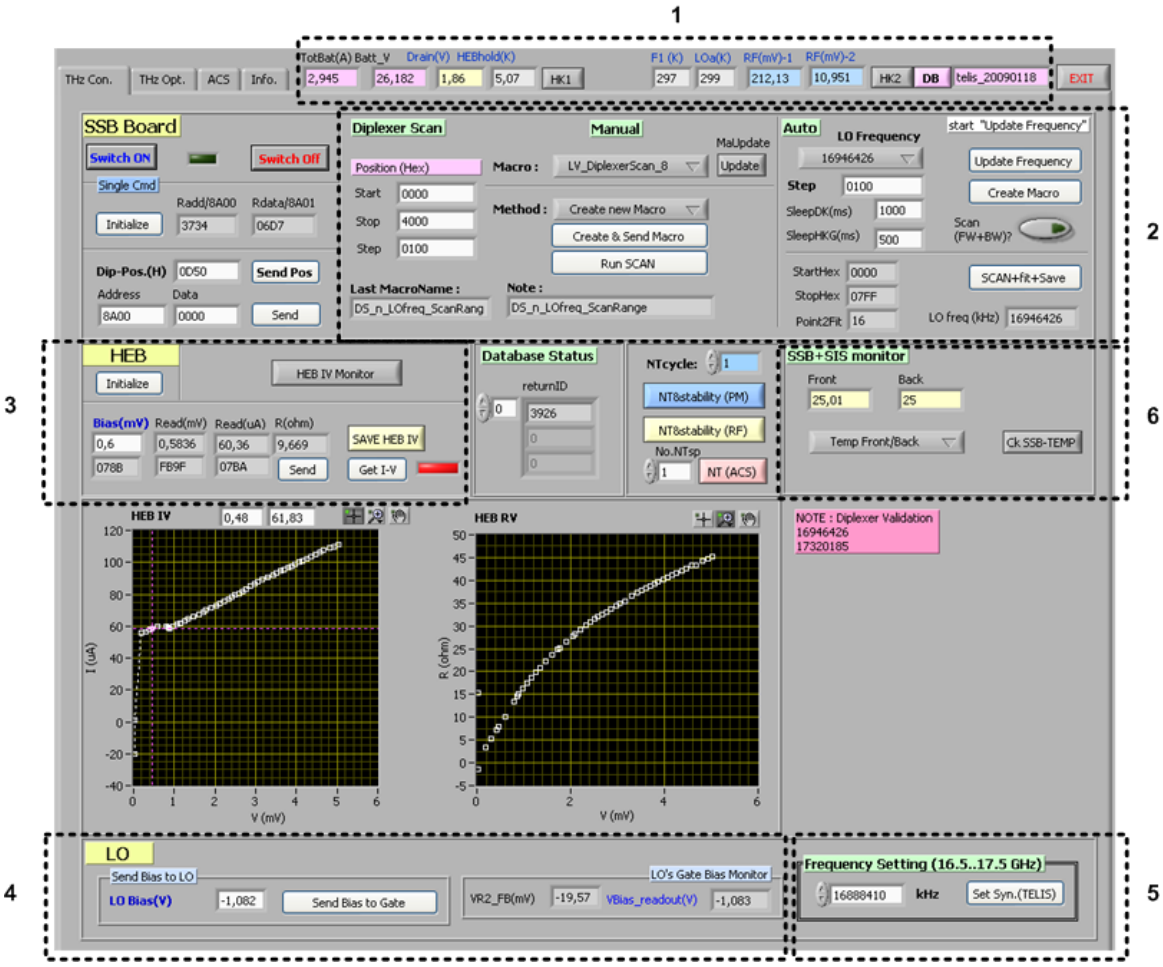

Figure G-2: Graphic User Interface of general tool for the 1.8 THz channel.

No.1: Monitor for all house keeping relevant for operating the 1.8 THz channel such as the current consumption of the batteries, the bias supply for the cold amplifier, temperature at the HEB holder, temperature at the LO warm part and the output absolute power retrieved by two RF detectors.

No.2: Tools for the diplexer consisting of the automatic macro generation for the diplexer scan and fit the minimum of the curve.

No.3: Control the HEB bias and monitor the readout of the HEB voltage, the HEB current.

No.4: Control/monitor the gate voltage of the LO.

No.5: Set the LO frequency by setting the frequency of the TELIS synthesizer (16.5 GHz to 17.5 GHz).

No.6: Monitor the temperature, the bias voltages and the current consumptions of the SIS card which is used to control the diplexer position, the HEB bias and the gate voltage of the LO warm part.

G.2 Characterization tool for the1.8 THz channel

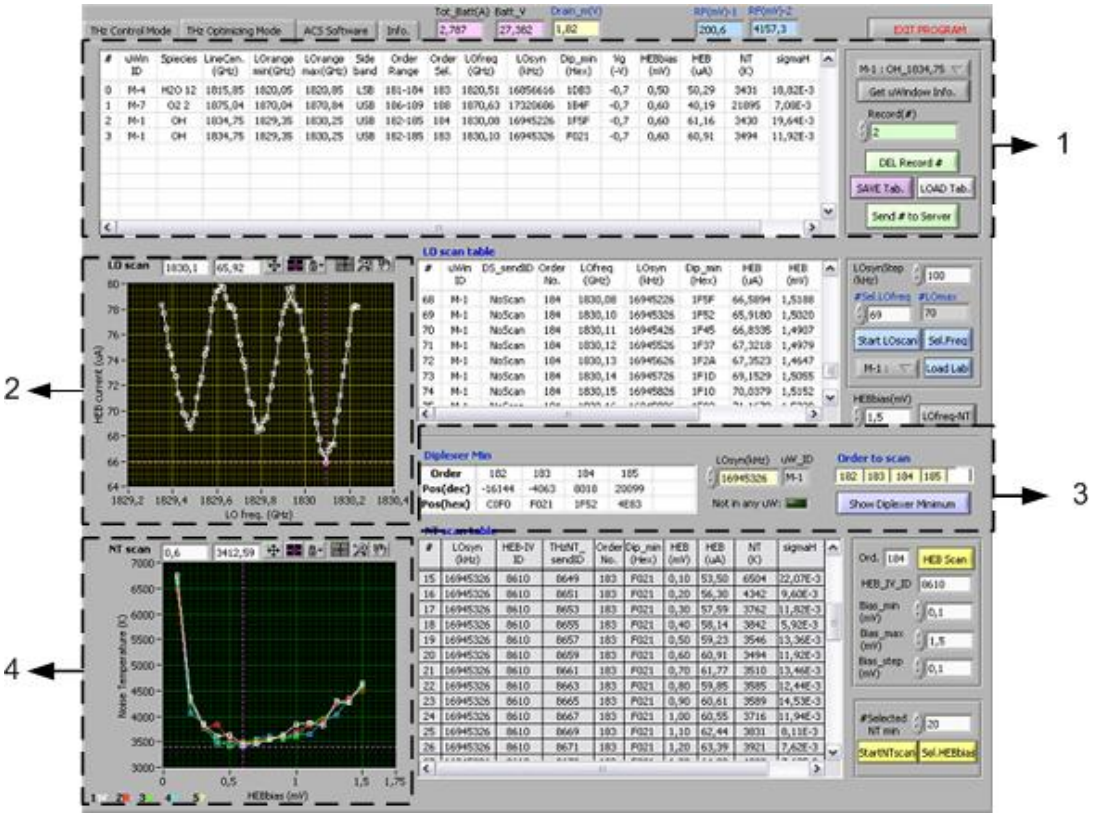

Figure G-3: Graphic user interface of the characterization tool of the 1.8 THz channel.

No.1: the main table recording all the selected parameters.

No.2: the LO power at observed LO frequencies will be shown in this graph (LO frequency-HEB current). The old measured in the laboratory can be retrieved as well as compared with the new measurement of the LO power. Not only the LO power at different frequencies can be measured but also the system noise temperature at different LO frequencies (which have different LO power) can also be measured.

No.3: the best adjustment of diplexer at each order calculated by the diplexer calibration function (chapter 6.1.4.4).

No.4: the relationship between the HEB bias, system noise temperature and the stability.

(see chapter 6.2.1)

G.3 Radiometric Calibration & ACS tools

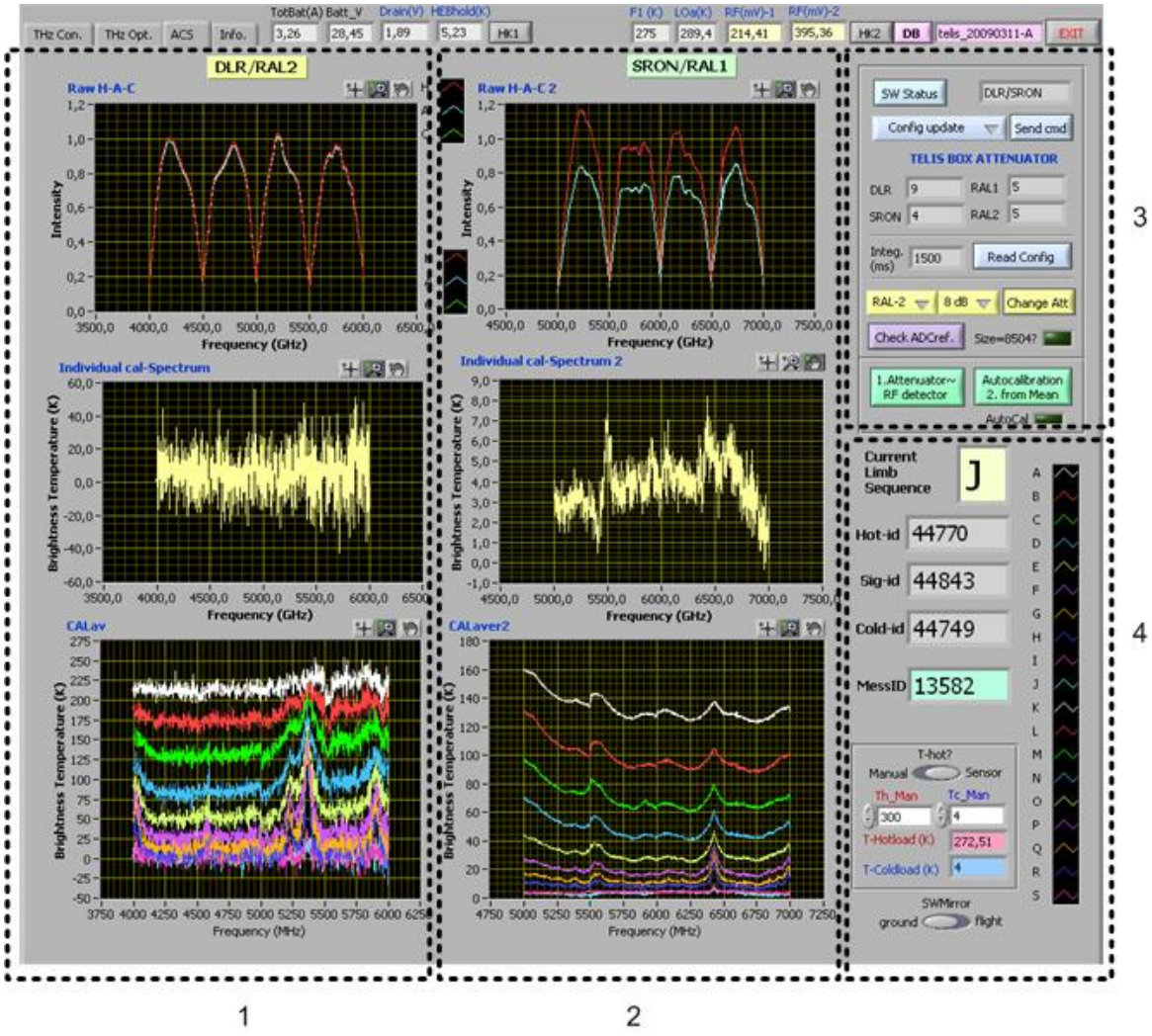

Figure G-4: Graphic user interface of the radiometric calibration and ACS tools.

No.1: the upper graph illustrates the hot, atmosphere, cold spectra for each calibrated spectrum of the 1.8 THz channel. The middle graph presents the individual calibrated spectrum calculated from three spectra shown in the upper graph. The lower one shows the averaged calibrated spectra for each limb sounding.

No.2: the meaning of each graph as described in No.1 but the illustrations are for 450-650 GHz channel.

No.3: The GUI for interfacing with the autocorrelator spectrometer. It consists of all command used for initializing/communicating the autocorrelator, monitoring the performance of the autocorrelator, checking and setting the ADC reference level and changing the internal attenuators inside the TELIS box (see chapter 6.3)

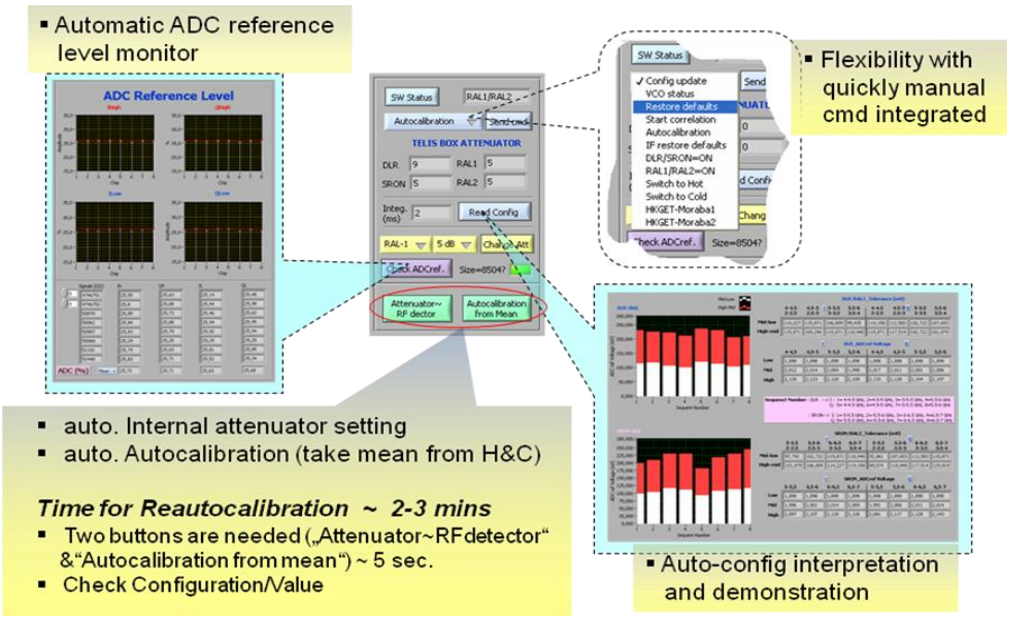

Figure G-5: Picture shows screen shots of the pop-up window for each significant buttons.

No.4: the additional information for the calibration such as the temperature measured by the PT100 at the hot cone blackbodies and the cold temperature set for this calibration, and the number of the measurement macro redone the calibration, the setting of the quantization time during the online-operation is always set to ‘none’ (see the explanation in F.4)

G.4 Post processing

During the flight the on-line calibrated spectra are done without the quantization correction due to the limitation of the time. Thus this software was implemented in order to redo the calibration later with either minimum or maximum quantization correction by using the measurement index.

Minimum quantization correction = minimum the time used for calculating the correction for the quantization by using the look up table.

Maximum quantization correction = full calculation of the quantization correction where the calculation process takes the longest time.

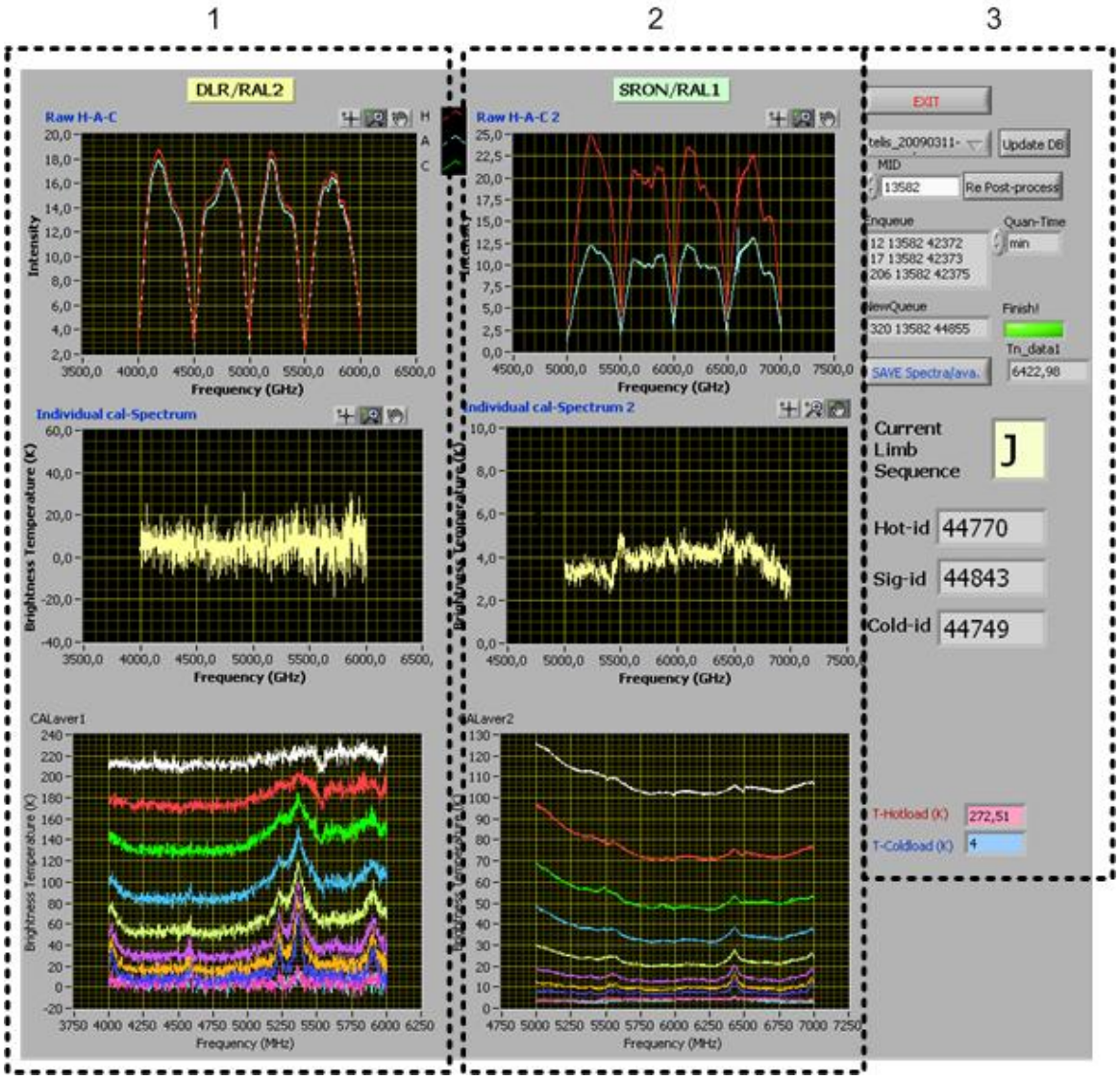

Figure G-6: Graphic User Interface of the software for performing post processing.

No.1: the upper graph illustrates the hot, atmosphere, cold spectra for each calibrated spectrum of the 1.8 THz channel. The middle graph presents the individual calibrated spectrum calculated from three spectra shown in the upper graph. The lower one shows the averaged calibrated spectra for each limb sounding.

No.2: the meaning of each graph as described in No.1 but the illustrations are for 450-650 GHz channel.

No.3: the additional information for the calibration such as the temperature measured by the PT100 at the hot cone blackgodies and the cold temperature set for this calibration, the absolute noise temperature, database and the number of the measurement macro redone the calibration, the setting of the quantization time (min/mid/max).

Appendix H: Gaussian beam of the 1.8 THz channel's warm optics

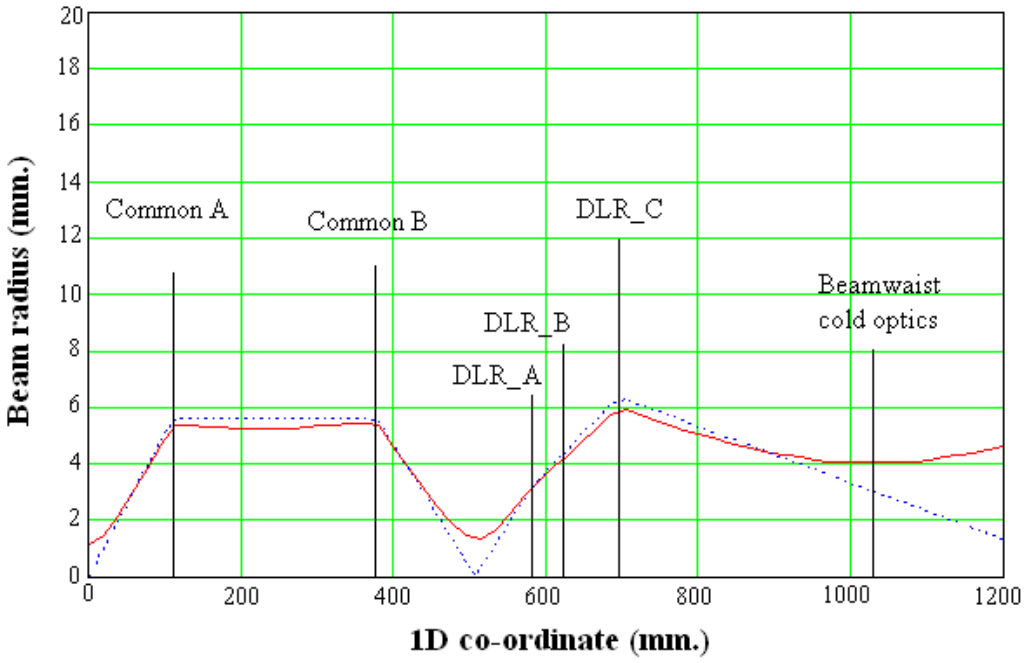

Figure H-1: 1-D Gaussian beam calculation for DLR channel, 1.8 THz. The red line shows Quasioptical beam and the blue one represents the geometrical beam. [Birk, et al., 2004]

Bibliography

Aalders, W. (2003). *Design description of the diplexer roof mirror translator (DRT).* Report, TELIS project.

Ahrens, C. D. (2007). *Essentials of Meteorology-an invitation to the atmosphere* (5 Ausg.). Brooks Cole.

Allan, D. (1990). *Time and Frequency (Time-Domain) Characterization, Estimation, and Prediction of Precision Clocks and Oscillators.* Washington D.C: U.S. Government Printing Office.

Anderson, G. P., Wang, J., Hoke, M. L., Kneizys, F. X., Chetwynd, J. .., Rothman, L. S., et al. (1994). *History of on a family of atmospheric radiative transfer codes.* Rome, Italy.

Anritsu. (2006). *Microwave detectors-70,75 Series 100 kHz to 50 GHz.*

Armstrong, B. (1967). Spectrum line profiles: The voigt function. *Journal of Quantitative Spectroscopy and Radiative Transfer* (7), S. 61-88.

Auton, J. (1967). Infrared Transmission Polarizers by Photolithography. *Applied Optics , 6* (6), S. 1023-1027.

Baubert, J., Merkel, H., Salez, M., & Khosropanah, P. (April 2003). A hot-spot model for memebrane-based HEB mixer. *Proceedings of the 14th International Symposium on Space Terahertz Technology* , S. 393-404.

Benford, D., Gaidis, M., & Kooi, J. (March 1999). Transmission properties of Zitex in the infrared to submillimeter. *Proc. 10th INternational Symposium on Space Terahertz Technology* .

Birk, M. (2007). *Absorption signatures of ambient air on ground @ 1.8 THz.* Report, TELIS project.

Birk, M. (2008). *Non-linearity investigation on THz channel : TELIS (TErahertz and submmw LImb Sounder).* Report, TELIS project.

Birk, M., & Georg, W. (2007). *Dichroric Measurement with Bruker.* Report,TELIS project.

Birk, M., & Wagner, G. (October, 2007). *DSB Microwindow Definition for 1.8 THz channel of TELIS.* Report, TELIS project.

Birk, M., & Wagner, G. (2008). *Impact of Autocorrelator performance on radiometric accuracy part II.* Report, TELIS project.

Birk, M., & Wagner, G. (2009). *Results of antenna beam profile measurements August 2009, TELIS.* Report, TELIS project.

Birk, M., & Wagner, G. (2004). *Warm optics design.* Report, TELIS project.

Birk, M., Wagner, G., & Suttiwong, N. (April,2008). *DSB Microwindow Definition for 1.8 THz channel of TELIS (update).* Report, TELIS project.

Birk, M., Wagner, G., & Suttiwong, N. (2008). *Results of TELIS balloon flight in Teresina, TELIS (TErahertz LImb Sounder).* Report, TELIS project.

Birk, M., Wagner, G., Lange, G. d., Lange, A. d., Ellison, B. N., Harman, M. R., et al. (23-25. March 2010). TELIS: TErahertz and submm LImB Sounder-Project Summary after first successful flight. *21st international symposium on space terahertz technology* .

Brune, W., Faloona, I., Tan, D., Weinheimer, A., Campos, T., Ridley, B., et al. (15. May 1998). Airborne in-situ OH and HO2 Observations in the cloud-free troposphere and

lower stratosphere during SUCCESS. *Geophysical Reseachletters , 10* (25), S. 1701-1704.

Callen, H. B., & Welton, T. A. (1951). Irreversibility and Generalized Noise. *Physical Review , 83* (1).

Chapman, S. (1930). A theory of upper atmospheric ozone. *Mem. Roy. Soc.* (3), S. 103-109.

Cherednichenko, S. (2007). *Coupling efficientcy ofTELIS HEB mixer.* Technical Note.

Cherednichenko, S. (2007). *HEB-Delivery Note.* Technical Note.

Cherednichenko, S., Drakinskiy, V., Berg, T., Khosropanah, P., & Kollberg, E. (2008). Hot-electron bolometer terahertz mixers for the Herschel Space Observatory. *Review of Scientific Instruments , 79* (034501).

Dominic, J. B., Gaidis, M. C., & Kooi, J. W. (2003). Optical properties of Zitex in the infrared to submillimeter. *Applied Optics , 42* (25).

Dorf, R. C., & Bishop, R. H. (2001). *Modern Control Systems* (9 th Edition Ausg.). New Jersey: Prentice-Hall, Inc.

Drayson, S. (1975). Rapid computation of the Voigt profile. *Journal of Quantitative Spectroscopy and Radiative Transfer* (16), S. 611-614.

Drouin, B. J. (5. January 2004). Laboratory and Field Studies in Rotational Spectroscopy at the Jet Propulsion.

Dyrland, M., Mulligan, F., Hall, C., Sigernes, F., Tsutsumi, M., & Deehr, S. (2010). Response of OH airglow temperatures to neutral air dynamics at 78°N, 16°E during the anomalous. *J. of Geophys. Res.* (115).

Ekström, H., Karasik, B., & Kollberg, E. (April 1995). Conversin Gain and Noise of Niobium Superconducting Hot Electron Mixers. *IEEE Trans. Microwave Tech. , 45* (4), S. 938-946.

Ekström, H., Karasik, B., Kollberg, E., & Yngvesson, S. (April 1995). Conversion Gain and Noise of Niobium Superconducting Hot-Electron-Mixers. *IEEE transactions on MIcrowave Theory and Techniques. , 4* (43), S. 938.

Engel, A., Schiller, C., Schmidt, U., Borchers, R., Ovarlez, H., & Ovarlez, J. (1996). The total hydrogen budget in the arctic winter stratosphere during the European Arctic Stratospheric Ozone Experiment. (101), S. 14495-14504.

Englert, C. R., Schimpf, B., Birk, M., Schreier, F., Krocka, Michael, et al. (2000). The 2.5 THz heterodyne spectrometer THOMAS Measurement of OH in the middle atmosphere and comparison with photochemical model results. *Geophys. Res. , D17* (105), S. 22211-22223.

Fahey, D. (2006). *TWENTY QUESTIONS AND ANSWERS.* Supplementary of the Panel Review Meeting for the 2006 Ozone Assessment (Les Diablerets, Switzerland, 19-23 June 2006).

Friedl-Vallon, F., Maucher, G., Seefeldner, M., Trieschmann, O., Kleinert, A., Lengel, A., et al. (June 2004). Design and Characterization of the Balloon-Borne Michelson Interferometer for Passive Atmospheric Sounding (MIPAS-B2). *Applied Optics , 43* (16), S. 3335-3355.

Graauw, T. d., Whyborn, N., Helmich, F., Dieleman, P., Roelfsema, P., Caux, E., et al. (2008). The Herschel-Heterodyne Instrument for the Far-Infrared (HIFI):Instrument and Pre-launch Testing. *Proc. of SPIE , 7010* (701004).

Gupta, R. P. (2003). *Remote Sensing Geology.* Berlin Heidelberg: Springer-Verlag.

Harman, M. (2002). *Project Proposal: A light weight Balloon borne Cryostat in support of the TELIS programme for DLR.* Rutherford Appleton Laborytory.

Heaps, W., McGee, T., Hudson, R., & Caudill, L. (1982). Stratospheric ozone and hydroxyl radical measurements by balloon-borne lidar. *Appl. Opt.* (21), S. 2265-2274.

Hofzumahaus, A., Rohrer, F., Lu, K., Bohn, B., Brauers, T., Chang, C.-C., et al. (2009). Amplified Trace gas Removal in the Troposphere. *Science , 5935* (324), S. 1702-.

Hollas, J. M. (2003). *Modern Spectroscopy* (4 nd Ausg.). Australia: John Wiley&Sons.

Hunter, T., Benford, D., & Serabyn, E. (1996). Optical design of the submillimeter high angular resolution camera (SHARC). *Pub. Astron. Soc. Pac.* (108), S. 1042.

Infrared Laboratories. (1980). *Instruction Manual - 4.2 bolometer with Winston cone.* Arizona, U.S.A.

IPCC. (2007). *Climate Change 2007:The physical Science Basis.* Cambridge, United Kingdom and New York, NY, USA.: Cambridge University Press.

Jacob, J. M. (1989). *Industrial control electronics; Applications and design.* United States of America: Prentice-hall international,Inc.

Janssen, M. A. (1993). *Atmospheric remote sensing by microwave radiometry.* Canada: John Willey&Sons, Inc.

Jöckel, P., Brenninkmeijer, C., Lawrence, M., Jeuken, A., & Velthoven, P. v. (October 2002). Evaluation of stratosphere-troposphere exchange and the hydroxyl radical distribution in three-dimensional global atmospheric models using observations of cosmogenic 14 CO. *Geophys. Res. , D20* (107), S. 4446.

Jucks, K., Johnson, D., Chance, K., Traub, W., Salawitch, R., & Stach, R. (1995). Ozone production and loss rate measurements in the middle stratosphere. *J. Geophys. Res.* (22), S. 1869-1971.

Kooi, J. W., Baselmans, J. J., Hajenius, M., Gao, J. R., Klapwijk, T. M., Dieleman, P. D., et al. (2007). IF impedance and mixer gain of NbN hot electron bolometers. *Jounal of applied physics , 044511* (101).

Kooi, J., Chan, M., Bumble, B., LeDuc, H., Schaffer, P., & Phillips, T. (1995). 230 and 492 GHz loiw-noise SIS waveguide received employing tuned Nb/ALOx/Nb tunnel junctions. *Int.J. Infrared Millim. Waves* (16), S. 2049-2068.

Krocka, M. (2002). *Optimierung und Erweiterung eines flugzeuggetragenen FIR heterodyn-Spektrometers im Himblick auf Emissions- und Absorptionsmessung.* Berlin.

Kroug, M. (2001). *NbN Hot Electron Bolometric Mixers for a Quasi-Optical THz Receiver.* Göteborg: Chalmersbibliotekets reproservice.

Kroug, M., Cherednichenko, S., Choumas, M., Merkel, H., Kollberg, E., Huebers, H., et al. (2001). *HEB Quasi-optical Heterodyne Receiver for THz Frequencies.* San Diego (USA).

Kroug, M., Yagoubov, P., Gol'tsman, G., & Kollberg, E. (1997). NbN Quasi optical Phonon Cooled Hot Electron Bolometric Mixers at THz Frequencies. *Inst. Phys. Conf.*

Land, D. V., Levick, A. P., & Hand, J. W. (2007). The use of the Allan deviation for the measurement of the noise and drift performance of microwave radiometers. *Measurement Science and Technology , 18,* S. 1917-1928.

Lesurf, J. (1990). *Millimetre-wave Optics: Devices and systems.* Bristol and New York: Adam Hilger.

Lesurf, J. (13. March 2002). *Radio&Coherent Techniques*. Von Scots Guide: https://www.st-andrews.ac.uk/ abgerufen

Liou, K.-N. (1980). *An introduction oto atmospheric radiation.* California: Academic Press, Inc.

Liou, K.-N. (2004). *An introduction to atmospheric radiation* (2. Edition Ausg., Bd. 84). California: Academic Press.

Mair, U. (2007). *Entwicklung und Aufbau eines 1.8 THz-Heterodynempfängers für die ballongestützte Fernerkundung von Spurengasen in der Erdatmosphäre.* Berlin: dissertation.de.

Martin, D., & Puplett, E. (1969). Polarised interferometric spectrometry for the millimetre and submillimetre spectrum. *Infrared Physics , 10*, S. 105-109.

Michelsen, H., Irion, F., Manney, G., Toon, G., & Gunson, M. (2000). Features and trends in Atmospheric Trace Molecule Spectroscopy (ATMOS) version 3 stratospheric water vapor and methane measurements. *Geophys. Res.* (105), S. 22713-22724.

Mohanakumar, K. (2008). *Stratosphere troposphere interactions: an introduction.* Springer Science and Business Media B.V.

Murk, A. (2005). *Reflection Measurements of the TELIS Calibration Hot Load at 625 GHz.* University of Bern.

NASA. (17. September 2009). *Ozone Hole Watch*. Abgerufen am 7. April 2010

National Research Council (U.S.). Global Tropospheric Chemistry Panel. (1984). *Global tropospheric chemistry: a plan for action.* Washington, DC, USA: National Academy press.

Newchurch, M., Yang, E.-S., Cunnold, D. M., Reinsel, G. C., Zawodny, J. M., & Russell III, J. M. (kein Datum). Evidence for slowdown in stratospheric ozone loss: frist stage of ozone recovery. *J. Geophys. Res. , D16* (108), S. 4507.

Nyquist, H. (July 1928). Thermal Agitation of electric charge in conductors. *Physical Review , 32*.

Oelhaf, H. (10. June 2008). SCOUT-O3 Large Balloons Equatorial Field Campaign (Teresina 2008). *SCOUT Campaign Newsletter* , S. 8-10.

Omnisys Instruments AB. (2005). *Final Report.* Technical Note.

Omnisys Instruments AB. (2004). *Project ABT-TELIS.* Technical Note, TELIS project.

Ortega, J. M., & Rheinboldt, W. C. (2000). *Iterative Solution of Nonlinear Equations in Several Variables.* Society for Industrial Mathematics.

Parylene Engineering. (2009). *www.paryleneengineering.com*. Abgerufen am 2010

Perrin, N., & Vanneste, C. (November 1983). Response of superconducting films to a periodic optical irradiation. *Physical Review B , 28* (9), S. 5150-5159.

Pickett, H. (May 2006). MIcrowave Limb Sounder THz module on Aura. *IEEE Transactions on Geoscience and REmote Sensing , 5* (44), S. 1122-1130.

Polavarapu, P. L. (1998). *Principles and applications of polarization-division interferometry*. West Sussex, England: John Wiley & Sons Ltd.,.

Prober, D. (April 1993). Superconducting terahertz mixer using a transition-degemicrobolometer. *Applied Physics Letters , 62* (17), S. 2119-2121.

QMC Instruments. (2008). *THz-Terahertz*. (Toolmaking for Terahertz Systems&Components) Von www.terahertz.co.uk abgerufen

Reimann, S., Manning, A., Simmonds, P., Cunnold, D., Wang, R., Li, J., et al. (2005). Low European methyl chloroform emissions inferred from long-term atmospheric measurements. *Nature* (433), S. 506-508.

Richter, H. H. (2005). *Entwicklung von HOt Electron Bolometer-Mischern für Terahertz-Heterodynempfänger.* Berlin.

Rothman, L., Gordon, I., Barbe, A., Benner, D., Bernath, P., Birk, M., et al. (2009). The HITRAN 2008 molecular spectroscopic database. *Journal of Quantitative&Spectroscopy&Radiative Transfer* (110), S. 533-573.

Schreier, F., Xu, J., Doicu, A., Birk, M., & Wagner, G. (16-19. November 2009). TELIS data Processing: Status and First Results. *5th International Atmospheric Limb Conference and Workshop* .

Scientific Committee on Antarctic Research (SCAR. (2009). *The review - Antarctic Climate Change and the Environment.*

Seinfeld, J., & Pandis, S. (2006). *Atmospheric chemistry and physics from air pollution to climate change.* Canada: John Wiley&Son.

Skou, N. (1989). *Microwave Radiometer Systems: Design and Analysis.* Boston: Artech House.

Smith, A. A. (1998). *Radio Frequency Principle and applications.* New York: IEEE Press.

Solomon, S., Rosenlof, K. H., Portmann, R. W., Daniel, J. S., Davis, S. M., Sanford, T. J., et al. (28. January 2010). Contributions of stratospheric Water Vapor to decadal changes in the rate of global warming. *Science Express , 5970* (327), S. 1219-1223.

Sparling, B. (May 2001). *Educational resources*. (NASA) Abgerufen am April 2010 von http://www.nas.nasa.gov

Stenman, U. (March 2006). Personal communication.

Stimpfle, R., & Anderson, J. (17. October 1988). In-situ detection of OH in the lowerstratosphere with a balloon borne high repetition rate laser system. *Geophys. Res. Lett. , 13* (15), S. 1503-1506.

Strong, J., & Plass, G. N. (November 1950). The effect of pressure broadening of spectral lines on atmospheric temperature. *The astrophysical journal , 3* (112), S. 365-379.

Suttiwong, N. (2004). *Control and measurement setup for laboratory use.* Master Thesis.

Suttiwong, N. (2006). *THz Channel cabling plan for flight module cryostat.* Technical Note, TELIS project.

Suttiwong, N. (2008). *THz Channel summerization.* Report, TELIS project.

Suttiwong, N., & Vogt, P. (25.02.2009). *THz Channel and Stability of DLR/SRON channels (Tests on 18-22.01.2008 in Kiruna).* Report, TELIS project.

Thomas, G., & Stamnes, K. (1999). *Radiative Transfer in the Atmosphere and Ocean.* UK: Cambridge university press.

Titz, R., Birk, M., Hausamann, D., Nitsche, R., Schreier, F., Urban, J., et al. (1994). Observation of stratospheric OH at 2.5 THz with an airborne heterodyne system. *Infrared Phys. Technol. , 36*, S. 883-890.

Ulaby, F. T., Moore, R. K., & Fung, A. K. (1981). *MIcrowave remote sensing-Active and passive (Volume 1).* Massachusetts: Addison-Wesley Publishing Company.

Vardavas, l. M., & Taylor, F. (2007). *Radiation and climate.* (I. s. physics, Hrsg.) New York: Oxford University Press Inc.

Vries, E. d. (2007). Personal communication.

Wallance, J., & Hobbs, P. (1977). *Atmospheric Science-An Introductory Survey.* New York: Academic Press.

Warneck, P., Junge, C. E., & Seiler, W. (December 1973). OH radical concentration in the stratosphere. *Pure and Applied Geophysics , 1* (106).

Weatherhead, E., & Andersen, S. (2006). The search for signs of recovery of the ozone layer. *Nature* (441), S. 39-45.

Weisenstein, D., Ko, M., & Rodriguez, J. (1993). Effects on stratospheric ozone from high-speed civil transport:sensitivity to stratospheric aerosol loading. *J. Geophys. Res.* (98), S. 23133-23140.

Wennberg, P., Cohen, R., Stimpfle, R., Koplow, J., Anderson, J., Salawitch, R., et al. (21. October 1994). Removal of Stratospheric O3 by Radicals: In Situ Measurements of OH, HO2, NO, NO2 ClO and BrO. *Science , 5184* (266), S. 398-404.

Wetzel, G. (2009). personal communication.

Widell, O. (14. March 2009). *Project Manager's report*. (Esrange Space Center) Abgerufen am 2010 von http://www.ssc.se

Wilmshurst, T. (1990). *Signal recovery from noise in electronic instrumentation* (2. Edition Ausg.). Bristol, England: IOP Publishing LTd.

Witt, T. (2001). *IEEE transaction on Instrument and Measurement , 50,* S. 445.

WMO. (2007). *Global Ozone Research and Monitoring Project.*

Yagoubov, P., & Pylypenko, O. (2004). *TELIS Room Temperature amplifiers performance.*

Yagoubov, P., Kroug, M., Merkel, H., & Kollbert, E. (November 1998). Noise temperature and local oscillator power requirement of NbN phonon-cooled hot electron bolometric mixers at terahertz frequencies. *Applied Physics Letters , 73* (19), S. 2814-2816.

Yagoubov, P., Lange, G. d., Golstein, H., Jong, L. d., Lange, A. d., Kuik, B. v., et al. (28-30. April 2008). Superconducting Integrated Receiver on Board TELIS. *19th International Symposium on Space Terahertz Technology* , S. 268-274.

Publications

Journal Articles

N. Suttiwong, M. Birk, G. Wagner, “Development and characterization of the 1.8 THz heterodyne receiver of the balloon-borne instrument TELIS (TErahertz and Submm Limb Sounder).”, 2010, in progress.

Articles in Conference Proceedings

N. Suttiwong, M. Birk, et al.,"Development and characterization of the balloon-borne instrument TELIS (TErahertz and Submm Limb Sounder): 1.8 THz receiver", in Proceedings of the 19th ESA Symposium on European Rocket and Balloon Programmes and Related Research, 7-11 June 2009, Bad Reichenhall, Germany (ESA SP-671), pp.165-168.

P. Yagoubov, R. Hoogeveen, M. Torgashin, A. Khudchenko, V. Koshelets, N. Suttiwong, G. Wagner, M. Birk, "550-650 GHz spectrometer development for TELIS", in Proceeding of the 17th International Symposium on Space Terahertz Technology, 10-12 May 2006, Paris, France.

Poster presentations

Nopporn Suttiwong, Ulrich Mair, Manfred Birk, Georg Wagner, Sergey Cherednichenko, “TErahertz and submm LImb Sounder (TELIS), Development and characterization a cryogenic THz heterodyne receiver for TELIS.”, EGU General Assembly, 15-20 April 2007, Wien, Austria.

U. Mair, N. Suttiwong, H.-W. Hübers, A.D. Semenov, H. Richter, G. Wagner, M. Birk,”Development of a 1.8THz receiver for the TELIS instrument”, 16th International Symposium on Space Terahertz Technology, 2-4 May 2005, Chalmers University of Technology, Göteborg, Sweden.

Acknowledgements

Without these very important people, I would never have been able to complete this ph.D work. I would like to thank all those who have helped and supported me during the completion of my study.

I owe my deepest gratitude to **Prof. Dr. Jutus Notholt** who supervised this thesis, **Prof. Dr. Klaus Künzi** who has taken the secondary supervising role of this work, **Dr. Harry Küllmann** who has provided an irreplaceable cooperation as well as all of the members the Institute of Environmental Physics (IUP), University of Bremen.

I am extremely grateful to all precious members of the department of Experimental methods (IMF-EV), Remote Sensing Technology Institute at DLR (German Aerospace Center) for their infinite help, especially **Dr. Peter Haschberger**, who gave me an opportunity to work in his department, encouraged me during my hard time as well as providing me with valuable suggestions, support. I would never get a chance to work with this challenge topic as well as achieve this doctoral work without a great support from my advisor **Dr. Manfred Birk**. This thesis would not have been possible without these people who saved me from leaving this work. Sincere thanks must also be given to my wonderful colleagues who gave me irreplaceable hospitality, technical supports and their valuable knowledge: **Hans-Otto-Stöhr**, **Dr. Michael Krocka, Andreas Wenisch**, **Erich Bogner** and **Jürgen Wörishofer**. Thanks for the useful advice and precious help of **Dr. Georg Wagner, Dr. Volker Tank**, **Dr. Christain Schwarz** and **Paul Schötz**. Furthermore, I appreciate all the cooperation of **DLR workshop**, and especially **Bernd Gabler** at the Microwaves and Radar Institute.

Since the second year of my work, I have had the chance to accumulate valuable experiences from sophisticated people from different groups such as SRON. It is a pleasure to thank them for their wonderful cooperation, sharing with me your knowledge, supporting my work and making me always laugh in dreadful times: **Leo de Jong, Willem Jan Vreeling, Ed de vries, Dr. Gert de Lange, Dr. Arno de Lange, Dr. Pavel Yagoubov,** and especially **Hans Golstein** who always conveyed to me his professional knowledge, spent his valuable time for proofing my dissertation, and that he didn't realize that he accidentally gave me an important insight-"*Aha..that is a meaning of doctoral work*!"

I am grateful to **Dr. Ulrich Mair** and **Dr. Christoph Englert** for spending their valuable time for proofing the dissertation as well as providing me useful suggestions.

I would never have the first step in Germany without their irreplaceable supports. Sincere thanks to **Prof. Dr. Teravuti Boonyasopon**, **Asst. Prof. Preecha Ongaree, Asst. Prof. Narong Bundit**, **Asst. Prof. Samarnmit Yousuksawadee** and **Jeerasak Chaungchai** (for all vital discussion about the work) at KMUTNB, Bangkok Thailand.

And last but not least…

…a sincere thanks to my mother and my godfather who have always been there for me.